

TECHNISCHE UNIVERSITÄT MÜNCHEN

Fakultät für Physik
Lehrstuhl für Funktionelle Materialien

**Investigation of nanostructured magnetic
thin polymer films**

Senlin Xia

Vollständiger Abdruck der von der Fakultät für Physik der Technischen Universität München zur Erlangung des akademischen Grades eines

Doktors der Naturwissenschaften (Dr. rer. nat.)

genehmigten Dissertation.

Vorsitzende: Prof. Dr. Andreas Weiler

Prüfer der Dissertation: 1. Prof. Dr. Peter Müller-Buschbaum
2. Prof. Dr. Friedrich C. Simmel

Die Dissertation wurde am 27.05.2019 bei der Technischen Universität München eingereicht und durch die Fakultät für Physik am 01.07.2019 angenommen.

Abstract

In the present thesis, magnetic thin films composed of various types of diblock copolymers (DBC) with embedded magnetic nanoparticles (NPs) are investigated with respect to their application as magnetic sensors. The main focus lies on the fabrication of magnetic anisotropic structures and the film deposition technique used for large scale production. For this, a printing technique is employed to fabricate magnetic films. The magnetic anisotropy is realized by either the employment of an external magnetic field during the printing process, or the use of solvent vapor annealing after printing. The latter method proves to be a more facile and straightforward route to prepare magnetically anisotropic films. Then, the kinetics of hybrid film formation, as well as the influence of magnetic NPs on the film growth is studied systematically via *in situ* grazing incidence small angle scattering (GISAXS). Results suggest magnetic NPs are advantageous in the formation of the NP-DBC films. In addition, dense magnetic nanostructures are created by incorporating NPs into the majority domain of DBC templates. Such magnetic films respond to the external magnetic field at an enhanced speed.

Zusammenfassung

In der vorliegenden Arbeit werden magnetische dünne Filme, die aus verschiedenen Arten von Diblockcopolymeren mit eingebetteten magnetischen Nanopartikeln (NP) bestanden, hinsichtlich ihrer Anwendungen als magnetische Sensoren untersucht. Das Hauptaugenmerk liegt auf der Herstellung von magnetisch anisotropen Strukturen und der Filmherstellungstechnik, die für die Produktion in großem Maßstab verwendet wird. Dazu wird zunächst eine Drucktechnik verwendet, um magnetische Filme herzustellen. Die magnetische Anisotropie wird entweder durch die Verwendung eines externen Magnetfeldes während des Druckprozesses oder durch die Behandlung mit Lösungsmittel-Dampf nach dem Drucken realisiert. Die letztere Methode erweist sich als ein einfacherer und direkterer Weg zur Herstellung magnetisch anisotroper Filme. Denn werden die Kinetik der Hybridfilmbildung sowie der Einfluss magnetischer Nanopartikel auf die Entstehung der Filme systematisch mittels Kleinwinkel-Röntgenstreuung unter streifendem Einfallswinkel (GISAXS) untersucht. Die Ergebnisse weisen darauf hin, dass magnetische Nanopartikel bei der Bildung der Hybridfilme vorteilhaft sind. Des Weiteren wird eine dichte magnetische Nanostruktur durch den Einbau von NPs in die Majoritätsdomäne von DBC-Templates erzeugt. Solche Magnetfilme sprechen auf das äußere Magnetfeld mit einer erhöhten Geschwindigkeit an.

Contents

| | |
|--|------------|
| Contents | iii |
| List of abbreviations | vii |
| 1 Introduction | 1 |
| 2 Theoretical aspects | 7 |
| 2.1 Polymer | 7 |
| 2.1.1 Polymer basics | 7 |
| 2.1.2 Phase separation | 12 |
| 2.1.3 Diblock copolymer in thin film geometry | 18 |
| 2.2 Magnetism | 20 |
| 2.2.1 Magnetism basics | 20 |
| 2.2.2 Magnetic materials | 23 |
| 2.2.3 Superparamagnetism | 25 |
| 2.2.4 Magnetic anisotropy | 28 |
| 2.2.5 Magnetic nanoparticles | 28 |
| 2.3 Scattering techniques | 29 |
| 2.3.1 Scattering basics | 29 |
| 2.3.2 Specular reflectivity | 31 |
| 2.3.3 Grazing incidence small angle X-ray scattering | 33 |
| 3 Characterization methods | 37 |
| 3.1 Structural characterizations | 37 |
| 3.1.1 Optical microscopy (OM) | 37 |
| 3.1.2 Atomic force microscopy (AFM) | 38 |
| 3.1.3 Scanning electron microscopy (SEM) | 39 |
| 3.1.4 Surface profilometry | 40 |
| 3.1.5 X-ray reflectivity (XRR) | 41 |
| 3.1.6 Grazing-incidence small-angle X-ray scattering | 43 |
| 3.2 Characterizations of magnetic properties | 45 |
| 3.2.1 SQUID magnetometry | 45 |

| | | |
|----------|--|-----------|
| 4 | Sample preparation | 47 |
| 4.1 | Materials | 47 |
| 4.1.1 | Diblock copolymer | 47 |
| 4.1.2 | Magnetic nanoparticles | 48 |
| 4.2 | Substrates | 49 |
| 4.2.1 | Acid bath cleaning | 50 |
| 4.2.2 | Basic bath cleaning | 50 |
| 4.3 | Film fabrication techniques | 51 |
| 4.3.1 | Solution preparation | 51 |
| 4.3.2 | Printing | 51 |
| 4.3.3 | Spray coating | 55 |
| 4.4 | Post-treatment | 56 |
| 4.4.1 | Thermal annealing | 57 |
| 4.4.2 | Solvent annealing | 57 |
| 5 | Printed magnetic anisotropic films with magnetic field | 59 |
| 5.1 | Printing magnetic films | 61 |
| 5.2 | Formation of NP wires and surface morphology | 62 |
| 5.3 | Inner morphology | 65 |
| 5.3.1 | Lateral structures perpendicular to the NP wires | 66 |
| 5.3.2 | Lateral structures parallel to the NP wires | 68 |
| 5.3.3 | Morphology evolution | 68 |
| 5.4 | Magnetic properties | 69 |
| 5.4.1 | Influence of temperature | 70 |
| 5.4.2 | Influence of NP concentration | 71 |
| 5.4.3 | Influence of orientation | 72 |
| 5.4.4 | Influence of film morphology | 73 |
| 5.5 | Summary | 75 |
| 6 | Printed magnetic anisotropic films without magnetic field | 77 |
| 6.1 | Solvent vapor annealing | 78 |
| 6.2 | Film thickness | 80 |
| 6.3 | Surface structure | 81 |
| 6.3.1 | Largescale structures | 81 |
| 6.3.2 | Nanoscale structures | 81 |
| 6.4 | Inner structure | 87 |
| 6.5 | Morphology evolution | 91 |

| | | |
|-----------|--|------------|
| 6.6 | Magnetic properties | 92 |
| 6.6.1 | Influence of temperature | 92 |
| 6.6.2 | Influence of NP concentration | 93 |
| 6.6.3 | Influence of morphology | 94 |
| 6.7 | Conclusion | 99 |
| 7 | In situ investigation on the magnetic film formation during spray coating | 101 |
| 7.1 | Spray coating | 102 |
| 7.2 | Surface structure | 104 |
| 7.3 | Inner structure | 106 |
| 7.3.1 | Formation of pure DBC film | 107 |
| 7.3.2 | Formation of hybrid film | 109 |
| 7.3.3 | Influence of NPs on the film formation | 113 |
| 7.4 | Magnetic properties | 114 |
| 7.5 | Conclusion | 117 |
| 8 | Printed thin magnetic films with dense magnetic nanostructure | 119 |
| 8.1 | Film thickness | 120 |
| 8.2 | Surface structure | 122 |
| 8.3 | Inner structure | 128 |
| 8.3.1 | Lateral nanostructure | 128 |
| 8.3.2 | Vertical nanostructure | 133 |
| 8.4 | Magnetic properties | 135 |
| 8.4.1 | Influence of temperature | 136 |
| 8.4.2 | Influence of NP concentration | 137 |
| 8.4.3 | Influence of magnetic structure density | 138 |
| 8.5 | Summary | 139 |
| 9 | Conclusion and outlook | 141 |
| 10 | Appendix | 145 |
| 10.1 | Materials and film fabrication | 145 |
| 10.2 | Chamber | 146 |
| 10.3 | Polarized neutron reflectivity | 146 |
| 10.4 | Surface structure | 149 |
| 10.5 | Magnetic structure | 149 |
| 10.5.1 | PNR data collected at three stages | 149 |
| 10.5.2 | Influence of temperature/humidity on the magnetic behavior | 152 |

| | |
|-----------------------------|------------|
| Bibliography | 155 |
| List of publications | 171 |
| Acknowledgements | 175 |

List of abbreviations

| | |
|-------------|---|
| D: | periodic domain distance |
| D_{spm} : | critical diameter of superparamagnetic nanoparticle |
| B_c : | coercivity |
| C: | concentration |
| M_s : | saturation magnetization |
| M_r : | remanence |
| M_w : | molecular weight |
| N: | degree of polymerization |
| R_{rms} : | root-mean-square roughness |
| T_g : | glass transition temperature |
| T_B : | blocking temperature |
| AFM: | atomic force microscopy |
| DBC: | diblock copolymer |
| DWBA: | distorted wave Born approximation |
| FFT: | fast Fourier transform |
| FWHM: | full width at half maximum |
| GISAXS: | grazing incidence small angle x-ray scattering |
| NPs: | nanoparticles |
| OM: | optical microscopy |
| PS: | polystyrene |
| PSD: | power spectra density |
| PMMA: | poly(methyl methacrylate) |
| PNIPAM: | poly(N-isopropyl acrylamide) |
| SDD: | sample-detector distance |
| SEM: | scanning electron microscopy |
| SLD: | scattering length density |
| SVA: | solvent vapor annealing |
| XRR: | x-ray reflectivity |

1 Introduction

Magnetic films can respond to an external magnetic field, which is largely used in compact field-responsive electromagnetic sensor applications [1–3]. Conventional magnetic materials are hard materials including metals, metal oxides and metallic alloys. The intrinsic hardness and stiffness of such materials seriously limit their use in bendable applications like flexible sensors and wearable electronics. In recent decades, the device fabrication has undergone a remarkable change due to the use of polymer materials. Because of their unique properties including flexibility, light weight, easy processability and transparency, polymer materials have received increasing attention when being incorporated into devices. Polymer materials can be used as a soft matrix to incorporate hard inorganic magnetic nanoparticles (NPs). Such a hybrid approach combining polymers and NPs provides the possibilities of versatile fabrication as known from pure polymer materials, which allows broadening the possible applications. The obtained magnetic NP–polymer hybrid materials combine the characteristic performance of both, polymer materials and the employed NPs. Thereby, they have attracted increasing research interest. For example, magnetic polymer hybrid films have shown potential applications in areas like magnetic sensors and information storage devices [4, 5]. Therefore, it is essentially important to investigate the interplay between the structure, properties and fabrication techniques of magnetic polymer hybrid films.

In many applications, such as magnetic sensors and switches, the assembly and ordering of NPs exhibit a strong influence on the properties of the resulting hybrid films. In particular, diblock copolymers (DBC) are widely considered as a powerful template to guide the localization of NPs, due to their ability to form spatially periodic nanostructures via self-assembly [6, 7]. Various nanostructures, such as hexagonally arrayed cylinders, spheres, lamellae and gyroids, can be formed by varying the parameters, such as molecular weight, molar fraction and interaction parameter of the constituent blocks. By post-treatment of the DBCs via thermal annealing or solvent vapor annealing, nanostructures with a high spatial order can be obtained [8, 9].

To obtain high-quality NP-DBC films, a homogeneous dispersion of magnetic NPs inside DBC matrix is necessary. However, the known incompatibility between magnetic

NPs and DBC could impair the dispersion of particles, which may lead to unexpected localization of magnetic NPs. The unfavorable miscibility originates from the metallic nature of the inorganic magnetic NPs and organic chemistry of the polymers. Additionally, most magnetic NPs are ferromagnetic or behaves like ferromagnetic materials at room temperature. Thus, the magnetic attractive force among magnetic NPs can lead to the formation of large agglomerates of NPs, which also impair the uniform dispersion of NPs in the organic matrices. Pioneering work has been done to tackle this issue.

It has been proved that surface modification on magnetic NPs, such as chemical treatment [10,11], grafting of synthetic polymers [12,13], ligands exchange [14,15] and adsorption of polymeric dispersants [16,17], are efficient and constructive techniques to enhance the affinity of magnetic NPs to the polymer template. For example, Sabzi et al. modified TiO₂ NPs with aminopropyltrimethoxysilane and achieved a homogeneous dispersion of NPs incorporated in a polyurethane matrix [10]. Barandiaran et al. grafted PMMA polymer chains on the surface of Fe₂O₃ NPs and accordingly enhanced the selectivity of NPs to PMMA blocks. From the fabricated films, a desirable localization of the NPs inside the poly(isoprene-block-methyl methacrylate) (PI-*b*-PMMA) template was achieved [12]. Among the techniques mentioned above, grafting magnetic NPs' surface with polymer chains has become one of the most successful and adopted routes. With the surface functionalization, the magnetic NPs, on the one hand, can get preferentially incorporated in a specified block of a DBC. On the other hand, the energy-minimization driven tendency of magnetic NPs aggregating to bigger agglomerates can be reduced through effects such as steric hindrance.

Generally, the integrated properties of the hybrid magnetic films depend not only on the properties of the individual components, but also on the spatial localization and arrangement of magnetic NPs within the DBC matrix. In the NP-DBC hybrid system, polymer nanostructures and NP dispersion are interplaying parameters. The nanostructure of the polymer matrixes plays an indispensable role in the corresponding magnetic property. Better ordered and more homogeneously distributed NPs contribute to a more desirable magnetic behavior [18,19]. Therefore, it is of great importance to investigate the hybrid systems in detail. For example, the influence of magnetic NPs and post-treatment on the DBC nanostructures, how to establish dense magnetic nanostructures in the hybrid systems, the kinetics of the hybrid films formation, the role of NPs arrangement in the finally obtained magnetic properties, and whether the investigated systems are influenced by external magnetic fields are fields of interests.

Moreover, the film fabrication technique is also crucial in achieving high-quality films. To date, most of the films investigated in literature were prepared via spin-coating, solution casting, or dip-coating. Concerning large-scale production, new effective techniques

are required. For instance, printing and spray coating, which have been successfully used in other research areas [20,21], can be considered. Both of these techniques can be applied for *in situ* investigations, which provides the opportunity to follow the kinetic process of film formation. Additionally, printing can be used in combination with external fields (eg. magnetic field), thus magnetic anisotropy of hybrid films can be realized.

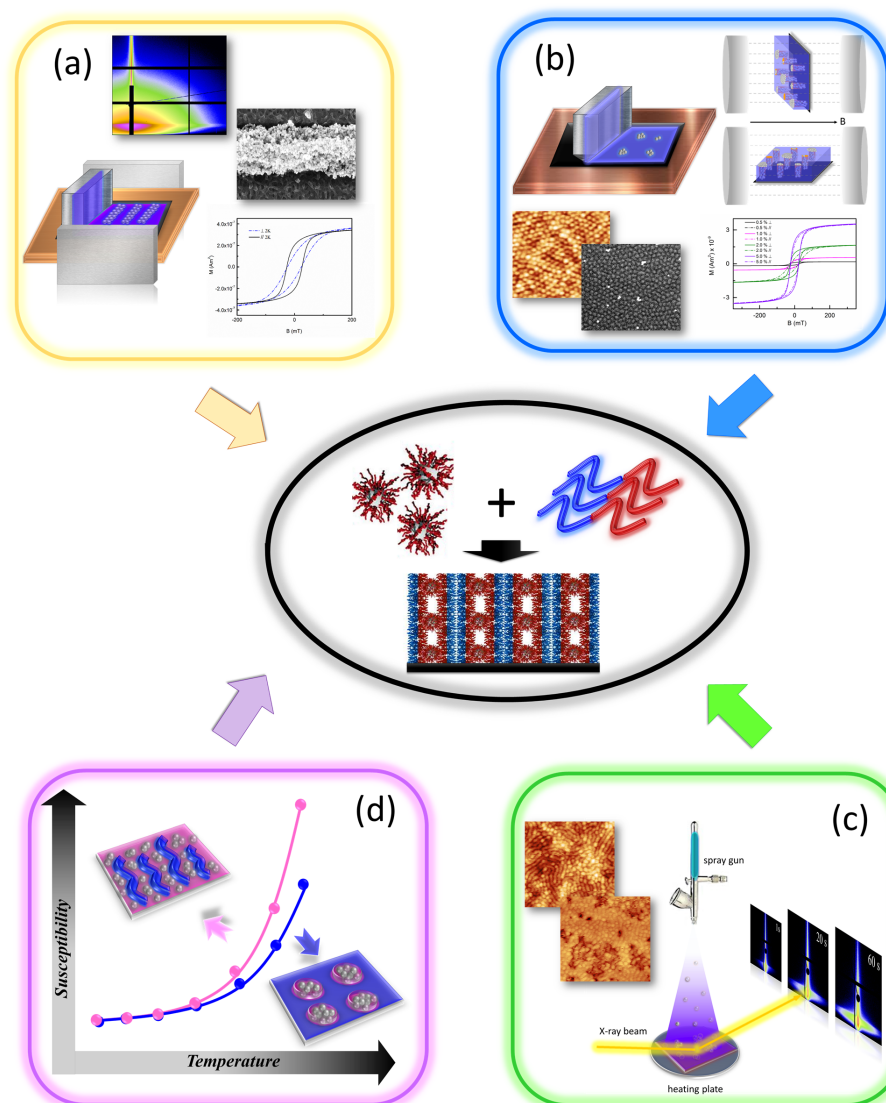


Figure 1.1: Schematic overview of different NP-DBC systems investigated in the present thesis. (a) Printed magnetic anisotropic films within an external magnetic field. (b) Printed magnetic anisotropic films without magnetic field. (c) Investigation on the kinetics of film formation during spray deposition. (d) Printed hybrid films with dense magnetic nanostructures

In the present thesis, the investigation is focused on the scalable fabrication techniques

with three individual, which are the magnetic anisotropy of hybrid films, the kinetics of NP-DBC film formation, and the establishment of dense magnetic nanostructures. To start with, the related theory background is introduced in chapter 2, which includes the basics of polymers, microphase separation of DBC, magnetism, superpara-magnetic behavior, the fundamentals of the employed scattering techniques for structure investigation. Then the characterization methods and the corresponding parameters used for measurements are stated in chapter 3, followed by chapter 4 describing the sample preparation techniques. The obtained results and related discussions are addressed from chapter 5 to chapter 8. Figure 1.1 depicts the overview of the different research topics. More details regarding the discussed points are as follows:

For sensor applications, the magnetic anisotropy is a decisive parameter of magnetic thin films. Also in the point of view of real application, large scale fabrication techniques of magnetic films, like printing and spraying, need to be taken into account. Chapter 5 and chapter 6 focus on preparing magnetically anisotropic NP-DBC films by printing technique. The optimization of printing parameters is addressed in chapter 5. In chapter 5 (Figure 1.1 a), an external magnetic field is employed to direct the alignment of magnetic NPs during printing, thus films with magnetic anisotropy are fabricated. While in chapter 6 (Figure 1.1 b), instead of magnetic field, solvent vapor annealing is applied in film preparation. This provides a new and facile to route to fabricate magnetically anisotropic films.

In addition to investigating the finally obtained dry films, it is also necessary to understand the formation process of NP-DBC films. In chapter 8 (Figure 1.1 c), the study is extended to the evolution of NP-DBC films. Spray coating is used for film deposition, during which the film growth behavior is monitored via *in situ* GISAXS technique. The involved kinetics and the influence of magnetic NPs on the overall structure formation are discussed.

To enhance the response ability of magnetic films to the external magnetic field, dense magnetic nanostructures are necessarily required. In chapter 8 (Figure 1.1 d), a PS-*b*-PMMA template with a high PS volume fraction is used. Via solvent vapor annealing, a cylindrical morphology orienting parallel to the substrate is achieved. The employed NPs are selectively located inside the majority PS domain, which offers a large accommodation capacity. The formation of large NP aggregates are suppressed, due to the parallel oriented morphology, in which the majority PS domains are separated by the minority PMMA domains. The obtained magnetic films show stronger response behavior to external magnetic field, as compared with the films fabricated in chapter 6, where identical NPs are used.

All the results obtained in these associated topics are systematically summarized in chapter 9. In the end, a brief outlook based on the present investigations is provided.

2 Theoretical aspects

The present thesis focuses on hybrid systems consisting of different types of magnetic nanoparticles (NPs) and diblock copolymers (DBC). For the applications in areas like magnetic sensors, the arrangement of NPs guided by DBC templates is a crucial parameter. Therefore, it is of great importance to investigate the morphology of the NP-DBC hybrid films at the nanoscale. For this purpose, the related theoretical basics of the whole hybrid system are presented in this chapter. The polymer basics are addressed in Section 2.1 with emphasis on the microphase separation of DBC. Following in Section 2.2 is the theory of magnetism, especially of the superparamagnetism. Finally, the grazing incidence x-ray scattering technique, which is applied for investigation on the inner structure of films, is addressed in the last Section 2.3.

2.1 Polymer

This section presents a fundamental introduction to polymers. General definitions and nomenclature, configuration and conformation, and glass transition temperature of polymer are described in Section 2.1.1. The microphase separation behavior of polymer is addressed in Section 2.1.2. Then, the basics of DBC films, which are used for templating magnetic NPs, are introduced in Section 2.1.3.

2.1.1 Polymer basics

Basic definitions

A polymer refers to a macromolecule composed of multiple repeating small units, which are covalently linked with each other. These small units are called monomers, which are always of relatively low molecular mass. In strict terms, a polymer has a molecular weight (M_w) of more than 10 kg mol^{-1} . Below this value, molecules are called oligomer ($1 \leq M_w \leq 10 \text{ kg mol}^{-1}$) and micromolecule ($M_w < 1 \text{ kg mol}^{-1}$) [22].

Based on the number of the types of repeating unit, polymers can be divided into two different categories, which are homopolymer and copolymer. If a polymer is composed of only one single type of repeating units, it is called homopolymer (see Figure 2.1). When two or more kinds of the repeating units are present in a polymer, it is then named as copolymer. Along the polymer chain, different repeating units can arrange themselves in various manners. Therefore, copolymer can be subdivided into several different categories. To simplify the representation, the copolymer categories are depicted by only two different kinds of repeating units, which are unit A and B (see Figure 2.1). In case the units repeat within certain rules, the copolymer is called statistical copolymer. If the units are arranged in random way, it is called random copolymer. When unit A and B repeat alternatively along the polymer chains, it is called an alternating copolymer. In case of a copolymer composed of two polymer blocks, it is called diblock copolymer. Another type of copolymer is graft copolymer, in which there exists a main homopolymer chain and side chains of a different homopolymer. Figure 2.1 shows the structure of different types of polymers mentioned above.

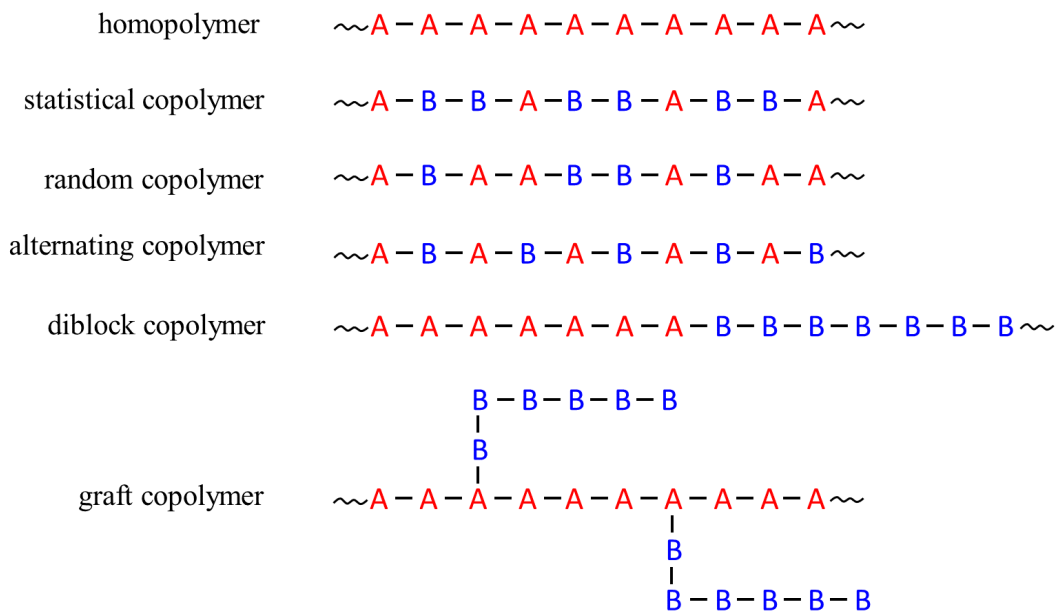


Figure 2.1: Structures of homopolymer and different types of copolymer present in this chapter.

The polymer properties have a strong dependence on the molar mass. Molar mass (or molecular weight) is the mass of 1 mol of the polymer. It is given in units of kg mol^{-1} or g mol^{-1} . The molar mass of a homopolymer is related to the polymerization degree (N),

which represents the number of the repeating units. Assuming that the molar mass of the repeat unit is M_u , then the molar mass of the homopolymer (M_H) can be given by:

$$M_H = NM_u \quad (2.1)$$

In case of a copolymer, the molar mass (M_C) can be calculated via:

$$M_C = N(\sum f_j M_j) \quad (2.2)$$

Where M_j and f_j represent the molar mass and molar fraction of the "j" type repeat unit in the copolymer, respectively. It is important to note that the polymer molar mass represents a distribution, since the polymers are composed of chains with a range of molar masses.

In the real application, the average molar weight is more frequently used. Two commonly used types of average molar mass are introduced in this thesis, which are number average molar mass and weight average molar mass. The number average molar mass (M_n) is defined as the average of the molar masses of all fractions:

$$M_n = \frac{\sum_i n_i M_i}{\sum_i n_i} \quad (2.3)$$

where n_i and M_i represent the macromolecule number and molar mass of component i , respectively. The weight average molar mass can be described as:

$$M_w = \sum w_i M_i = \frac{\sum_i n_i M_i^2}{\sum_i n_i M_i} \quad (2.4)$$

Moreover, the ratio of M_w/M_n is known as the polydispersity (PDI), describing the width of distribution. Normally, M_w is slightly larger than M_n , therefore the PDI can be described by:

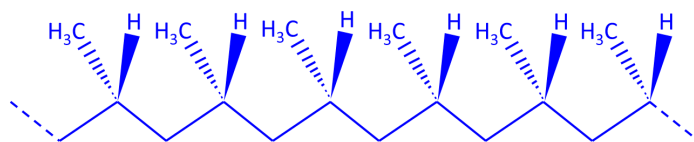
$$PDI = \frac{M_w}{M_n} = U + 1 \quad (2.5)$$

where U is the inconsistency, which also describes the distribution width as PDI. For a polymer with a uniform distribution of molar mass, $U = 0$ is observed.

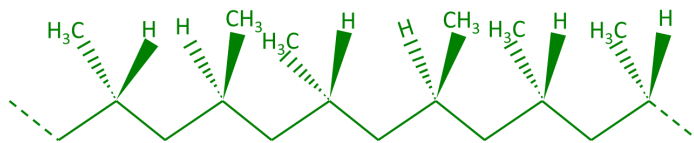
Configuration and conformation

In addition to the molar mass, the configuration and conformation are also crucial parameters of a polymer, on which the materials properties, like melting temperature, chain flexibility, and solubility in solvent, have a strong dependence. The configuration describes the spatial order of different side groups or substituents along the polymer main chain. The polymer configuration is fixed and not changeable unless the covalent bonds between chemical atoms are broken and relinked. Generally, based on the spatial order of the substitute groups (with respect to the carbon double bond), polymer configuration can be categorized into two basic geometries which are named as *cis* and *trans*. The *trans* configuration describes the geometry where the substitute groups are located on the opposite sides of the carbon double bond. In case all substitute groups are on the same side of the double bond, the polymer is showing a *cis* configuration. The stereoregularity of a polymer chain is called tacticity, which represents the steric order of the pendant groups along the polymer backbone. If all the pendant groups on the same side, the configuration is called isotactic (see Figure 2.2 a). In case of alternating placement of the side groups, such arrangement is called syndiotactic (see Figure 2.2 b). Random localization of the substitute groups on either side results in a atactic configuration (see Figure 2.2 c).

(a) isotactic configuration:



(b) syndiotactic configuration:



(c) atactic configuration:

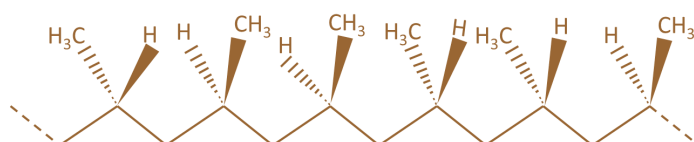


Figure 2.2: Schematics of (a) isotactic, (b) syndiotactic and (c) atactic configuration of polymer. Graphs are modified based on the reference [23].

In contrast to configuration, conformation refers to the 3D spatial arrangement of atoms or substituents on the polymer chains. It is convertible and can be changed simply by the rotations around carbon-carbon single bonds. According to the potential energy related to the rotation angle, three different types of conformations are defined in a polymer, which are trans, gauche + and gauche -, seen in Figure 2.3.

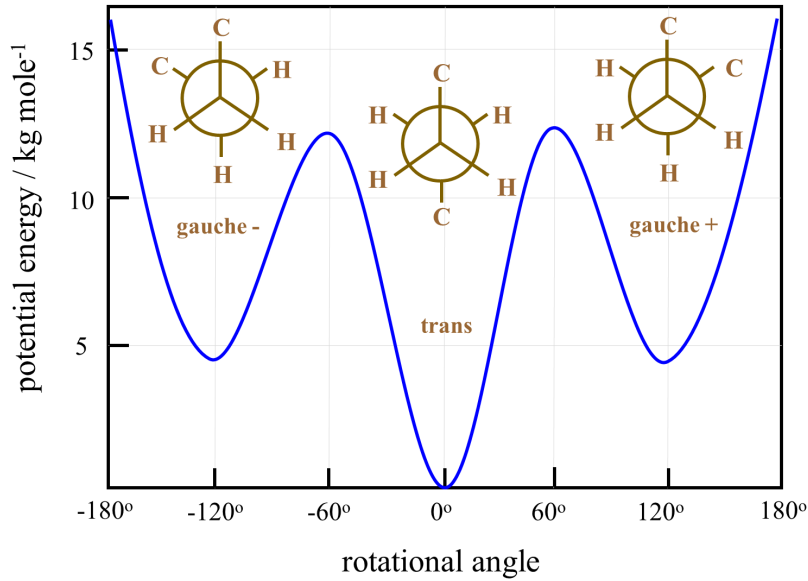


Figure 2.3: Three different conformations of polymer based on the rotation angle. Graphs are modified based on the reference [24].

Glass transition temperature

The glass transition temperature (T_g) is an indispensable parameter in the investigation of amorphous polymer in the present thesis. It is a critical temperature, at which polymer material transits from a glassy and hard state (below T_g) into a rubbery and soft state (above T_g) [25]. In the glassy state, only atoms on the polymer chains are vibrating or rotating in short range. In the rubbery state, long-range rotational motion of polymer segments are present. Usually, differential scanning calorimetry (DSC) is employed to measure the T_g of a polymer.

So far, two different theories are applied by scientists to describe the polymer transition process from the glassy state into the rubbery state, or vice versa. One is the molecular theory focusing on the convertible conformation of polymer chains [25]. According to this theory, the number of conformations is limited due to the frozen polymer segments at $T < T_g$, therefore polymer shows a glassy solid state. Whereas at $T > T_g$, the polymer

segments have sufficient mobility to reach all possible conformations by rotating around the carbon-carbon single bonds. In this case, the polymer behaves like a soft rubber. The other theory, the free-volume theory, is based on the concept of free volume created by the gap between polymer chains [26]. As defined, the free volume refers to the space which is unoccupied by molecules in the polymer, and it is larger in a liquid than in a solid. Therefore at temperatures above T_g , the molecular motion is allowed due to the free space. As temperature is lowered, the free volume is reduced. Thus the molecular motion is limited at the temperature below T_g . The T_g of a polymer can be influenced by many factors, like the chain flexibility, steric effects, additional plasticizer, cross linking and copolymerization.

In the present thesis, annealing at suitable temperature is used as a post-treatment technique to allow the polymer film morphology to reach the equilibrium state. Therefore, the annealing temperature is a key factor for the thermal annealing process. Normally a temperature higher than the T_g of the employed polymer is used, so that the free motion of polymer chains can be realized. However, the annealing temperature should not be too high, otherwise the ordered structure established initially in the polymer film will be damaged.

For all studies in the present thesis, DBCs are used for investigation. According to the Flory-Fox relationship [27], the approximate T_g of a DBC can be estimated by equation 2.6, ignoring the chemical bond between two blocks.

$$T_g = \frac{T_g^A}{\psi_A} + \frac{T_g^B}{\psi_B} \quad (2.6)$$

in which T_g^A and T_g^B are the T_g of block A and B in a DBC, respectively. ψ_A and ψ_B represent the volume fraction of block A and B in the entire DBC, respectively.

2.1.2 Phase separation

Most of polymer-related applications so far have been contributed by polymer blends, since combination of various polymers can offer different properties. Also in the present thesis, DBCs are employed for investigations. Therefore, it is necessary to have an insight into the mixing properties. For instance, under which conditions will the polymer blends form a homogeneous phase or a two-phase structure? How are the structures developed and how can they be tuned and controlled? This section will focus on the phase separation to address the topics mentioned above. The related interpretation and discussion are based on textbooks [25, 26, 28].

The mean-field theory, which was developed by M. L. Huggins and P. J. Flory, is generally used to explain the mixing properties of polymer blends [29,30]. In case of a polymer blend consisting of two different components, a complete phase separation will be frequently observed due to the unfavorable interactions between them. Based on the thermodynamics, the miscibility of different blend parts can be described by the changes of the Gibbs free energy (ΔG_m):

$$\Delta G_m = \Delta H_m - T\Delta S_m \quad (2.7)$$

where ΔH_m and ΔS_m represent the enthalpy and entropy of mixing at the given temperature T . Therefore, a complete miscibility, meaning a stable one-phase system, can be obtained when ΔG_m is negative.

The miscibility of a polymer blend is influenced by many factors, like the interaction energy, entropy of mixing, special interactions between molecules and so on. In case of a blend composed of nonpolar polymers, the miscibility can be described by the Flory-Huggins equation:

$$\frac{\Delta G_m}{RT} = \frac{\phi_A}{N_A} \ln \phi_A + \frac{\phi_B}{N_B} \ln \phi_B + \phi_A \phi_B \chi \quad (2.8)$$

where R is the gas constant. ϕ_A and ϕ_B are the volume fraction of component A and B, respectively. N_A and N_B are the polymerization degrees of A and B polymers, respectively. In equation 2.8, $\frac{\phi_A}{N_A} \ln \phi_A + \frac{\phi_B}{N_B} \ln \phi_B$ describes the entropy of mixing, while the enthalpy of mixing is addressed by $\phi_A \phi_B \chi_{AB}$. χ represents the Flory-Huggins interaction parameter between A and B polymer, which includes enthalpic (χ_H) and entropic (χ_S) contributions. By setting up χ as equation 2.9:

$$\chi = \frac{\chi_H}{T} + \chi_S \quad (2.9)$$

The entropic part can be expressed as equation 2.10:

$$\chi_S = \frac{\partial}{\partial T}(\chi T) \quad (2.10)$$

and the enthalpic contribution as equation 2.11:

$$\chi_H = -T \frac{\partial \chi}{\partial T} \quad (2.11)$$

In case of $\chi > 0$, mixing is unfavored since the entropic contribution is mostly positive. At $\chi < 0$, mixing occurs.

For a symmetric mixture where the polymerization degrees of both parts are equal, namely:

$$N = N_A = N_B \quad (2.12)$$

the Flory-Huggins equation (equation 2.8) can be written as:

$$\Delta G_m \frac{N}{RT} = \phi_A \ln \phi_A + \phi_B \ln \phi_B + \chi N \phi_A \phi_B \quad (2.13)$$

One can note that χN is the only relevant parameter in equation 2.8.

Figure 2.4 shows the phase diagram of a symmetric polymer blend, in which both polymers have equal polymerization degree. The binodal (solid line in Figure 2.4) shows the boundary between the homogeneous and two-phase state of a polymer blend. By calculating the second derivative of ΔG_m (equation 2.8), the critical interaction parameter χ_{crit} can be give as:

$$\chi_{crit} = \frac{1}{2} \left[\frac{1}{\sqrt{N_A}} + \frac{1}{\sqrt{N_B}} \right]^2 \quad (2.14)$$

From Figure 2.4, it can be noted that the phase diagram is symmetric. In case of a polymer blend composed of polymers with different polymerization degrees, meaning $N_A \neq N_B$, an asymmetric phase diagram can be observed.

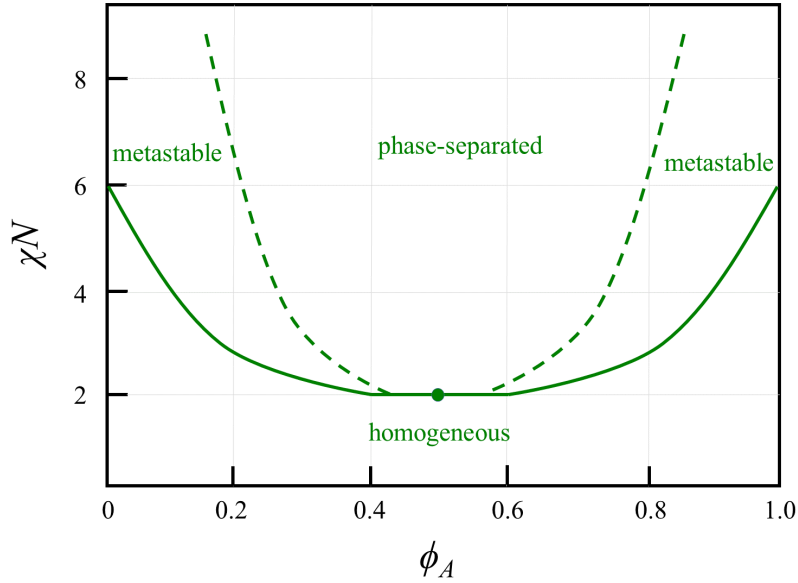


Figure 2.4: Phase diagram of a symmetric system where both polymers have equal polymerization degree. Different states of polymer blend are indicated. The solid line shows the binodal, and the dashed one is the spinodal. The critical point is suggested by the solid dot. Graphs are modified based on the reference [25].

Microphase separation of DBC

A DBC is composed of two chemically different blocks, which are linked via a covalent bond. On one hand, the two blocks have the tendency for separation due to the repulsive force between the two blocks. On the other hand, however, a macroscopic demixing behavior is hindered since the two blocks are covalently bonded. As a consequence, a microphase separation appears in a DBC with a characteristic morphology depending on the length of each block. Due to the homogeneous dimension of all resulting domains, a nanostructure with periodic center-to-center domain spacing can be achieved for a DBC.

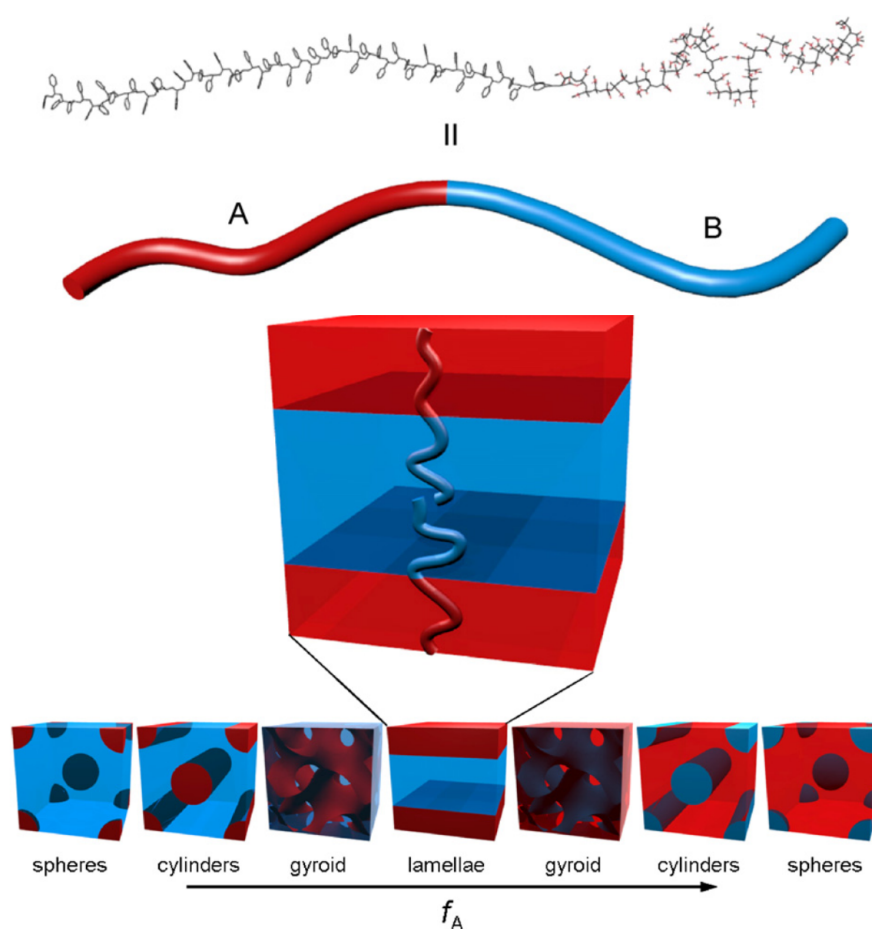


Figure 2.5: Schematics of thermodynamically stable DBC (PA-*b*-PB) phases. The DBC molecules are depicted at the top. For simplicity, A and B blocks are colored as red and blue, respectively. f_A represents the volume fraction of A block in the DBC. The image is reprinted with permission from [7], Darling, S. Directing the self-assembly of block copolymers. *Progr. Polym. Sci.* 32, 1152–1204 (2007). ©2007, Elsevier

Figure 2.5 shows the typical stable morphologies resulted from microphase separation

of DBC systems. The types of mesoscopic structures depends on the volume fractions of the polymer blocks. For a given DBC PA-*b*-PB, the volume fraction of A block (f_A) is defined as:

$$f_A = \frac{N_A}{N_A + N_B} \quad (2.15)$$

where N_A and N_B are the polymerization degrees of block A and B, respectively.

At $f_A < 0.17$, a body-centered cubic spherical morphology with A spheres dispersed in the continuous B matrix is favored. At $0.17 < f_A < 0.30$, a cylindrical geometry with A domains aligning inside the continuous B matrix is preferred. At $0.30 < f_A < 0.50$, a bicontinuous morphology with gyroidal A domains interpenetrating the B matrix can be obtained. At $f_A \approx 0.50$, a lamellar structure with sheet domains A and B arranged alternatively is formed. With f_A further increasing, similar but inverse structures appear.

According to the discussion in previous sections, in addition to the polymerization degree (N) and volume fraction (F), the Flory-Huggins interaction parameter χ and architectural constraint (n) of molecules are also important parameters determining the morphological phase state of a DBC. As known, F and n are already included in χ . Therefore, it is sufficient to discuss the phase state of a DBC in the framework of two factors N and χ . In case of short polymer chains and/or high temperatures, namely the DBC system is dominated by entropy, since N and/or χ are small, leading to a small value of χN . In case of long polymer chains and/or low temperatures, namely the system is dominated via enthalpy, N and/or χ are large. Thus a large value of χN is achieved.

Based on the value of χN , two main theories are developed to address the DBC phase diagram. In case of $\chi N \ll 1$, the interactions between A and B blocks in the PA-*b*-PB DBC are quite weak and the DBC melt is in a disordered state. When the χN increases to around 10, a disorder-to-order (DTO) phase transition occurs due to a balance between the entropic and enthalpic contributions. In the vicinity of DTO transition, the interactions between A and B blocks still remain weak. This regime is referred to the weak segregation limit (WSL). The composition profile of WSL is shown as Figure 2.6 a, where a smooth fluctuation of the local composition ($f(r)$) with the distance r from an arbitrary molecules is present. The microdomain period (D_{wsl}) is scaled as equation 2.16

$$D_{wsl} \sim R_g \sim a\sqrt{N} \quad (2.16)$$

where R_g and a represent the DBC radius of gyration and characteristic segment length, respectively.

For $\chi N \gg 10$, the strong segregation limit (SSL) theory is applied. In this regime, sharp A-B interfaces are developed, which leads to the formation of microdomains containing pure A or B composition. The composition file ($f(r)$) varies periodically and sharply with the distance (r). The corresponding microdomain period (D_{ssl}) is scaled as follows:

$$D_{ssl} \sim aN^{2/3}\chi^{1/6} \quad (2.17)$$

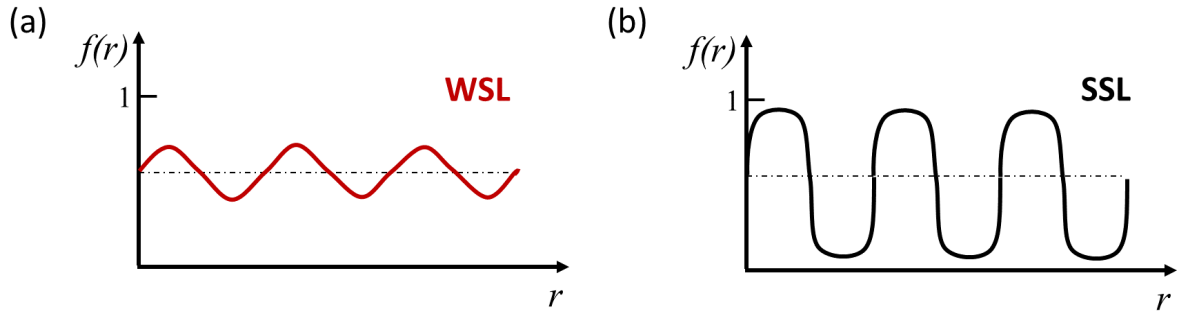


Figure 2.6: The local volume fraction $f(r)$ in different limiting regimes: (a) weak segregation limit and (b) strong segregation limit. r is the distance from an arbitrary molecule. The image is modified based on the reference [31].

To address the phase separation of DBCs in the strong segregation limit, a lot of notable theoretical studies have been done by researchers. To quantify the calculation of composition profiles, free energies and chain conformations, Helfand and Wasserman developed a self-consistent field theory [32]. Their theory describes that the free energy has contributions from three factors, which are the contact enthalpy at the A-B block interfaces, the entropy of the extended chain configuration and the confinement entropy caused by the covalent bonding between the two blocks. Further, they proposed a numerical procedure to calculate the phase diagram of the ordered phases in the SSL. Based on their theory, a characteristic interface thickness can be obtained as $a/\sqrt{\chi}$. By assuming $N \rightarrow \infty$, a microdomain period D_{HW} can be estimated by equation 2.18

$$D_{HW} \sim aN^\delta\chi^\mu \quad (2.18)$$

where $\delta \approx 0.643$, and $\mu \approx 0.143$

Based on the analogy to classic mechanics, Semenov *et al.* developed an analytical method in order to estimate the free energy in case of $N \rightarrow \infty$. The method only works for the polymer chains with strong stretching, but is less complicated than that from Helfand and Wasserman. Semenov's approach suggests that the DBC molecules display a non-uniform stretching behavior, and the polymer chain ends tend to be located inside the

microdomains. According to Semenov's prediction, the domain size can be estimated as $D_S \sim aN^{2/3}\chi^{1/6}$. It allows to predict the phase compositions which have no temperature dependence. The difference between theories provided by Helfand and Wasserman and Semenov results from the numerical calculations, when the numerics are only extended to $D/aN^{1/2} \approx 3$. At $D/aN^{1/2} \rightarrow \infty$, the difference disappears.

2.1.3 Diblock copolymer in thin film geometry

For bulk DBCs, the structures resulting from microphase separation are oriented in a random way. For applications, ordered structures, which can be achieved in DBC thin films, are highly favorable. In the present thesis, thin films are fabricated by DBCs. Therefore, the discussion of DBCs in this section is mainly focused on thin films.

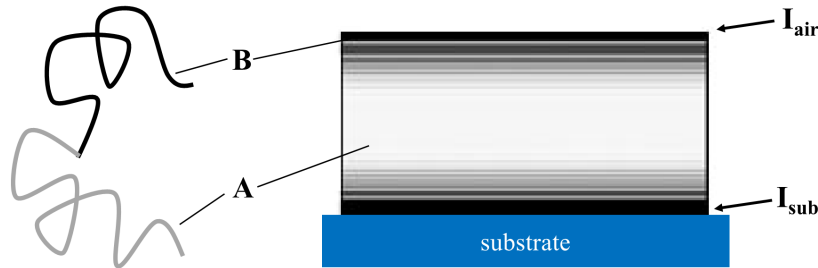


Figure 2.7: Schematic morphology of a DBC (PA-*b*-PB) thin film. Grey and black parts correspond to the two blocks A and B in the DBC, respectively. I_{sub} and I_{air} indicate the substrate/DBC and DBC/air interfaces, respectively. The image is modified based on the reference [33].

The morphology of DBC thin films is mainly determined by three factors, which are the boundary conditions at the film interfaces, the DBC domain spacing and the film thickness. Since the DBC films in the present thesis are established on solid substrates with the film top surface facing the air, two interfaces are included as substrate/DBC (I_{sub} in Figure 2.7) and DBC/air (I_{air} in Figure 2.7). As a consequence, two different interface boundary conditions can be discussed: symmetric wetting conditions and asymmetric wetting conditions. The symmetric wetting condition refers to a DBC system where the polymer blocks exhibit no preference to the two different interfaces. In contrast, the asymmetric wetting condition describes a DBC system in which one block shows affinity to the DBC/air interface, and the other block is favored by the DBC/substrate interface. Moreover, literature shows that domain orientation in a DBC film has a strong dependence on the film thickness. Generally, a perpendicular orientation with respect to the substrate

is favored, when the film thickness is smaller than the DBC period. Otherwise, a parallel orientation is present in the DBC film. Details are discussed in the following section.

Symmetric DBC thin films

For the thin films made of compositionally asymmetric DBCs, structures, like spheres or gyroids, are formed with curved interfaces, which lead to extra complexity in addressing the morphological behavior. So far, theoretical investigations have been carried out rarely. In the present thesis, the discussion focuses on the compositionally symmetric DBC films. In case of a compositionally symmetric PA-*b*-PB film ($f_A = 0.5$, $\gamma_A \neq \gamma_B$), the morphology orientation results from the interfacial and surface energy minimization, as illustrated by Figure 2.7. The overall trend is directed by the relation between the film thickness d and the DBC period D_0 .

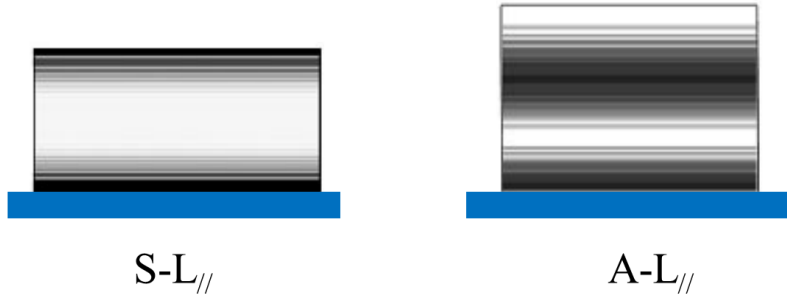


Figure 2.8: Morphologies of a compositionally symmetric DBC thin film at $d \geq D_0$. $S-L_{//}$ and $A-L_{//}$ represent the morphology in symmetric and asymmetric wetting conditions, respectively. The image is modified based on the reference [33].

(1) At $d \geq D_0$, lamellar structures (parallel with respect to the substrate) can be found for both symmetric ($S-L_{//}$ in Figure 2.8) and asymmetric ($A-L_{//}$ in Figure 2.8) wetting conditions. For such morphologies, the boundary conditions at both interfaces (I_{sub} and I_{air}) are fulfilled. Also an equilibrium period D_0 can be achieved from the ordering. In the symmetric wetting condition, the morphology $S-L_{//}$ is stable at $d = nD_0$ (n is an integer), whereas, stable morphologies are obtained at $d = (n + 1/2)D_0$ in the asymmetric wetting condition [33].

(2) At $d \leq D_0$, the parallel orientation (with respect to the substrate) of the lamellar morphology is no longer favored, since a domain size smaller than D_0 is required. In this case, a perpendicularly oriented morphology (with respect to the substrate) is favorable, which consequently maintains the equilibrium period D_0 laterally in the DBC film. Researchers have reported hybrid structure S-H and perpendicular lamellar structure $S-L_{\perp}$

for the symmetric wetting condition, and hybrid structure A-H and parallel half-lamellar structure A-HL_{//} for the asymmetric wetting condition (see Figure 2.9) [34–36].

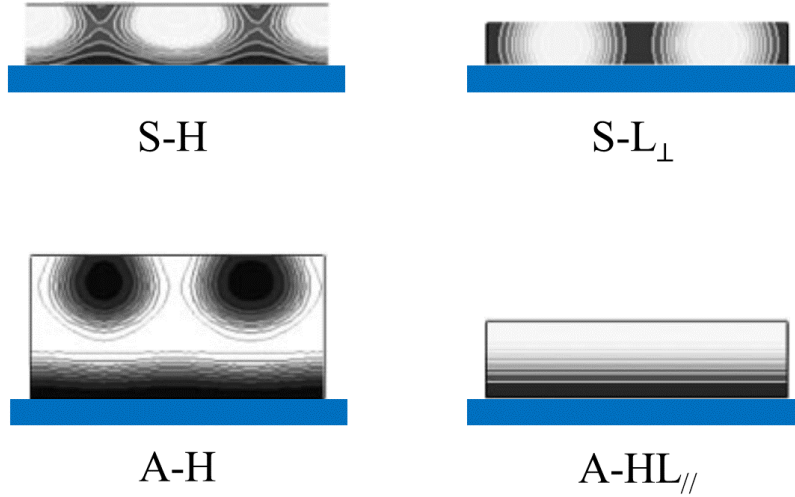


Figure 2.9: Morphologies of a compositionally symmetric DBC thin film at $d \leq D_0$. *S-H* and *S-L_⊥* are the morphologies in symmetric wetting condition, and *A-H* and *A-HL_{//}* in asymmetric wetting conditions. The image is modified based on the reference [33].

2.2 Magnetism

In the present thesis, magnetic nanoparticles (NPs) are templated by DBC thin films described in section 2.1.3 for investigation. Hence, basic terms and phenomena related to magnetism, including magnetic moment, magnetic domains, magnetic structures and anisotropy, are introduced in this chapter. The introduction to magnetism theory is based on the standard textbooks [37–39].

2.2.1 Magnetism basics

In this section, basic terms concerning magnetism, including magnetic moment, magnetization, magnetic susceptibility and magnetic domains, are introduced.

Magnetic moment

The magnetic moment (μ) is the basic object in classical electromagnetism. An infinite current loop (see Figure 2.10) can be employed to address the magnetic moment. Assuming that a current I running in an infinite loop with an area of dS , the produced magnetic moment $d\mu$ can be expressed as equation 2.19.

$$d\mu = IdS \quad (2.19)$$

The direction of the magnetic moment μ can be determined by the right-hand rule. Therefore, the magnetic moment of a finite current loop can be calculated by equation 2.20, since the currents in the neighboring loops cancel each other, resulting in a current running only along the perimeter of the loop [39].

$$\mu = \int d\mu = I \int dS \quad (2.20)$$

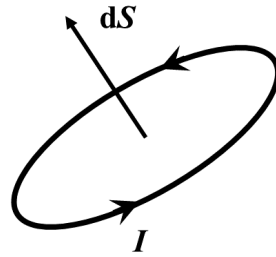


Figure 2.10: A magnetic moment created by a current loop.

Magnetization

Generally, a magnetic material contains numerous atoms with magnetic moments. The magnetization M refers to the total magnetic moment per unit volume, and can be given as equation 2.21

$$M = \mu \frac{N}{V} \quad (2.21)$$

with the number of the magnetic moments N in the volume V . In vacuum where there is no magnetization, two vector fields, H and B , can be used to describe the magnetic field, shown as equation 2.22:

$$B = \mu_0 H \quad (2.22)$$

Where μ_0 is the permeability of free space. Both H and B are magnetic fields, and are scaled version from each other.

In a magnetic solid material, the expression of a magnetic field is different due to the existence of material's magnetization M . In this case, the correlation of vector fields can be give as:

$$B = \mu_0(H + M) \quad (2.23)$$

Magnetic susceptibility

In case the magnetization M orients parallel to the applied magnetic field H , such material is named as linear magnetic material. The magnetization M can be described as:

$$M = \chi H \quad (2.24)$$

where χ is the magnetic susceptibility of the material, which is dimensionless. Combined with equation 2.23, one can get:

$$B = \mu_0(1 + \chi)H = \mu_0\mu_r H \quad (2.25)$$

where μ_r is the relative permeability of the material.

Magnetic domain

The concept of magnetic domains was first proposed by P. Weiss. He assumed that a ferromagnetic material contains lots of small regions, and the magnetization of each region is saturated [40]. Such small regions are called magnetic domains, which are separated by domain walls. On one hand, the formation of magnetic domains is beneficial in saving the magnetostatic energy (i.e. demagnetization energy). On the other hand, however, the domain wall energies increase progressively with the domains surface areas. As a consequence, a critical domain is energetically favored, in order to reach the lowest energetic state of the whole system. When a material's size is below the critical domain size, the domain walls are energetically no longer favored. In this case, the material is composed of single domain, which can perform like a tiny permanent magnet. The radius of the critical dimension (R_c) can be estimated by equation

$$R_c \approx 9 \frac{\sqrt{AK_\mu}}{\mu_0 M^2} \quad (2.26)$$

where A and K_μ represent the exchange constant and uniaxial anisotropy constant, respectively.

2.2.2 Magnetic materials

Based on the magnetic susceptibility (see Section 2.2.1), magnetic materials can be mainly classified into three different types, which are ferromagnetic, paramagnetic and diamagnetic materials.

(a) Ferromagnetic materials ($\chi \gg 0$). Such materials show strong magnetization behavior in external magnetic field. For instance, iron, cobalt, nickel and their alloys.

(b) Paramagnetic materials ($10^{-5} \leq \chi \leq 10^{-3}$). This type of materials, like aluminum, platinum and manganese, possess positive but weak susceptibility.

(c) Diamagnetic materials ($-10^{-6} \leq \chi \leq -10^{-5}$). These materials have negative and small susceptibility. Examples are silver, beryllium, gold and copper.

Concerning applications, the magnetization behavior of a material to an external magnetic field plays an important role. Hence, a basic introduction on the magnetic behavior of different types of magnetic materials is given in the following sections.

Ferromagnetism

For ferromagnetic materials, multiple magnetic domains with oriented magnetic moments exist in the absence of an external magnetic field (see Figure 2.11 a). The orientation of magnetic moments differs in different domains, resulting in a zero net magnetization of the materials in an unmagnetized state. Once an external magnetic field is applied, all the magnetic moments will align parallel to the direction of the magnetic field (see Figure 2.11 b). Ferromagnetic materials can easily get magnetized to a saturation even if the applied magnetic field is weak. This explains the strong magnetic susceptibility of ferromagnetism. Figure 2.11 c shows the typical magnetization curves of ferromagnetism. Within an external magnetic field, the magnetization increases with the strength of the applied field and reaches a maximum, which is called saturation (shown as step S1 in Figure 2.11 c). After the external magnetic field is removed, a remanent magnetization, which is called remanence, is retained due to the parallel alignment of magnetic moments (step S2 in Figure 2.11 c). For ferromagnetic materials, the remanence is close to the saturation [40]. In order to cancel the remanence, another magnetic field needs to be applied opposite to the initial magnetization direction (step S3 in Figure 2.11 c). Such field is called coercive force or coercivity. Further magnetization leads to the formation of a hysteresis loop, from which the whole magnetic history is achievable.

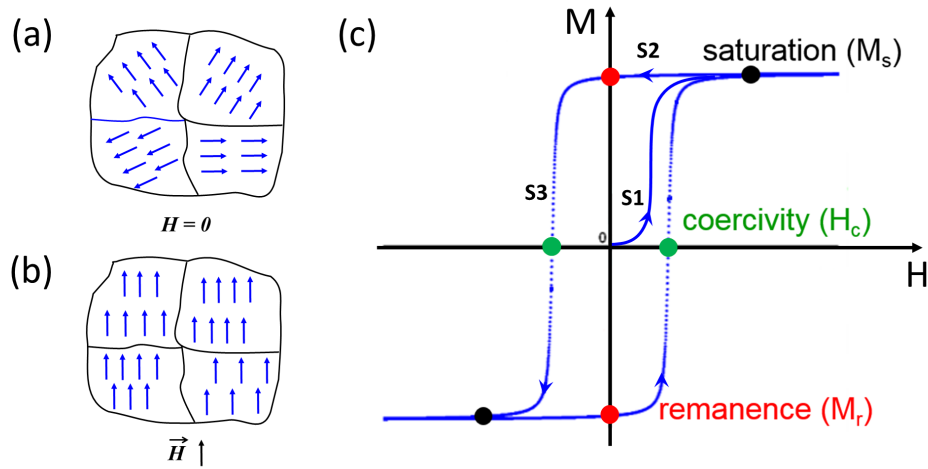


Figure 2.11: States of magnetic moments in domains of ferromagnetic materials in the absence (a) and presence (b) of an external magnetic field \vec{H} . The direction of the external field is indicated by the black arrow. (c) The typical magnetization behavior of ferromagnetic materials within an external magnetic field. Magnetization steps are shown by S_1 , S_2 and S_3 . Dots with different colors suggest the positions of saturation M_s (black), remanence M_r (red) and coercivity H_c , respectively.

Paramagnetism

Paramagnetism originates from the ions or atoms with unpaired electrons in their outer shells. The spins of these unpaired electrons, which create magnetic moments, do not have paired spins with the opposite direction. As a consequence, intrinsic magnetic moments exist in these individual ions or atoms even if there is no external magnetic field applied. For a bulk paramagnetic material, which contains a large number of paramagnetic ions or atoms, it does not show any magnetization behavior, due to the random orientation of magnetic moments (see Figure 2.12 a). Once an external magnetic field is applied, the paramagnetic spins respond and align parallel to the direction of the magnetic field (see Figure 2.12 b). A magnetization is accordingly observed and is proportional to the magnitude of the external magnetic field, shown as the typical magnetization curve in Figure 2.12 c. Different as ferromagnetic materials, no remanence is left inside the paramagnetic materials when the external magnetic field is reduced to zero. Such non-remanence phenomenon results from the random orientation of the magnetic moments in individual domains of the paramagnetic materials.

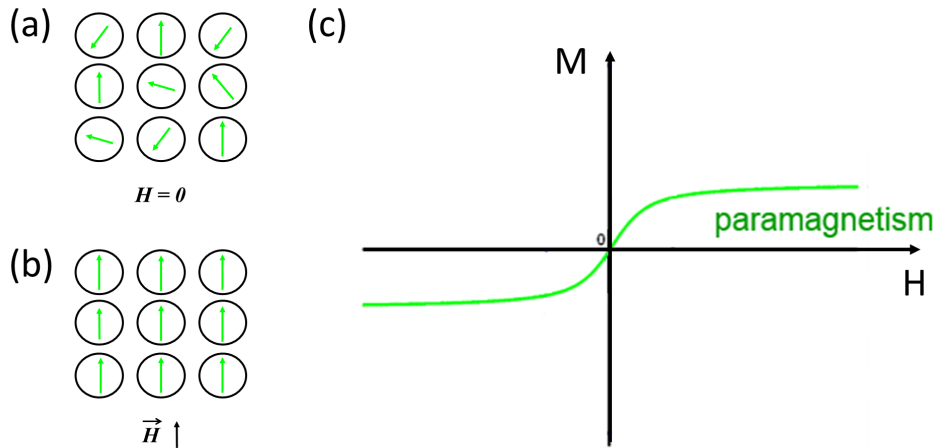


Figure 2.12: States of magnetic moments in domains of paramagnetic materials in the absence (a) and presence (b) of an external magnetic field \vec{H} . The direction of the external field is indicated by the black arrow. (c) The typical magnetization curve of a paramagnetic material.

Diamagnetism

Diamagnetic materials are those having atoms with paired electrons in all the energy sub-levels. In the absence of an external magnetic field, the magnetic moment produced by the spin of each individual electron is canceled by its pair spinning in the opposite direction. Therefore, no net magnetic moments are present in the diamagnetic materials (shown as Figure 2.13 a). When an external magnetic field is employed, magnetic moments orienting opposite to the magnetic field are induced (shown as Figure 2.13 b). Thus, an anti-parallel magnetization behavior is observed, shown as Figure 2.13 c. The diamagnetic behavior is derived from the asymmetric alteration of the orbital motions in the atoms [37]. Compared with ferromagnetic and paramagnetic materials, diamagnetic materials have a very weak and negative magnetic susceptibility. For Example, the molar susceptibility of diamagnetic water at 300 K is -0.7×10^{-6} , whereas, the molar susceptibility of paramagnetic FeCl_3 is 1.46×10^{-2} at 300 K [41].

2.2.3 Superparamagnetism

Superparamagnetism refers to the thermal equilibrium magnetization behavior of a system with single-domain particles, which behaves similar as an atomic paramagnet [42]. Reports show that ferromagnetic particles, which are small enough, can be regarded as single-domain particles, since higher energy is required for the formation of domain walls

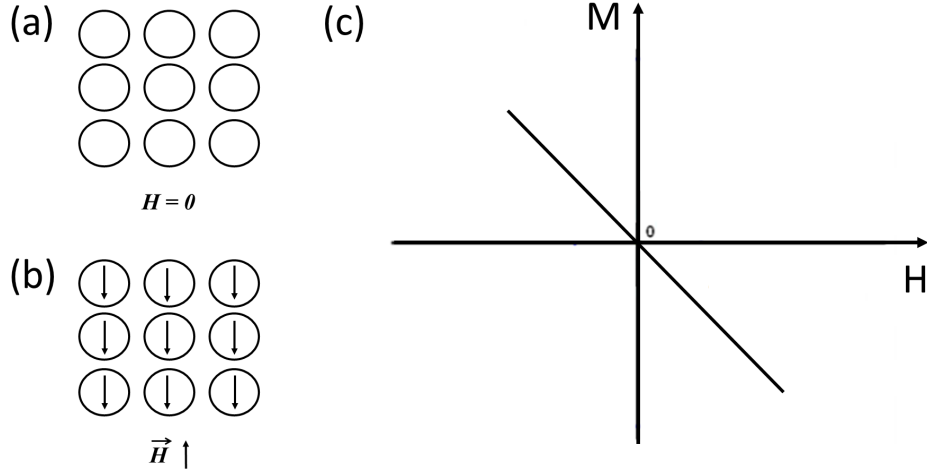


Figure 2.13: States of magnetic moments in domains of paramagnetic materials in the absence (a) and presence (b) of an external magnetic field \vec{H} . The direction of the external field is indicated by the black arrow. The direction of the external field is indicated by the black arrow. (c) The typical magnetization curve of a diamagnetic material.

compared with that for demagnetization [43]. Due to the different energy anisotropy contributions, the magnetization of these single-domained particles tends to preferentially align along certain specific direction which is defined as the easy axis (see Figure 2.14). Assuming that the anisotropy energy density of a single-domained particle is defined as bellow:

$$E = KV \sin^2 \theta \quad (2.27)$$

where K is the uniaxial anisotropy constant, V is the particle volume, and θ is the angle between the easy axis and the magnetization. Therefore, two energy minima can be achieved at $\theta = 0$ and $\theta = \pi$, which correspond to the magnetization parallel and antiparallel to the easy axis (see Figure 2.14). If the magnetization changes from one easy axis to the other, an energy barrier, described as $\Delta E_B = KV$ needs to be overcome.

Néel classified the flip behavior into three different categories based on the relationship between the energy fluctuation $k_B T$ (k_B is the Boltzmann constant, T is the temperature) and anisotropy energy KV [44].

(1) $k_B T \gg KV$. If the particle is small enough, KV will be small. Therefore, the anisotropy energy can be outweighed by the energy fluctuation, leading to a spontaneous reversal of the magnetization of the particle between two easy axes even without applying an external magnetic field. In this case, the superparamagnetism is defined as isotropic.

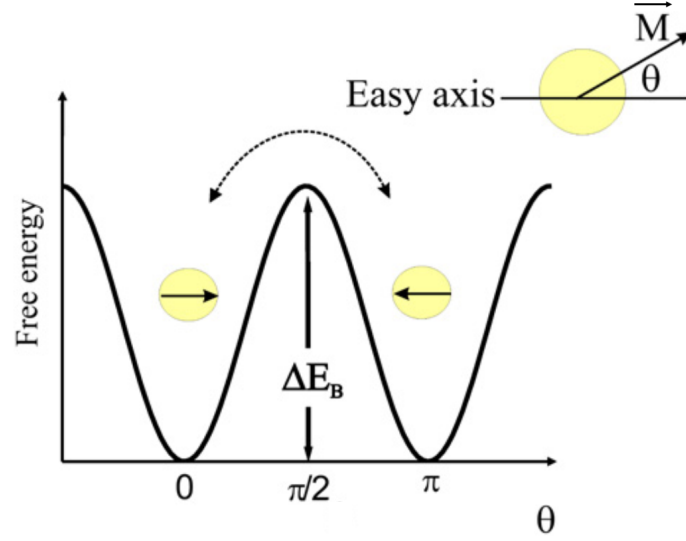


Figure 2.14: The free energy versus magnetization direction of a single-domained particle with uniaxial anisotropy. θ shows the angle between the easy axis and the magnetization \vec{M} . ΔE_B represents the energy barrier for switching the states. The image is taken from reference [42]

(2) $k_B T \approx KV$. The dynamics of the flip behavior are in an anisotropic state of superparamagnetism. In this case, the rotation of the magnetic moments can be either free or blocked depending on the temperature in a given experiment.

(3) $k_B T < KV$. The flip behavior will be frozen on a time scale of the applied experiment.

The following discussion is focused on the anisotropic superparamagnetism for the interest on the temperature-dependent magnetization behavior. In the region of $k_B T \approx KV$, The fluctuation between two energy minima is described via a characteristic relaxation time τ , which can be given as the Néel-Brown equation:

$$\tau = \tau_0 \exp\left(\frac{KV}{k_B T}\right) \quad (2.28)$$

where $\tau_0 \sim 10^{-10}$ s is the inverse attempt frequency. The state of the investigated magnetic system is dependent on the relation between the relaxation time τ and the experimental measuring time τ_m . In case of $\tau > \tau_m$, the whole magnetic system is static. When $\tau < \tau_m$, an average value of magnetization can be observed. If $\tau \sim \tau_m$, the magnetic moments are blocked.

As discussed above, temperature is also an indispensable parameter which can influence the magnetic behavior of particles. For superparamagnetic materials, there exists a critical

temperature, which is called blocking temperature T_B . Above T_B , the whole system has enough thermal energy to overcome the energy barrier, resulting in a spontaneous flipping of magnetic moments. Below T_B , the magnetic moments are frozen on the measurement timescale ($\tau \sim \tau_m$). From equation 2.28, one can describe the T_B as follows:

$$T_B = \frac{KV}{k_B \ln(\tau_m/\tau_0)} \quad (2.29)$$

It needs to be noted that equation 2.29 is only valid for a particle system without size distribution or interaction between particles. Otherwise, a distribution of T_B will be observed.

In general, superparamagnetic materials need to meet the following requirements. Below T_B , the magnetization behavior is temperature dependent. Magnetic hysteresis exists in the measured magnetization curves and narrow down with increasing temperature. Above T_B , magnetic hysteresis disappears.

2.2.4 Magnetic anisotropy

Magnetic anisotropy refers to the phenomenon where the magnetization is preferentially aligned along a certain particular direction. In the investigation of magnetic thin films, two most common types of anisotropy are magnetocrystalline anisotropy and shape anisotropy [45]. Magnetocrystalline anisotropy derives from the atoms' arrangement, which is determined by the crystal structure. Shape anisotropy describes the preferential alignment of the magnetization vector along the easy axis, which is the direction of the minimum magnetostatic energy. The present thesis mainly focuses on the magnetic shape anisotropy for investigation on the magnetic properties of aligned magnetic nanoparticle wires. The magnetic shape anisotropy only exists in shape-asymmetric magnetic materials.

2.2.5 Magnetic nanoparticles

Magnetic nanoparticles (NPs) commonly describe the nanometer scaled magnetic particles with a size of below 100 nm. Due to the high surface to volume ratio, magnetic NPs possess promising features which opens them a wide field of application, such as flexible disk recording media, drug carries in the biomedical therapy, as well as active component of ferrofluids [1, 46, 47]. Compared with bulk hard magnetic materials, magnetic NPs can be combined with soft materials to fabricate flexible applications. DBC films are favorably employed as a hosting matrix to template the magnetic NPs. To achieve homogeneous

dispersion inside the organic matrix, surface treatment, such as grafting with organic ligands or polymer chains, is proved to be an effective method. On one hand, by tailoring the types of grafting ligands, the magnetic NPs can be equipped with a preference to one particular block of the DBC, which allows for a specified local arrangement of NPs in the DBC template. On the other hand, the organic shell of the NPs can prevent the formation of agglomerate driven by the magnetic attractive force among the NPs. Thus a homogeneous dispersion can be expected. In the present thesis, two types of magnetic NPs, maghemite $\gamma\text{-Fe}_2\text{O}_3$ (10 nm, grafted with PS chains) and magnetite Fe_3O_4 (10 nm, grafted with oleic acid chains), are investigated. Magnetic thin films composed of different NPs and DBCs are fabricated and studied to explore their potential application in the field of magnetic sensors.

2.3 Scattering techniques

Investigation on the morphologies, including both the surface and inner morphologies, of NP-DBC hybrid films is important in understanding the whole hybrid system. The surface morphologies can be accessed by the real-space imaging methods like AFM and SEM. To probe the morphologies buried inside films, the reciprocal-space technique, x-ray scattering, can be applied. The advanced scattering characterization method is non-destructive to the studied sample, and allows for inner structure detection with a high statistical relevance. The scattering basics are discussed in section 2.3.1, followed by an introduction of x-ray reflectivity (XRR) in section 2.3.2, and grazing incidence small angle x-ray scattering (GISAXS) in section 2.3.3.

2.3.1 Scattering basics

The incident X-ray can be described as an electromagnetic plane wave, the electric field vector of which can be given as follows:

$$\vec{E}(\vec{r}) = \vec{E}_0 \exp(i\vec{k}_i \cdot \vec{r}) \quad (2.30)$$

where \vec{E}_0 includes the polarization direction and amplitude of the electric field, and \vec{r} represents the position vector. When an X-ray travels through a medium with a refractive index $n(\vec{r})$, the propagation of the electromagnetic wave can be described with the Helmholtz equation [48]:

$$\Delta \vec{E}(\vec{r}) + k^2 n^2(\vec{r}) \vec{E}(\vec{r}) = 0 \quad (2.31)$$

where $k = \frac{2\pi}{\lambda}$ denotes the modulus of the wave vector \vec{k} . The refractive index $n(\vec{r})$ can be given by:

$$n(\vec{r}) = 1 - \delta(\vec{r}) + i\beta(\vec{r}) \quad (2.32)$$

where $\delta(\vec{r})$ and $\beta(\vec{r})$ are the dispersion and absorption, respectively. Both dispersion and absorption parts are related to the wavelength of the X-ray, and can be written as:

$$\delta(\vec{r}) = \frac{\lambda^2}{2\pi} \rho(\vec{r}) = r_e \frac{\lambda^2}{2\pi} \rho_e(\vec{r}) \quad (2.33)$$

$$\beta(\vec{r}) = \frac{\lambda^2}{2\pi} \mu(\vec{r}) \quad (2.34)$$

whereby ρ denotes the scattering length density (SLD) of the penetrated medium. $r_e = 2.814 \times 10^{-5} \text{ \AA}$ is the classical electron radius. ρ_e is the electron density of the investigated materials, and μ is the linear absorption coefficient. Thus, a material's SLD is strongly dependent on the electron density of the involved elements. For a material containing components with different electron densities, the different SLDs result in differentiated scattering contrasts in the X-ray scattering experiments.

The principles of specular and diffuse scattering in a grazing mode are schematically depicted in Figure 2.15 a and Figure 2.15 b, respectively. For both scattering geometries, the X-ray beam impinges on a film with an incident angle α_i , then the reflected beam leaves the film with an exit angle α_f . The scattering vector can be accordingly defined as (shown in Figure 2.15):

$$\vec{q} = \vec{k}_f - \vec{k}_i \quad (2.35)$$

where the modulus of \vec{q} stays unchanged for the elastic scattering, which is used in the present thesis.

For the specular scattering geometry, the incident angle α_i is equal to the exit angle α_f , and both of them stay in the same xz -plane. In case of the diffuse scattering geometry, the scattering beam is not necessarily limited in the xz -plane, but with an additional angle ψ_f present in the xy -plane (shown in Figure 2.15 b).

At the air/film interface, the X-ray beam can get either transmitted or reflected, shown in Figure 2.15 a. The transmission angle α_t can be related to the incidence angle α_i via the Snell's law:

$$n_0 \cos(\alpha_i) = n \cos(\alpha_t) \quad (2.36)$$

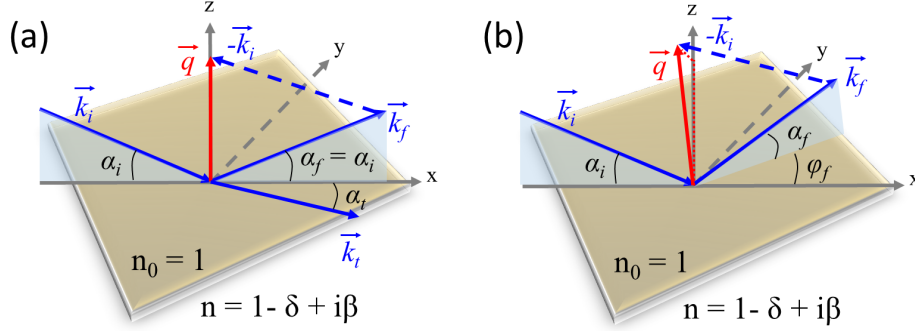


Figure 2.15: Basic definitions of angles and directions in the geometry of (a) specular scattering and (b) diffuse scattering.

where $n_0 = 1$ and n are the reflective indices of air and film, respectively. When $\alpha_t = 0$, the X-ray beam gets totally reflected. In this case, the incident angle is named as the critical angle α_c of the probed material. Thereby,

$$\cos(\alpha_c) = n \quad (2.37)$$

Accordingly,

$$n^2 = \cos^2(\alpha_c) \approx 1 - \alpha_c^2 \quad (2.38)$$

Thus, the critical angle α_c can be written as:

$$\alpha_c \approx \sqrt{2\delta} = \lambda \sqrt{\rho/\pi} \quad (2.39)$$

In case $\alpha_i > \alpha_c$, the whole film can be penetrated by the x-ray beam. In case $\alpha_i < \alpha_c$, the beam gets totally reflected, and only a local surface part is probed.

2.3.2 Specular reflectivity

X-ray reflectivity (XRR) refers to the specular scattering recorded as a function of the incident angle (α_i), namely $\alpha_i = \alpha_f$, and $\psi_f = 0$ (Figure 2.15 a). As a consequence, the scattering vector is always along the z axis, and only the z -component q_z differs from 0 [49].

$$q_z = \frac{4\pi}{\lambda} \sin(\alpha_i) \quad (2.40)$$

Therefore, the electron intensity distributed along the z direction is measured in the XRR. When an X-ray beam reaches the interface of A/B materials ($n_A \neq n_B$), the beam is split into two parts: reflected and transmitted parts. The exit angle α_t of the transmitted beam can be described by the Snell' law shown as equation 2.36. The ratio of the amplitudes of the transmitted and reflected beams can be addressed by the Fresnel transmission coefficient t^F and reflection coefficient r^F , respectively. The transmission T^F and reflectivity R^F can be described as:

$$T^F = |t^F|^2, \quad R^F = |r^F|^2 \quad (2.41)$$

So far, the discussion is based on the assumption that the interfaces are perfectly smooth without any interfacial roughness involved. The interfacial roughness shows the deviation from a smooth surface, and can be described by the root-mean-square surface roughness σ_{rms} [50]:

$$\sigma_{rms} = \sqrt{\frac{1}{N_{\sigma_{rms}}} \sum_{i=1}^{N_{\sigma_{rms}}} \Delta z_i^2} \quad (2.42)$$

where $N_{\sigma_{rms}}$ represents the number of the measured spots along the interface, and Δz_i shows the deviation from the specific measured spot i to the mean average interface. In case of the roughness below the film thickness, the Névot-Croce factor with an exponential function can be used to correct the Fresnel reflection coefficient [51]. More details on XRR theory are described elsewhere [49].

Figure 2.16 depicts the typical XRR data of a PS-*b*-PNIPAM DBC film deposited on a silicon wafer. Featured scattering behaviors can be observed at different incidence angle regions.

- (1) At $\alpha_i < \alpha_c^{DBC}$, the beam is totally reflected.
- (2) At $\alpha_i = \alpha_c^{DBC}$ and $\alpha_i < \alpha_c^{Si}$, intensity minima can be observed. Thus, XRR can be employed to probe the SLD of a material (see equation 2.39).
- (3) At $\alpha_i > \alpha_c^{Si}$, intensity oscillations, which are named as Kiessig fringes, are present. These fringes provide information on the film thickness t : [52]

$$t \approx \frac{2\pi}{\Delta q_z} \quad (2.43)$$

where Δq_z represents the distance between two neighboring intensity minima, namely the two valleys in the fringes, in the XRR curve.

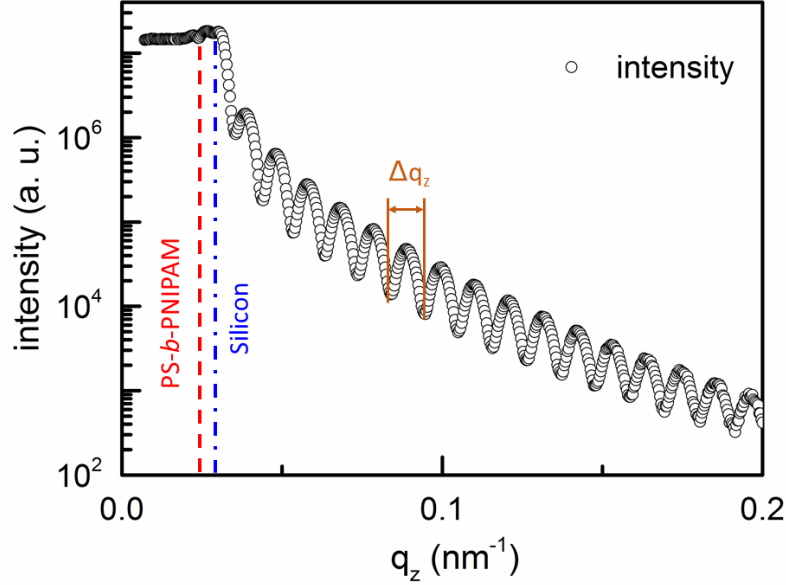


Figure 2.16: XRR curve of the PS-b-PNIPAM film on a silicon wafer. Δq_z shows the distance between two neighboring intensity minima of the Kiessig fringes. The dashed red and blue lines indicate the critical q_z of DBC and silicon, respectively.

2.3.3 Grazing incidence small angle X-ray scattering

Grazing incidence small angle X-ray scattering (GISAXS) can probe structures in a wide length scale ranging from several nanometers up to micrometers. Compared with the transmission geometry, a larger foot-print of the beam inside the probed film can be achieved in the GISAXS measurement, due to the applied shallow incident angle α_i ($< 1^\circ$). Thus, a good statistics information on the film morphology can be obtained even for very thin films. By varying the incident angle, both surface and bulk morphologies can be accessed. Within the framework of elastic scattering, the scattering wave vector \vec{q} can be given as:

$$\vec{q} = \frac{2\pi}{\lambda} \begin{pmatrix} q_x \\ q_y \\ q_z \end{pmatrix} = \frac{2\pi}{\lambda} \begin{pmatrix} \cos(\alpha_f) \cos(\psi) - \cos(\alpha_i) \\ \cos(\alpha_f) \sin(\psi) \\ \sin(\alpha_f) + \sin(\alpha_i) \end{pmatrix}. \quad (2.44)$$

According to the widely employed distorted wave Born approximation (DWBA), the diffuse scattering events can be described as a perturbation of an ideal system. To calculate the differential cross-section of a scatterer, the first-order perturbation theory is applied. Within the framework of DWBA, the ideal system is a perfectly smooth inter-

face, while the perturbation derives from the lateral structure and the film roughness. As a consequence, the differential cross-section can be written as:

$$\frac{d\sigma}{d\Omega} = \frac{S\pi^2}{\lambda^4} (1 - n^2)^2 |T_i|^2 |T_f|^2 P_{diff}(\vec{q}) \propto P_{diff}(\vec{q}) \quad (2.45)$$

where S is the illuminated area, and $P_{diff}(\vec{q})$ represents the diffuse scattering factor. A maximum of the Fresnel transmission coefficients (T_i and T_f) can be reached at the critical angle of the investigated material. Thus, in the scattering map, a featured intensity maximum which is called Yoneda peak can be observed. Since α_c is determined by the scattering length density ρ , the Yoneda peak is the material-sensitive characteristic feature.

Through GISAXS measurement, only an intensity map of the scattering signals is obtained. In order to extract the structural information, a model needs to be applied to interpret the intensity signals. Within the effective interface approximation, for a system with identical objects arranged in a certain geometry, the diffuse scattering factor $P_{diff}(\vec{q})$ can be described as:

$$P_{diff}(\vec{q}) \propto N |F(\vec{q})|^2 S(\vec{q}) \quad (2.46)$$

where N is the number of identical scatterers. $F(\vec{q})$ is the form factor describing the shape and size of the scatterer. $S(\vec{q})$ is the structure factor which represents the spatial arrangement of the scatterers [53].

In the present thesis, the GISAXS data interpretation is based on equation 2.46, so that the information on the inner morphology of the NP-DBC hybrid films can be extracted [54]. In order to study the lateral structure, horizontal line cuts of the 2D GISAXS data are made at the Yoneda peak position of the probed materials. The cuts are then analyzed with a constructed model consisting both form factor and structure factor. Typically, cylindrical geometry is adopted as the form factor $F(\vec{q})$ due to the rotational isotropy. One-dimensional paracrystalline lattice (1DDL) is employed as the structure factor $S(\vec{q})$. The cylindrical scatterers are assumed to be periodically arranged in a paracrystal, and the position deviation of the cylinders increases with the distance from the origin. Therefore, a short-range order is present in $S(\vec{q})$, instead of a long-range order. In order to take the size distribution into consideration, a local monodisperse approximation (LMA) is included. More details concerning the LMA can be found elsewhere [55].

To model the horizontal line cuts obtained from the 2D GISAXS data, a Gaussian distribution function is employed and written as:

$$f(x) = \frac{1}{\sigma\sqrt{2\pi}} \exp\left[-\frac{(x - x_0)^2}{2\sigma^2}\right] \quad (2.47)$$

where σ and x_0 represent the standard deviation and the peak center position, respectively. To explore the degree of the structural order, the full width at half maximum (FWHM) can be calculated using the standard deviation:

$$FWHM = 2\sqrt{2 \ln 2} \sigma \approx 2.355\sigma \quad (2.48)$$

3 Characterization methods

In the present chapter, all the characterization techniques employed for this thesis are described. The surface and inner structures of fabricated films are probed via real-space and reciprocal-space techniques, respectively. The magnetic properties of the NP-containing films are investigated via a superconducting quantum interference device (SQUID).

In detail, the real-space techniques include optical microscopy (Section 3.1.1), atomic force microscopy (Section 3.1.2) and scanning electron microscopy (Section 3.1.3). The reciprocal technique utilized in the thesis is grazing-incidence small-angle X-ray scattering (Section 3.1.6). Surface profilometry (Section 3.1.4) and X-ray reflectivity (Section 3.1.5) are used to measure the film thickness. The SQUID magnetometry employed to prove the magnetic properties is explained in Section 3.2.1.

3.1 Structural characterizations

3.1.1 Optical microscopy (OM)

Optical microscopy (OM) is utilized to check the films' quality in microscale by probing the homogeneity of fabricated films. Also in some of our investigations where magnetic nanoparticle (NP) wires are obtained, OM is also applied for size determination.

| magnification[\times] | resolution [$\mu\text{m}/\text{pixel}$] |
|---------------------------|---|
| 1.25 | 6.26 |
| 2.5 | 3.11 |
| 10 | 0.82 |
| 50 | 0.17 |
| 100 | 0.082 |

Table 3.1: Resolution of the optical microscopy for various magnifications.

To perform OM measurements, an Axiolab A microscope (Carl Zeiss), which is equipped with objectives with different magnifications (1.25, 2.5, 10, 50 and 100-fold), is used. The

microscope is combined with a PixelLink USB capture BE 2.6 charge coupled device camera, recording images with a resolution of 1280×1024 pixels. The real-space distance can be calculated based on the resolutions per pixel provided in Table 3.1. To determine the size of NP wires in this thesis, hybrid films with NP wires are imaged at the magnifications of 50 and 100 fold. ImageJ is used for data processing and analysis [56].

3.1.2 Atomic force microscopy (AFM)

Atomic force microscopy (AFM) is a mapping technique, which is based on laser and photodiode detectors. It allows picturing surfaces on a molecular level. Through AFM measurements, not only the structures' shape and sizes can be obtained, but also the information in the vertical dimension of samples, like height or depth of nanostructures, are accessible.

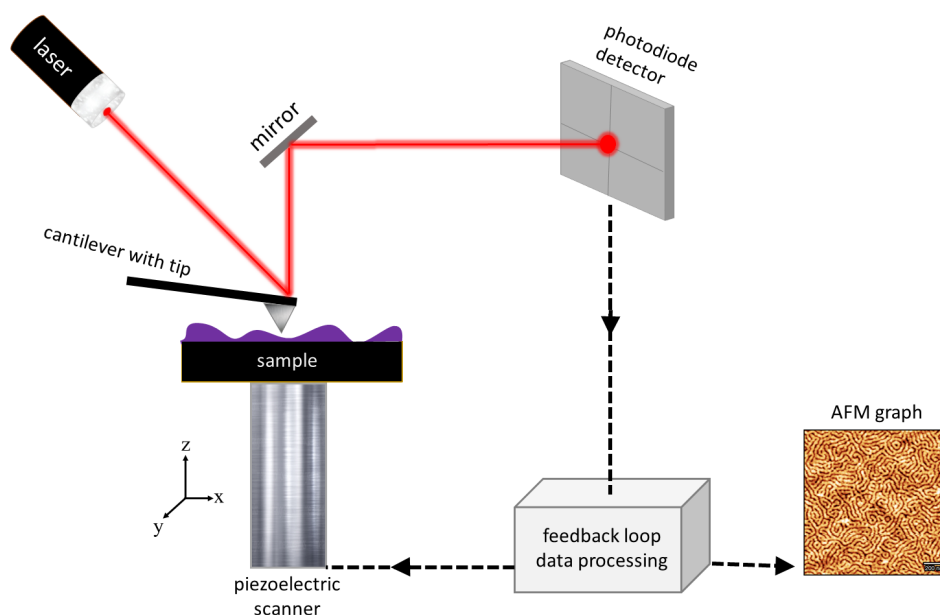


Figure 3.1: Simplified sketch of the used AFM set-up. The sample is placed on a piezoelectric scanner which can move in three dimensions. The cantilever with a tip performs raster scan over the sample surface. A laser beam is applied to monitor the deflection of the cantilever, and the reflected signal is detected by a photodiode detector. A feedback system is used to adjust the sample position and process the data.

Figure 3.1 pictures the simplified sketch of the AFM instrument, which contains five main parts: piezoelectric scanner, cantilever with AFM tip, laser source, photodiode detector, and feedback controller. The AFM working principle is based on the atomic forces between the sharp tip of the cantilever and the molecules on the sample surface.

According to the different tip–sample interactions, three main scanning modes are developed, which are contact mode, tapping mode and non–contact mode. Compared with contact and non–contact modes, tapping mode offers the opportunity to record images with high lateral resolution, and meanwhile the possible damage to the sample surface can be minimized. In the present thesis where soft polymer films are investigated, all AFM measurements are conducted with a MFP–3D instrument (Asylum Research) using tapping mode. The tip positioned on the cantilever has a curvature radius of 7 nm. The spring constant of the cantilever (OMCL–AC240TS–R3, Asylum Research) is 2 Nm^{-1} with a resonance frequency of 70 kHz. For the measurement, the cantilever is firstly driven to oscillate close to its resonance frequency. Then the cantilever is brought downwards till the tip is very close to the film surface. Afterwards, the tip touches the film surface repeatedly during the tapping mode operation. Due to the film’s surface structure and roughness, the interaction between molecules on the film surface and the tip changes with scanning time. Therefore the amplitude of the oscillating cantilever changes, which can be detected by the reflected laser beam shown in Figure 3.1. The laser beam gets reflected a second time at a mirror and then detected by a position–sensitive photodiode detector which consists of four segments. In this way, the deflection of cantilever can be converted into electronic signals, which are proportional to the displacement of the cantilever. The electric signals are then transferred to the feedback electronics, and afterwards the sample stage is driven by the feedback loop to move along the z –axis direction in order to keep a constant tip–film distance at each xy –position. Finally, the height and phase images are recorded based on the stage’s motion.

The films are scanned line–wise over an area of $1 \times 1 \mu\text{m}$ and $2 \times 2 \mu\text{m}$. The achieved images consists of 1024 lines and each line contains 1024 data points. All AFM data are processed and analyzed with the software Gwyddion 2.42 [57], mainly for image contrast adjustment and height information extraction.

3.1.3 Scanning electron microscopy (SEM)

To access the nanostructure of fabricated films, scanning electron microscopy (SEM) is utilized. Compared with optical microscopy, SEM works based on electrons instead of optical light. The short wavelength of electrons provides SEM a high spatial resolution (below 10 nm), therefore surface morphology examination in the nanometer range is accessible via SEM.

All SEM images in the present thesis are obtained from the FESEM Gemini NVision 40 instrument controlled by the software SmartSEM (both by Carl Zeiss). During the SEM measurement, electrons are generated by a field emission electrode (a tungsten filament).

Afterwards, the electrons get focused via magnetic and electrostatic lenses to form an electron beam, which is then accelerated by a voltage of several kV. The generated beam hits the film and scans line-wise the chosen area on the film surface. The incident electrons interact with the film surface, resulting in the release of secondary electrons from the area close to the illuminated film surface. The secondary electrons are collected by an InLens detector placed at a small sample-to-detector distance. The intensity of the secondary electrons is dependent on the beam size, the incident angle between beam and film surface, and the film's surface morphology. The recorded electronic signals are then converted to a gray-scale image with different brightness depending on the topography of film surface and different materials.

Due to the poor conductivity of the investigated polymer film in the work, relatively low acceleration voltages of 1.8 and 2.5 kV are employed with the working distance of 1.0 and 1.7 mm, respectively. For all measurements in the present thesis, the applied aperture is 10 μm , and the vacuum pressure of the system and gun are 2×10^{-6} and 2×10^{-9} mbar, respectively. The received SEM images are processed and analyzed with the software ImageJ v1.44p [56].

To improve the quality of the obtained SEM images, conductive silicon substrates are used for all films in this thesis. In addition, two alternative methods are also adopted, which are pre-etching to films (PS-*b*-PMMA films in Chapter 5 and 6) and use of conductive tape during the measurement (PS-*b*-PNIPAM films in Chapter 7). Oxygen plasma is employed for the etching process, in which the covalent chemical bounds of PMMA chains get more easily broken and converted into more hydrophilic groups compared with PS chains [58]. As a consequence, the contrast between PS and PMMA chain can be improved. It is important to note that the etching time and power are the key factors during the pre-treatment. Long etching time under high power can completely destroy the films. Therefore, preliminary tests are necessary to find out the suitable etching parameters. In the present thesis, films in Chapter 5 and 6 are etched at the power of 83% for 30 s and 10 s, respectively. In case of measuring the PS-*b*-PNIPAM films, a long conductive graphite tape is placed close to the probing area and connected to the copper sample stage. In this way, the accumulation of charges can be reduced dramatically.

3.1.4 Surface profilometry

Profilometry is a technique used to determine the film thickness in a fast way. The simplified sketch (Figure 3.2) depicts the basic working principle of a profilometer. Before the measurement, a scratch is made on the sample surface by the edge of a clean tweezer to expose the substrate. After the sample is positioned on the stage, the stylus with

diamond tip is brought down to touch the film surface. A constant force is applied to ensure the contact between the stylus and film surface. Before scanning, the position of the sample needs to be adjusted to allow the stage movement perpendicular to the direction of the scratch (see Figure 3.2). Then the sample stage moves and the tip crosses the scratch. The height variation of the film surface can be detected, and converted by a differential transformer to digital signals. Finally the film thickness can be calculated by analyzing the obtained height profile.

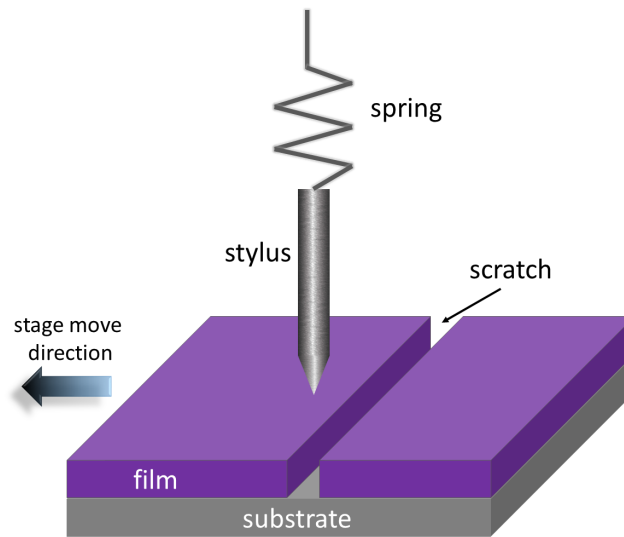


Figure 3.2: *Simplified sketch of the profilometer. The scratched film is placed on a mobile stage. The stylus touches the film surface under a certain force. The scanning is realized by moving the stage under the stylus.*

A DektakXT® stylus profiler (Brucker Corp.) is used in this thesis. For all measurements, the used contact force is 1 mN. And the scan speed and scan distance are 100 $\mu\text{m/s}$ and 3 mm, respectively. For each sample, 5 different spots are probed to determine an average film thickness.

3.1.5 X-ray reflectivity (XRR)

X-ray reflectivity (XRR) is a technique based on specular reflection of X-rays. It is applied to obtain information along the vertical direction of films (with respect to the film surface). In detail, the film thickness, especially for the very thin films, can be precisely achieved. The theoretical basics concerning XRR can be found in Chapter 2 (Section 2.3.2).

A Bruker D8–Advance is utilized for XRR measurements, which are controlled and programmed by the software XRDcommander and XRDwizard, respectively. Principally, the XRR instrument consists of three main parts, which are X-ray source, sample stage and detector (shown in Figure 3.3). The X-ray beam ($\lambda = 0.154 \text{ nm}$) is generated by a copper anode, and impinges the horizontally placed sample on a circular stage. The reflected and scattered signals are collected by a point detector positioned on the other side. The X-ray beam is collimated by narrow slits positioned after the X-ray source and before the detector. To ensure the accuracy of experiments, a sample size larger than $2.5 \text{ cm} \times 2.5 \text{ cm}$ is required. During the measurement, the incident angle θ is changed stepwise, and simultaneously the angle between detector and incoming beam is set to vary by 2θ . To confine the illuminated area, a knife edge is placed over the sample with a short edge-to-surface distance. In the present thesis, the XRR measurements are performed with the 2θ moving between 0° and 5° at a resolution of 0.01° . To protect the detector from too high intensity of the reflected beam, an absorber is used at low angle. The film thickness is extracted from the reflectivity curves via fitting data with the software Parratt algorithm [59].

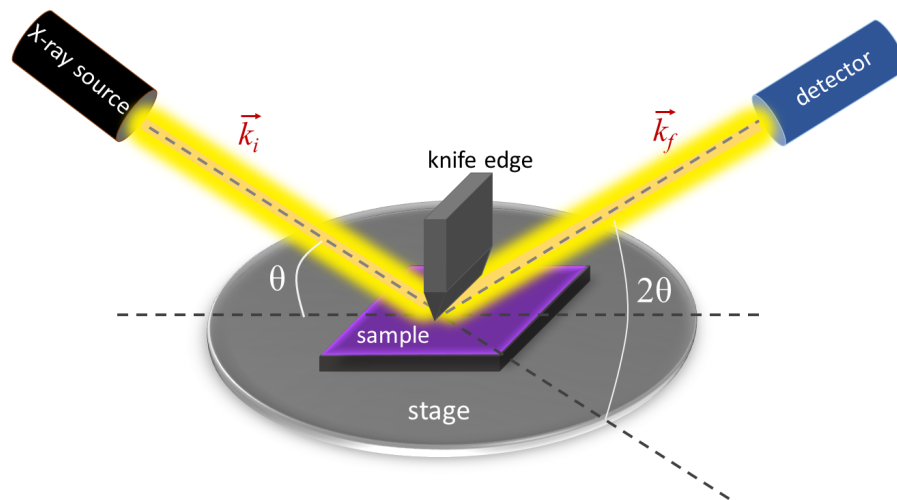


Figure 3.3: Simplified sketch of the used XRR instrument. The X-ray beam is generated by the source and impinging onto the film surface at certain angle θ . A point detector is placed on the other side at an exit angle of 2θ to collect the reflected X-ray beam. A knife edge is installed at a short edge-to-surface distance to avoid overillumination at small angle.

3.1.6 Grazing-incidence small-angle X-ray scattering

In order to investigate the inner structure of films with high statistical relevance, grazing-incidence small-angle X-ray scattering (GISAXS) is carried out. The related theoretical basics are provided in Chapter 2 (Section 2.3.3).

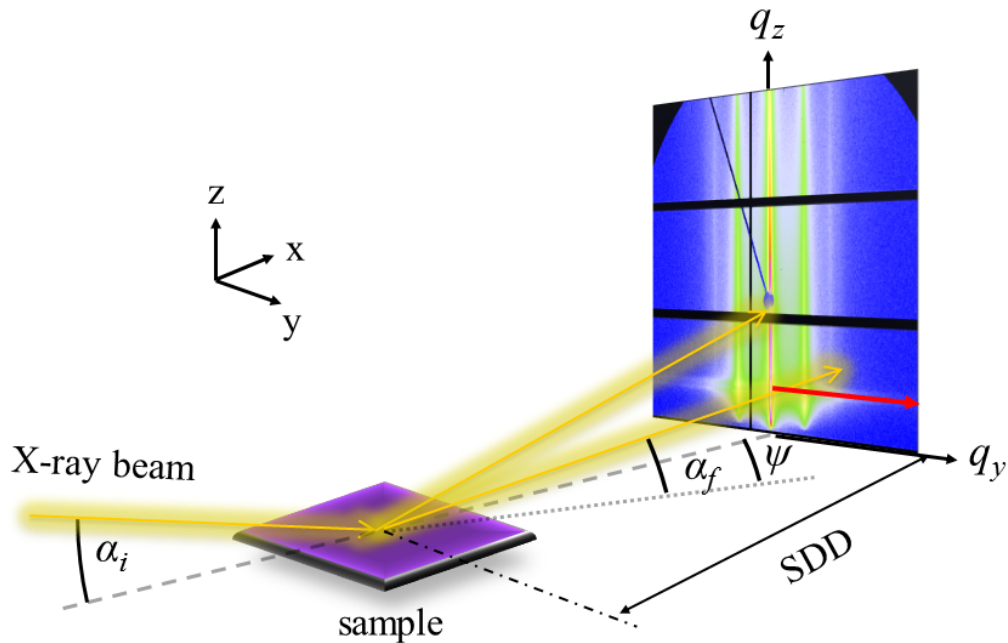


Figure 3.4: Sketch of the GISAXS measurement geometry. The x-ray impinges on the film at a small incident angle α_i , and the scattered signal with an exit angle α_f is recorded by a Pilatus 2D detector. ψ is the angle of the scattered beam relative to the incident beam in the x - y plane. Based on the structure size of the probed sample, a suitable sample-to-detector distance is set.

The GISAXS measurements are carried out at two different synchrotron facilities. The samples in Chapter 5, 7 and 8 are measured at the beamline P03, Micro- and nanofocus x-ray scattering (MiNaXS) of the PETRA III storage ring (DESY, Hamburg, Germany). The films investigated in Chapter 6 are probed at the I22 beamline of the Diamond Light Source (Oxfordshire, United Kingdom).

Figure 3.4 depicts the schematic view of the GISAXS experiment. The X-ray beam with selected wavelength impinges to the film at a certain incident angle (α_i). To ensure the penetration of the entire film, the incident angle is set to be above the critical angles (total reflection angles) of all materials involved in the probed film, but normally below

1°. In this case, the structure information over the full depth of the film can be gained from the scattering data.

To perform the measurements, samples are positioned on a stage which can move in a 3D fashion. A 2D detector, which is used for collecting scattering signals, is placed at a certain sample-to-detector (SDD) distance to the sample. The SDD is varied based on the desired dimension range of structure. A vacuum flight tube with adjustable length is installed and positioned in between the detector and sample stage, so that the scattering noise from the air can be minimized. To protect the detector from oversaturation, two beam stops are placed in front of the detector at the positions of the specular reflection and direct beam, respectively. The parameters used for measuring films in different chapters are detailed in Table 3.2.

| chapter | λ (nm) | α_i (°) | SDD (mm) | detector type | detector size (pixels) | synchrotron |
|---------|-------------------|-------------------|-------------|---------------|---------------------------|-------------|
| 5 | 0.094 | 0.40 | 4377 | Pilatus 1M | 981 × 1043 | DESY |
| 6 | 0.100 | 0.35 | 4650 | Pilatus P3-2M | 1475 × 1679 | Diamond |
| 7 | 0.108 | 0.40 | 4377 | Pilatus 1M | 981 × 1043 | DESY |
| 8 | 0.094 | 0.35 | 4229 | Pilatus 1M | 981 × 1043 | DESY |

Table 3.2: Detailed parameters of GISAXS measurements for different samples. The pixel size of all detectors is $172 \mu\text{m} \times 172 \mu\text{m}$.

For a quantitative analysis of the lateral structure present inside the probed films, horizontal line cuts of the 2D GISAXS data are made along the q_y direction (shown as the red arrow in Figure 3.4) via the software fit2d (Andy Hammersley, ESRF, Grenoble). To analyze the data from *in situ* GISAXS measurements, the software DPDAK (Gunthard Benecke, DESY Hamburg & MPIKG Potsdam) is employed. Afterwards, the extracted horizontal line cuts are modeled within the framework of the Distorted Wave Born Approximation (DWBA) assuming the effective interface approximation and the local mono-dispersion approximation. The applied model contains form and structure factors, and the length scales of the scattering objects are assumed to have a Lorentzian distribution [60]. From the modeling, information regarding the size of lateral structure, size distribution and the center-to-center spacing can be achieved.

Particularly, due to the oriented nanoparticle wires present in the films of Chapter 6, the wire-containing films are measured in two orientations with x-ray parallel and perpendicular to the wires (see Figure 3.5). In this case, the lateral structure perpendicular and parallel to the wires can be investigated.

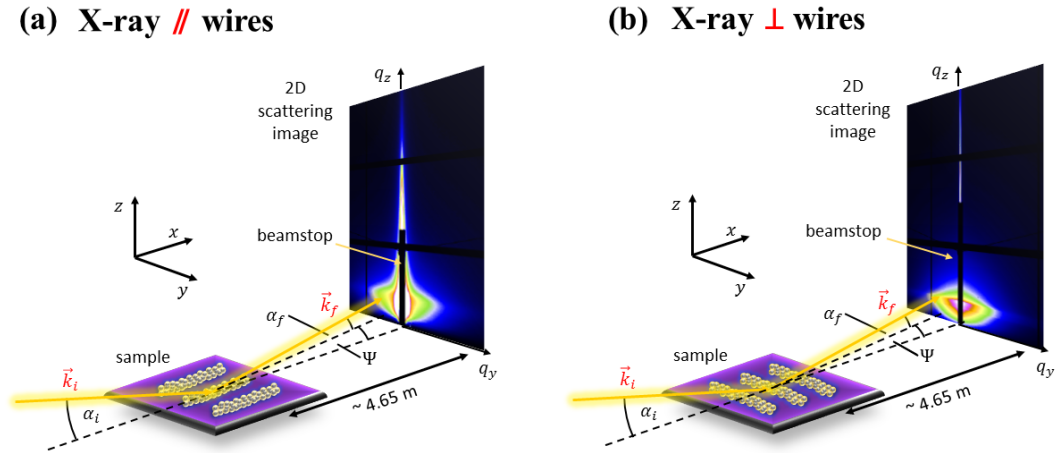


Figure 3.5: The applied two measuring orientations with incoming X-ray beam parallel (a) and perpendicular (b) to the wires for the wire-containing films in Chapter 6.

3.2 Characterizations of magnetic properties

3.2.1 SQUID magnetometry

The magnetic properties of the investigated hybrid films are probed via a superconducting quantum interference device (SQUID) magnetometer (MPMS XL-7, Quantum Design, San Diego, CA, USA). The measurements are performed in a DC (direct current) mode to record the magnetization as a function of temperature. Figure 3.6 depicts the schematic view of the employed SQUID instrument.

Before the measurement, the studied sample is cut into the size of $0.6 \text{ cm} \times 0.6 \text{ cm}$, and then placed inside a sample holder, which is a long plastic straw without magnetic disturbance. After the sample being positioned in the center of a superconducting solenoid, the sample chamber is sealed and then filled with liquid helium. For the measurement, the applied magnetic field runs from -700 mT to 700 mT . In this case, the saturation magnetization of the investigated magnetic NPs can be reached. The magnetic signals from the sample are collected by a superconducting pick-up coil installed around the sample, and then transferred to an rf-SQUID through a SQUID sensor which is connected to the pick-up coil. In this case, the magnetic flux can be converted into voltage signals, which are then amplified and displayed via the magnetometer electronics. During the measurement, the sample is oscillating with an amplitude of 3 cm in the vertical direction. Such oscillation leads to the alteration of the magnetic flux detected by the pick-up coil. As a consequence, the output voltage, which is proportional to the measured magnetic moments, changes in

the SQUID. Due to the weak response of the magnetic nanoparticles in the studied films, high sensitivity of the employed instrument is used. In our measurement, the readout frequency to the movement frequency is locked for this purpose [61].

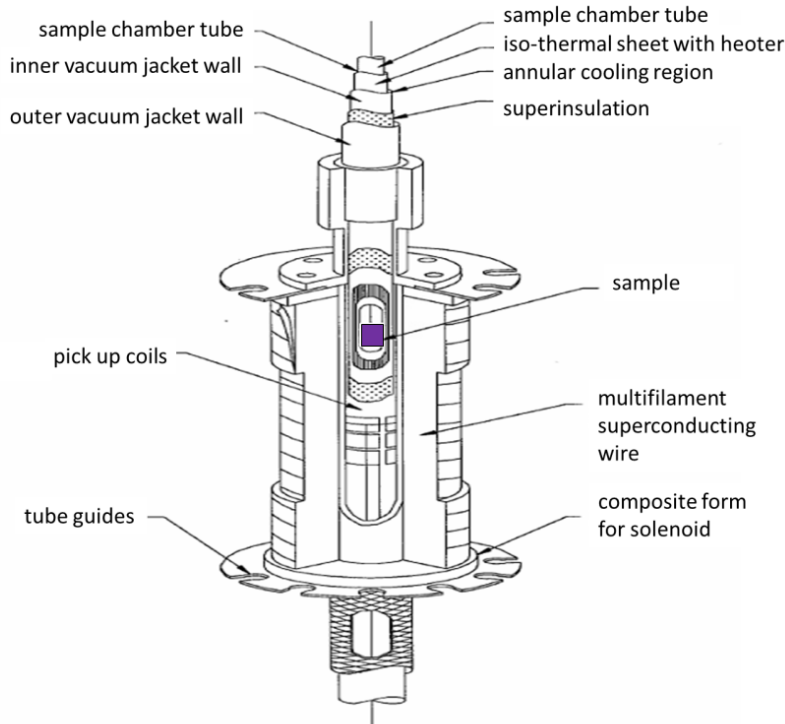


Figure 3.6: A simplified sketch of the SQUID instrument. The graph is taken from reference [62].

To probe the superparamagnetism, the samples are measured at various temperatures: 2, 5, 20, 50, 100 and 200K. For two batches of samples (in Chapter 6 and 7) where nanoparticle wires are present, the magnetic anisotropy is examined by performing the measurements in two orientations: with the direction of magnetic field parallel and perpendicular to the wires. Before the data analysis, the diamagnetic contribution from the silicon substrate is subtracted. For data interpretation, important parameters like saturation magnetization, coercivity, remanence, magnetic susceptibility and blocking temperature are extracted from the obtained magnetization curves.

4 Sample preparation

Various materials and film fabrication techniques are employed in the present work. In chapter 5, films are printed by cylinder structured PS-*b*-PMMA and magnetite nanoparticles. In chapter 6, maghemite nanoparticles are incorporated inside lamella structured PS-*b*-PMMA via printing. In the following chapters 7 and 8, printing and spray deposition are utilized respectively to prepare films out of PS-*b*-PNIPAM and magnetite nanoparticles. The specific differences are stated at the beginning of each corresponding chapter.

All investigated materials including diblock copolymer, magnetic NPs and solvent are presented in section 4.1. Different substrate cleaning procedures are displayed in section 4.2. This chapter is followed by film fabrication techniques in chapter 4.3, and finally post-treatment methods are detailed in chapter 4.4.

4.1 Materials

4.1.1 Diblock copolymer

In order to fabricate magnetic films with desirable nanostructures, different diblock copolymers (DBC) are employed for the present investigations. Generally, two types of DBCs are used: polystyrene-*block*-polymethyl methacrylate (PS-*b*-PMMA) and polystyrene-*block*-polyN-isopropylacrylamide, (PS-*b*-PNIPAM). The chemical structures and detailed information of the investigated DBCs are displayed in Figure 4.1 and Table 4.1, respectively.

All employed DBCs are purchased from Polymer Source Inc., Based on the theoretical phase diagram of DBCs discussed in Chapter 2.1.3, lamella structure is expected for the PS-*b*-PMMA ($f_{PS} = 0.5$), and cylindrical structures for both PS-*b*-PMMA ($f_{PS} = 0.685$) and PS-*b*-PNIPAM ($f_{PS} = 0.34$).

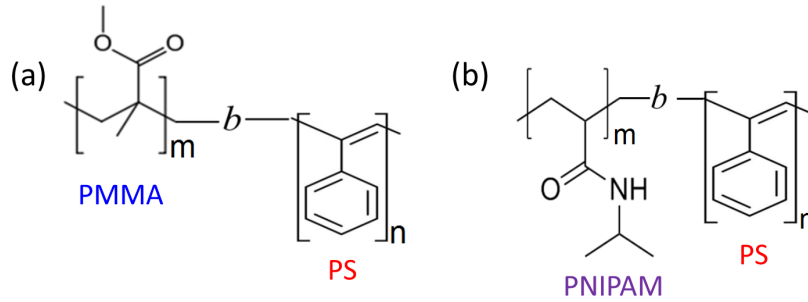


Figure 4.1: Chemical structures of investigated DBCs.

| polymer | M_n (kg/mol) | PDI | polymer block | M_n (kg/mol) | T_g (°C) |
|----------------------|-------------------|------|---------------|-------------------|---------------|
| PS- <i>b</i> -PMMA | 89 | 1.12 | PS | 45 | 106 |
| | | | PMMA | 44 | 135 |
| PS- <i>b</i> -PMMA | 66.5 | 1.13 | PS | 45.55 | 105 |
| | | | PMMA | 20.95 | 125 |
| PS- <i>b</i> -PNIPAM | 35.5 | 1.2 | PS | 11.5 | 105 |
| | | | PNIPAM | 24 | 132.8 [63] |

Table 4.1: Details of investigated DBCs including polymer name, number average molar mass M_n , polydispersity index (PDI), and glass transition temperature (T_g) of respective blocks of DBCs.

4.1.2 Magnetic nanoparticles

In the present work, two types of magnetic nanoparticles (NPs) are used, one of which is maghemite ($\gamma\text{-Fe}_2\text{O}_3$) NP and the other magnetite (Fe_3O_4) NP. Both types of magnetic NPs are functionalized with hydrophobic organic layers on the surfaces, which can improve the dispersion of magnetic NPs inside polymer matrices [64–68]. Therefore the magnetic NPs are employed with a core-shell structure, exhibiting an inorganic magnetic particle core surrounded by a layer of inorganic coating as a shell. The functional shell is beneficial to magnetic NPs dispersion inside polymer matrices. On one hand, it can improve the interaction between magnetic NPs and DBCs at the interface due to the enhanced chemical affinity resulting from their common organic nature [69, 70]. By tuning the organic layer, magnetic NPs can arrange inside the desired block of a DBC. On the other hand, the presence of organic coatings can impair the aggregation tendency of magnetic NPs to a certain extent caused by the magnetic attractive forces [71, 72]. Therefore, such surface-functionalized magnetic NPs are beneficial for NPs-DBC hybrid film fabrication.

The magnetite NPs (Fe_3O_4) are purchased from the supplier Sigma-Aldrich. The received magnetic NPs are grafted with a monolayer of oleic acid ligands, and dissolved in toluene with the concentration of 5 mg ml^{-1} . The mean diameter of the magnetite NPs is 10 nm, and the thickness of the organic layer is around 1.5 nm. The maghemite NPs ($\gamma\text{-Fe}_2\text{O}_3$) grafted with PS chains are synthesized using α -lithium polystyrenesulfonate (LPSS) and ferric chloride (FeCl_2 and FeCl_3). Details of the synthesis can be found elsewhere [73, 74]. The obtained maghemite NPs are soluble in toluene with a density of 1.09 g/cm^3 and a weight ratio of 2 wt %. The size and chemistry of the synthesized maghemite NPs are characterized by small angle scattering X-ray scattering (SAXS) and Mössbauer spectroscopy, respectively [75]. By modeling the SAXS data (Figure 4.2), a mean diameter of 10 nm with the width of log-normal size distribution of 0.2 is obtained. The Mössbauer spectroscopy (Figure 4.3) was carried out at two different temperatures. A magnetic sextet is clearly observed in both spectra data, which confirms the chemistry of the synthesized maghemite NPs.

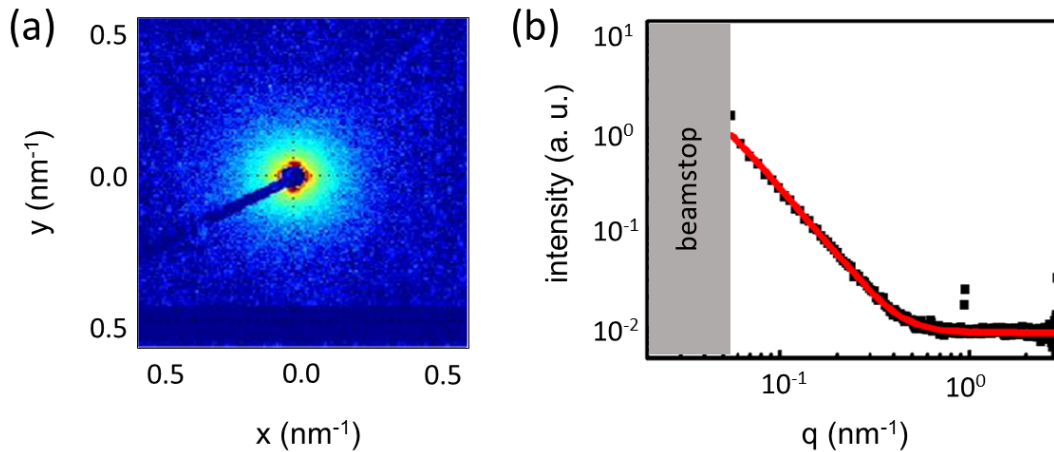


Figure 4.2: (a) 2D SAXS data of the synthesized maghemite NPs in toluene. (b) Radially averaged cuts (black symbols) extracted from the 2D SAXS data with corresponding fit (red line). Images are taken from reference [75].

4.2 Substrates

Silicon substrates (Si 100, n-type, Silchem) with a diameter of 10 cm and a thickness of $525 \mu\text{m}$ are employed for film deposition. The entire silicon substrates are cut into small pieces with different sizes according to the requirement of different film fabrication techniques: $25 \times 75 \text{ mm}^2$ for printing and $25 \times 25 \text{ mm}^2$ for spray coating. Prior to

film application, all substrates undergo a cleaning step. To achieve specific well-defined silicon surfaces for different DBC film systems, two types of substrate cleaning methods are applied in the present thesis.

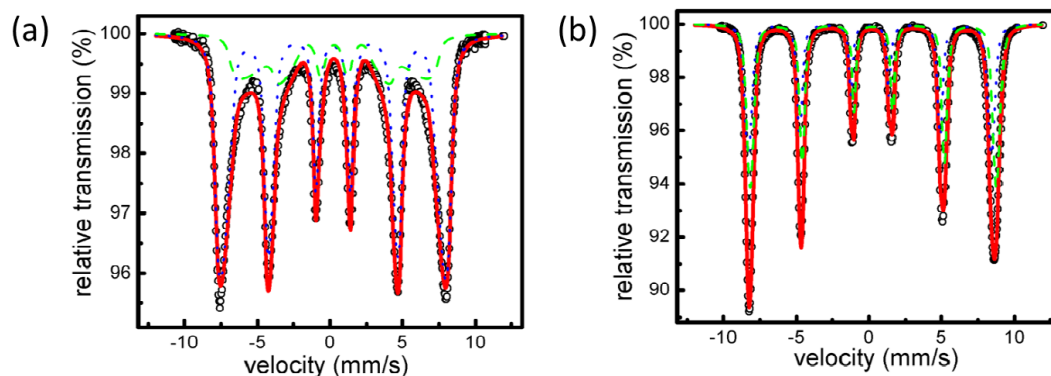


Figure 4.3: Mössbauer spectroscopy data measured at two different temperatures. Gauss and Lorentzian distribution functions are used to fit the data obtained at 295 K (a) and 4.2 K (b), respectively. The red lines are the fits to the data (black symbols). Two different Fe^{3+} lattice constructions are suggested by green dashed line (octahedral) and blue dotted line (tetrahedral), respectively. Images are taken from reference [75].

4.2.1 Acid bath cleaning

For the NP-DBC systems templated by PS-*b*-PMMA, a hydrophobic surface is favored for better film deposition. Accordingly, an acidic cleaning step based on sulfuric acid and hydrogen peroxide is applied. All pre-cut substrates are vertically mounted in a PTFE holder, and dust particles are removed via nitrogen stream. Afterwards, all substrates are immersed in an acid bath for 15 min at 80 °C. The employed acid bath solution consists of 200 mL of H_2SO_4 (purity 95.0 %), 70 mL of H_2O_2 (purity 30.0 %) and 130 mL of deionized water (purity 99.9 %). Thereafter, each substrate piece is rinsed thoroughly with deionized water, and then dried in a nitrogen flow. All cleaned substrates are stored in petri dishes and used for film preparation on the same day [76].

4.2.2 Basic bath cleaning

For the hybrid system where PS-*b*-PNIPAM is employed as the template, a basic bath cleaning procedure is applied, through which 1 nm of hydrophilic silicon oxide layer can be established on the substrate surface [77, 78]. Similar to acid bath cleaning, substrates

are placed on a PTFE holder and oil-free nitrogen is used to remove dust particles. Then all substrates are inserted into dichloromethane (purity 99.5 %) at 46 °C for half an hour. After being rinsed with deionized water, all substrates are transferred to a basic bath at 76 °C for 2 hours. The basic bath consists of 30 mL of $\text{NH}_3 \cdot \text{H}_2\text{O}$ (purity 30.0 %), 300 mL of H_2O_2 (purity 30.0 %) and 350 mL of deionized water (purity 99.9 %). Afterwards, the substrates are shortly stored in deionized water. Before film deposition, all substrates are rinsed with deionized water and then dried via nitrogen flow [18].

4.3 Film fabrication techniques

Since all investigated DBCs and magnetic NPs are soluble in organic solvents, it is easy to deposit films on silicon wafers via casting or coating. For the purpose of large-scale production, printing and spray coating are utilized for hybrid film fabrication, which are detailed in the following sections 4.3.2 and 4.3.3 of this chapter.

4.3.1 Solution preparation

To ensure the obtained films are homogeneous, all employed DBCs need to be well dissolved in the selected solvents. Therefore, various organic solvents need to be pre-tested for the investigated DBCs. For the final experiments, toluene is selected for the system based on the DBCs of PS-*b*-PMMA, and tetrahydrofuran (THF) is applied to the PS-*b*-PNIPAM based system.

To achieve the desired thickness of the obtained films, the concentrations of the polymer solution need to be selected accordingly. Based on the desired concentrations, a suitable amount of polymer is weighed accordingly by a precise electronic balance, and transferred into clean glass bottles. Afterwards, corresponding solvents with calculated volumes are added into the bottles via a pipette. To prevent solvent evaporation, the glass bottles are firmly sealed with parafilms, and then placed on a shaker for 4 h to ensure a complete dissolution. To investigate the influence of magnetic NPs on the DBC films structure, various weight ratios of magnetic NPs over DBCs are experimented. Details regarding the solution preparation are given at the beginning of each chapter.

4.3.2 Printing

The printer is designed laboratorily based on the working principal of slot-die coating. Generally, the whole printing device consists of three main parts: printhead, syringe

pumping system, and linear stage. The printer was developed by S. Günther from the group [79].

Printhead

As one crucial part of the printing device, the printhead consists of five different components, which are front endplate, solution guide mask, meniscus guide mask, gasket frame and back endplate (shown in Figure 4.4). Among those printhead components, the two masks (solution guide mask and meniscus guide mask) are the most important ones, which allows user to vary the printhead-specified parameters without changing printheads, but by simply exchanging the corresponding masks.

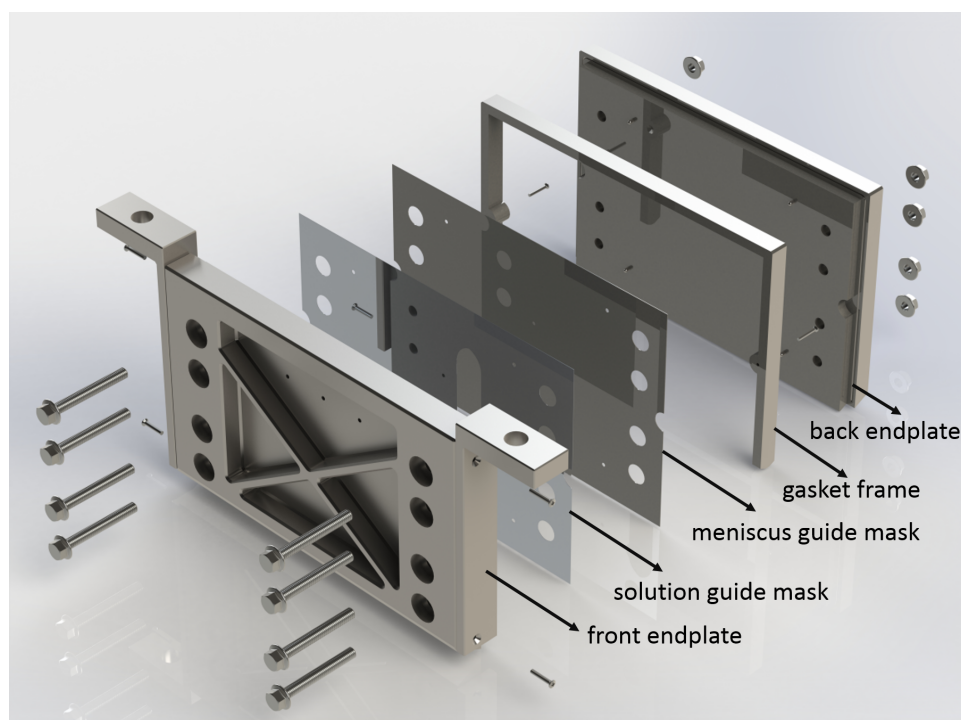


Figure 4.4: Schematic overview of the printhead. The names of different parts are shown in the figure accordingly. The figure is from the reference [79].

The schematic view of the two masks is shown in Figure 4.5. Via tuning the thickness and length of meniscus guide mask, the size and shape of printed films can be controlled. Two independent solution channels are designed in the solution guide mask, which allows for printing different films at the same time.

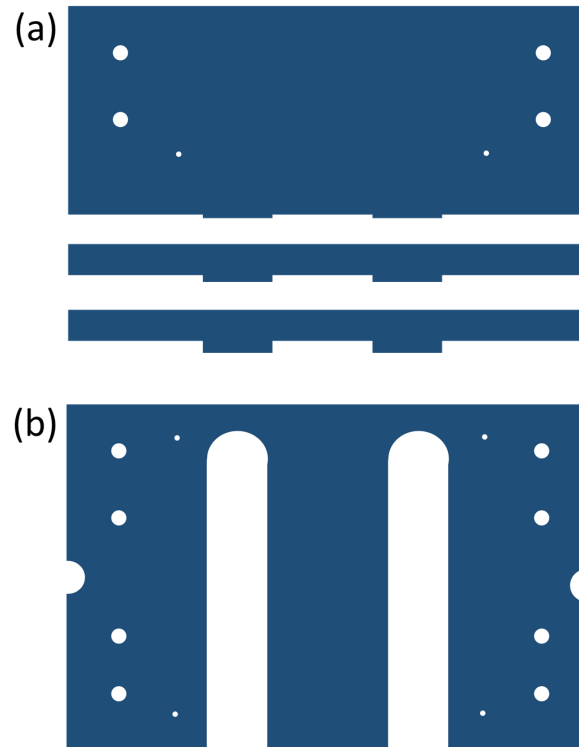


Figure 4.5: (a) *Meniscus guide mask (top part removed), and three guides with different length are illustrated.* (b) *Solution guide mask with two printing channels.*

Syringe pumping system

A syringe pumping system is used to feed the printhead with ink and control the flowrate of the solution. Calibration of the system is done by using a 5 ml-volume syringe (Braun Omnifix). The whole system is connected with a specially designed program, through which the flowrate can be controlled in the $\mu\text{l/s}$ regime. For printing solution transportation, a PTFE semitransparent tube is employed. First, the two ends of the tube are connected to syringe and solution bottle. After certain amount of solution being sucked into the clean tube, the tube end in the solution bottle is released and connected to the inlet on the front endplate of the printhead. Then the solution can be printed onto the substrate through the printhead.

Linear stage

In addition to the printhead and syringe pumping system, the linear stage is also one core part of the printing device. The functionality of the linear motorized stage is to translate the substrate holder along the printing direction. Therefore, the substrate staying on

the holder is also translated in the same manner. Figure 4.6 displays the assembly of the linear stage. A 3-point mounted stage is employed to adjust the distance between meniscus guide and substrate. The linear motor is controlled via a software, accordingly the printing velocity, printing length and acceleration profiles can get tuned. Concerning the printer used in this work, a translation distance of 100 mm, a velocity of 0.001 mm/s - 12 mm/s and deep acceleration profiles are accessible.

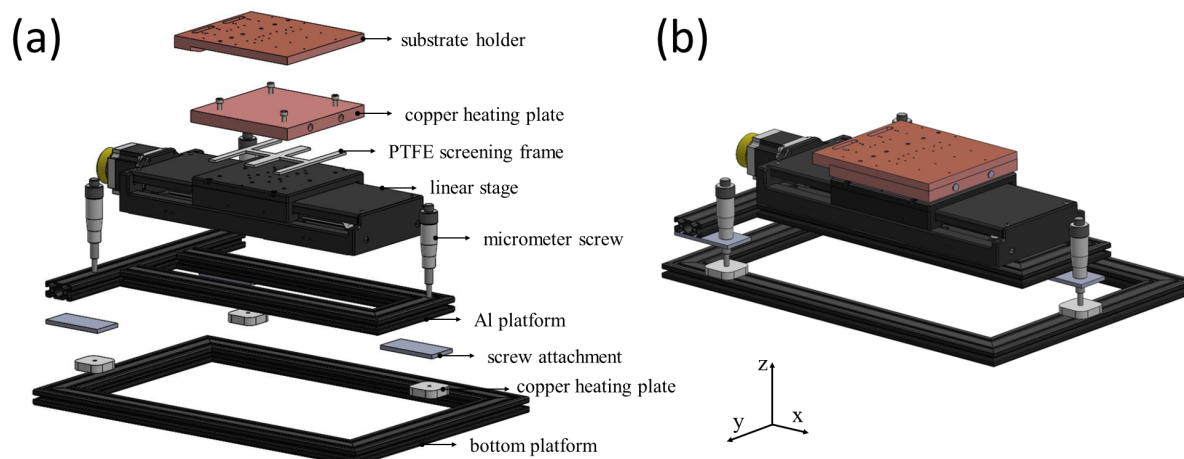


Figure 4.6: Exploded (a) and assembled (b) view of the linear stage.

Printing

Before printing, the printhead needs to be disassembled and all parts are required to be clean. A stepwise basic cleaning procedure, using Alconox, ethanol, acetone and isopropanol, is used for a thorough cleaning, then followed by drying the printhead with nitrogen flow. After all the parts are reassembled, the printing ink is transferred to the printhead using the syringe pumping system, shown in Figure 4.7. To print films with desirable thickness, printing parameters like solution concentration, printhead-to-substrate distance, solution flowrate and substrate moving speed need to be found via initial printing tests. Thereafter, films can be printed using suitable parameters. During printing process, magnetic field can be applied to direct the alignment of magnetic NPs. To grant the magnetic NPs enough time for arrangement, the substrate holder is controlled to be at room temperature. After the printing process is finished, the film is kept on the holder until the solvent evaporation is complete. Then the film can be taken out for post-treatment and characterization. After all films are printed, the printhead needs to be cleaned again. For different DBC films investigated in the present thesis, different printing parameters are selected and summarized in Table 4.2.

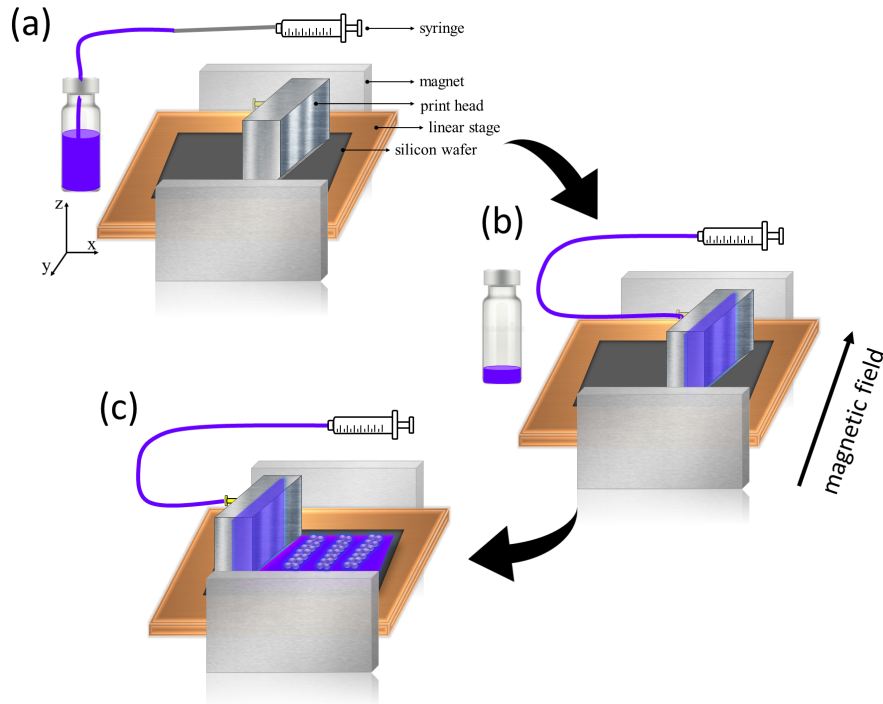


Figure 4.7: Sketch of set-up used in the whole printing process: (a) Solution is transferred from bottle to tube, (b) Solution is transferred to printhead, (c) Printing.

| polymer | M_n (kg/mol) | $C_{polymer}$ (mg/ml) | distance (mm) | flowrate ($\mu\text{l/s}$) | velocity (mm/s) | magnetic field |
|----------------------|-------------------|--------------------------|------------------|---------------------------------|--------------------|-------------------|
| PS- <i>b</i> -PMMA | 89 | 10 | 1 | 50 | 5 | yes |
| PS- <i>b</i> -PMMA | 66.5 | 7 | 1 | 10 | 10 | no |
| PS- <i>b</i> -PNIPAM | 35.5 | 25 | 1 | 15 | 5 | no |

Table 4.2: Parameters of printing different DBC films including DBC concentration, printhead-to-substrate distance, solution flowrate and velocity of substrate holder.

4.3.3 Spray coating

Due to the simplicity of spray coating, PS-*b*-PNIPAM is also prepared via spray deposition for kinetic investigation. The spray set-up is simplified in Figure 4.8.

The whole height-tunable spray set-up is installed in a specially designed chamber with a dimension of around $60 \times 60 \times 60 \text{ cm}^3$, which is used to control the emission of organic solvent via 8 nitrogen inlets located on the chamber (four on the top and four at the bottom). The spray set-up is motorized and connected to a computer program, therefore remote control of spraying can be realized. The spray gun (Grafo T3, Harder & steenbeck

GmbH & Co. KG) is mounted on the spray set-up with a nozzle-to-substrate distance of 17 cm. Oil-free nitrogen is used with a pressure of 1.5 bar to create the solution flowrate of $33 \mu\text{l/s}$. The employed spray protocol is 30 spray cycles followed by 20 s of annealing. Each spray cycle consists of 1 s of spray shot and 1 s of drying. Pre-cleaned silicon substrate with the size of $25 \times 25 \text{ mm}^2$ is placed on the holder during the whole spray process. The temperature of the substrate holder is controlled to be $50 \text{ }^\circ\text{C}$ in order to ensure fast solvent evaporation.

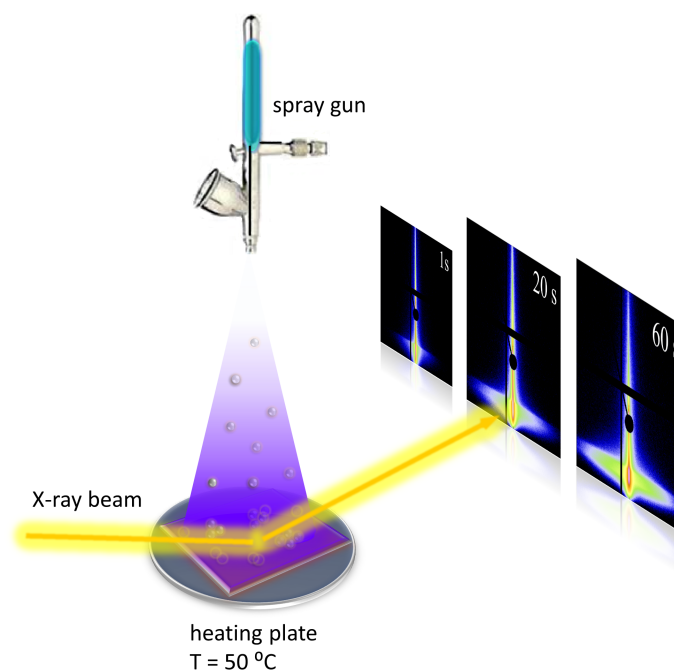


Figure 4.8: Schematic view of the spray set-up.

4.4 Post-treatment

For DBC films prepared from solution, non-equilibrium could exist inside the films due to a fast solvent evaporation. Since the polymer chains have not enough time for equilibration, the obtained films are kinetically trapped in a non-equilibrium state showing disorganized or ill-defined structures, which are unfavorable for applications [8]. To enhance the structure order of DBC films, post-treatments, like thermal annealing or solvent vapor annealing are employed.

4.4.1 Thermal annealing

Thermal annealing at the temperature above the glass transition temperature (T_g) provides polymer chains with sufficient mobility for microphase separation and rearrangement. By annealing DBC films at suitable temperature for certain time, the order can be improved [80–82].

In the present thesis, thermal annealing is done in a glovebox in which inert nitrogen is present to avoid possible degradation and oxidation. The applied temperature is controlled by a hotplate and set to be between glass transition temperature (T_g) and the order-to-disorder temperature (T_{ODT}). Accordingly the equilibrium state can be realized by macromolecule movement, and the structure can be improved. Also solvent left inside the films can be removed completely. Detailed parameters of thermal annealing treatment are stated in the corresponding chapters.

4.4.2 Solvent annealing

Similar to thermal annealing, solvent vapor annealing (SVA) also aims at establishing highly ordered structures predicted for equilibrium. Instead of thermal energy, SVA provides sufficient mobility to the polymer chains by swelling the DBC films with solvent molecules. Generally, SVA is a process in which the DBC film is placed in a solvent vapor atmosphere for the purpose of structural reorganization. During the SVA process, the DBC film is swollen by small solvent molecules, which results in a decreased T_g of the employed DBC and enhanced mobility of the polymer chains [83, 84]. As a consequence, long-ranged lateral ordering of the DBC film can be realized at room temperature within short time.

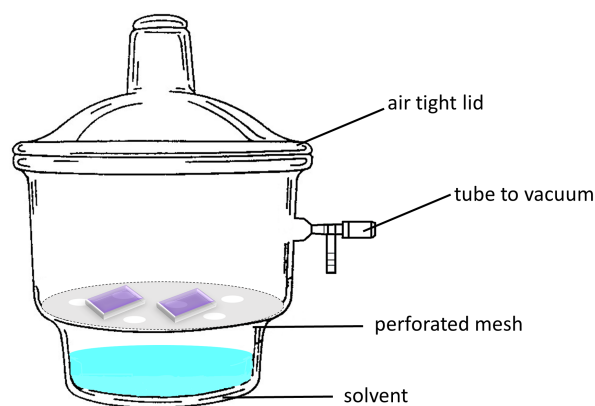


Figure 4.9: *Desiccator set-up used for solvent vapor annealing.*

So far, there has been no standardized routine for SVA, and experimental devices range from basic to highly sophisticated based on different purposes. In the present thesis, SVA is carried out in a desiccator with a volume of 2.4 L (shown in figure 4.9). Generally, samples are placed on the perforated mesh which is over the solvent liquid, Then the lid is tightly sealed by parafilms, and the desiccator is vacuumed through a outlet tube located aside. After proper SVA time, samples can be taken out.

Compared with thermal annealing, SVA is a more complex process. The finally obtained structure is influenced by many factors, such as the type of solvent, the annealing time, the pressure and the rate of solvent removal [8, 9, 85, 86]. Due to the different affinity of solvents to different blocks, mixed solvents need to be used in order to achieve the desired structures [84]. Therefore, the volume fraction of the solvent components needs to be considered. In the present thesis, specific SVA parameters are described in the corresponding chapters.

5 Printed magnetic anisotropic films with magnetic field

Parts of this chapter have been published in the article: Printed thin magnetic films based on diblock copolymer and magnetic nanoparticles [87] (Reprinted with permission from (S. Xia et al., *ACS Appl. Mater. Interfaces*, 2018, 10, 2982–2991). Copyright (2018) American Chemical Society. DOI: 10.1021/acsami.7b16971.)

Our previous works show that the localization of NPs inside DBC matrices and the resulting overall structure of the obtained hybrids are important factors in the NP–DBC film fabrication [18, 88, 89]. However, the preparation and post-processing methods can also be key factors in influencing the desired morphology of the NP–DBC hybrid materials [80, 90]. To date, several techniques have been explored for hybrid film fabrication, including spin coating [91], solution casting [92], spray coating [93], and dip coating [94]. In addition, film deposition via printing is very attractive, since it is a low-cost technique, enables large-scale processing, is simple to scale up, and is compatible with many different types of substrates [95]. Moreover, it is material efficient, because all of the ink supplied to the print head is printed with no loss. The thickness, morphology and surface topography of printed hybrid films can be controlled by the print parameters during the film fabrication. In research, the use of printing for film deposition is gaining strong interest for a variety of different applications. For example, Chen et al. printed the first all-polymer filter circuit using a soluble conducting polymer mixture [96]. Their investigation illustrates the advantages of printing in comparison to more traditional film deposition methods [96]. Pierre et al. have demonstrated the fabrication of fully printed organic thin-film transistors [95]. The printed devices exhibited high reliability, low variability, and an ideal electrical behavior [94]. However, reports involving printing techniques so far have mainly focused on homopolymers or polymer blends with applications in organic electronics [94–99] or photovoltaics [20, 100–102]. Examples on printing block copolymer films are still rare. To achieve block copolymer based hybrid materials with NPs in particular, the used inks need to be optimized for the print process. The viscosity and volatility

of the ink can significantly influence the film quality, and an in-depth understanding will be highly beneficial.

Since printing is also a solvent evaporation based processing method, the investigation of the drying kinetics is necessary. Recently, for example, Palumbiny et al. and Pröller et al. used synchrotron radiation based *in situ* measurements to study the structure formation of printed films for use in organic photovoltaics [20, 102]. Due to the uniaxial deposition method in combination with the solvent evaporation step, the print technique can be combined with the use of an external field such as a magnetic field, which is very difficult to be realized with spin coating or spray deposition. For example, Kokkinis et al. recently employed a rotating external magnetic field to control the orientation of magnetized platelets in their 3D printing platform [103]. Also, Yao et al. demonstrated that hybrid film systems of a block copolymer matrix and magnetic NPs show a superparamagnetic behavior and a remarkable shape anisotropy when combining solution casting with a magnetic field guiding the NPs [75]. In principle, magnetic anisotropy linked with sample geometries is the subject of many studies, as it can be used in devices [101]. Such samples are typically prepared with lithography techniques [104]. The field-directed assembly of magnetic NPs can provide an economical, simple, and reliable technique to realize magnetic anisotropy, when using print techniques to deposit the hybrid film of block copolymer and magnetic NPs in combination with magnetic field guidance of the NPs.

In the present work, we use a printing technique to fabricate hybrid magnetic films composed of maghemite ($\gamma\text{-Fe}_2\text{O}_3$) NPs and polystyrene-*block*-poly(methyl methacrylate) (PS-*b*-PMMA) diblock copolymer (DBC). The films are deposited on solid supports with slot die coating, a method compatible with roll-to-roll printing. The maghemite NPs are coated with PS to achieve a preferred localization and dispersion of the NPs inside the PS blocks of the DBC. Furthermore, an external magnetic field is applied during the printing step. The combination of printing and magnetic field exposure ensures the production of continuous hybrid films with an oriented anisotropic magnetic nanostructure. Under the external magnetic field, the magnetic NPs assemble into elongated clusters or wires aligning along the magnetic field direction. Due to the use NPs of a small size, a superparamagnetic behavior of the printed hybrid film is achieved and probed. Compared with films fabricated via solution casting, the printed films exhibit a higher magnetic susceptibility due to the higher density of nanostructures containing dispersed single NPs or nanosized clusters [75]. The high sensitivity to external magnetic fields renders the printed films interesting potential candidates in magnetic sensing applications. Combining an external magnetic field with the printing technique enables the preparation of homogeneous hybrid films with highly oriented mesoscopic structures. Given the possi-

bilities of up-scaling, printing of magnetic sensors is of particular interest for real world applications.

5.1 Printing magnetic films

Films are fabricated by printing as described in chapter 4.3.1 and chapter 4.3.2. In the present chapter, the number average molecular weight of PS-*b*-PMMA is 89 kg/mol with the volume fraction of PS block as 0.5. The employed maghemite NPs (γ -Fe₂O₃) are coated with PS chains. The mean diameter of the NPs is 10 nm with a lognormal size distribution (width 0.2) [75]. To enable a sufficiently high mobility of NPs in the ink, the polymer concentration in toluene is fixed to be 10 mg/ml. To investigate the influence of NPs on the film morphology, the NP concentration is varied: 0.005, 0.2, 0.5, 1, 2, and 5 wt%. After the preparation of mixed solutions (see chapter 4.3.1), all films are printed onto pre-cleaned silicon substrates with the size of 25 × 75 mm². During printing, an external magnetic field is oriented vertically to the print direction in the plane of the sample (see chapter 4.3.2). The permanent magnets used for this setup are obtained from Magnets4you GmbH. The strength of the applied magnetic field is fixed to 149 G at the center of the sample. After printing, samples are kept on the printing stage for half an hour to ensure complete solvent evaporation. The whole printing process is performed in air at room temperature. Next, all samples are annealed in the same magnetic field at 120 °C in N₂ for 3 days. The annealing post-treatment is carried out in a glovebox filled with inert N₂ (see Figure 5.1). All investigated films are prepared following the same printing procedure.

By employing printing, we can get control over the thickness and morphology of the prepared hybrid films consisting of PS-*b*-PMMA and maghemite NPs. Generally, the dry film thickness can be estimated via the simplified equation 5.1 [101].

$$d = \frac{f}{S} \frac{c}{w \rho} \quad (5.1)$$

where d is the dry layer thickness in cm, c is the solid concentration of the ink in g/cm³, f is the ink flow rate in cm³/min, ρ is the density of the dried ink materials in g/cm³, S is the printing speed in cm/min, and w is the printing width in cm. Profilometry measurements show the obtained films have a thickness of around 1.3 μm.

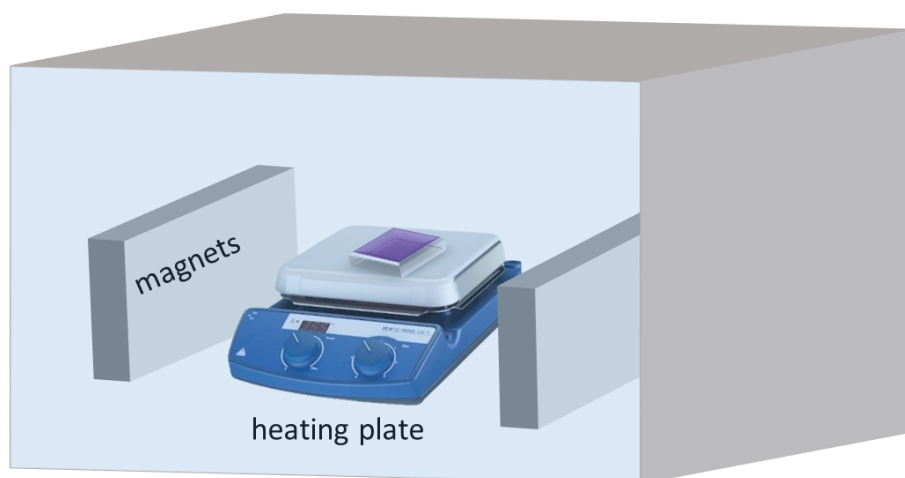


Figure 5.1: Hybrid film annealed within magnetic field in glovebox.

5.2 Formation of NP wires and surface morphology

According to previous investigations [105, 106], the solute concentration is higher at the liquid–air interface than that near the solid/liquid interface due to the fast solvent evaporation during the printing. Thus, under an external magnetic field applied during printing of the hybrid films, an excess concentration of NPs will initially be formed at the air–liquid interface, creating ordered mesoscale NP wires on the surface which successively grow deeper into the film. Assemblies of NP wires with different dimensions are observed for various NP concentrations, as shown in Figure 5.2. In Figure 5.2, the light yellow parts represent the polymer matrix, whereas the dark parts show the aggregated NPs assembled into wires which have aligned parallel to the external magnetic field and perpendicular to the movement of the print head (see Figure 4.7 c).

The average width of wires and mean separation distance between two neighboring wires is presented in Figure 5.3 as a function of the NP concentration. These data are extracted from OM images with the help of software ImageJ. At lower NP concentrations, the NPs assemble into elongated clusters and short narrow wires which exhibit a broad distribution in lengths. No wires elongating over the complete measured film surface are observed (Figure 5.2 a). Short wires are densely packed but oriented parallel to each other to form characteristic domains of short wire bundles. The applied magnetic field controls the assembly of NP wires. All isolated wires align parallel to the magnetic field. The angular dependence of the dipolar forces between randomly oriented wires prevents aggregation in a random way. In contrast, wires form head-to-tail chains along the magnetic field due to interwire interactions [107]. Provided the case where two wires are aligned along the

magnetic field collinearly, the attractive force between two neighboring short wires can be calculated as follows [107]

$$f(r) = -Q_m^2 \left[\frac{1}{r^2} - \frac{1}{(r + L_1)^2} - \frac{1}{(r + L_2)^2} + \frac{1}{(r + L_1 + L_2)^2} \right] \quad (5.2)$$

where Q_m is the magnetic charge at one end of the wire, L_1 and L_2 are the lengths of two NP wires, respectively, and r is the end-to-end separation in the y axis direction.

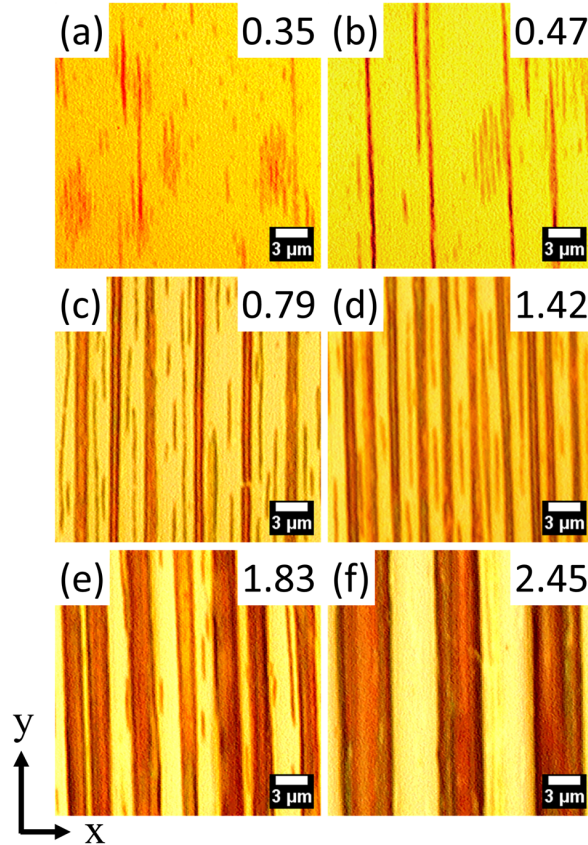


Figure 5.2: Optical microscopy images of the hybrid films at different NP concentrations of (a) 0.05, (b) 0.2, (c) 0.5, (d) 1, (e) 2, and (f) 5 wt%. Samples are prepared under a constant external applied magnetic field (149 G) along the y axis. The analysis is limited to an image size of $30 \times 30 \mu\text{m}^2$, and neighboring distances are only analyzed for the wires which extend along the long-axis beyond this area. The top right numbers show the root-mean-square roughness values (R_{rms} , units: nm) of the wire-free areas for each sample. (Reprinted with permission from [87] Copyright 2018 American Chemical Society.)

When increasing the NP loading, the separation distance r becomes smaller, leading to a higher attractive force $f(r)$. Therefore, short wires become long extending over several hundred micrometers. In addition, wires also grow in width with increasing NP concentration. As the number of NP wires increases, the separation distance between

neighboring wires (in the x axis direction) decreases due to the limited sample area. At a NP concentration of 1 wt%, the separation distance reaches a minimum. The narrower and shorter wires tend to be located in between two larger wires (see Figure 5.2 c and d), where the local magnetostatic energy is the lowest. As the NP concentration is increased further, the number of NP wires decreases, while the width starts to increase significantly with the wire-to-wire separation distance, to ensure the minimum energy of the whole system [107].

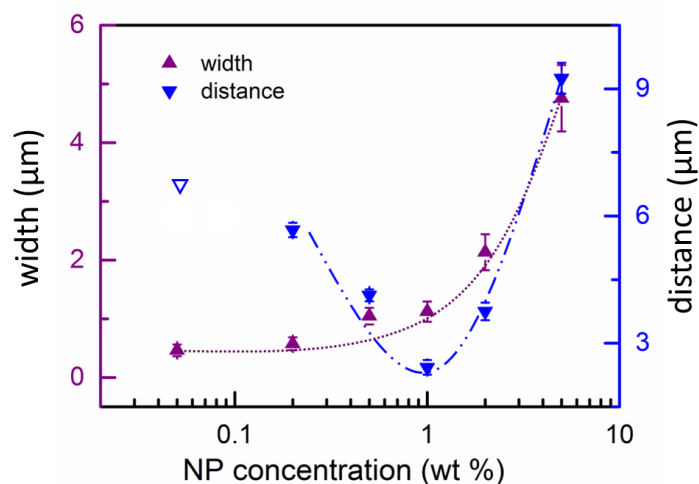


Figure 5.3: Average width of NP wires (purple triangles) and mean separation distance between two neighboring NP wires extracted from OM images and plotted as a function of NP concentration. At 0.05 wt % NP concentration, the interwire distance is poorly defined (open symbol). Two dashed lines serve as a guide to the eyes. (Reprinted with permission from [87] Copyright 2018 American Chemical Society.)

On a more local scale, the topography of the assembled NPs and the nanostructure of the DBC are probed via AFM and SEM (see Figure 5.4). While NP wires are composed of aggregated NPs (Figure 5.4 c and d), homogeneously dispersed NPs are additionally found inside the PS domains of the DBC film forming a lamellar morphology (Figure 5.4 b, e and f).

Generally, the self-assembly of magnetic NPs is a complex process due to numerous competing effects. Magnetic dipole-dipole interactions [107], electronic polarization interactions [108], the coupling of each particle's dipole moment to the applied magnetic field [109], thermal kinetics [110], the media in which the NPs are aligned, and the ambient conditions during alignment [111] are of importance among other factors [112]. Presently, the authors are not aware of a rigorous theory or models accounting for all these effects and describing the NP self-assembly in block copolymer matrices. In a simplified view,

the process guiding individual NPs into large NP wires can be divided into three steps: (1) At low NP concentrations, the NP can be accommodated by the diblock copolymer matrix and the driving force from microphase separation dominates the system, leading to the incorporation of functionalized NPs into the PS domains. (2) With increasing NP concentration, the initially dispersed single NPs aggregate into clusters, which can no longer be incorporated inside the PS domains. (3) The NPs within each cluster have a uniaxial anisotropy and therefore tend to align lengthwise parallel to the applied magnetic field. Thus, NP wires form in the hybrid films. Additional information concerning NP wires formation can be found in our previous studies [18, 75, 88].

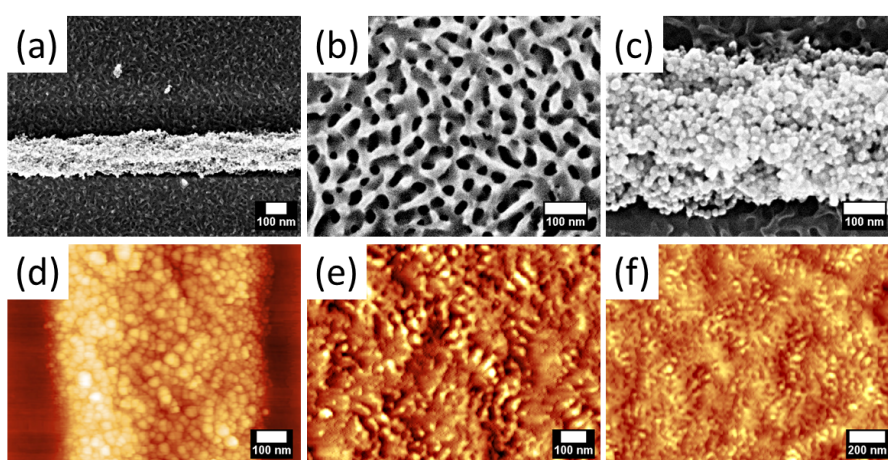


Figure 5.4: (a–c) SEM and (d–e) AFM images of the selected sample with a NP concentration of 0.5 wt% in different magnifications and at different positions. (b,e,f) show the polymer film surface and (c,d) focus on the NP aggregate. (Reprinted with permission from [87] Copyright 2018 American Chemical Society.)

5.3 Inner morphology

In order to investigate the buried nanostructure with a high statistical relevance, all printed films are measured via GISAXS at an incident angle above the critical angle of the films. Details of the GISAXS technique are described in the theory part and elsewhere [55, 113]. Due to the presence of NP wires on the film surfaces, GISAXS probing is carried out in two orientations with X-ray parallel and perpendicular to the wires. In this way, the influence of NP wires on the inner morphology can be studied. Figure 5.5 shows the 2D GISAXS data obtained from two different orientations. Similar in both groups of data, the scattering intensity changes significantly with the incorporation of magnetic NPs. However, obvious differences can be observed at high NP concentrations

due to the existence of NP wires. To get a quantitative analysis, horizontal line cuts are made at the Yoneda peak position of PS-*b*-PMMA, and a comparison is made between both orientations.

5.3.1 Lateral structures perpendicular to the NP wires

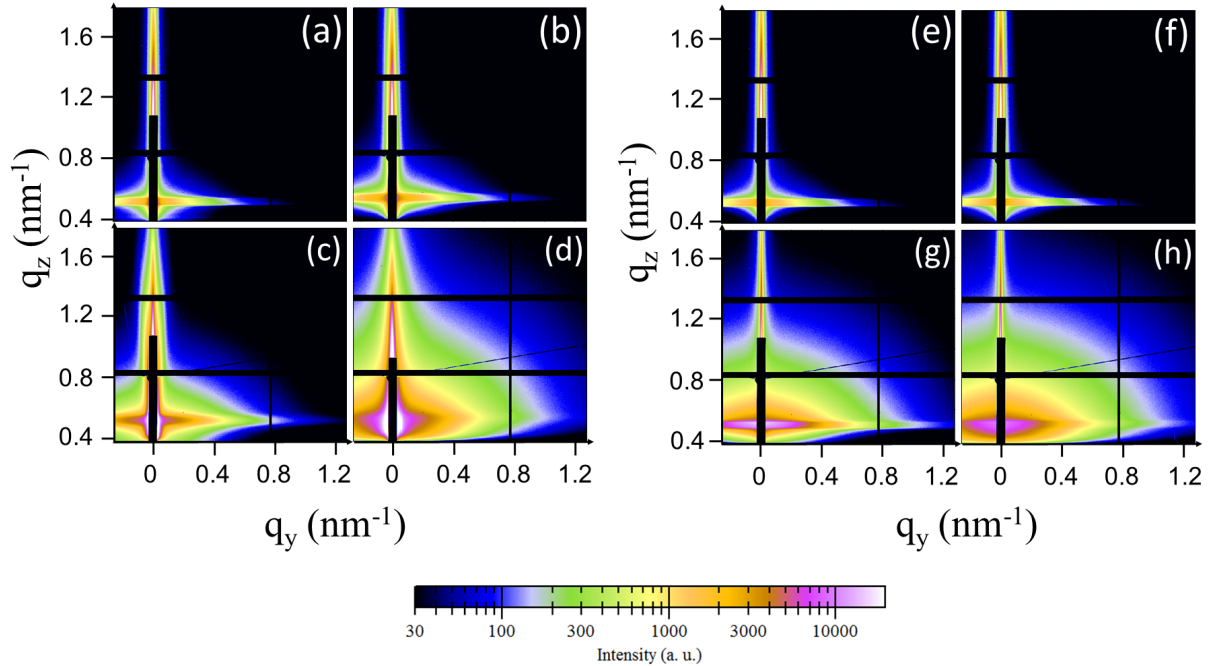


Figure 5.5: Selected 2D GISAXS patterns of NP-DBC hybrid films with various NP concentrations, with the X-ray beam oriented (a-d) parallel and (e-h) vertical to the NP wires: (a, e) 0.2, (b, f) 0.5, (c, g) 2, and (d, h) 5 wt%. All images are shown under identical intensity scale bar as indicated. (Reprinted with permission from [87] Copyright 2018 American Chemical Society.)

Figure 5.6 displays the horizontal line cuts as well as the corresponding fits. In the parallel orientation, meaning X-ray beam parallel to NP wires, the buried nanostructure perpendicular to wires can be investigated. Three main characteristics, suggested as arrow I, II and III, are present in Figure 5.6a. In the low- q_y area, a structure factor originating from the DBC microphase-separated nanostructure is applied to fit the line cuts. In the fitting model, the structure size is assumed to exhibit a Lorentzian function, from which the inter PS domain distance (D) can be yielded. The corresponding positions of D are indicated by arrow I in Figure 5.6a. At low NP concentrations ($C_{NP} < 1$ wt%), peak I shifts to a slightly lower q_y position, suggesting a smooth increment of D . Such increase is caused by the incorporation of magnetic NPs into DBC films. Since the NPs

are grafted with PS chains, they show strong affinity to the PS domains. The favorable enthalpic interaction can lead to the preferential localization of NPs inside the PS blocks, ending up with swollen PS domains. Therefore, the interdomain distance D increases. With further NP doping ($C_{NP} > 0.5$ wt%), peak I shifts to much smaller q_y positions progressively, which suggests a sharp increase of D (shown as Figure 5.7). Such a feature is caused by the overload of NPs, which leads to ill-defined structures present inside the hybrid films [75]. Accordingly, the long-range order of the DBC structure is perturbed. In the region of high q_y values of the scattering profile, broad peaks, indicated as peaks II and III, are visible. They result from the contribution of the form factor of single NP and NP aggregates, respectively. Therefore, the state in which NPs exist inside the DBC matrix at various concentrations can be interpreted from the scattering behavior. Initially NPs are dispersed individually inside PS domains at low NP concentrations, but form aggregates (size around 25 nm) with increasing concentration. Due to the constant position of peak III, it can be concluded that the nanosized NP aggregates are also present at high concentrations ($C_{NP} > 1$ wt%).

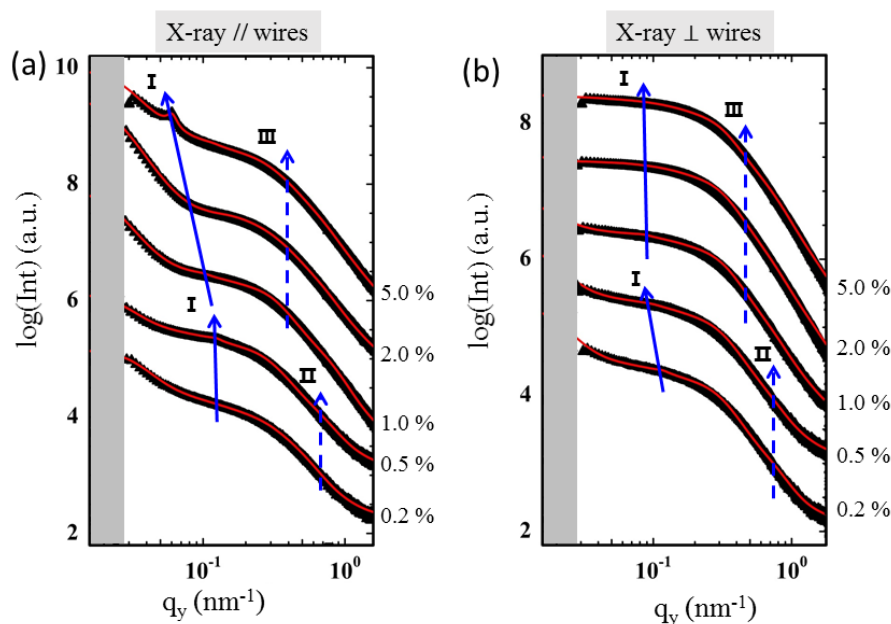


Figure 5.6: Horizontal line cuts (black symbols) obtained from corresponding 2D GISAXS data measured at different orientations with X-ray beam parallel (a) and vertical (b) to NP wires. All line cuts are displayed together with the fits (red solid lines), and are shifted along the y axis for clarity. NP concentrations are indicated in the profile. Arrows in the graph serve as guides to the eyes. (Reprinted with permission from [87] Copyright 2018 American Chemical Society.)

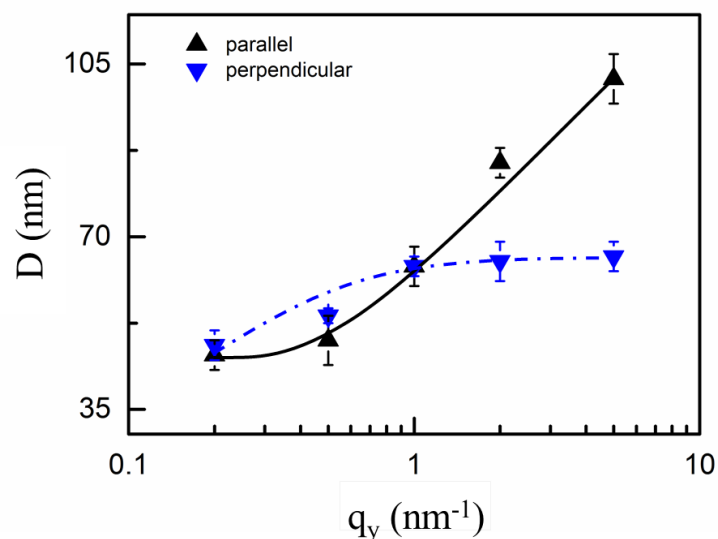


Figure 5.7: Interdomain distance (D) extracted from the fitting plotted as a function of NP concentration. blue down-triangles and black up-triangles display the D of the inner structures parallel and vertical to NP wires, respectively. Lines serves as guides to the eyes. (Reprinted with permission from [87] Copyright 2018 American Chemical Society.)

5.3.2 Lateral structures parallel to the NP wires

The 2D GISAXS data gained in the perpendicular orientation is shown in Figure 5.5e–h. The extracted horizontal line cuts with corresponding fits are displayed in Figure 5.6b. From the perpendicular geometry, information on the lateral structure parallel to the NP wires can be probed. Compared with Figure 5.6a, Figure 5.6 b exhibits similar scattering features in the high q_y area despite the NP concentrations. This proves that NPs and NP aggregates are dispersed in the same fashion as discussed in chapter 5.3.1, and no preferential orientation is observed. However, the DBC nanostructure is greatly influenced by the orientation of the applied magnetic field (shown as arrow I in Figure 5.6b). The different changes of the interdomain distances D are displayed in Figure 5.7. In parallel orientation, the interdomain distance D increases smoothly at low NP concentration, and stays almost as a constant at high NP loading.

5.3.3 Morphology evolution

According to the above discussion, it can be concluded that the external magnetic field applied during printing has a strong influence on the DBC nanostructure. Sketch 5.8 shows the evolution of both nano- and macro-morphology as a function of NP concentration.

On the nanoscale, individual NPs are selectively dispersed inside the PS domains at lower NP concentrations. To accommodate NPs, PS domains expand, leading to the increased interdomain distance D in both orientations (perpendicular and parallel). At higher NP concentrations, NPs aggregate into nanosized agglomerates, which are still located inside the PS blocks. The application of an external magnetic field induces the alignment of agglomerates along the direction of magnetic field. As a consequence, the preferential arrangement of NP aggregates induces a shape anisotropy, which leads to the different elongation behavior of DBC domains in both orientations. During the thermal annealing in the magnetic field, such anisotropic orientation gets further enhanced. At macroscale, NPs are driven by magnetic field to form wires, and the wires are growing in both length and width as the NP concentration increases, which is evidenced by the optical microscopy images (see Figure 5.2).

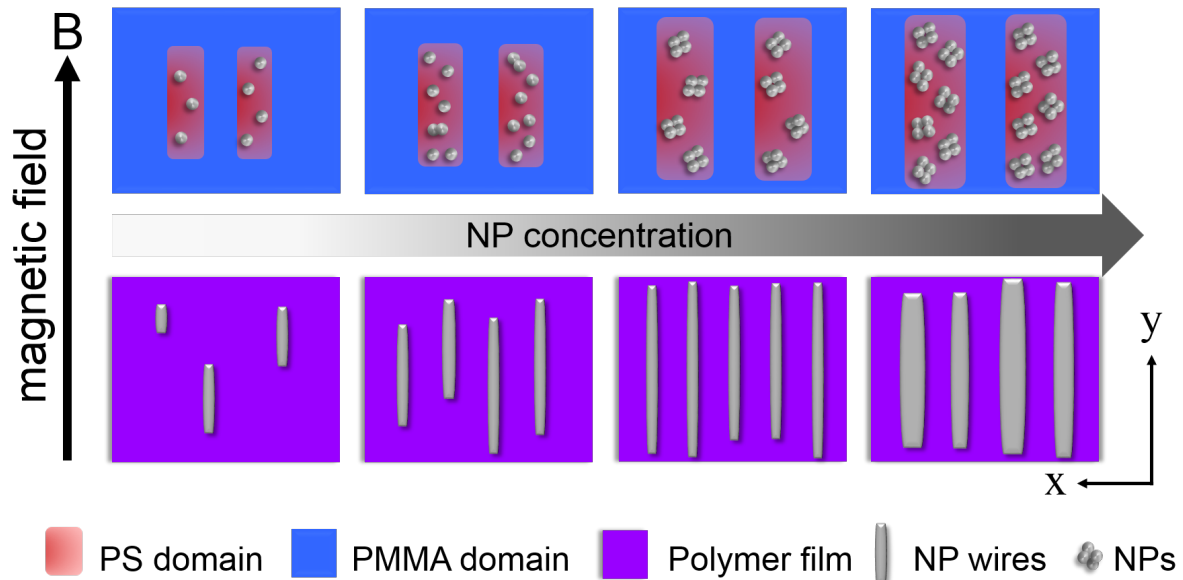


Figure 5.8: Simplified sketch showing the morphology evolution at macroscale (bottom row) and nanoscale (top row) as a function of NP concentration. The external magnetic field is oriented as indicated. (Reprinted with permission from [87] Copyright 2018 American Chemical Society.)

5.4 Magnetic properties

The magnetic properties are probed with a superconducting quantum interference device (SQUID). During the measurement, the magnetic field is applied in two orientations (the magnetic field parallel or perpendicular to the NP wires), so that the magnetic anisotropy

can be investigated. To detail the magnetic properties of the printed hybrid films, the influences of temperature, NP concentration, and orientation of magnetic field are studied. Additionally, a comparison of magnetic susceptibility between present investigation and previous work is made in order to probe the influence of film morphology on the magnetic property.

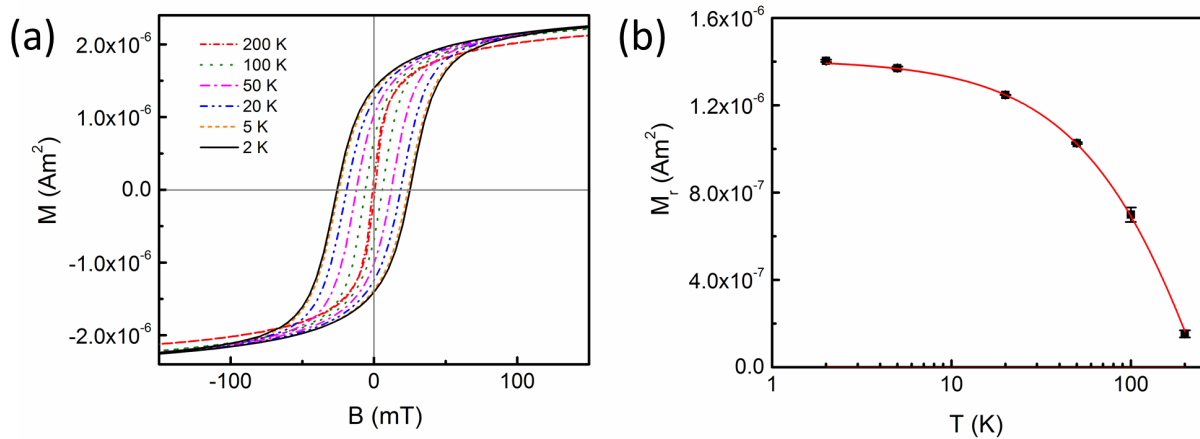


Figure 5.9: Selected hybrid film containing 5 wt% NPs: (a) Magnetization M as a function of external magnetic field B collected at different temperatures. The magnetic field is oriented parallel to the NP wires. (b) remanence vs temperature extracted from the magnetization curve. (Reprinted with permission from [87] Copyright 2018 American Chemical Society.)

5.4.1 Influence of temperature

Figure 5.9 shows the magnetization data collected at different temperatures. At 2 K, a magnetic hysteresis loop is clearly observed, but the loop becomes narrower with increasing temperature and disappears at 200 K. Also, the coercivity (H_C) and remanence (M_r) decrease almost to zero at high temperature. Such behavior is in accordance to the typical superparamagnetic characteristics. To address the blocking temperature T_B , the collected coercivity is fitted with the method described in Chapter 5. In the present system with preferentially oriented NPs, b is set to 0.5 [114]. Fitting the data (Figure 5.10a) yields a blocking temperature of 182 ± 12 K, which conforms with the observation in Figure 5.9a where hysteresis magnetization behavior is absent at 200 K. To further address the thermal dependence of the magnetization process, field-cool (FC) and zero-field-cool (ZFC) measurements are performed. The obtained ZFC/FC curves are profiled in Figure 5.10b, where two distinguishable characteristics are present. At ~ 200 K in the ZFC curve, a broad peak appears, which suggests the blocking temperature. Meanwhile, the ZFC curve parts from the FC one at around 230 K, which indicates the irreversibility temperature

(T_{irr}) where the magnetization state alters from superparamagnetic to isotropic. Also two curves intersect around T_{irr} . This is caused by both the highly ordered antiferromagnetic contribution which produces no signals in FC, and disordered contribution in ZFC where positive signals are produced. Moreover, the distribution of T_B can be determined from the ZFC/FC data. Literature shows the T_B distribution can be determined by equation 5.3 [115].

$$\frac{d[M_{FC} - M_{ZFC}]}{dT} = \frac{M_S^2}{3K} \left[\ln\left(\frac{\tau_m}{\tau_0}\right) - 1 \right] f(T_B) \quad (5.3)$$

in which M_S represents the magnetization saturation, τ_0 is around 10^{-9} s, and $f(T_B)$ is the distribution function of T_B , with the assumption that the dependencies of both K and M_S on temperature can be ignored. The derivative of the FC–ZFC curve is shown as the inset in Figure 5.3. A maximum peak is observed in the curve, indicating the maximum T_B from the distribution $f(T_B)$, which suggests a NP size distribution in the investigated system.

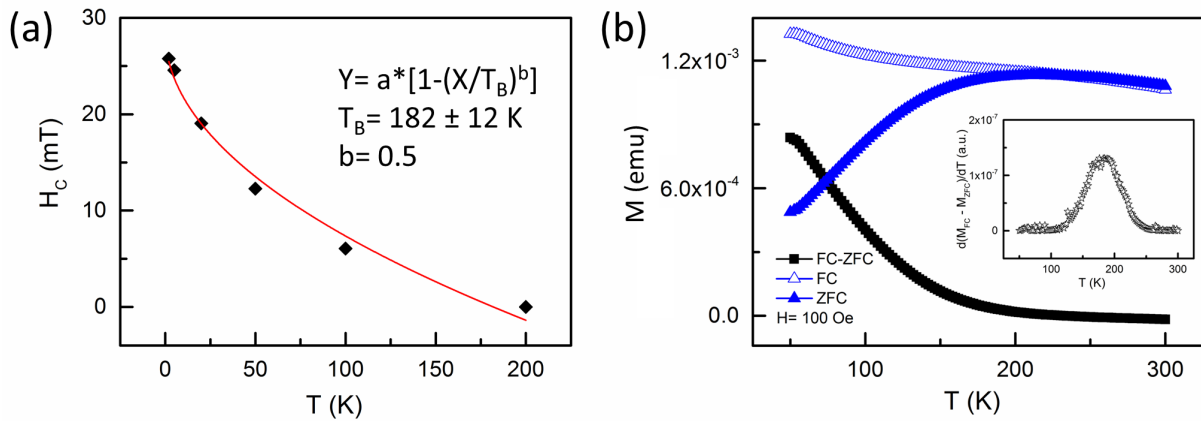


Figure 5.10: (a) Fitting of H_C versus T for the sample containing 5 wt% NPs. (b) FC, ZFC and (FC–ZFC) curves for the sample containing 5 wt% NPs. The $M_{FC} - M_{ZFC}$ curve is shown as the middle inset. (Reprinted with permission from [87] Copyright 2018 American Chemical Society.)

5.4.2 Influence of NP concentration

Figure 5.11 depicts the influence of the NP concentration on the magnetic properties of the printed hybrid films. The magnetization data obtained at 2 K with the external magnetic field applied parallel to wires are displayed in Figure 5.11a. For a deeper understanding, the saturation magnetization M_s , remanence M_r , and relative remanence M_r/M_s are extracted at different temperatures (2 K, 20 K, and 200 K) and plotted as a function

of the NP concentration in Figure 5.11b. From the profile, a linear increasing behavior along NP concentration is observed for both M_s and M_r , and the growing tendency is similar at all measured temperatures. Consequently, constant relative remanence M_r/M_s independent of NP concentration is obtained at all corresponding temperatures. High temperatures or more NPs can contribute to more thermal activation energy or free flips of magnetic moments, respectively. Thereafter, the observed NP concentration dependence of the magnetization behavior confirms the superparamagnetic property of printed hybrid films.

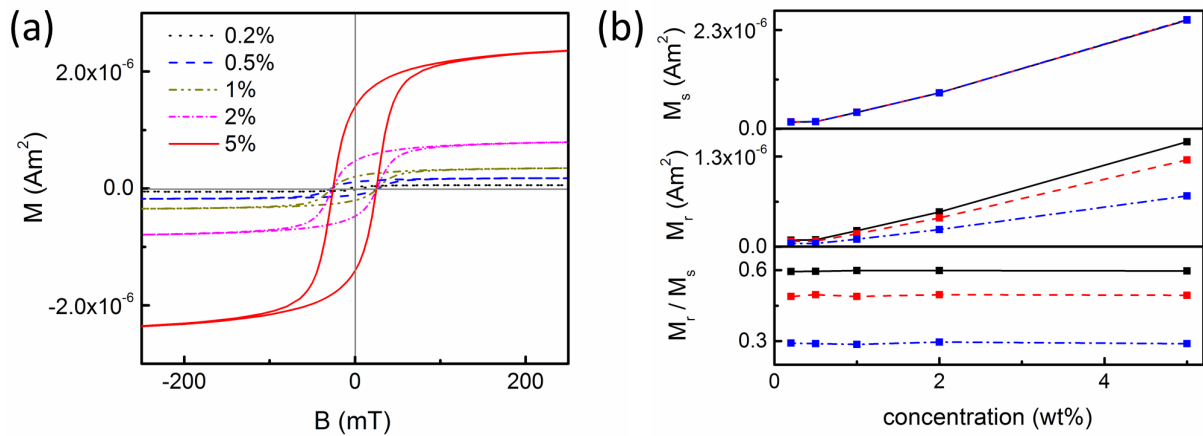


Figure 5.11: (a) Influence of NP concentration on the magnetization measured at 2 K as a function of external magnetic field. Samples are measured with magnetic field parallel to wires. (b) NP concentration dependence of saturation magnetization M_s , remanence M_r , and relative remanence M_r/M_s at 100 K (blue dashed–dotted line), 20 K (red dashed line) and 2 K (black solid line). (Reprinted with permission from [87] Copyright 2018 American Chemical Society.)

5.4.3 Influence of orientation

To probe the magnetic anisotropy of the hybrid films, SQUID measurements are performed with different orientations of the applied magnetic field (with magnetic field parallel and perpendicular to the NP wires). The collected curves are shown in Figure 5.12a, from which a clear effect from the magnetic field orientation is observed. To make a detailed comparison, values of remanence, saturation and coercivity are extracted and plotted in Figure 5.12b. One can see that an obviously higher remanence is present in the parallel orientation. Such behavior is due to the anisotropic behavior of individual particles with uniaxial anisotropy [115–120]. In the measurement performed in the parallel geometry, the magnetic field is oriented along the easy axis of NPs, which results in increased coercivity

and remanence compared to the perpendicular measurement orientation [87]. Concerning the saturation magnetization, a slight difference is observed in the comparison. This can be explained by the blocking temperature, below which the NPs display a ferromagnetic behavior. Thus, all magnetic moments inside NPs orient along the easy axis. When the measurements are carried out in the perpendicular orientation, some blocked magnetic moments can not flip along the magnetic field direction because of insufficient thermal energy at low temperatures. As a consequence, slightly higher saturation magnetization is observed in the parallel orientation.

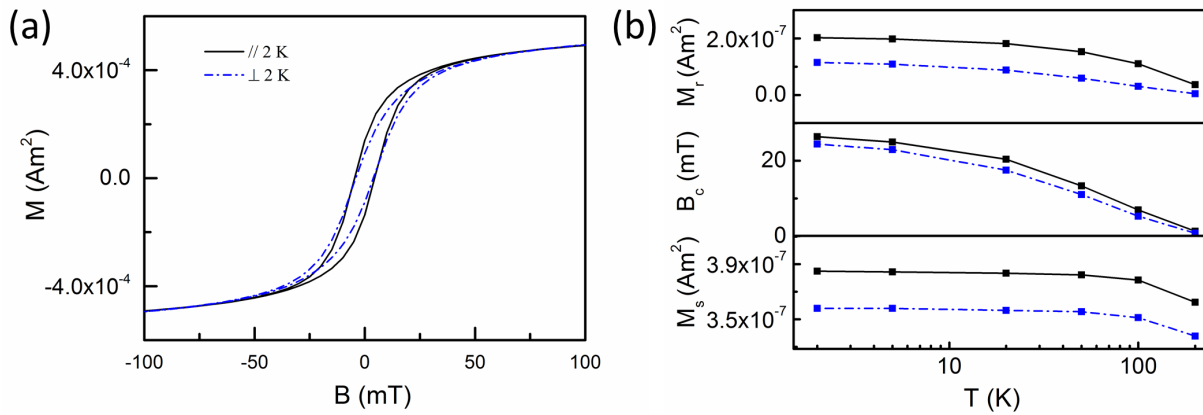


Figure 5.12: (a) Magnetization curves collected in different orientation. (b) Temperature dependence of saturation magnetization M_s , remanence M_r , and coercive force H_c . The probed film contains 2 wt% of NPs and is measured at 2 K. Data collected from parallel (black solid line) and perpendicular (blue dashed–dotted line) orientations are compared. (Reprinted with permission from [87] Copyright 2018 American Chemical Society.)

5.4.4 Influence of film morphology

In case of real applications, the responsive behavior of materials to external magnetic field is playing the decisive role. Therefore, it is of great importance to investigate the magnetic susceptibility which indicates the responsive performance of hybrid films. The initial magnetic susceptibility $\chi_{initial}$ can be extracted from the virgin magnetization curve according to equation 5.4 [43].

$$\chi_{initial} = \lim_{B \rightarrow 0} \frac{dM}{dB} \quad (5.4)$$

where M and B represent the magnitude of internal magnetization and strength of the external magnetic field, respectively. In case of superparamagnetic materials, the internal magnetization shows the same orientation as the applied magnetic field. Therefore, stronger internal magnetization indicates higher susceptibility at a given external magnetic field. Higher magnetic susceptibility is observed at higher temperatures (Figure 5.9a) and NP concentrations (Figure 5.11a) in the investigated films. To probe the influence of morphology on the magnetic susceptibility, the present results (lamellar PS domains) are compared with our previous investigations where PS domains are spherical [75]. In our previous work, identical magnetic NPs and the same type of DBC (PS-*b*-PMMA), though with a different volume fraction of the PS block, were employed. The samples were prepared via solution casting, and the obtained films contained PS nano-spheres with magnetic NPs located inside [75]. For the measurements performed at $T > T_B$, no hysteresis loop was observed in the magnetization curves, which are the same as their corresponding virgin curves. Thus, the initial magnetic susceptibility $\chi_{initial}$ could be achieved. At $T < T_B$, χ_{H_c} is calculated by applying a linear fit at the zero-remanence region where the highest susceptibility was present. Figures 5.13a and b display the obtained susceptibility (χ_{H_c} and $\chi_{initial}$) plotted versus temperature and NP concentration, respectively. A comparison shows that the susceptibility of the lamella-structured hybrid film increases more pronouncedly with temperature than that of the sphere-structured ones (Figure 5.13a). Meanwhile, a much stronger influence of NP concentration is observed on the susceptibility of lamella-structured films (Figure 5.13b). Such difference in susceptibility can be explained by the different structure of films resulting from various block ratios, also well as the different film fabrication techniques.

As mentioned above, the same type of DBC (PS-*b*-PMMA) and identical magnetic NPs are used in both investigations. Only the volume fraction of the PS block (f_{PS}) differs. In our previous study, the experimented DBC had a small f_{PS} of 0.15, which resulted in a spherical nanostructure in the films prepared by solution casting. Results show that PS spheres (diameter ≈ 23 nm) were dispersed inside a PMMA matrix with large interdomain distances (≈ 90 nm for the pure film). In the present work, however, f_{PS} is larger (0.5), which leads to a lamellar structure (size ≈ 21 nm) with shorter interdomain distances (≈ 45 nm for the pure film). GISAXS results suggest that the NPs are dispersed individually inside PS domains at low NP concentrations (< 1 wt%). In that case, the number of single NPs located inside the PS blocks is the same in both types of films, since the critical accommodation capacity of PS domains is not reached yet. Therefore, the magnetic susceptibilities are similar within experimental errors, and increase smoothly for both films at low NP concentrations (Figure 5.13b). As the NP concentration increases, the critical capacity of PS domains is gradually reached. Above a certain concentration,

NPs form nanosized aggregates dispersing inside the whole DBC matrix. In case of the sphere-structured film, the PS critical capacity for locating NPs is reached at lower concentrations. Therefore, lamellar films are able to accommodate more NPs, leading to a more pronounced increase in susceptibility with NP concentration (Figure 5.13b). As a consequence, higher PS block fractions turn out to be effective in improving the magnetic properties of hybrid films. Additionally, lamellar domains are less likely to be influenced by the forces induced by magnetic NPs. The morphology of sphere-structured films become less ordered at high concentration of NPs.

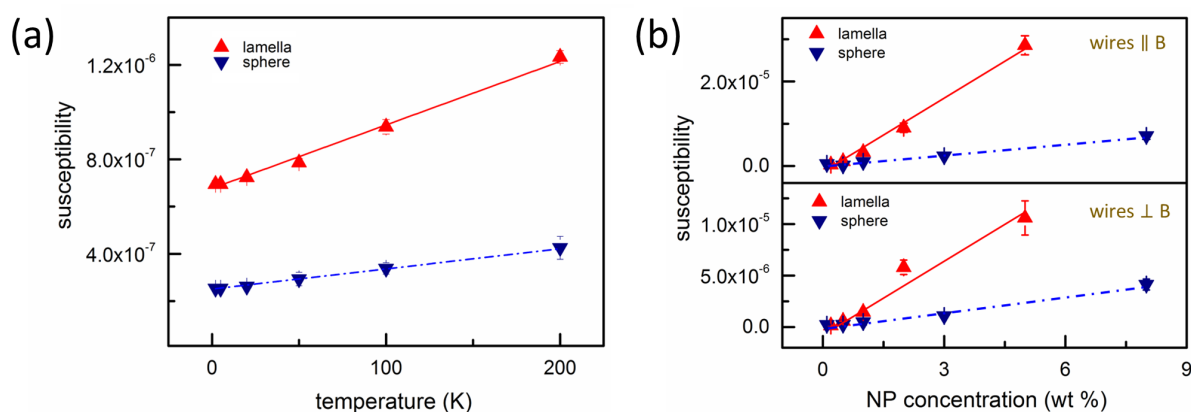


Figure 5.13: (a) Magnetic susceptibility (χ_{H_c}) as a function of temperature with magnetic field applied parallel to NP wires. χ_{H_c} is calculated at the zero-remanence point. Data of films with 1 wt% NPs having a spherical (blue spheres) and lamellar (red triangles) morphology is compared. (b) NP concentration dependence of the initial magnetic susceptibility ($\chi_{initial}$) at 200 K with magnetic field perpendicular (lower) and parallel (upper) to the NP wires. All lines serve as guides to the eyes. (Reprinted with permission from [87] Copyright 2018 American Chemical Society.)

5.5 Summary

The present chapter focuses on the fabrication of anisotropic magnetic thin films with dense magnetic nanostructures. A printing technique combined with external magnetic field is employed to deposit films with magnetic anisotropy. In order to achieve dense magnetic nanostructure, a DBC (PS-*b*-PMMA) containing high PS volume fraction is used as a template to arrange PS-coated magnetic NPs.

Hybrid films are printed with a lamella-structured PS-*b*-PMMA ($f_{PS} = 0.5$) and superparamagnetic NPs (γ -Fe₂O₃). During the printing process, an external magnetic field (149 G) is applied to direct the alignment of the magnetic NPs. The optical microscopy

images show that NPs form wires in the printed films under the applied magnetic field, and both width and length of the wires increase with increasing NP concentrations. AFM and SEM data prove that the wires are composed of NPs in close packing. Due to the microphase separation, lamellar nanostructures are obtained in the printed films, and the structure order is further enhanced after the thermal post-treatment. Because the surface is grafted with PS chains, magnetic NPs are preferentially incorporated inside PS domains. GISAXS data reveal that NPs are individually dispersed inside PS blocks at low NP concentrations. As their concentration increases, NPs aggregate into nanosized agglomerates which are still located inside PS domains.

SQUID measurements demonstrate that all the printed hybrid films follow a superparamagnetic behavior and show magnetic anisotropy. To investigate the responsive behavior of hybrid films to external magnetic field, magnetic susceptibility is extracted from obtained magnetization curves. Compared with our previous work, where identical magnetic NPs are located inside spherical PS domains, the printed lamella-structured films show a higher magnetic susceptibility and stronger sensitivity to external magnetic field. Such behavior is caused by the different morphologies. In the present investigation, PS domains are dispersed inside a PMMA matrix with much shorter interdomain distances compared to the previous study. Therefore, a denser magnetic nanostructure consisting of individually dispersed NPs or nanosized NP aggregates is obtained in the printed hybrid films. Such printed films with enhanced magnetic properties can be promising candidates in sensor applications.

6 Printed magnetic anisotropic films without magnetic field

Parts of this chapter have been published in the article: Magnetic nanoparticle-containing soft–hard diblock copolymer films with high order [121]. (Reprinted with permission from (S. Xia et al., *Nanoscale*, 2018, 10, 11930–11941.). Copyright 2018 The Royal Society of Chemistry. DOI: 10.1039/c8nr02760a).

In the previous work (chapter 6), magnetic hybrid thin films are fabricated by printing solutions within an external magnetic field. The obtained films have NP wires on the film surfaces, displaying magnetic anisotropy. The SQUID results show that the wire-containing hybrid films response to an external magnetic field differently when measuring them in different orientations [87]. Such magnetic anisotropic films are promising materials for the sensor applications where a special alignment of NPs is required. In literature, a lot of reports can be found that an additional magnetic field is employed to achieve the arrangement of magnetic NPs [87,122–125]. For instance, Allia *et al.* fabricate films containing a distribution of elongated chains formed by NPs self-assembly under an external magnetic field [123]. However, the employment of magnetic field to control the alignment of magnetic NPs renders the film fabrication processes complicated. Principally, large scale fabrication process, like printing and roll-to-roll casting, are adaptable to employ additional magnetic fields [87]. However, it would greatly simplify the film fabrication process without applying external magnetic field.

The main idea of this chapter is to develop a facile, straightforward, and reproducible method to fabricate magnetic anisotropic films without a magnetic field. In this respect, an asymmetric DBC polystyrene-*block*-poly(*N*-isopropylacrylamide) (PS-*b*-PNIPAM) is used as well as commercialized magnetite NPs (Fe₃O₄). The investigated PS-*b*-PNIPAM has a number average molecular weight of 35.5 kg/mol with a PS block volume fraction of 0.34. Hence, it is possible to achieve a structure with PS cylinders standing perpendicularly (with respect to the substrate) inside PNIPAM matrix. The magnetite NPs are grafted with oleic acid ligands for stabilization purpose, and dissolved in toluene with a

concentration of 5 mg/ml. The mean diameter of NPs is 10 nm. More details on the materials can be found in chapter 4.1. Due to the organic grafting of the surface, NPs can be selectively located and aggregate inside the PS domains. To achieve the desired film thickness, the DBC concentration in toluene is controlled to be 25 mg/ml via initial tests. The weight ratio of magnetite NPs to PS-*b*-PNIPAM is varied from 0, 0.5, 1, 2, 5, 7, 10, to 20 wt%. By applying printing technique (see chapter 4.3.2), films are casted on silicon substrates with the size of 25 mm × 75 mm. The used silicon substrates are pre-cleaned following a basic bath cleaning protocol (see chapter 4.2.2). After printing, all films are annealed in a mixed solvent vapor ($V_{THF} / V_{methanol} = 2/1$) for 15 min.

The film thickness is examined with white light interferometry using a Filmetric F20 in reflectance mode. The surface morphologies are probed with OM, AFM and SEM. AFM measurements are performed in tapping mode. SEM is carried out with the accelerating voltage of 1.5 kV and the working distance of 1.7 mm. The buried structure is investigated by GISAXS with a wavelength of 0.108 nm, an applied incidence angle of 0.4°, and a sample-to-detector distance of 5330 mm. Furthermore, SQUID is utilized to study the magnetic properties of the fabricated hybrid films. To probe the magnetic anisotropy, all hybrid films are measured in two orientations, with the direction of magnetic field parallel and perpendicular to the film surface.

6.1 Solvent vapor annealing

As described previously, one of the main goals in the present chapter is to fabricate a highly ordered structure with PS cylinders standing vertically in the PNIPAM matrix. Literature shows that solvent vapor annealing (SVA) is an effective post-treatment to enhance the lateral long-range order of DBC films [83]. During SVA, polymer chains become mobile, therefore they can stretch freely and rearrange to form a more ordered structure [8]. Nevertheless, reports can also be found that long-range order is hardly obtained by applying only a single solvent [126]. Therefore, the use of solvent mixture for SVA and also the selectivity of different solvents to each block can be considered, in order to achieve a highly spatial order. In the present chapter, most frequently used laboratory organic solvents, THF, methanol and toluene are chosen for test. According to literature, the vapor pressure of the three solvents at 25 °C is 21.6 kPa for THF, 16.9 kPa for methanol and 3.79 kPa for toluene [126]. Consequently, methanol and THF are more suitable solvents for SVA as compared to toluene, since both exhibit similar vapor pressures at room temperature.

To explore the affinity of the employed solvents to the DBC blocks, the solvent–polymer interaction parameter (χ_{sp}) is applied. Based on the Flory–Huggins theory, smaller values of χ_{sp} represent higher selectivity of the solvent to a certain polymer block. The miscibility between the polymer and solvent is expressed by equation 6.1 [127,128].

$$A_{sp} = (\delta_{Dp} - \delta_{Ds})^2 + 0.25(\delta_{Pp} - \delta_{Ps})^2 + 0.25(\delta_{Hp} - \delta_{Hs})^2 \quad (6.1)$$

in which δ_D represents the dispersive solubility parameter, δ_P the polar bond contribution, δ_H the hydrogen bond contribution, and the indices s and p are the solvent and polymer block, respectively. In equation 6.2 .

$$\chi_{sp} = \frac{VA_{sp}}{RT} \quad (6.2)$$

where V is the molar volume of the solvent, R shows the ideal gas constant and T represents the absolute temperature. For the present work, we obtain $\chi_{THF-PNIPAM} = 0.46$, $\chi_{THF-PS} = 0.78$, $\chi_{methanol-PNIPAM} = 1.13$ and $\chi_{methanol-PS} = 2.14$. As a consequence, methanol is regarded as a better solvent for PNIPAM compared to PS. THF is neutral to both blocks, but slightly selective to the PNIPAM chains.

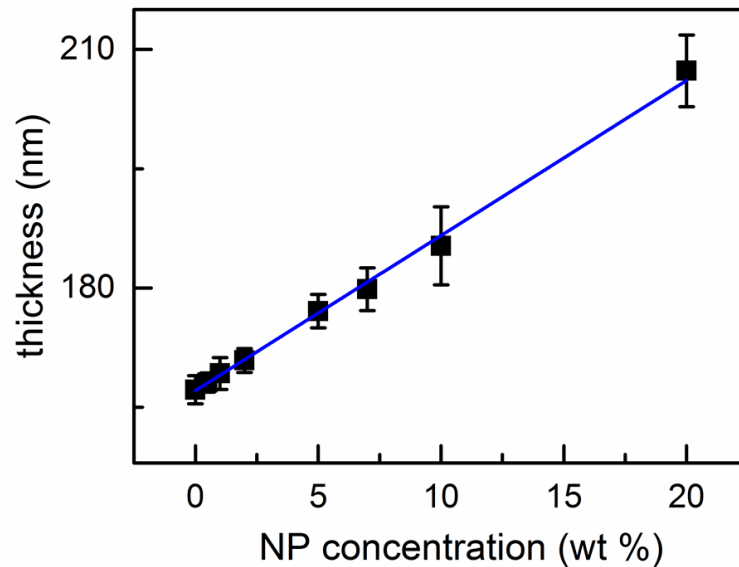


Figure 6.1: Thickness of films plotted as a function of NP concentration. The blue solid line is used as a guide to the eye. (Reprinted with permission from [121]. Copyright 2018 The Royal Society of Chemistry.)

6.2 Film thickness

The thickness of the investigated films is measured by white light interferometry, and the result is displayed in Figure 6.1. As one can see, the film thickness shows a linearly increasing behavior. It increases from 168.2 ± 0.3 nm (NP-free film) to 207.5 ± 0.7 nm (20 wt%). Such an increase is caused by the incorporation of NPs, since all films are fabricated following the same printing protocol. To accommodate NPs, the polymer blocks need to expand, which ends up with increased film thicknesses.

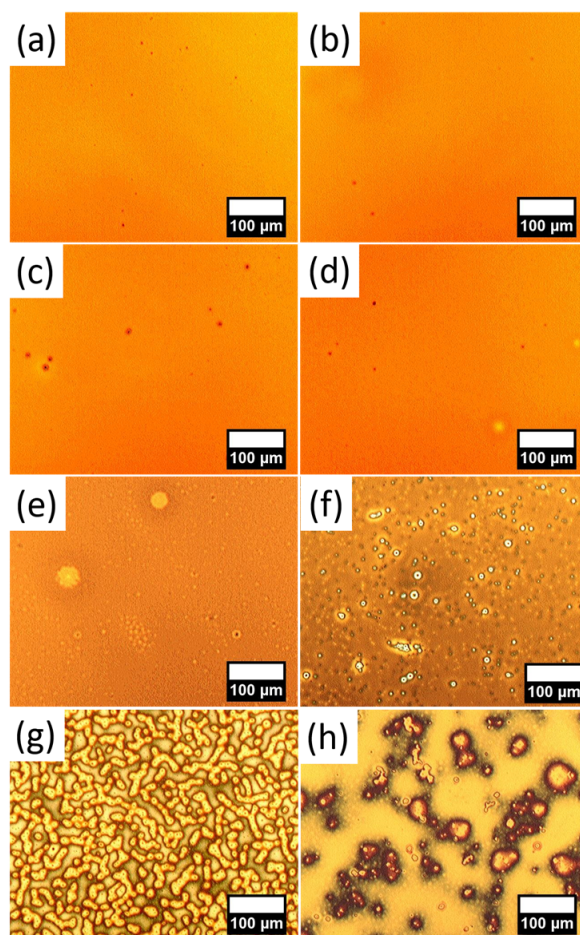


Figure 6.2: Optical microscopy graphs of films with different NP concentrations: (a) 0, (b) 0.5, (c) 1, (d) 2, (e) 5, (f) 7, (g) 10 and (h) 20 wt%. (Reprinted with permission from [121]. Copyright 2018 The Royal Society of Chemistry.)

6.3 Surface structure

6.3.1 Largescale structures

Concerning real applications, the uniformity and the homogeneity of the films play an indispensable role. Both of them are affected by the printing process including the employed printer instrument and the printed ink (polymer solutions). To print films of high quality, the printing parameters and the solutions' concentrations need to be optimized. When a DBC solution with a high concentration is used, the highly viscose ink gives rise to strong frictions, which can limit the NPs mobility, ending up with nonuniform films. Through initial printing tests, the polymer concentration is set as 25 mg/ml to achieve films exhibiting macroscopic uniformity. Since the printing is a solvent-based film fabrication technique, solvent evaporated gradiently in the perpendicular direction of the wet film [105,106]. Consequently, heterogeneous nanostructures may be created unexpectedly. To solve this problem, SVA is carried out on all films to improve the films homogeneity, and enhance the structure order as well.

Figure 6.2 shows the optical microscopy images of printed films with different NP concentrations. All films display homogeneity on a large scale. At low NP concentrations, NP agglomerates can be found distributed on the film surface. These agglomerates are formed due to the attractive force among magnetic NPs. As NP concentration increases, these agglomerates increase in size, and further form small islands and network-like structure at very high concentrations.

6.3.2 Nanoscale structures

SEM is performed to investigate the film morphology at the nanoscale. Figure 6.3 shows the obtained SEM images in grey scale. Figure 6.3a displays the surface structure of the pure film. The dark and bright parts belong to PNIPAM and PS domains, respectively. Based on the self-constant field theory, a cylindric morphology would be caused by the PS volume fraction of 0.34. Literature shows that cylinder structures with a parallel orientation (with respect to the substrate surface) are favored at film thicknesses larger than the periodic interdomain spacing of the DBC system [129]. However, in the present work, PS cylinders with vertical orientation are observed in the PNIPAM matrix even if the film thickness (168.2 ± 0.3 nm for the pure film) is larger than the periodic interdomain distance (35 nm). Such a phenomenon is caused by the application of SVA, in which the PS-poor solvent methanol is used. Since methanol is unfavorable for PS blocks, PS tend to hide inside the PNIPAM matrix to be as less as possible exposed to the solvent vapor.

As a consequence, a perpendicular orientation of structure (with respect to the substrate) is achieved.

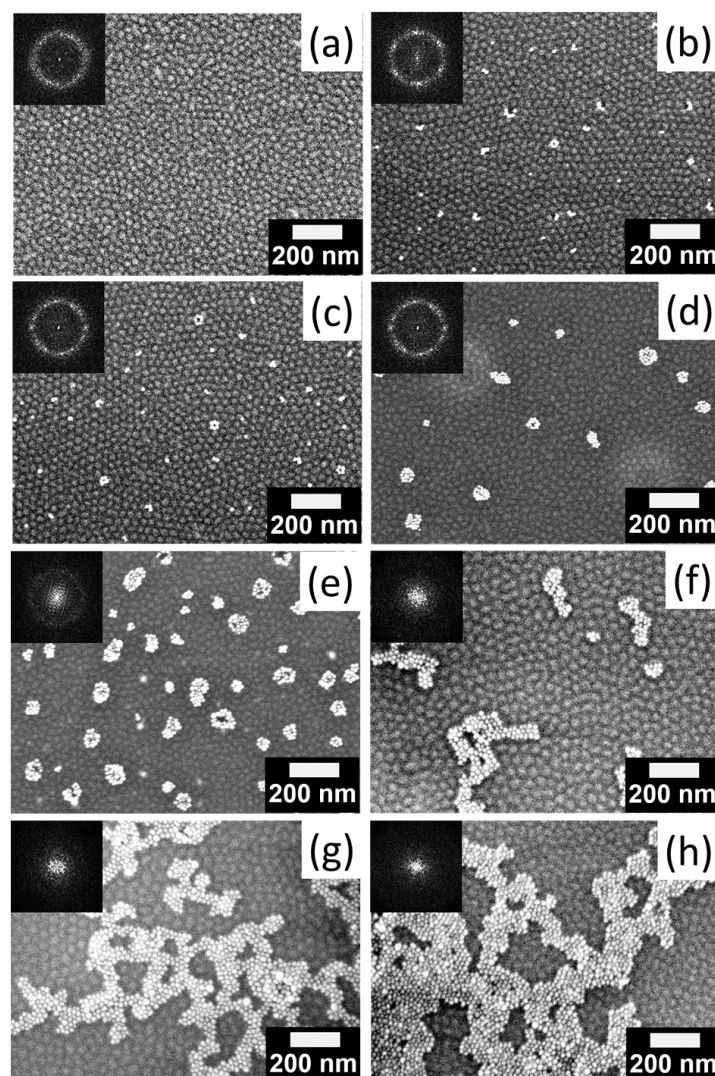


Figure 6.3: SEM images of films with different NP concentrations: (a) 0, (b) 0.5, (c) 1, (d) 2, (e) 5, (f) 7, (g) 10 and (h) 20 wt%. The corresponding 2D fast Fourier transform (FFT) patterns are given at the top-left corners. (Reprinted with permission from [121]. Copyright 2018 The Royal Society of Chemistry.)

With incorporating NPs, white objects can be observed on the film surfaces. These objects are NP agglomerates, which are selectively located in the PS-dominated parts. Additionally, the DBC structure order of the films (Figure 6.3b–d) gets obviously enhanced as suggested by the corresponding fast Fourier transform (FFT) pattern (shown as the insets in Figure 6.3). The functional oleic acid layer enhances the affinity of NPs to PS block, but dislikes NPs in the PNIPAM blocks. Therefore, NPs are preferentially dispersed

in the PS nanocylinders. To accommodate NPs, the PS chains need to rearrange, which leads to an improvement of the DBC structure order. This can be explained by the selective diffusion of NPs inside PS blocks during SVA, which improves the spacial order of the NP-containing cylinders. Similar reports can be found in literature where the addition of NPs enhances the order of DBC nanostructures [18,88]. Further loading NPs perturbs the long-range order of nanostructure, due to the excessive expansion of PS domains to incorporate more NPs. After the PS domains are saturated, NPs are squeezed out and located on the film surface. The excess NPs form aggregates with increasing size on the film's surface as NP concentration increases (Figure 6.3e and f). At high NP concentrations, the diffusion and localization of the PS domains are limited by the large number of NPs. As a consequence, the PS chains lose the ability to reorganize and optimize the morphology. Meanwhile, the whole hybrid system is dominated by the entropy penalty. Despite the organic ligands on the surfaces, NPs can still aggregate under the magnetic attractive force, which agrees with Monte Carlo simulations of the NP-DBC hybrid system with a high NPs loading [130]. SEM graphs (Figure 6.3 g and h) show that NP agglomerates start to form network-like structure, which covers a large area of the film surface. In spite of the movement of excess NPs to the film surface, some NPs can be still located inside the PS blocks due to the entanglement between PS chains and oleic acid chains. Therefore, the further irregular expansion of PS domains results in a perturbed morphology.

For a further analysis of the surface structure order, FFT pattern are extracted from the corresponding SEM graphs, and shown as the insets on the top left in Figure 6.3. The observation of a bright ring in the FFT pattern suggests that PS nanocylinders distribute isotropically on the film surface. Slight incorporation of NPs ($C_{NP} \leq 2$ wt%) results in narrower rings with enhanced intensity maxima in the FFT pattern, which suggests that the lateral structure order gets improved. Further loading of NPs ($C_{NP} > 2$ wt%) broadens the FFT rings and the rings vanish at high NP concentrations, indicating the loss of structure order. To investigate the order evolution further, power spectra density (PSD) functions are extracted from the corresponding FFT patterns and profiled in Figure 6.4. A remarkable peak (indicated as peak I in Figure 6.4), which derives from the microphase-separated DBC structure, is obviously present in the PSD profile. The peak position shifts to lower q_y values, indicating an increase of the interdomain distance as the NP concentration increases. The interdomain distance increases from around 32 nm ($C_{NP} = 0$ wt%) to 40 nm ($C_{NP} = 5$ wt%). Besides, peak I also changes in shape from sharp to broad, which reveals the structure order increases first then decreases. From $C_{NP} = 7$ wt%, peak I moves to a much lower q_y value and with a broader shape. Such behavior is attributed to the progressive expansion of interdomain spacing and the formation of a

ill-defined structure resulted from the heavy loading of NPs. An interdomain distance of 89 nm is found for the hybrid film containing 15 wt% of NPs.

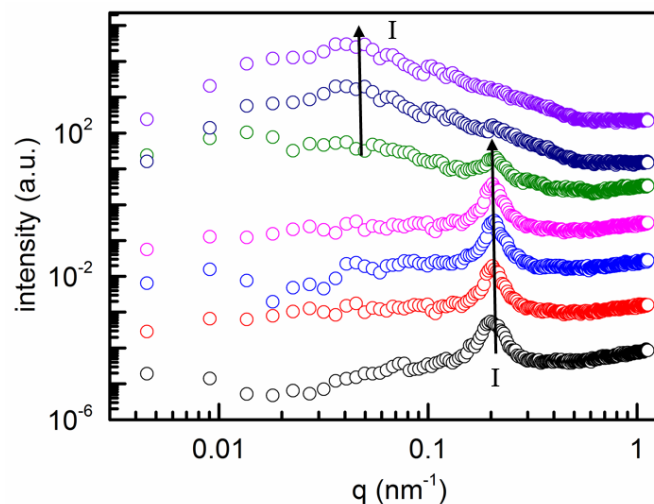


Figure 6.4: Power spectral density (PSD) functions obtained from azimuthal integration of the intensity distribution in the FFT patterns at various NP concentrations: 0, 0.5, 1, 2, 5, 7, 10 and 15 wt%, from bottom to top. Peak I indicates the q value of the lateral structure resulted from DBC microphase separation. The PSD curves are shifted along y axis for better display. (Reprinted with permission from [121]. Copyright 2018 The Royal Society of Chemistry.)

In order to probe the topography of the films, AFM is used. The obtained height AFM graphs are displayed in Figure 6.5. Basically the AFM data reveals the same trend of the surface structure evolution with NP concentration as observed in the SEM images. For all AFM images, bright areas and dark areas correspond to the PS and PNIPAM areas, respectively. At low NP concentrations, the order of the cylindrical domains increases with increasing loading of NP, whereas, the addition of NPs in high concentrations perturbs the order. At considerable high NP concentration ($C_{NP} \geq 10$ wt%), there are substantial NP aggregates, forming irregular sizes and accumulating randomly on the film surface instead of following the alignment of the PS domains from the DBC template (Figure 6.5f–h). Because the NP clusters cannot be further accommodated inside the PS cylindrical domains, the localization of the NPs is no longer correlated with the DBC template and the structures are deformed.

To further evidence the localization of NPs, another AFM topography graph of the selected sample with 1 wt% of NPs is present at higher magnification in Figure 6.6. It is obvious that the hybrid film surface consists of three different parts, which are NPs (white), PS (bright yellow) and PNIPAM (dark yellow). Besides, dark dots (labeled with

green dashed circles), which are caused by the stiffness of NPs, can be observed inside the PS domains (bright yellow parts).

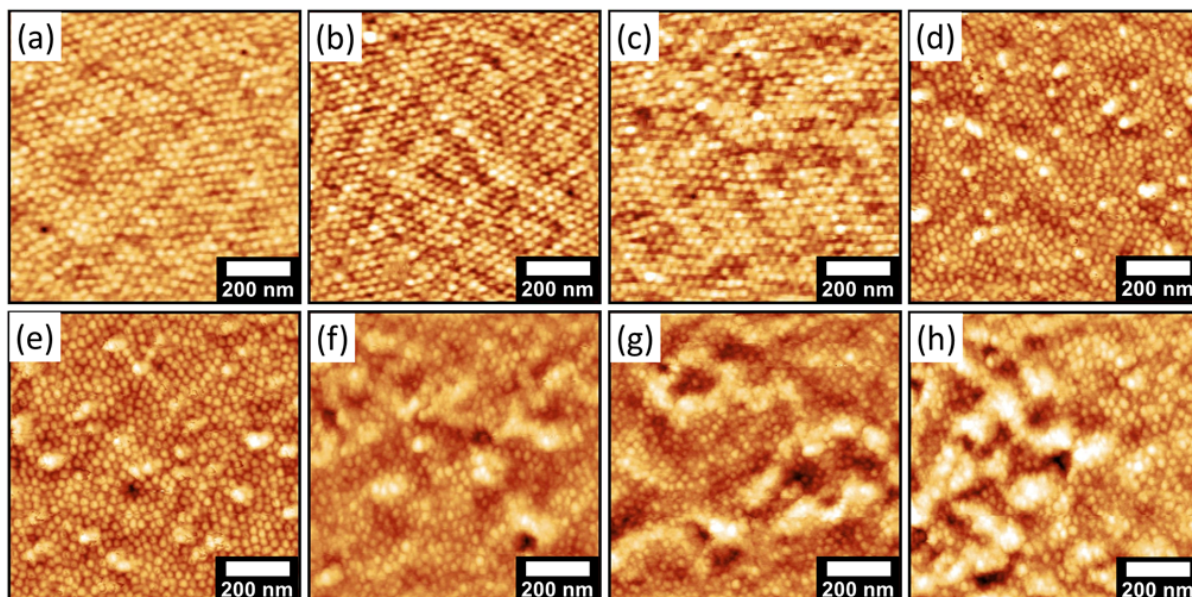


Figure 6.5: AFM height images of films with different NP concentrations: (a) 0, (b) 0.5, (c) 1, (d) 2, (e) 5, (f) 7, (g) 10 and (h) 20 wt%. (Reprinted with permission from [121]. Copyright 2018 The Royal Society of Chemistry.)

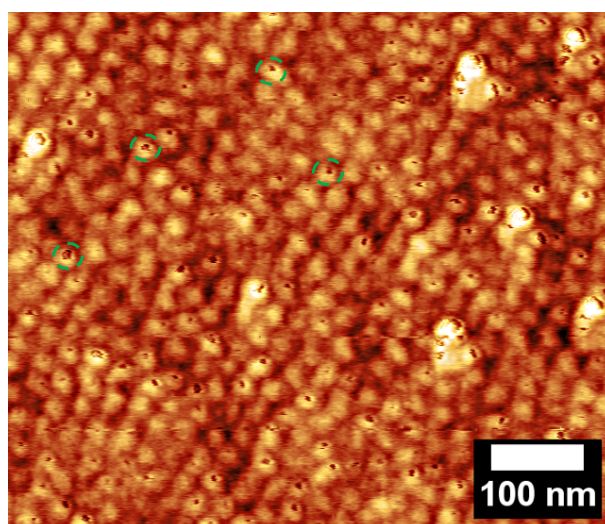


Figure 6.6: AFM topography graph of selected film with 1 wt% of NPs. Green dashed circles indicate the localization of NPs inside PS domains. (Reprinted with permission from [121]. Copyright 2018 The Royal Society of Chemistry.)

To gain the local height information of the films, line cuts are made at three random positions (indicated as dotted lines with different colors in Figure 6.7a and b). The results

are displayed in Figure 6.7c and d. In case of the pure film, the local height appears to be in the range of nm (Figure 6.7c), however, the mean height difference is observed to be around 3 nm on a larger scale (Figure 6.8a). For the film with high NP concentration, the mean height difference increases to more than 20 nm (Figure 6.8a), with the observation of small local height difference (Figure 6.7d). Such increased difference in mean height is caused by a rougher film surface, which results from the NP incorporation. Additionally, the 2D FFT data are also extracted from the AFM images. The corresponding PSD function curves are plotted in Figure 6.8 b, and a comparison is made between the pure film and the hybrid film containing 20 wt% of NPs. The featured intensity maxima in the PSD profiles are marked as peak I and II, which are consistent with the observation in SEM data. In addition, the root-mean-square roughness (R_{rms}) is extracted out of the corresponding AFM topography images. With increasing NP concentrations, R_{rms} increases from 0.2 nm (NP-free film) to 1.2 nm ($C_{NP} = 20$ wt%) (Figure 6.8a). Such increased roughness is caused by the localization of NPs and NP agglomerates on the film surface.

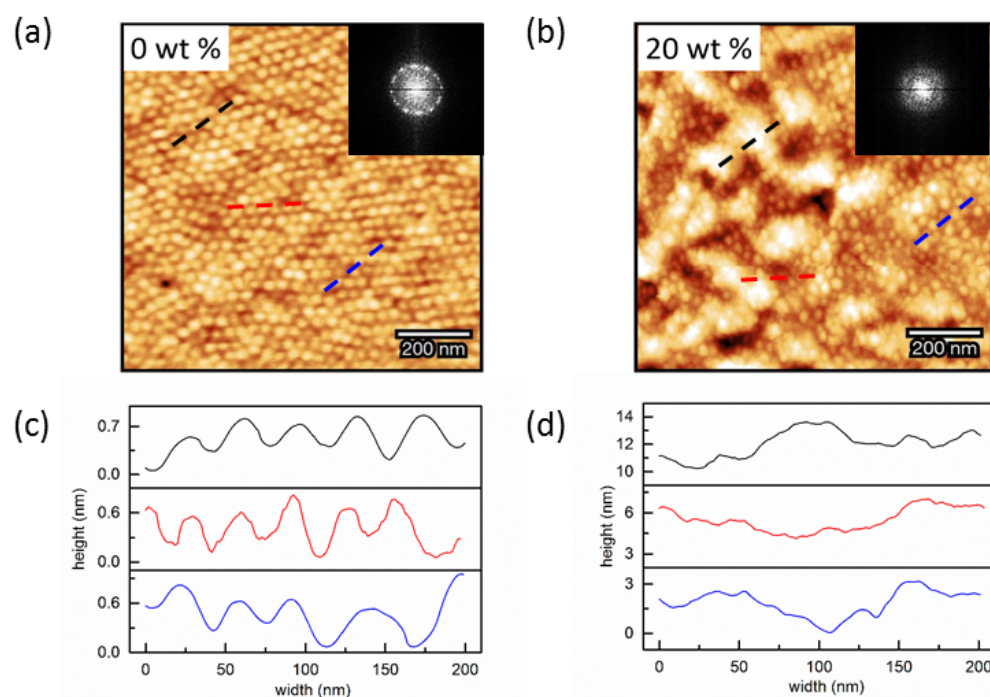


Figure 6.7: AFM height images with corresponding FFT patterns of films containing different NP concentrations: (a) 0 wt%, (b) 20 wt%. Line cuts from the AFM height images of (c) pure film and (d) hybrid film with 20 wt% of NPs performed at three random positions shown as the colored dotted lines in the corresponding AFM images. (Reprinted with permission from [121]. Copyright 2018 The Royal Society of Chemistry.)

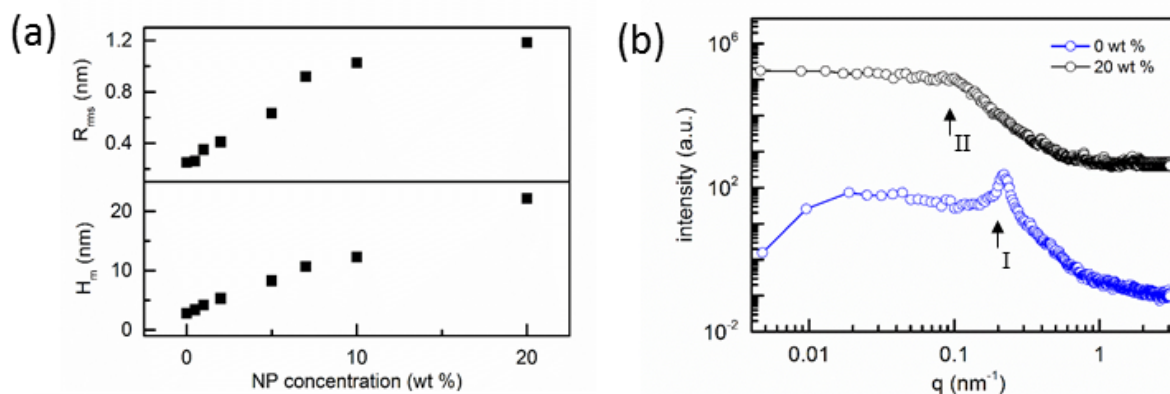


Figure 6.8: (a) Root-mean-square roughness (R_{rms}) and mean height (H_m) plotted versus NP concentration. (b) PSD functions extracted from the FFT data of films with 0 and 20 wt% of NPs. The PSD curves are shifted along the y axis for clarity. Peak I and II show the position of featured intensity maximum. (Reprinted with permission from [121]. Copyright 2018 The Royal Society of Chemistry.)

6.4 Inner structure

To gain an insight into the inner structure of the printed films, the GISAXS technique is employed for investigation. The obtained 2D GISAXS data are displayed in Figure 6.9 showing distinct features at different NP concentrations.

Along the q_y direction, pronounced scattering patterns can be observed in all the 2D GISAXS data. For the pure film, two intensity maxima can be observed at $q_y = 0.228 \text{ nm}^{-1}$ (the first order Bragg rod, shown by a red arrow) and at $q_y = 0.387 \text{ nm}^{-1}$ (the second order Bragg rod, shown by a blue arrow) in Figure 6.9a. Both intensity maxima originate from DBC highly ordered nanostructure. Such intensity streaks can be found for the films with NP concentration below 5 wt%. The intensity of the side peak gets slightly enhanced upon NPs incorporation, which is due to the improved scattering contrast and enhanced order resulted from localization of NPs inside PS blocks. Further loading NPs leads to the gradual vanishing of the second order Bragg peaks. The first order Bragg peak also starts to disappear from $C_{NP} = 7 \text{ wt}\%$ because of the gradual loss of the structural order. Meanwhile, a different side peak, which is originated from the strong diffuse scattering of the NPs, appears at much lower q_y values from $C_{NP} = 5 \text{ wt}\%$. And the intensity of this peak gets more and more pronounced with increasing NP concentration.

To further interpret the scattering data, horizontal line cuts are performed at the Yoneda peak region of the DBC. Figure 6.10 displays the obtained cuts with the corresponding fits, out of which the lateral structure information are extracted. Peak I, II,

and III shown in the cuts profile indicate the featured peaks, which are attributed to the ordered structure within the printed films.

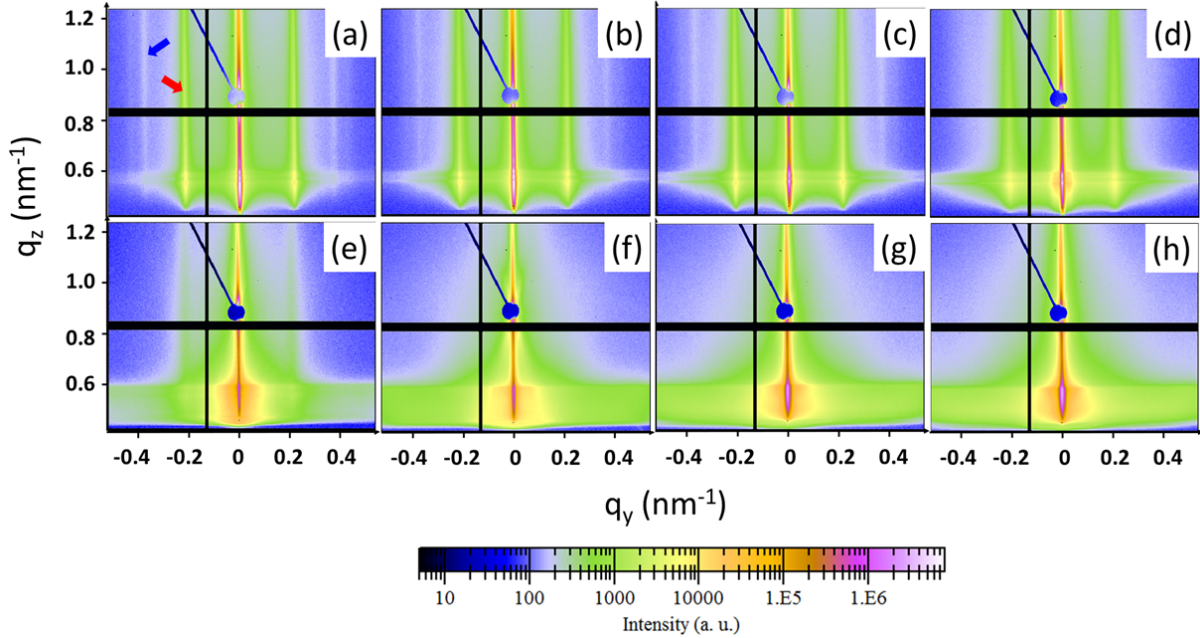


Figure 6.9: 2D GISAXS data of films with different NP concentrations: (a) 0, (b) 0.5, (c) 1, (d) 2, (e) 5, (f) 7, (g) 10 and (h) 20 wt%. All data are displayed at the same intensity scale bar. Both horizontal and perpendicular black lines are the gap areas between detector modules. A beamstop is positioned at the position of specular peak to prevent from over saturation. The red and blue arrows in the (a) show the first and second order peak, respectively. (Reprinted with permission from [121]. Copyright 2018 The Royal Society of Chemistry.)

To obtain detailed structure information, the peak position is fitted with a model including structure and form factors, both of which are assumed to have a Lorentzian distribution. In case of the pure film, the obtained curve displays a strong main peak at $q_y = 0.228 \text{ nm}^{-1}$ (peak II, shown as the blue arrow in Figure 6.9a), and a weaker peak at $q_y = 0.387 \text{ nm}^{-1}$ (shown as the dashed red arrow in Figure 6.9a) which is the second-order peak. The ratio of these two q_y values equals $0.589 \approx 1/\sqrt{3}$, which matches the presumption that a cylindrical structure with perpendicular orientation can be achieved on the substrate surface. The fitting results suggest the presence of the same morphology for the films with NP concentration below 5 wt%. Consequently, the dispersion of PS nanocylinders inside PNIPAM matrix is highly ordered for the NP-free film and the hybrid films with low NP concentrations. For the data modeling, an interdomain spacing of 31.8 nm is extracted from the pure film, which is consistent with the observation in the SEM and AFM measurements. As NP concentration increases from 0 wt% to 7 wt%,

peak II, which indicates the featured interdomain spacing, slightly shifts to a smaller q_y value and turns to be broader and weaker. Meanwhile, the second-order peak gradually fades and vanishes. Such observation suggests a slight increment of the interdomain spacing (shown as Figure 6.10b), which is caused by the expansion of PS domains after the selective incorporation of NPs inside PS blocks.

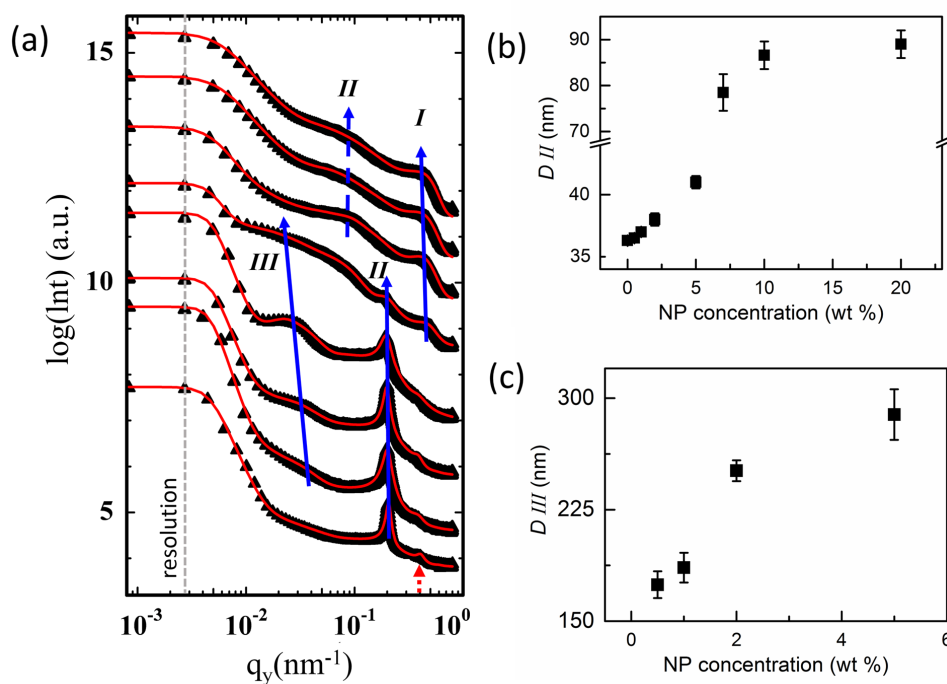


Figure 6.10: (a) Horizontal line cuts obtained from corresponding 2D GISAXS data of films with different NP concentrations. From bottom to top: 0, 0.5, 1, 2, 5, 7, 10, and 20 wt%. The line cuts are plotted together with corresponding fits and shifted along the y axis for clarity. Characteristic peaks are present: peak I (individual NP contribution), peak II (distance between NP aggregates) and peak III (interdomain spacing of DBC structure). The dashed red peak at the bottom shows the second-order peak of peak II. The interdomain spacing of DBC structure (b) and the inter-aggregate distance (b) are extracted from the fitting. (Reprinted with permission from [121]. Copyright 2018 The Royal Society of Chemistry.)

Additionally, another broad peak (peak III) can be found at the lower q_y area for low NP concentrations (≤ 5 wt%). This peak represents the distance of neighboring NP aggregates. The growth of the aggregates' sizes leads to an increase of the inter-NP aggregates' distance, therefore, the peak III shifts smoothly to a lower q_y region as NP concentration increases. Figure 6.10c shows the inter-NP aggregates' distance (D_{III}) obtained from the fitting. D_{III} increases from 174 ± 11 nm to 289 ± 23 nm with a corresponding large size distribution. At $C_{NP} > 5$ wt%, the scattering intensity in the lower q_y area decreases, which indicates ill-defined and large-sized NP clusters with large inter-cluster spacing

distributions. At $C_{NP} = 7$ wt%, peak III vanishes because of the presence of large content of loaded NPs. According to the SEM and AFM analysis, NP networks are observed at high concentrations (see Figure 6.3 f–h and Figure 6.5f–h).

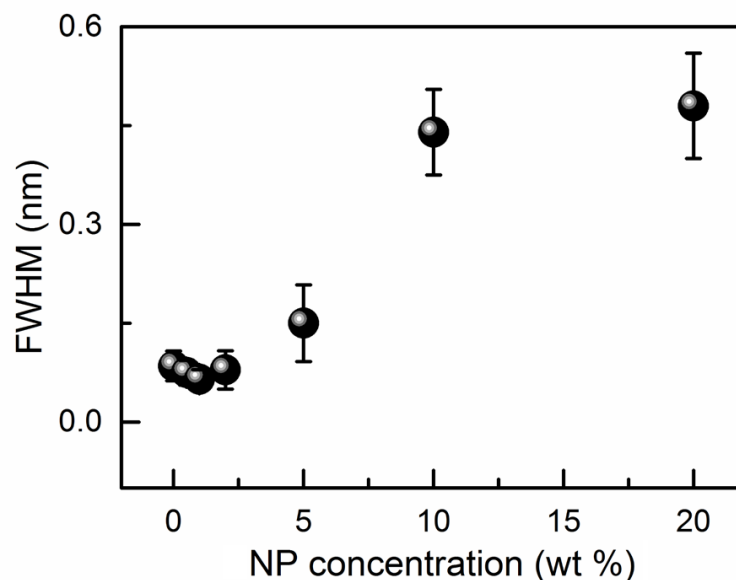


Figure 6.11: Values of the full width at half maximum (FWHM) of peak II versus NP concentration. Values are obtained from modeling the horizontal line cuts. (Reprinted with permission from [121]. Copyright 2018 The Royal Society of Chemistry.)

At $C_{NP} \geq 7$ wt%, peak II shifts to a much smaller q_y value (shown as dashed blue arrow in Figure 6.10a). Moreover, the new peak II is quite broad and turns to be even weaker and broader as NP concentration increases. Correspondingly, the interdomain spacing increases from 41 ± 1 nm ($C_{NP} = 5$ wt%) to 89 ± 3 nm ($C_{NP} = 20$ wt%). Such increment is attributed to the further expansion of PS domains, which is resulted from the continuous accommodation of NP. During SVA, THF is a neutral solvent for both blocks, and accordingly enhances the mobility of both types of polymer chains. Therefore, at high NP concentrations, the mobile polymer chains can rearrange themselves to incorporate more NPs, which in return ends up with a perturbed cylindrical morphology. In addition, another peak (peak I) can be seen in the high q_y region ($q_y = 0.63 \text{ nm}^{-1}$), and it gets more pronounced at higher NP concentrations (Figure 6.10a). According to the analysis above, NPs form network-like structures at high concentrations. Thus peak I results from the structure factor of the individual NPs which are closely packed. Based on the data modeling, a NP diameter of 10 ± 1 nm is obtained, which agrees with the mean NP diameter.

To follow the lateral structure order evolution, the full width at half maximum (FWHM) of peak II (in Figure 6.10a) is extracted from the modeling, and the values are plotted as a function of NP concentration in Figure 6.11. As one can see, the FWHM first decreases gently, and reaches a minimum at 1 wt%, then increases with increasing concentration. Such observation reveals that the structure order initially gets enhanced upon slight NP incorporation, but decays at high concentration. The optimal structure order is obtained at the NP concentration of 1 wt%.

6.5 Morphology evolution

For a better illustration of the structural evolution, a simplified sketch of the films with different NP concentrations is present in Figure 6.12.

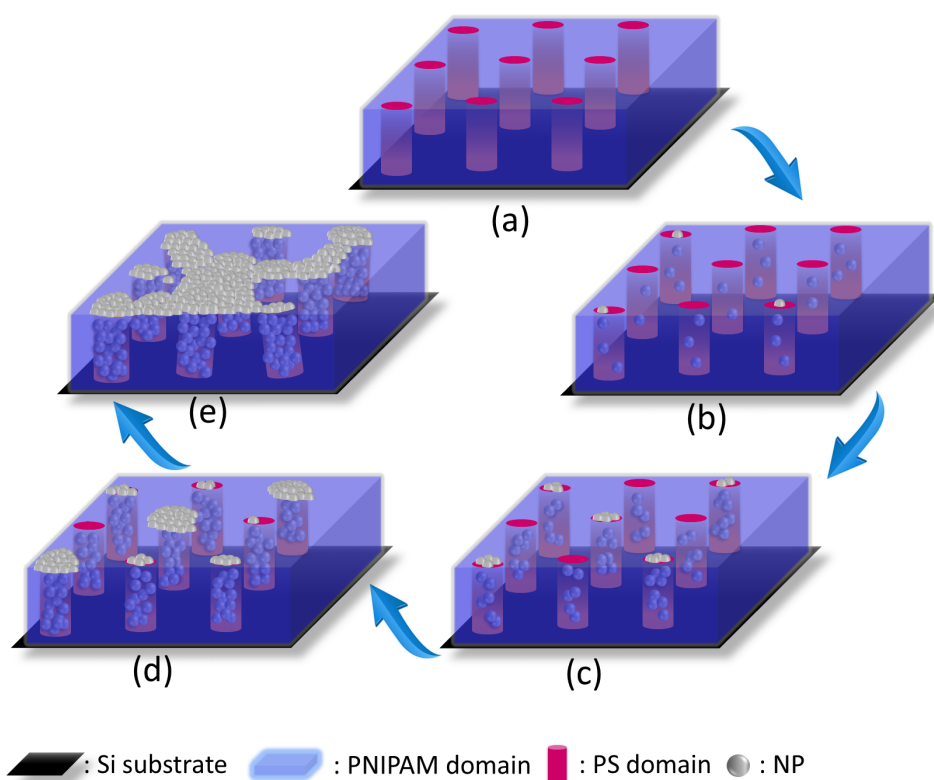


Figure 6.12: Simplified sketch showing the morphology of films at different NP concentrations: (a) NP-free, (b) 0.5 wt%, (c) 1 wt%, (d) 2 wt% and (e) above 5 wt%. (Reprinted with permission from [121]. Copyright 2018 The Royal Society of Chemistry.)

In case of the NP-free film (Figure 6.12a), microphase separation leads to a cylindrical nanostructure since the PS volume fraction is 0.34. Due to the incompatibility between

PS chains and methanol, the solvent annealing gives rise to PS cylinders standing vertically on the silicon substrate, although the film thickness is far exceeding the DBC periodic distance. Therefore, a polymer template with a perpendicularly oriented cylindrical nanostructure is achieved. At very low NP concentrations (Figure 6.12b), the NPs are preferentially dispersed inside the PS domains because of the favorable interaction between the PS blocks and the surface-modified NPs. As the concentration increases (Figure 6.12c), the NPs start to aggregate both inside and on the top of the PS blocks. Meanwhile, the inter-spacing of the PS cylinders increases slightly because of the selective incorporation of NPs. Further doping with NPs contributes to the formation of large aggregates and a saturation of the PS cylinders with NPs (Figure 6.12d). To a certain degree, the structures remain being long-range ordered, which suggests an array of vertically aligned NP aggregates. At high NP concentrations, the initially well-ordered cylindrical nanostructure is massively stretched and deformed due to an oversaturation of the PS domains (Figure 6.12e). An excess of NPs cannot be accommodated inside the PS domains and is located at the film surface, forming network-like aggregates.

6.6 Magnetic properties

The magnetic properties of hybrid films are probed via a superconducting quantum interference device (SQUID). The magnetization data are recorded by applying a magnetic field first parallel, and then vertical to the film surface. Thus, magnetic information perpendicular and parallel to the PS cylinders can be obtained, respectively. For a detailed analysis, the influence of temperature, NP concentration and NPs orientation on the magnetic properties will be discussed in the following sections.

6.6.1 Influence of temperature

To investigate the influence of temperature on the magnetic properties, all hybrid films are probed at various temperatures. Figure 6.13a shows the data of the film with 2 wt% of NPs measured at different temperatures. The measurement is carried out with the magnetic field parallel to the film surface. Clearly, magnet hysteresis loops can be observed at low temperatures. As the temperature increases, the hysteresis loop gradually narrows and disappears at 200 K. Such a phenomenon relates to a typical superparamagnetic behavior. Compared with earlier work, the saturation magnetization is achieved at a much lower magnetic field (350 mT) in the present study, due to the highly-ordered and well-oriented structure [19]. To detail the responsive behavior of the hybrid film, coercivity (B_c), remanence (M_r) and magnetic susceptibility (χ) are calculated and plotted

as a function of temperature in Figure 6.13b. As temperature increases, both coercivity and remanence initially decrease slightly, then drop progressively and finally vanish at high temperatures. Such a behavior is due to the blocking temperature of the employed superparamagnetic NPs [131]. Also, the magnetic susceptibility shows a strong temperature dependence, responding faster to the external magnetic field at higher temperatures. Such temperature-dependent magnetic behaviors can be explained via thermal activation.

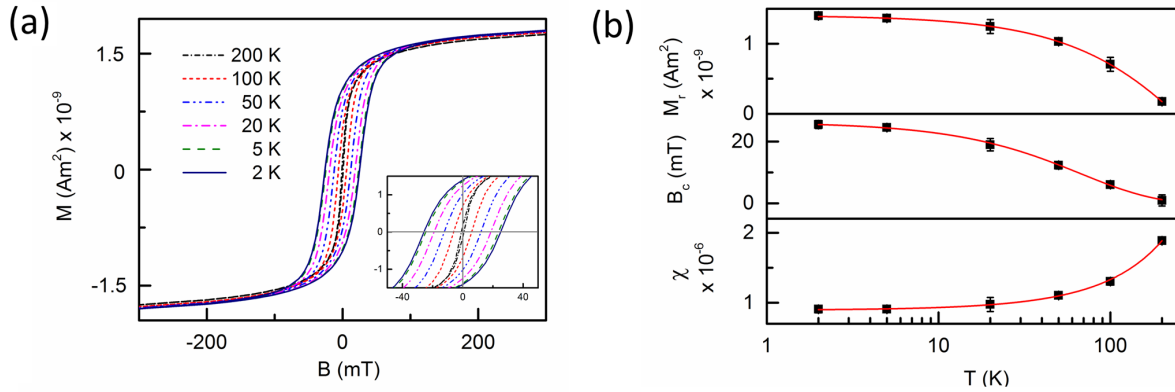


Figure 6.13: (a) Magnetization curves of a hybrid film measured at different temperatures with the magnetic field parallel to the film surface. The selected film contains 2 wt% of NPs. The inset at the right bottom shows the partially zoomed-in hysteresis loop. (b) Coercivity (B_c), remanence (M_r) and magnetic susceptibility (χ) extracted from (a) and plotted versus temperature. (Reprinted with permission from [121]. Copyright 2018 The Royal Society of Chemistry.)

To detail the blocking temperature (T_B) of the present hybrid system, the collected coercivity is fitted with the method described in Chapter 5. In the present system, b is set as 0.77, since NPs are oriented in a random way [114]. Values of B_c at different temperatures are extracted from corresponding magnetization curves, and are fitted based on the equation described in chapter 5. The fitting suggests a T_B of 115 ± 21 K, shown as Figure 6.14a. To further analyze T_B , zero-field-cooled (ZFC) and field-cooled (FC) protocols are employed for the measurement. The obtained FC-ZFC profile shows a prominent peak at around 120 K, which reveals a T_B of around 120 K, and keeps constant with the fitting data.

6.6.2 Influence of NP concentration

Figure 6.15 displays the influence of the NP concentration on the magnetic properties of the hybrid films. The films are probed at 2 K with the magnetic field oriented parallel to

the film surface. The values of remanence (M_r), saturation (M_s) and relative remanence (M_r/M_s) are obtained from Figure 6.15a, and plotted in Figure 6.15b as a function of NP concentration. As the NP concentration increases, both the remanence and the saturation increase. Consequently, the relative remanence M_r/M_s stays constant and shows no concentration dependence. Such behavior can be explained by the increased number of NPs at high concentrations. More free flips of magnetic moments are present in the films with high NP concentrations, which leads to higher remanence and saturation.

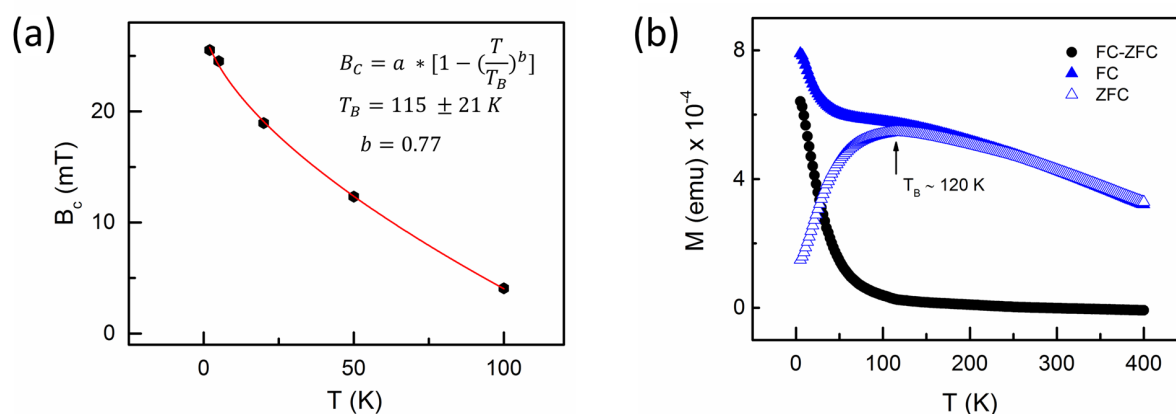


Figure 6.14: (a) Coercivity data fit as a function of temperature. The employed model, exponent b and result are displayed on the top right. (b) FC, ZFC and (FC-ZFC) curves obtained at a magnetic field of 300 Oe. (Reprinted with permission from [121]. Copyright 2018 The Royal Society of Chemistry.)

6.6.3 Influence of morphology

Based on the previous findings, the NP-hosting PS domains are standing vertically on the substrate surface with a high order. Therefore, long NP aggregates aligned in a perpendicular geometry (with respect to the film surface) can be expected at certain concentration. In order to probe the magnetic anisotropy of the hybrid films, all measurements are performed in two orthogonal directions with the magnetic field parallel and perpendicular to the film surface. In that case, the magnetic behavior vertical and parallel to the PS nanocylinders can be gained, respectively.

Figure 6.16a depicts the magnetization behavior of selected films in both measurement directions at 2 K. Typical magnetic hysteresis loops are present in all curves, but differences can be observed for the two orientations of the magnetic field. At $C_{NP} < 2$ wt%, the hysteresis loops obtained in both orientations almost overlap with each other. At higher

concentrations (2 wt% and 5 wt%), however, orientation–dependent magnetization behaviors can be observed. To detail the different magnetic behaviors, remanence M_r , coercivity B_c and magnetic susceptibility (χ) are extracted from the corresponding magnetization curves and plotted versus the NP concentration in Figure 6.16b. The remanence increases with increasing NP concentrations in both orientations, but the remanence measured parallel to the film surface is slightly lower than that measured perpendicular to the surface ($0.5 \text{ wt}\% < C_{NP} < 5 \text{ wt}\%$). The difference is hard to see due to the scale of the figure. Beyond this concentration region, identical values are obtained. The coercivity obtained in both orientations shows a similar decaying behavior with increasing NP concentration, but differences can be clearly discovered. At $C_{NP} = 0.5 \text{ wt}\%$, identical values of coercivity are achieved in both orientations, which suggests a hybrid film with magnetic isotropy. Differences appear from 1 wt% and get larger at 2 wt% and 5 wt%. Therefore, the hybrid films display magnetic anisotropy at certain NP concentrations.

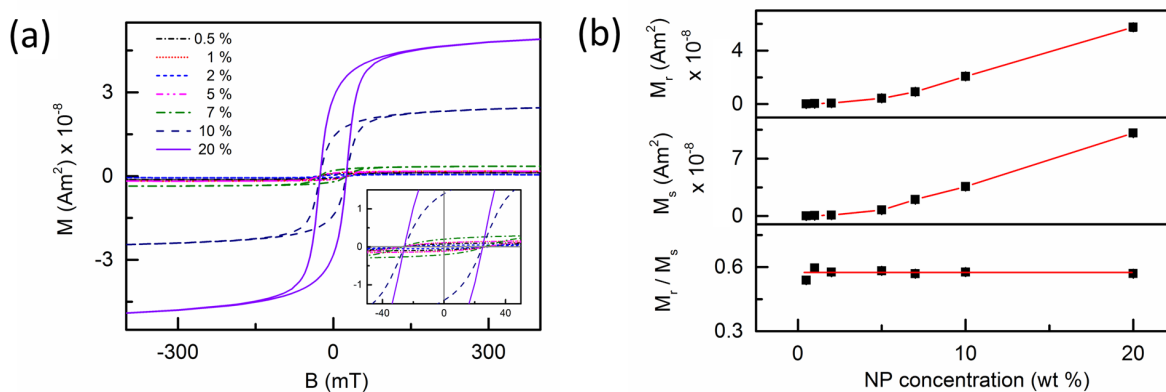


Figure 6.15: (a) Magnetization data of films with different NP concentrations. Measurements are performed at 2 K with the magnetic field parallel to the film surface. The inset at the bottom right shows the partially magnified hysteresis loop. (b) The remanence (M_r), saturation (M_s) and relative remanence (M_r/M_s) plotted as a function of NP concentration. Values are extracted from (a). Red lines are guides to eyes. (Reprinted with permission from [121]. Copyright 2018 The Royal Society of Chemistry.)

To further analyze the orientation–dependent responsive behavior to external magnetic field, magnetic susceptibilities are extracted in the remanence–free region for both measuring orientations ($\chi_{//}$ and χ_{\perp}). The ratio ($\chi_{\perp}/\chi_{//}$) is calculated accordingly and plotted versus NP concentration for comparison. In Figure 6.16 b, a maximum susceptibility ratio can be observed at $C_{NP} = 2 \text{ wt}\%$, which suggests the strongest magnetic anisotropy. Such a phenomenon can be explained by the highly ordered PS nanocylinders which stand vertically on the substrates, and the preferential dispersion of magnetic NPs inside these PS cylinders. SEM and GISAXS data evidence that PS cylinders are aligning perpendic-

ularly on the substrate with a high order inside PNIPAM matrix at $C_{NP} \leq 2$ wt%. Due to the functional oleic acid ligands grafted on the surfaces, magnetic NPs are selective to PS chains, which leads to a preferential localization of NPs inside the PS cylinders. Increasing NP concentration facilitates the formation of NP aggregates inside the PS cylinders. The scattering data proves that the nanocylinders are still in a highly ordered alignment event at $C_{NP} = 2$ wt%. Based on this point, an easy magnetization axis, aligning parallel to the PS cylinders and vertical to the film surface, is present in the magnetic thin film. At $C_{NP} < 2$ wt%, only small-sized agglomerates with ill-defined structure exist in the PS cylinders, therefore, magnetic anisotropy can be hardly achieved. At $C_{NP} > 2$ wt%, the large number of NPs causes an irregular expansion of PS domains, ending up with the deformation of the initially ordered structure. As a consequence, the magnetic anisotropy starts to vanish with the loss of structural order.

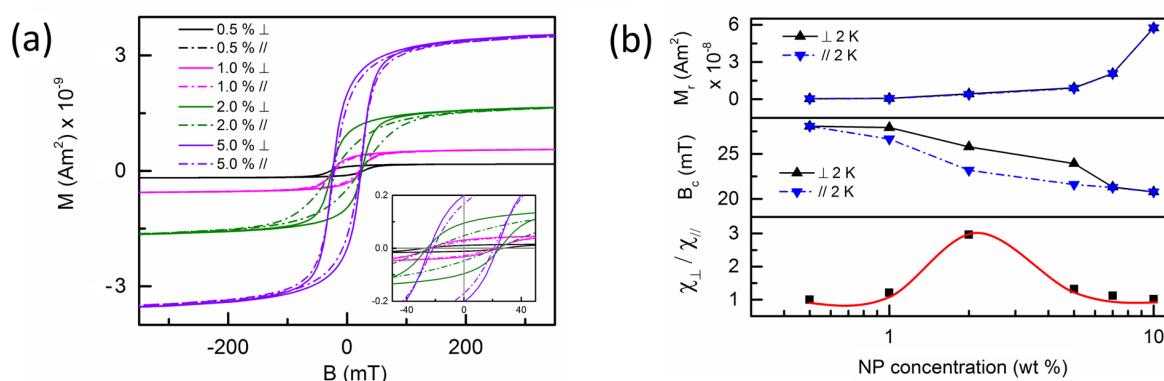


Figure 6.16: (a) Magnetization data of selected films with different NP concentrations obtained in two directions (magnetic field parallel and vertical to the film surface). The inset at the right bottom shows the partially zoomed-in hysteresis loops. (b) Comparison of remanence, coercivity and susceptibility in both measurement directions. Data are collected at 2 K. The magnetic susceptibility in both parallel ($\chi_{//}$) and vertical (χ_{\perp}) orientations are obtained from a linear fit at the zero-field region. The susceptibility ratio ($\chi_{//}/\chi_{\perp}$) is calculated and plotted as a function of NP concentration. The red solid line is a guide to the eye. (Reprinted with permission from [121]. Copyright 2018 The Royal Society of Chemistry.)

Figure 6.17a displays the magnetization profile of films containing 2 wt% of NPs. The influence of the direction of measurement on the magnetization behavior can be observed. The remanence achieved in parallel orientation is obviously lower than that from the perpendicular orientation. To investigate the influence of temperature on the magnetic anisotropy, this selected film is probed in both orientations at two different temperatures. Figure 6.17b suggests that the remanence, coercivity and saturation show a similar

temperature dependence in both directions. This means that the magnetic anisotropy is hardly affected by the temperature.

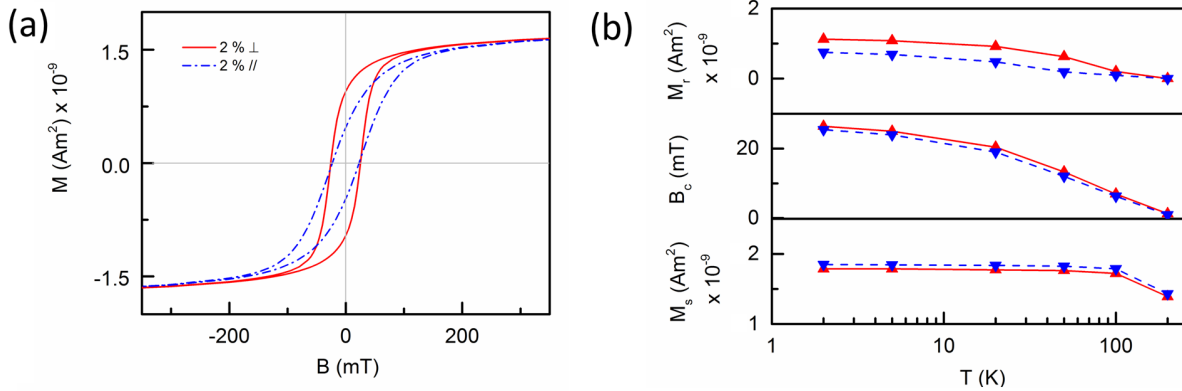


Figure 6.17: (a) Magnetization data collected at 2 K in both orientations. (b) Influence of temperature on the coercivity, remanence and saturation in both orientations. Blue (face down) and red (face up) triangles are the data from the parallel and vertical orientation, respectively. The measured film contains 2 wt% of NPs. (Reprinted with permission from [121]. Copyright 2018 The Royal Society of Chemistry.)

| temperature | data source | $B_{c//}/B_{c\perp}$ | $M_{r//}/M_{r\perp}$ |
|-------------|-------------|----------------------|----------------------|
| 5 K | literature | 2.36 | 1.82 |
| | our work | 1.08 | 1.21 |
| 100 K | literature | 1.57 | 1.18 |
| | our work | 1.02 | 1.04 |

Table 6.1: Comparison of magnetic data between literature [118] and our present work. $B_{c//}$ and $B_{c\perp}$ are the coercivity measured with NP wires parallel and perpendicular to the applied magnetic field, respectively. $M_{r//}$ and $M_{r\perp}$ represent the remanence obtained in the parallel and perpendicular orientations. (Reprinted with permission from [121]. Copyright 2018 The Royal Society of Chemistry.)

A comparison is also made between present work and that reported in literature [118]. Y. Sahoo *et al.* also employed a magnetic field in order to align magnetic NPs (Fe_3O_4) and found that the fabricated NP wires are magnetic anisotropic. Table 6.1 shows the comparison which suggests a similar magnetic anisotropy behavior in both studies. In both works, the values of remanence and coercivity measured for NP wires parallel to the magnetic field are higher than that for the perpendicular orientation. Whereas, higher remanence increment is reported at both measuring temperatures in literature, we

observe similar values of remanence in our work. This suggests that only similar fields are required to cancel the film's magnetic memory induced in both orientations. Such a difference could be caused by factors like the nature of magnetic NPs, the NPs' size and size distribution, the characters of NP wires and the film homogeneity.

Additionally, a comparison is also made between our present work and our previous investigations, where a magnetic field is applied during the film fabrication (based on solution casting [75] and printing [87]). The prepared films from previous works have a thickness of above 1 μm and contain macroscale NP wires. They show much higher absolute values of magnetic susceptibility when compared to the present work. To quantify the responsive behavior in both orientations, the magnetic susceptibility ratio $\chi_{//}/\chi_{\perp}$ is calculated and presented in Figure 6.18. From the comparison of the susceptibility ratios, one can see that the magnetic anisotropy achieved at 2 wt% from the present study is comparable with the values from previous work. This indicates that the presently employed film fabrication technique without using additional magnetic field is promising.

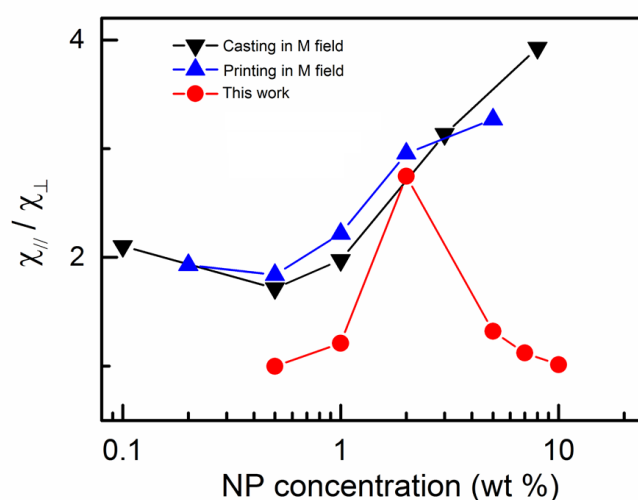


Figure 6.18: Comparison of magnetic anisotropy of films prepared with different fabrication techniques (with and without magnetic field). Red solid circles show the data of the present study, where no additional magnetic field is applied. Blue and black solid triangles present the data of films fabricated by printing [87] and solution casting [75] within a magnetic field, respectively. The magnetic susceptibilities in both parallel ($\chi_{//}$) and vertical (χ_{\perp}) orientations (with respect to NP wires) are calculated by applying a linear fit at the zero-remnant region. The susceptibility ratio $\chi_{//}/\chi_{\perp}$ is obtained and plotted as a function of NP concentration. All lines serve as a guide to the eye. (Reprinted with permission from [121]. Copyright 2018 The Royal Society of Chemistry.)

6.7 Conclusion

In this chapter, we present a facile, low-cost and straightforward printing technique to prepare magnetic anisotropic hybrid film without applying any additional magnetic fields.

In order to direct the orientation of DBC nanostructure and enhance the nanostructure order, solvent vapor annealing with selected mixed solvents is used. Optical microscopy images prove that the printed magnetic films are homogeneous. According to the SEM and AFM measurements, a highly ordered clindrical morphology, which results from the microphase separation, forms after printing. Due to the solvent vapor annealing, the PS nanocylinders align vertically (with respect to the substrate surface) inside the PNIPAM matrix, which is unexpected at the film thickness larger than the periodic domain spacing of the DBC. Meanwhile, the order of the cylindrical structure is also enhanced during the solvent vapor annealing. Due to the oleic acid ligand grafted on the surfaces, magnetic NPs are selectively incorporated and form aggregates inside the PS nanocylinders. A slight loading of NPs has rare negative influence on the nanostructure order. GISAXS characterization reveals that the structural order remains high even at the NP concentration of 2 wt%. This indirectly indicates that highly ordered long NP aggregates aligning perpendicularly with respect to the substrate surface exist inside the hybrid film.

SQUID data suggest that all the fabricated hybrid films are superparamagnetic, and magnetic anisotropy is present at certain NP concentrations (1, 2, and 5 wt%). The highest degree of magnetic anisotropy is obtained for the hybrid film with 2 wt% of NPs. Beyond this concentration region, the prepared hybrid films are magnetic isotropic due to the insufficient amount of NPs (< 1 wt%) or the less-ordered structure (> 5 wt%).

In general, the method combining printing and solvent vapor annealing is easy and reproducible for the fabrication of magnetic anisotropic films, which makes it attractive and promising in applications concerning nanostructured magnetic sensors.

7 In situ investigation on the magnetic film formation during spray coating

Parts of this chapter have been published in the article: Spray-coating magnetic thin hybrid films of PS-*b*-PNIPAM and magnetite nanoparticles [132]. (Reprinted with permission from (S. Xia et al., *Adv.Funct.Mater.*, 2019, 29, 1808427.). Copyright 2019 WILEY-VCH Verlag GmbH & Co. KGaA, Weinheim. DOI: 10.1002/adfm.201808427).

In previous chapters, the importance of magnetic NPs' spatial arrangement is discussed [1, 3, 133]. Diblock copolymers (DBC), which can form various nanostructures due to microphase separation, are used as a template to guide the alignment of magnetic nanoparticles (NPs). By applying post-treatments, like solvent vapor annealing (chapter 5 and chapter 7) and thermal annealing (chapter 6), the order of the DBC nanostructures can be enhanced [83, 134]. Accordingly, the spacial order of NPs can be improved, if NPs are selectively located inside the minor domains.

So far, various fabrication techniques of NP-DBC films have been reported, such as melt blending [135], solution casting [89, 119], spin-coating [136], flow coating [72] and slot-die printing [87]. For example, Wilson et al. fabricated NP-polymer hybrid films via a melting blend technique, and obtained composite films with homogeneous dispersion of NPs [135]. Gass et al. prepared films by spin-coating solutions made of Fe₃O₄ NPs and poly(methyl methacrylate) (PMMA). The casted films show homogeneously dispersed NPs inside the PMMA matrix [136]. Yuan et al. obtained hybrid films containing cobalt NPs by magnetic flow coating. The application of a weak external magnetic field during flow coating directed the alignment of cobalt NPs, and long NP wires were fabricated [72]. Also, in our previous work, various techniques were employed to prepare NP-DBC films successfully, in which different DBC nanostructures with magnetic NPs were achieved [87, 89, 91].

In addition to the film fabrication techniques mentioned above, spray-coating has received huge attention due to its possible application in large-scale production of films and many other benefits as well. For example, spray-coating allows continuous fabrication of films at high production speed [137–139]. Moreover, since solutions with very low concentration is required for spray-coating, less toxic solvents can be chosen to dissolve materials concerning the spray solution preparation [140]. Additionally, spray-coating is a process based on solvent evaporation, which allows for *in situ* investigation of the film formation process with scattering techniques. For example, K. Sarkar *et al.* [141], B. Su *et al.* [142] and L. Song *et al.* [21] successfully used *in situ* GISAXS technique to monitor the growth behavior of zinc oxide and titanian films during spray deposition, respectively. Via *in situ* GISAXS measurement, M. Al-Hussein *et al.* followed the kinetics of NPs self-assembly while spraying gold NPs onto conductive films [143].

Regarding NP-DBC hybrid films, however, the focus of most studies so far was only on the film fabrication or the characterization of final films. Rarely, the hybrid film formation process has been reported, and the arrangement of magnetic NPs during the film-drying. The formation of NP-DBC hybrid films is known as a complicated process, in which the evolution of the DBC structure and the arrangement of NPs are involved and may differ at different film formation times. Therefore, *in situ* GISAXS can be a powerful technique, from which the knowledge of the involved kinetic process during the NP-DBC film formation can be gained.

In the present chapter, NP-DBC films, which are composed of magnetite NPs (Fe_3O_4) and polystyrene-*block*-poly(*N*-isopropylacrylamide) (PS-*b*-PNIPAM), are fabricated via spray-coating. *In situ* GISAXS measurements are employed to monitor the whole film formation process. To investigate the influence of NPs on the kinetic process, an NP-free film is prepared as a reference following the same spray protocol. The final dried films are studied via *ex situ* characterization techniques. The thickness and surface structure are probed by profilometry and atomic force microscopy (AFM), respectively. The magnetic property of the hybrid film is examined via superconducting quantum interference device (SQUID) magnetometry.

7.1 Spray coating

The solutions used for spray-coating are prepared from a mixture of magnetic NPs and PS-*b*-PNIPAM dissolved in tetrahydrofuran (THF). The employed PS-*b*-PNIPAM has a number average molecular weight of 35.5 kgmol^{-1} with the polydispersity of 1.12. The volume fraction of PS block is 0.34. Therefore, a cylindrical morphology is expected for

the DBC films. The mean diameter of magnetic NPs is 10 nm, excluding 1.5 nm of hydrophobic shell consisting of oleic acid chains. The DBC concentration is controlled to be 1.8 mgml^{-1} according to initial tests. For comparison, two types of solution are prepared with different NP concentrations (weight ratio of NPs to DBC: 0 wt% and 2 wt%). Silicon wafers are cut into the size of $2.5 \text{ cm} \times 2.5 \text{ cm}$ and cleaned via an acid-cleaning procedure before use [77].

The whole spray process is performed in a closed chamber, in which a height-adjustable and remote controllable spray set-up is installed. The spray gun is positioned on the set-up with a nozzle-to-substrate distance of 17 cm. Nitrogen is used to atomize the solution with a working pressure of 1.5 bar, and the solution flow rate is adjusted to be $33 \text{ } \mu\text{Ls}^{-1}$. The whole spray protocol consists of 30 cycles of spray deposition followed by annealing for 20 s. Each cycle of the spray deposition is completed by 1 s of spray (spray on, shown as purple part in Figure 7.1) and 1 s of drying (spray off, shown as gray part in Figure 7.1). During the whole spray process, the substrate is controlled to be at $50 \text{ }^\circ\text{C}$ through a heating stage. The structure formation is followed by *in situ* GISAXS simultaneously. The measurements are performed at the MiNaXS beamline P03 of the PETRAIII storage ring at DESY, Hamburg. The X-ray with the wavelength of 0.94 \AA is impinged on the film surface with a chosen incidence angle of 0.35° . At a sample-to-detector distance of 4229 mm, a Pilatus detector (1M, Dectris Ltd.) with 981×1043 pixels (pixel size $172 \text{ } \mu\text{m} \times 172 \text{ } \mu\text{m}$) is positioned to collect scattering signals. Figure 7.2 depicts simplified sketch of the spray experiment investigated via *in situ* GISAXS.

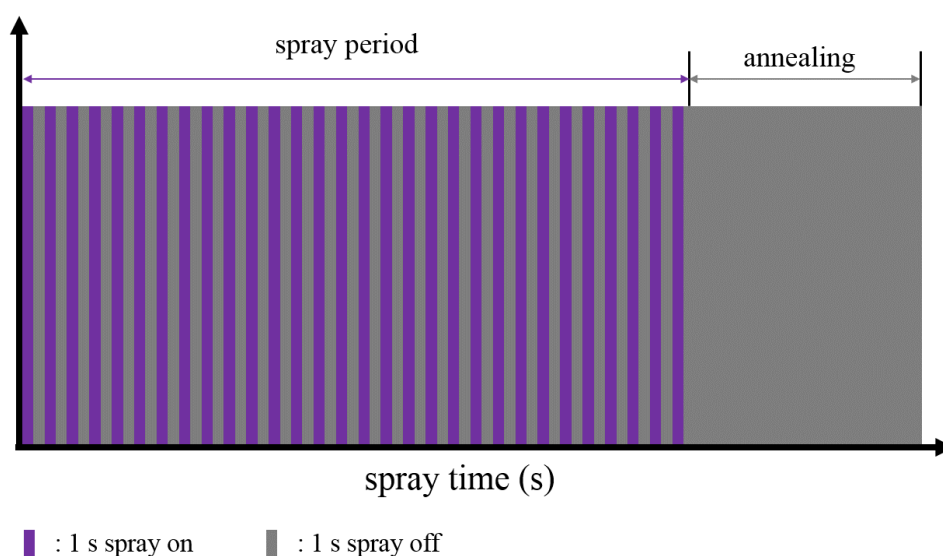


Figure 7.1: Sketch of the spray protocol composed of 30 cycles of spray deposition and 20 s of annealing. Each spray cycle consists of 1 s spray (purple part) and 1 s drying (gray part).

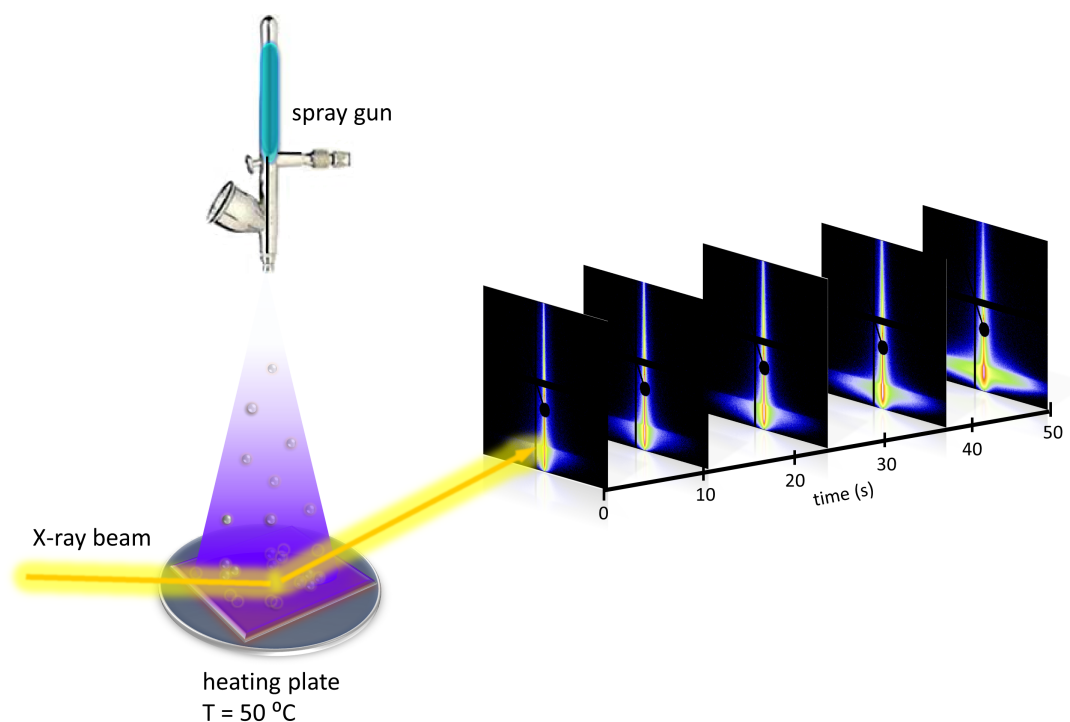


Figure 7.2: *Simplified sketch of the spray experiment investigated via in situ GISAXS.*

7.2 Surface structure

The surface nanostructures of the fabricated films are probed via AFM and the results (height images) are displayed in Figure 7.3. Both films are obtained after 30 spray cycles following the identical spray protocol. More details are described in 7.1. Figure 7.3a shows the topography of the NP-free film. A cylindrical morphology oriented parallel to the substrate surface is observed. An enlarged view of Figure 1a can be found in Figure 7.4, where the parallel orientation of structure can be better identified. In this graph, the brighter parts are PS domains, and the darker parts belong to the PNIPAM domains [126]. Based on the volume fraction of the PS block (0.34), the film morphology is composed of PS nanocylinders dispersed inside the PINIPAM matrix. The profilometry measurement gives a film (pure film) thickness of 343 ± 11 nm, which is larger than the diameter of the PS nanocylinders (35 ± 1 nm) and the average center-to-center domain distance ($D_{AFM-pure} = 37 \pm 1$ nm), extracted from the AFM images with ImageJ. Therefore, the cylindrical morphology prefers a parallel orientation (with respect to the substrate surface) [129].

For the hybrid films, the thickness and the average center-to-center domain distance ($D_{AFM-hybrid}$) increase slightly to (351 ± 15) nm and (40.7 ± 0.8) nm, respectively. Due to the incorporation of 2 wt% magnetic NPs, the thickness of the hybrid film increases

to 351 ± 15 nm. Instead of parallel aligned cylinders, the morphology of the hybrid film shows a perpendicular orientation, meaning that the PS nanocylinders are standing vertically on the substrate (Figure 7.3b).

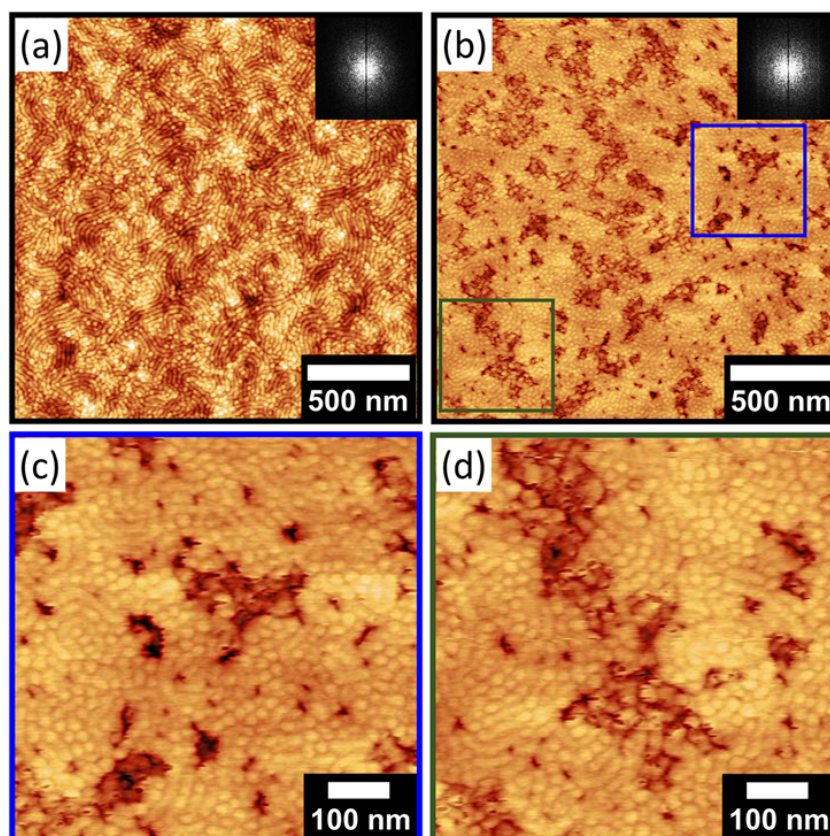


Figure 7.3: AFM height images of films with different NP concentrations; (a) 0 wt%, (b) 2 wt%. The corresponding Fast Fourier Transform patterns are displayed on the top right corners. In figure (b), the blue and green boxes are used to show the magnetic NP aggregates and partially parallel cylinders, respectively. Zoomed-in images are shown in (c): blue box and (d): green box. (Reprinted with permission from [132]. Copyright 2019 WILEY-VCH Verlag GmbH & Co. KGaA, Weinheim.)

The alteration of structure orientation is caused by the localization of magnetic NPs inside PS nanocylinders. Due to the oleic acid capping layer of particles, the compatibility between magnetic NPs and PS block is enhanced and much greater than that between NPs and PNIPAM block. In order to reduce the entropy loss of the polymer chains, functional magnetic NPs tend to be driven to the film surface [18, 88]. Since magnetic NPs are preferentially located in PS domains, the moving tendency of particles induces the perpendicular orientation. Similar reports on NPs inducing orientation transition are also found in literatures [6, 18, 88]. In addition to the perpendicularly standing cylinders, parallel cylinders (indicates as the green box in Figure 7.3b and Figure 7.3d) can also be

observed in partial areas of the AFM image. Thus, the equilibrium state of the hybrid film was not reached. Aggregates formed by magnetic NPs (black objects shown by the blue box in Figure 7.3b and Figure 7.3c) are also present inside the hybrid film, which leads to a rougher film surface compared to the pure film. To elucidate the order of the surface nanostructure, Fast Fourier Transform (FFT) patterns are extracted from the corresponding AFM graphs and presented on the top right corners of Figures 1a and 1b. No ring-like intensity maximum can be found in the FFT patterns, suggesting the absence of high structural order on the film surfaces.

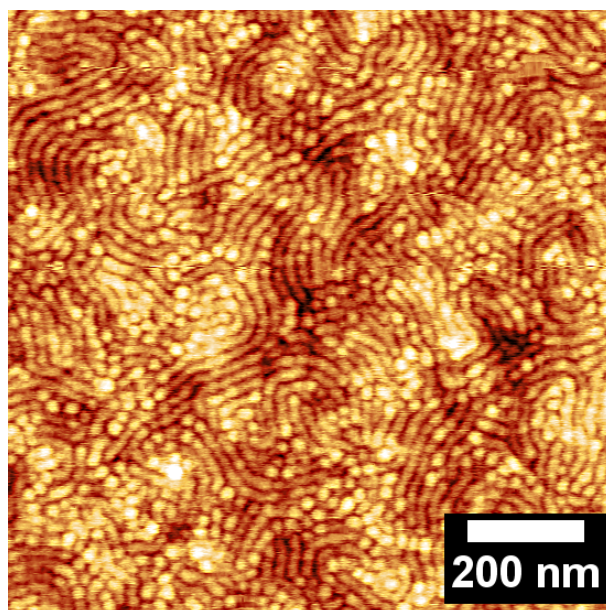


Figure 7.4: A magnified part of the AFM height image (Figure 7.3 a) of the pure reference DBC film. (Reprinted with permission from [132]. Copyright 2019 WILEY-VCH Verlag GmbH & Co. KGaA, Weinheim.)

7.3 Inner structure

The inner structure evolution of films during spray-coating is monitored with *in situ* GISAXS. In order to address the influence of magnetic NPs on the film formation, a comparison is made between the data of the pure film (0 wt%) and that of the hybrid film (2 wt%).

7.3.1 Formation of pure DBC film

The obtained 2D GISAXS data of the pure DBC film are displayed in Figure 7.5 at different spray times. The overall scattering intensity is enhanced with increasing spray time, which is due to the increasing amount of polymer deposited on the substrate. After the spray deposition, the GISAXS measurement runs for additional 20 s to study the influence of annealing on the structure formation. As compared with the 2D GISAXS data obtained at the end of spray deposition, those achieved after annealing show similar scattering features. Such observation suggests no significant changes of the morphology during the annealing. To quantify the evolution of buried structure during film deposition, horizontal line cuts are made at the Yoneda peak position of PS-*b*-PNIPAM in the corresponding 2D GISAXS data [144]. The selected horizontal line cuts from different spray cycles are plotted in Figure 7.6a, and the 2D scattering intensity mapping of q_y versus spray time is displayed in Figure 7.6b. In the 2D mapping, no significant intensity changes are observed in the q_y direction with spray time, which indicates a stable film.

To further extract structure information from the scattering data, all horizontal line cuts are modeled using the effective interface approximation (EIA) in the framework of Distorted Wave Born Approximation (DWBA) [145]. A cylinder form factor is employed in the applied model [146]. To model the cuts obtained in the initial 20 s (10 cycles), two structure factors, representing the mean center-to-center distance of scattering objects, are used. From the 11th cycle on, only one structure factor is needed for modeling the data. Figure 7.6c shows the results extracted from the modeling. As spray time increases, the value of the large structure (D_I) decreases from 152 ± 60 nm to 112 ± 22 nm and disappears after the 10th cycle. Correspondingly, the radius (R_I) of the large structure increases from (43 ± 1) nm to (55 ± 2) nm. In contrast, the value of the small structure (D_{II}) decreases slightly during the initial phase from (39 ± 4) nm until a constant value of (36.5 ± 0.8) nm with a stable radius of (16.9 ± 0.2) nm is established for the rest of the measurement. The extracted distance (D_{II}) is found to be similar to the average center-to-center distance of PS cylinders ($D_{AFM-pure} = 37 \pm 1$ nm) as determined by AFM measurements. Therefore D_{II} represents the interdomain spacing of the DBC nanostructure. Two different form factors, which represent the radii of polymer island (R_I) and domain (R_{II}), are also used to fit the data obtained before the 10th spray cycle. Results from fitting show constant values of D_{II} and R_{II} , which suggests a stable DBC nanostructure present during the whole spray deposition after the small decrease at the initial stage. During the spray process, the nitrogen flow atomizes the polymer solution into small droplets, which then leave the gun nozzle and fly onto the silicon substrate [147]. During the transportation from the nozzle to the substrate, part of the solvent evaporates. Moreover, the evaporation of solvent is further accelerated on the

substrate due to the heated sample stage, which limits the mobility of materials to some extent. As a consequence, small islands made of polymer materials are formed on the substrates. As spray deposition continues, more solution droplets arrive on the substrate, leading to the growth of polymer islands.

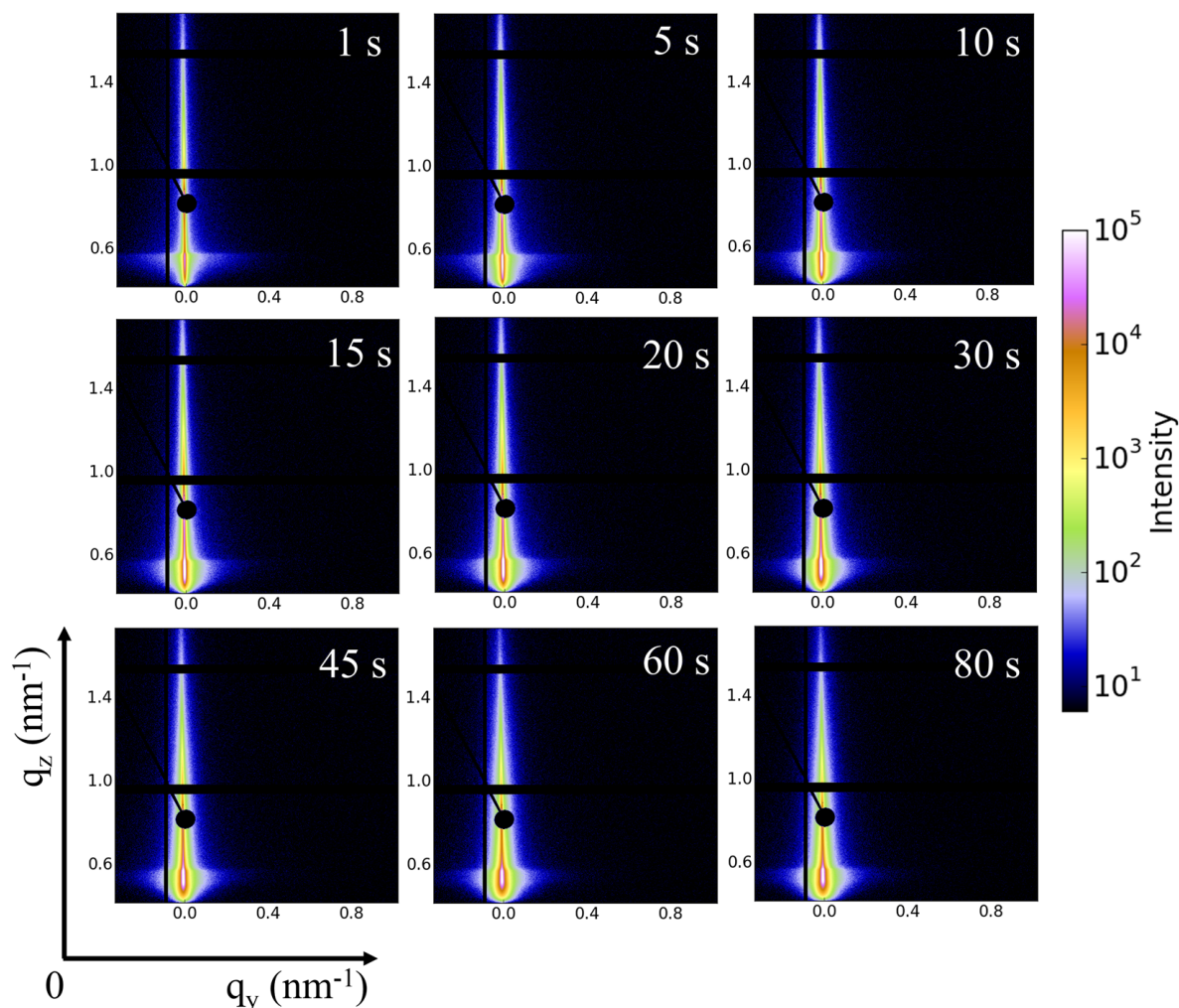


Figure 7.5: Selected 2D GISAXS data of the pure film acquired at different spray times as shown on the top right corners. A beamstop is positioned in front of the specular peak to protect the detector from oversaturation. Vertical and horizontal black bars are gaps between detector modules. (Reprinted with permission from [132]. Copyright 2019 WILEY-VCH Verlag GmbH & Co. KGaA, Weinheim.)

An increase of R_I is observed. The inter-island spacing decreases accordingly followed by the formation of a complete film on the substrate. Therefore, the structure factor used for modeling inter-island distance (D_I) disappears after the 10th spray cycle. However, the interdomain distance (D_{II}), which represents the center-to-center spacing of PS nanocylinders, stays almost constant during the whole spray deposition. Such observation

reveals that the morphology, which originates from the microphase separation of DBC, is rarely influenced by the spray coating process.

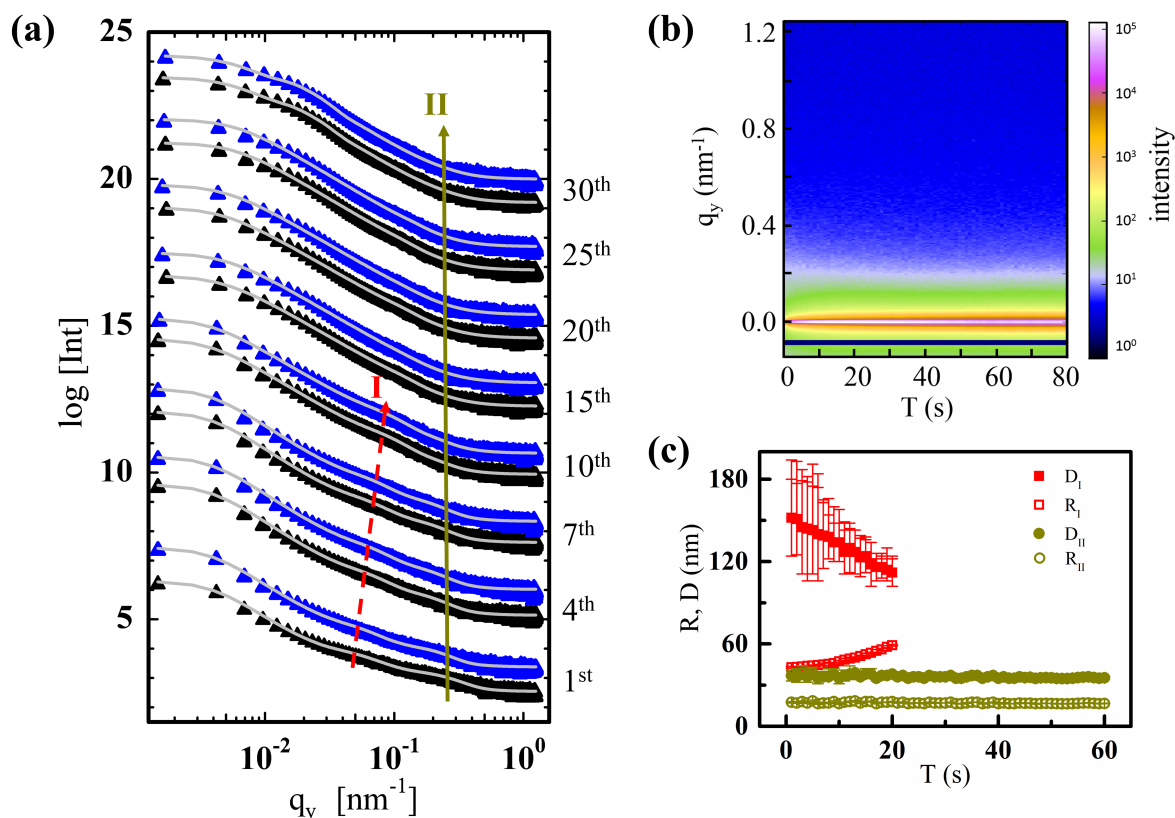


Figure 7.6: (a) Horizontal line cuts (black: spray on, blue: spray off) achieved from selected 2D GISAXS data of the pure film with corresponding fits (solid white lines). The spray cycle number increases as indicated on the right side of figure (a). The red dashed arrow shows the evolution of polymer islands (peak I), and the dark yellow solid arrow indicates the DBC structure evolution (peak II). (b) Mapping extracted from horizontal line cuts from 2D GISAXS data. All line cuts are integrated over $\Delta q_z = 0.51\text{--}0.56\text{ nm}^{-1}$ and plotted as a function of spray time. (c) Values of inter-island distance (D_I), island radius (R_I), interdomain distance (D_{II}) and domain radius (R_{II}), obtained from the modeling are shown versus spray time. (Reprinted with permission from [132]. Copyright 2019 WILEY-VCH Verlag GmbH & Co. KGaA, Weinheim.)

7.3.2 Formation of hybrid film

The 2D GISAXS data of the hybrid film formation ($C_{NP} = 2\text{ wt}\%$) selected at different deposition times are displayed in Figure 7.7. As one can note, the scattering patterns evolve following a similar trend as observed for the NP-free film. With increasing spray

time, the overall scattering intensity is enhanced. Difference can be seen along lateral direction (q_y direction) in the 2D GISAXS data. As spray deposition proceeds, an intensity maximum appears at around $q_y = 0.8 \text{ nm}^{-1}$ (shown as the bold yellow arrow in the last figure in Figure 7.7), which is caused by the presence of magnetic NPs. Continuous deposition leads to an increasing number of magnetic NPs located inside the DBC film. As a consequence, a gradually enhanced intensity maximum at $q_y = 0.8 \text{ nm}^{-1}$ is observed during the spray process.

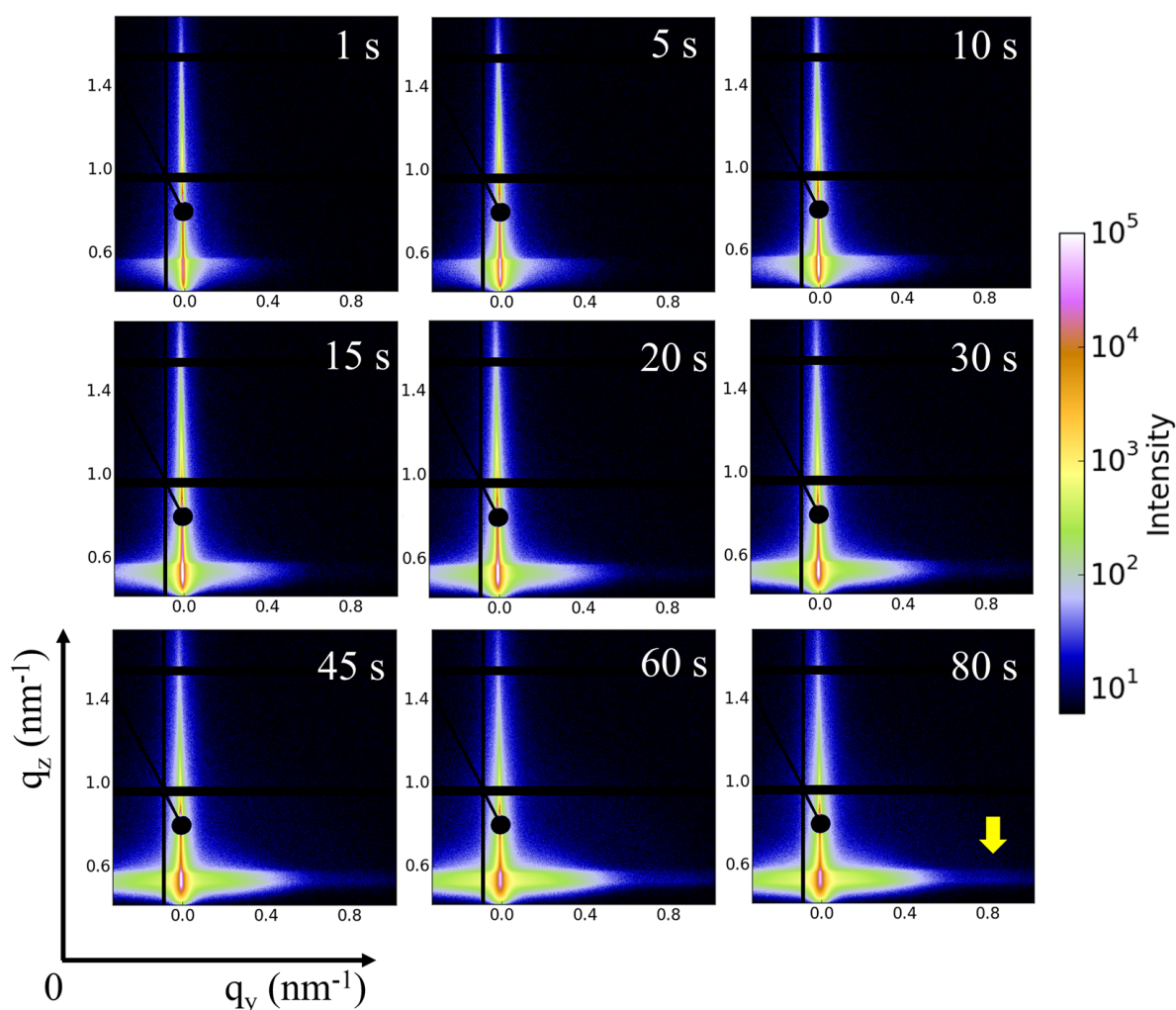


Figure 7.7: Selected 2D GISAXS data of the hybrid film formation (2 wt%) acquired at different spray times as shown on the top right corners. A beamstop is positioned in front of the specular peak to protect the detector from oversaturation. Vertical and horizontal black bars are gaps between detector modules. The yellow arrow in the last graph (80 s) indicates the weak local intensity maximum in the q_y direction. (Reprinted with permission from [132]. Copyright 2019 WILEY-VCH Verlag GmbH & Co. KGaA, Weinheim.)

Figure 7.8a shows the horizontal line cuts in conjunction with the corresponding fits obtained from the 2D scattering data. Distinguishable characteristics (marked as peak I, II, III and IV) can be clearly observed in the respective cuts. Similar to the pure polymer reference film, two different structure factors are applied for fitting the cut at the initial spray stage. One structure factor represents the inter-distance of polymer islands (peak I), the other corresponds to the inter-domain distance of the DBC microphase-separated structure (peak II).

Major differences are found with the 10th spray cycle, where the structure factor modelling the polymer islands disappears. Therefore, structure factors for modelling NP aggregate distances (peak III) and the size of single NPs (peak IV) are needed, respectively. The corresponding time-dependent evolution of extracted average sizes and distances can be found in Figure 7.8c. The inter-island distance (D_I) changes with time similarly as compared to the pure polymer reference sample. Nevertheless, a closed polymer film formation is reached already after the 7th spray cycle, which is faster as compared to the reference sample. With increasing spray time, an increasing amount of NPs are deposited on the substrate, which are first detected through GISAXS measurements starting with the 8th cycle and modelled through an additional structure factor. The number of NPs is successively increasing, which leads to the formation of NPs agglomerates. With further spraying, peak III (Figure 7.8a) becomes broader and slightly shifts to the lower q_y region, which is ascribed to an increase in inter-NPs agglomerate distance and found as the result of entropy-driven processes. Meanwhile, peak IV stays at a constant q_y position, but gets more pronounced due to an increasing amount of NPs inside on the substrate. From the 2D mapping of the scattering data (Figure 7.8b), one can also observe a local intensity maximum appearing after 15 s, which is getting more intense with time. Similar to the pure polymer reference film, the microphase-separated nanostructure of the hybrid film remains constant at (38.5 ± 0.5) nm for the inter-domain distance and (17.8 ± 0.3) nm for the radius irrespective of spray time (shown as peak II in Figure 5a and D_{II} in Figure 7.8c), which is consistent with the observation from AFM measurements ($D_{AFM-hybrid} = 40.7 \pm 0.8$ nm). Slight deviations can be explained from the fact that AFM only probes the surface structure, whereas GISAXS accesses the inner structure of the films. Additionally, concerning the position of peak II, a small difference between Figure 7.6a (reference film) and Figure 5a (hybrid film) can be found. Peak II appear at $q_y = 0.168 \text{ nm}^{-1}$ for the reference film, but at $q_y = 0.191 \text{ nm}^{-1}$ for the hybrid one. The corresponding inter-domain distance (D_{II}) increases from (36.5 ± 0.8) nm for the reference film to (38.5 ± 0.5) nm for the hybrid film. Such shift to higher q_y values is caused by the orientation transition of the PS nanocylinders. The calculation of the distance of parallel nanocylinders ($D = 2\pi/q$) differs from that of perpendicular nanocylinders

($D = 4\pi/(\sqrt{3}q)$) [18]. These findings match the observation from the AFM images where the structural orientation alters from parallel to perpendicular.

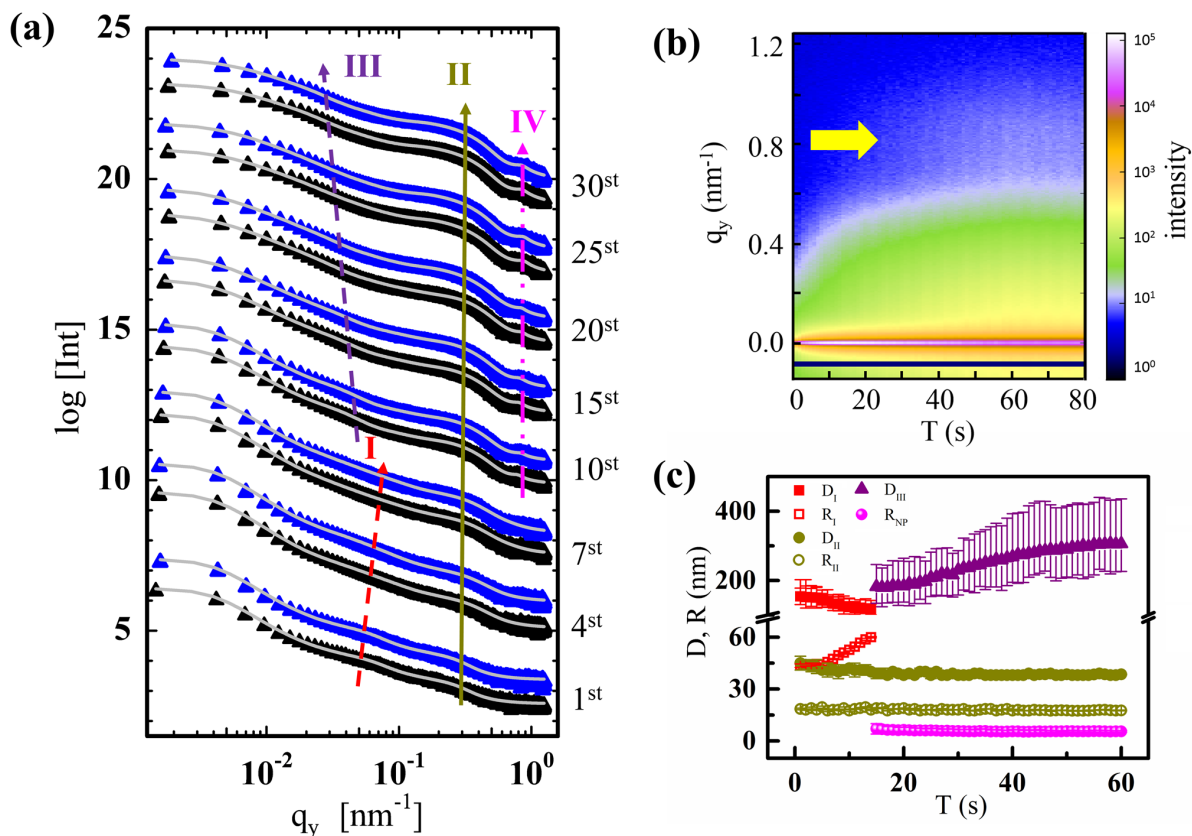


Figure 7.8: (a) Horizontal line cuts (black: spray on, blue: spray off) achieved from selected 2D GISAXS data of the hybrid film with corresponding fits (solid white lines). The spray cycle number increases as indicated on the right side of figure (a). The red dashed arrow, dark yellow solid arrow, the purple dashed arrow and the pink dashed arrow show the structure factor of polymer islands (peak I), microphase-separated structures (peak II), magnetic NP aggregates (peak III) and individual NPs (peak IV). (b) Mapping of horizontal line cuts extracted from the 2D GISAXS data of the hybrid film. All horizontal line cuts are integrated over $\Delta q_z = 0.51\text{--}0.56 \text{ nm}^{-1}$ and plotted as a function of spray time. The yellow arrow at around $q_y = 0.8 \text{ nm}^{-1}$ indicates the presence and evolution of scattering intensity caused by magnetic NPs. (c) Averaged inter-island distance (D_I), island radius (R_I), inter-domain distance (D_{II}), domain radius (R_{II}), inter-aggregates distances of magnetic NPs (D_{III}) and radius of magnetic NPs (R_{NP}) are extracted from the data modeling and plotted versus spray time. (Reprinted with permission from [132]. Copyright 2019 WILEY-VCH Verlag GmbH & Co. KGaA, Weinheim.)

7.3.3 Influence of NPs on the film formation

The previous analysis suggests that the evolution of the film differs between the pure film and hybrid film. Compared with the NP-free film, the composite film shows a larger domain size and interdomain spacing during the whole deposition period. The increase is caused by the swelling of PS domains with NPs. Since NPs are grafted with oleic acid ligands, they are more selective to the PS blocks than the PNIPAM blocks. Therefore, NPs are preferentially located inside the PS domains, leading to the expansion of the PS nanocylinders. Similar phenomena have been reported in literatures working on NP-DBC systems, which were not detected via spray coating [18, 75].

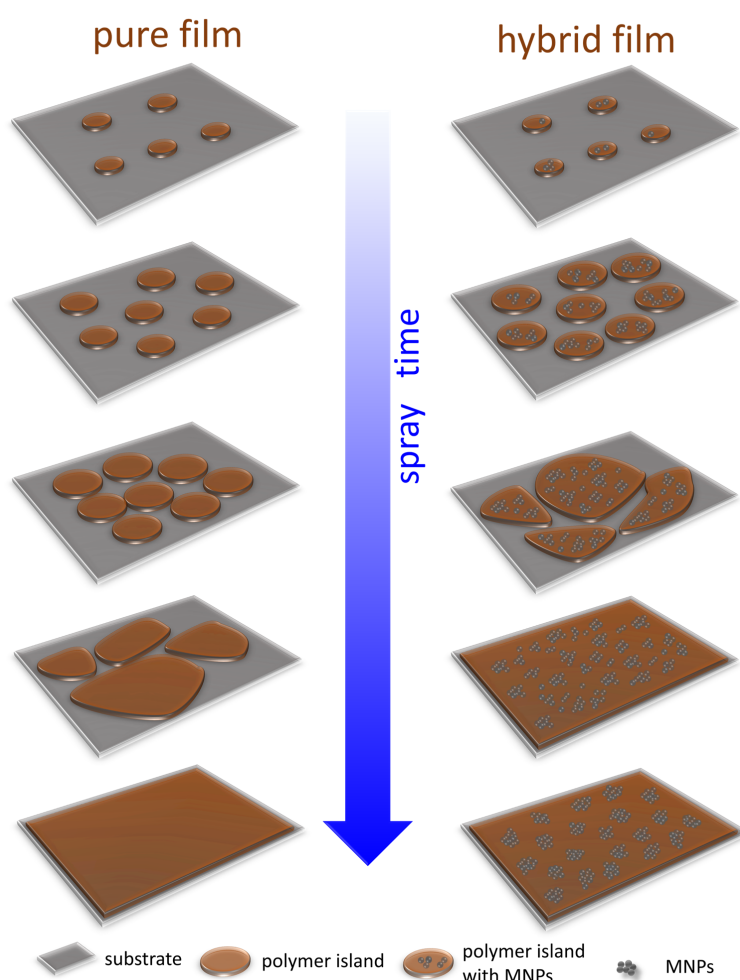


Figure 7.9: Simplified sketch picturing the influence of magnetic NPs on the film formation with spray time. The left column shows the evolution of pure film, and the right column represents that of the hybrid film. (Reprinted with permission from [132]. Copyright 2019 WILEY-VCH Verlag GmbH & Co. KGaA, Weinheim.)

Additionally, the evolution of polymer islands to a closed film also differs between the

two experimented systems. Figure 7.9 pictures the film formation of both system at different spray stages. In case of the hybrid system, polymer islands disappear after the 7th cycle, which is much earlier than that for the pure system (10th cycle). This reveals that a complete film forms at a much faster speed for the hybrid system than for the pure system, which can be explained by the existence of magnetic NPs inside the hybrid film.

Literature reports that the dewetting behavior of polymer films can be depressed by incorporating NPs [148–150]. For example, Sharma *et al.* found that the wetting behavior of PS film on the substrate can be improved by adding silica NPs [148].] In case of the present investigation, the NPs are present in the hybrid film during the entire deposition process. The affinity of the NPs to the substrate contributes to an improved wetting behavior of the hybrid film. Meanwhile, due to the preferential localization of the NPs inside the PS domains, the PS cores tend to follow the movement of the NPs, leading to a faster merging of the polymer islands. The temperature of the substrate is set to 50 °C, which is slightly lower than the boiling temperature of THF (66 °C). Thus, the polymer islands formed on the substrate will stay wet only shortly, especially after a large amount of solutions has arrived on the substrate. This provides the opportunity of facilitating the merging progress under the attractive forces induced by the NPs. Therefore, a quicker establishment of complete local film is observed for the hybrid system compared with the pure one where no NPs are present (see Figure 7.9). Also it should be noted that the employed NP precursors are stored in toluene, the boiling temperature of which is higher than THF. However, considering the dilute polymer solution (1.8 mg/ml), the weight ratio (2 wt %) of NPs and the concentration of NP precursor (5 mg/ml), the THF volume V_{THF} in the hybrid spray solution is way higher than the toluene volume $V_{toluene}$ ($V_{THF} / V_{toluene} = 138$). Therefore, the influence of the toluene to the hybrid film formation can be ignored in the present investigation.

7.4 Magnetic properties

As discussed in previous sections, the arrangement of NPs differs at different spraying stages. Before the formation of the complete film, NPs are dispersed individually inside the PS domains. While NP aggregates appear in the following continuous film and increase in size as the deposition proceeds. However, the kinetics of the magnetic properties during the spray deposition cannot be technically monitored with present instruments. Therefore, only the final dry hybrid film is measured in the present work. To probe the magnetic properties of the sprayed hybrid film (2 wt%), a superconducting quantum interference device (SQUID) magnetometer is used. The influence of temperature on the magnetic properties of the hybrid film is investigated.

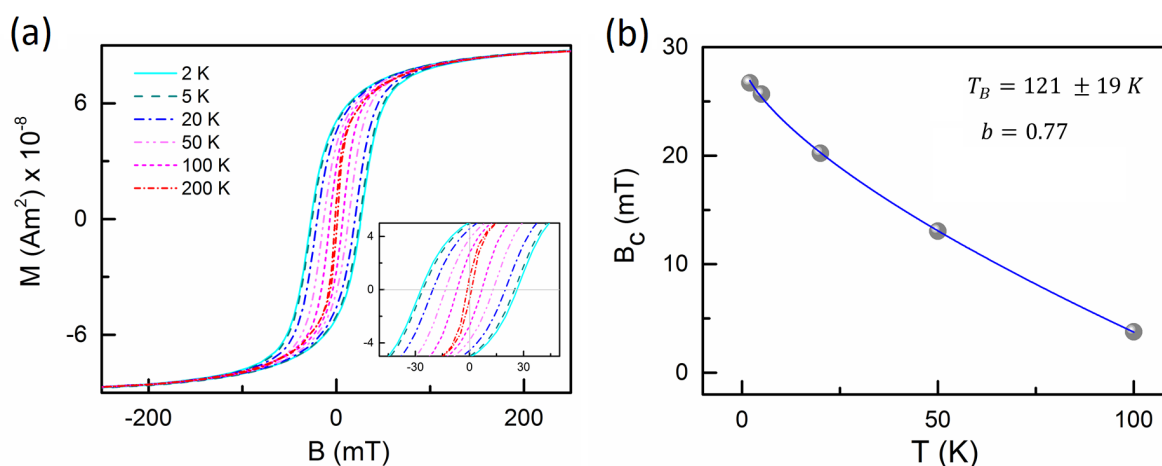


Figure 7.10: (a) Magnetization (M) versus external magnetic field (B) of the sprayed hybrid film. Data are collected at different temperatures. The partially magnified hysteresis region is shown at the right bottom. (b) Coercivities extracted from corresponding magnetization data plotted as a function of temperature. The data are fitted with the model described in Chapter 5. The obtained blocking temperature is also provided in the inset. (Reprinted with permission from [132]. Copyright 2019 WILEY-VCH Verlag GmbH & Co. KGaA, Weinheim.)

The magnetization curves collected at different temperatures are profiled in Figure 7.10. The measurements are performed with the magnetic field oriented parallel to the film surface. It can be clearly noticed that the magnetization behavior strongly depends on the temperature. An obvious magnetic hysteresis loop can be observed at low temperatures (for example, 2 K and 5 K). As temperature increases, the hysteresis loop gets narrower and tends to disappear at high temperature. Such observation follows the typical superparamagnetic behavior, which agrees with our previous investigations on NP–DBC systems prepared via other deposition techniques such as spin-coating [89], solution casting [18] and printing [87].

To achieve the blocking temperature of the sprayed composite film, the coercivity data is fitted with the method described in Chapter 5. From the fitting, a blocking temperature of $121 \pm 19 \text{ K}$ is obtained, which keeps constant with our previous work, where identical magnetic NPs are investigated [121].

To gain a deeper understanding of the magnetic behavior of the sprayed hybrid film, the values of both remanence (M_r) and susceptibility [87] are calculated and plotted as a function of temperature in Figure 7.11. With increasing temperature, the remanence decreases while the susceptibility increases. Such observation can be explained by the increased thermal energy of the hybrid system at higher temperatures. Higher energy

results in faster reversal of magnetization direction, which leads to less magnetic memory left and quicker response to external magnetic field, as seen before in printed [87] and casted [75] hybrid films.

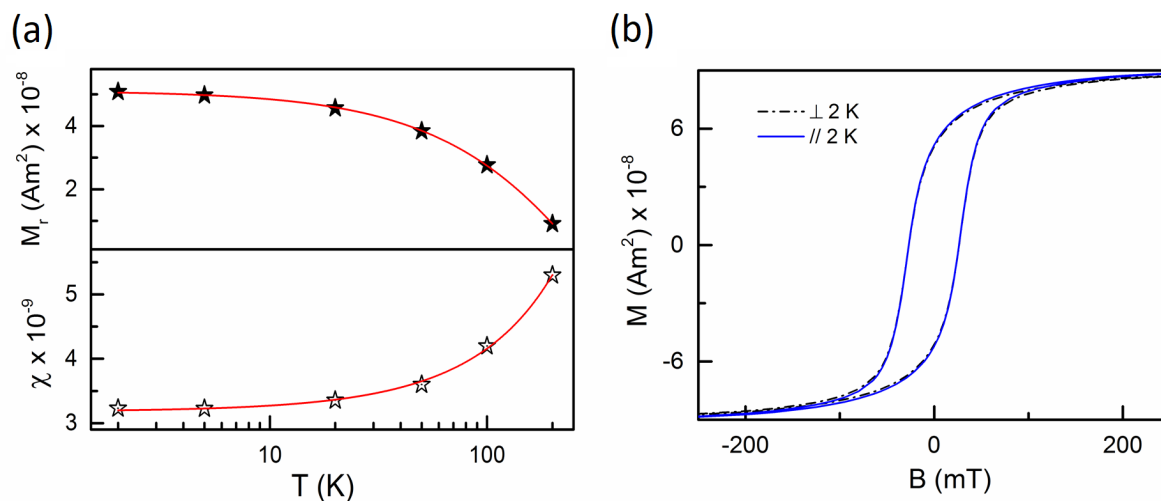


Figure 7.11: (a) Remanence (M_r) and magnetic susceptibility (χ) extracted from corresponding magnetization curves plotted as a function of temperature. The magnetic susceptibility is obtained by applying a linear fit in the zero-remanence region. Both red solid lines are served as a guide to the eye. (b) Magnetization data obtained at 2 K in two orientations with the magnetic field parallel (blue solid line) and perpendicular (black dashed line) to the film surface. (Reprinted with permission from [132]. Copyright 2019 WILEY-VCH Verlag GmbH & Co. KGaA, Weinheim.)

Since the observed PS nanocylinders are aligning perpendicularly on the substrate, it is necessary to probe the magnetic anisotropy of the sprayed hybrid film. For this purpose, the SQUID measurements are performed in two orientations, with the direction of magnetic field parallel and then vertical to the film surface. Figure ?? displays the data collected in both orientations at 2 K. The two curves almost overlap with each other, which suggests a magnetic isotropic hybrid film. The AFM data (see section 7.2) shows that small amount of parallelly aligned PS nanocylinders are still existing in the PNIPAM matrix. Also according to the GISAXS data analysis, the obtained cylindrical nanostructures are not highly ordered. As a consequence, the magnetic NP aggregates are arranged in a less ordered way following the DBC template, ending up with a isotropic magnetic nanostructure.

7.5 Conclusion

In this chapter, the kinetics of NP-DBC hybrid film formation is investigated. The influence of magnetic NPs on the film evolution is addressed via a comparison with a NP-free DBC reference film.

The GISAXS data shows that small islands composed of polymer (or polymer and NPs) are formed at the early deposition stage. Then the polymer islands merge into larger ones and form a closed film in the end as spray deposition continues. Compared with the pure film, the hybrid film displays a faster formation process of a complete film. Due to the incorporation of magnetic NPs, the dewetting behavior of the composite film is depressed to certain extent. As a consequence, the merging process is facilitated, which results in an accelerated film formation process. In addition, GISAXS data reveals that magnetic NPs aggregate into clusters with increasing size as the spray deposition proceeds. For both pure and hybrid films, the respective microphase-separated nanostructures and their corresponding size stay stable during the whole spray deposition. The inter-spacing of PS nanocylinders of the hybrid film is slightly larger than that of the pure film. This is caused by the swelling behavior of PS domains, in order to accommodate magnetic NPs.

AFM measurement on the final dry films show that a morphology with PS nanocylinders dispersing isotropically inside PNIPAM matrix is present for the pure film. The observed PS nanocylinders are aligning parallel to the substrate. In contrast, the incorporation of magnetic NPs changes the nanostructure orientation from parallel to perpendicular, meaning that PS nanocylinders are standing perpendicularly on the substrate in the hybrid film. SQUID measurements prove that the sprayed hybrid film is superparamagnetic, and thus can be potentially used in the field of magnetic applications.

8 Printed thin magnetic films with dense magnetic nanostructure

Parts of this chapter have been published in the article: Printed thin diblock copolymer films with dense magnetic nanostructure [151] (Reprinted with permission from (S. Xia et al., *ACS Appl. Mater. Interfaces*, 2019, 11, 21935–21945). Copyright (2019) American Chemical Society. DOI: 10.1021/acsami.9b06573.)

In previous chapters, the magnetic NPs' localization inside specific hosting domains, the influence of magnetic NPs on DBC nanostructures and the effect of an external field on the film morphology and the corresponding magnetic properties have been discussed. However, typically the related research so far focused only on thick hybrid films, which had a thickness in the range from several hundred nanometers to micrometers. Thin hybrid films with a thickness of tens of nanometers were less studied so far. Such thin magnetic polymer films, especially the ones with a high density of magnetic NPs, appear highly promising nowadays for use in modern microelectronics and as magnetic sensor devices. To fabricate such thin magnetic polymer films, several challenges need to be overcome. Due to the unfavorable affinity between polymers and inorganic substrates, dewetting of an initially homogeneous hybrid film may occur [152–154], which prevents application of homogeneous films. Moreover, a suitable film thickness is required, in order to accommodate the NPs inside the films and to achieve the desired magnetic properties [155]. In addition, to gain dense magnetic structures, the nanostructure of the DBC templates needs to be fine-tuned, in order to host as many NPs as possible, but avoid the formation of large-sized NP clusters and a collapse of the DBC structure.

In this chapter, thin hybrid films were fabricated with PS-*b*-PMMA and magnetite NPs via the printing technique (see chapter 4). The used DBC has a number average molecular weight of 66.5 kg/mol with a high PS volume fraction of 0.685. The NPs are coated with oleic acid chains with an average diameter of 10 nm. Polymer solutions were prepared using toluene as solvent with a fixed polymer concentration of 7 mg/ml. Magnetic NP

concentrations (weight ratio between NPs and DBC) were varied: 0, 0.5, 1, 3, 7, 15 wt%. All hybrid films were fabricated following identical printing procedure. All films were post-treated by solvent vapor annealing (see chapter 4) with a solvent mixture containing acetone and tetrahydrofuran (THF) in a volume ratio of 1:1. After 10 min, all samples were taken out and dried in air at room temperature.

8.1 Film thickness

Previous studies showed that the incorporation of magnetic NPs can change the orientation of the printed polymer nanostructures [18,19]. Also SVA was reported in literature as a powerful tool to tune the order and orientation of polymer nanostructures [8,83,156,157]. We use both approaches to control the final architecture of the hybrid films. For this purpose, all films are printed with a thickness close to the periodic interdomain distance of the DBC. Post-treatment is applied to all films in order to reach highly ordered nanostructures. Due to the presence of acetone, which is a good solvent for PMMA [157], a geometry with PMMA cylinders lying parallel to the substrate surface is expected. The periodic interdomain distance (D) can be estimated via the following formula 8.1:

$$D \sim aN^{\frac{2}{3}}\chi^{\frac{1}{6}} \quad (8.1)$$

in which $a = 0.64$ nm is the statistical segment length [34], $N = 645$ is the polymerization degree, and $\chi = 0.042$ represents the Flory–Huggins interaction parameter of both polymer blocks [158]. From this equation, D of the pure DBC film is estimated to be around 38 nm. One needs to note that the above formula is based on the strong segregation limit (SSL) theory, which is specified for the melt materials. But to simplify the calculation in our experiment, where SVA was applied, the SSL theory is used for a rough estimation of D .

The film thickness as a function of the NP concentration is presented in Figure 8.1. As the NP concentration increases from 0 wt% to 15 wt%, the thickness increases from (35.5 ± 1.7) nm to (58.3 ± 2.1) nm. Since all hybrid films have been fabricated with an identical printing protocol, the increase is directly related to the presence of the NPs, which changes the viscosity of the printed liquid and which need to be accommodated inside the hybrid films. Interestingly, the film thickness evolves in a non-linear fashion. It increases significantly with NP concentration for concentrations below 7 wt% (stage I in Figure 8.1), and remains almost constant at higher concentrations (stage II in Figure 1). Differences in the localization of the NPs can explain such concentration dependence [19]. At low concentrations (stage I), the NPs are located preferentially inside the polymer

domains, which results in the expansion of the respective domains and a swelling of the films (thickness increase). At high concentrations (stage II), the NPs can no longer be accommodated inside the polymer domains due to saturation and form aggregates on the film surface.

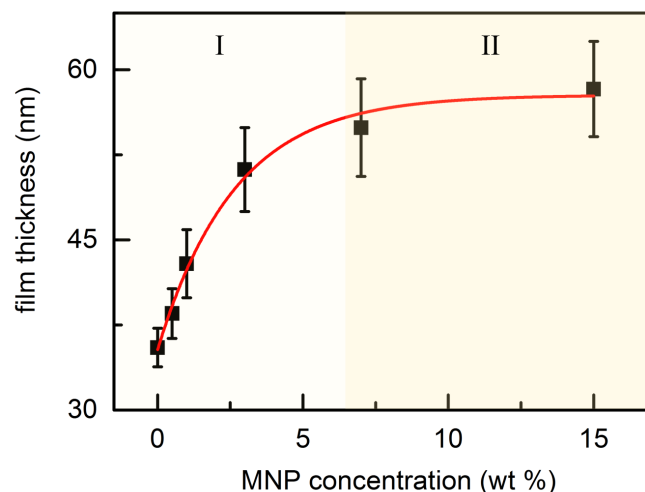


Figure 8.1: Thickness of NP-DBC hybrid films at different NP concentrations (the red solid line is a guide to the eye). Two different stages are identified: Stage I (swelling, light yellow) and stage II (saturation and NP aggregates formation, yellow). (Reprinted with permission from [151] Copyright 2019 American Chemical Society.)

Figure 8.1 shows the thickness of films at different NP concentrations (C_{NP}). As C_{NP} increases, the film thickness increases from 37.5 ± 1.7 nm ($C_{NP} = 0$ wt%) to 58.3 ± 2.1 nm ($C_{NP} = 15$ wt%). This increase is caused by the incorporation of magnetic NPs, since an identical film preparation method is used. This increasing trend can be divided into two stages. With $C_{NP} < 7$ wt%, a pronounced increase is observed (shown as stage I in Figure 8.1), whereas at $C_{NP} > 7$ wt%, the film thickness remains almost constant (stage II in Figure 8.1). Such tendency results from different localization behavior of the NPs at different concentrations [88]. In stage I (low C_{NP}), the NPs are swollen by DBC, leading to the expansion of individual polymer domains and consequently the entire film. In stage II (high C_{NP}), the PS domains are saturated with NPs, and NP aggregates are found being distributed randomly on the film surface.

8.2 Surface structure

The nanostructure of the hybrid film surfaces is probed with SEM. Figure 8.2 shows the SEM images with distinct features at the corresponding NP concentrations. For the NP-free film (Figure 8.2a), a morphology with cylinders parallel to the substrate surface is observed, which matches the assumption based on the volume fraction of the PMMA block ($f_{PMMA} = 0.315$). The brighter parts correspond to the PS blocks, and the darker parts show the PMMA blocks (also see Figure 8.3). The SEM image shows that the PMMA cylinders form the classical fingerprint-like morphology, which is commonly achieved in case of having a limited degree of order [35,159,160]. As discussed above, the thickness of the pure DBC film ($d_m = 35.5 \pm 1.7$ nm) is quite similar to the theoretically calculated periodic interdomain spacing ($D = 38$ nm). The relevance of the film thickness with respect to the film morphology was reported for such a confinement situation [34,160,161]. For thicker films ($d_m > D$), a parallel oriented cylinder morphology can be achieved, because of the surface boundary conditions. For thinner films ($d_m < D$), a perpendicular orientation is expected in order to maximize the polymer chains' conformational entropy [34,160]. In the present work, a parallel orientation is observed for the pure film with the thickness slightly smaller than the characteristic periodicity. This behavior can result from the SVA post-treatment, in which a PMMA-favorable solvent (acetone) has been used. According to the literature, the interaction parameters between polymer and solvent ($\chi_{solvent-polymer}$) are $\chi_{acetone-PMMA} = 0.29$, $\chi_{acetone-PS} = 1.1$, $\chi_{THF-PMMA} = 0.88$, and $\chi_{THF-PS} = 0.34$ [157]. Therefore, acetone is a selective solvent to the PMMA block, and THF is more neutral to both blocks. When the DBC films are placed in such mixed solvent vapor, the PMMA chains will stretch to maximize their exposed volume. Meanwhile, the strong attraction of the native SiOx layer on the substrate to the PMMA chains will also prevent the formation of a perpendicularly oriented morphology [162].

After incorporation of a low concentration of NPs (0.5 wt%, Figure 8.2b), the SEM contrast of the whole system is enhanced. Also several small white dots are found being located preferentially on the brighter PS domains on the film surface (also see Figure 8.4). These dots are NP agglomerates, which evidence the affinity of the NPs to the PS domains. To follow the evolution of structural order, two-dimensional fast Fourier transform (2D-FFT) patterns are extracted from the SEM images. Compared with the pure DBC film, in case of the hybrid film a second-order ring appears in the FFT pattern (0.5 wt%, shown as the white arrow in Figure 8.2b). This finding reveals an enhanced degree of order upon NP loading, which results from the more stretched polymer chains after NPs incorporation [155,163]. However, incorporation of NPs has no influence on the general film morphology as compared with our previous investigation, in which the entire morphology turns from

a parallel orientation into a perpendicular orientation after addition of small amounts of NPs [18]. This suggests that the influence of the selective acetone vapor dominates the structure orientation over the impact of the NPs during the films' fabrication in the present work. Therefore, a cylindrical nanostructure with parallel orientation is also found with NPs.

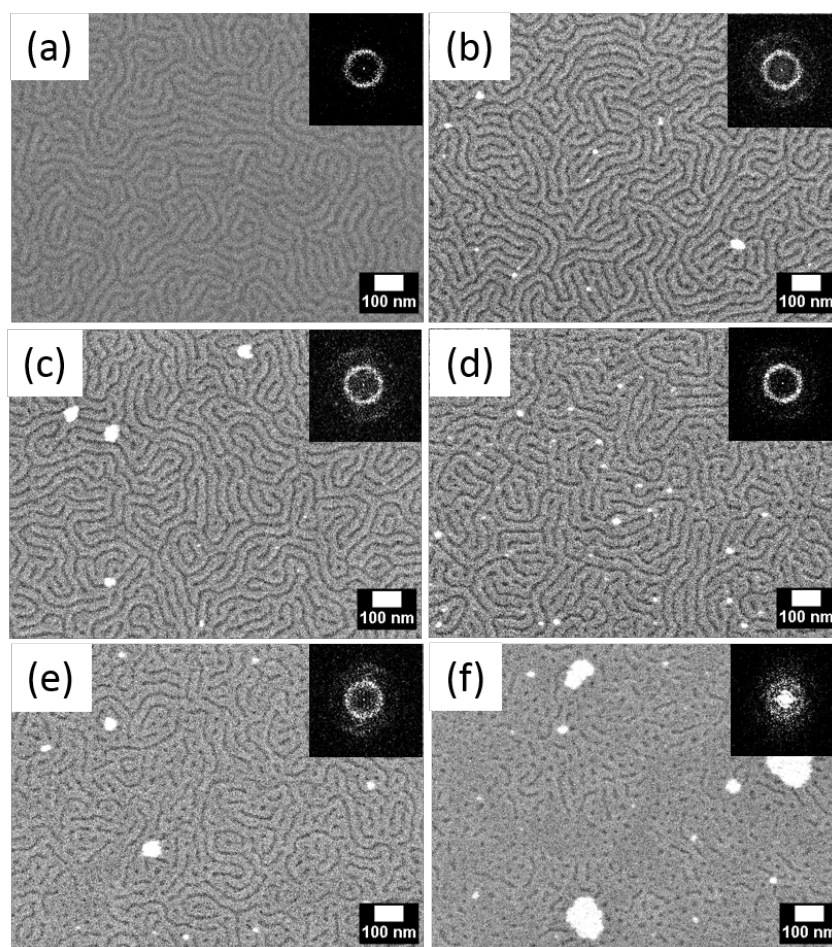


Figure 8.2: SEM images of films with different NP concentrations: (a) 0, (b) 0.5, (c) 1, (d) 3, (e) 7, (f) 15 wt%. The top right insets are the corresponding 2D FFT patterns. (Reprinted with permission from [151] Copyright 2019 American Chemical Society.)

Further increasing the NP concentration (1 wt%) leads to a sharper second-order ring in the corresponding FFT pattern, showing that an even higher order is achieved. When the concentration reaches 3 wt%, the number of NP agglomerates increases together with a slight change of the morphology. The initially continuous PMMA phase (darker part) partially changes into isolated islands (small darker dots), which results from a possible morphology transition of the DBC film. This means that the morphology is perturbed at 3 wt% NPs, although well-ordered as suggested by the second-order ring in the FFT

image. Moreover, it can be understood as an indication that the PS domains are saturated with NPs at 1 wt% and higher loading starts to perturb the DBC morphology. From 7 wt% on, the formation of larger NP clusters on the film surface and the presence of darker dots (PMMA domains) reveals the further alteration of the film morphology.

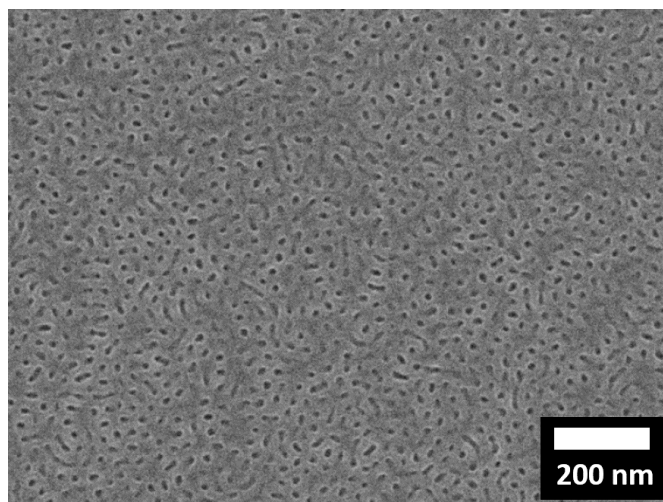


Figure 8.3: SEM of the pure PS-b-PMMA film with the thickness of 50 nm. The film was strong etched for 30 s before the SEM measurement. (Reprinted with permission from [151] Copyright 2019 American Chemical Society.)

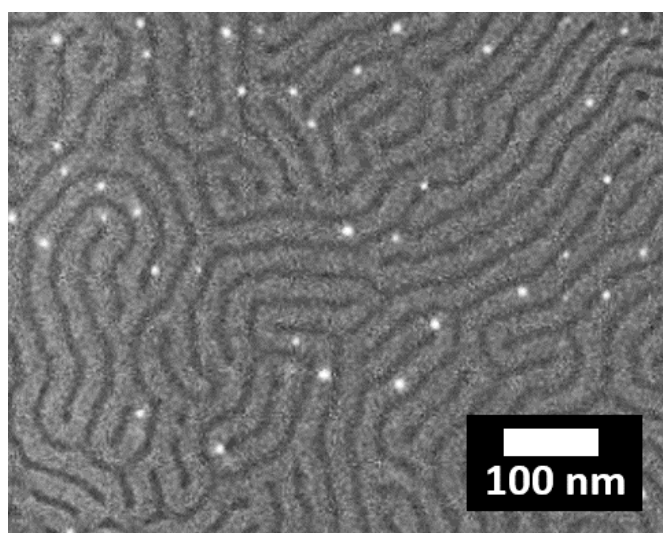


Figure 8.4: SEM of the PS-b-PMMA film with 3 wt% NPs at higher magnification. The preference of NPs to the brighter PS domains is evidenced. (Reprinted with permission from [151] Copyright 2019 American Chemical Society.)

Additionally, the decay of the 2D-FFT second-order ring demonstrates the loss of order. At the highest probed concentration (15 wt%), no continuous ordered PMMA phases are

observed on the film surface. Moreover, only large NP clusters are found on the film surface. This differs from our previous investigation on NP-DBC hybrid films, where large areas of the film surface were covered by a layer of NPs [19,87]. The possible reason may lie in the NP-hosting domains. In our previous study, the NPs were located in the minority domains, which had small volume fractions. In the present work, however, the hosting domain is the majority PS matrix, which offers a larger capacity for accommodating the NPs. Therefore, more NPs can be dispersed inside the films instead of dwelling on the film surfaces, indicating the possibility to achieve dense magnetic structures for the presently probed thin hybrid films.

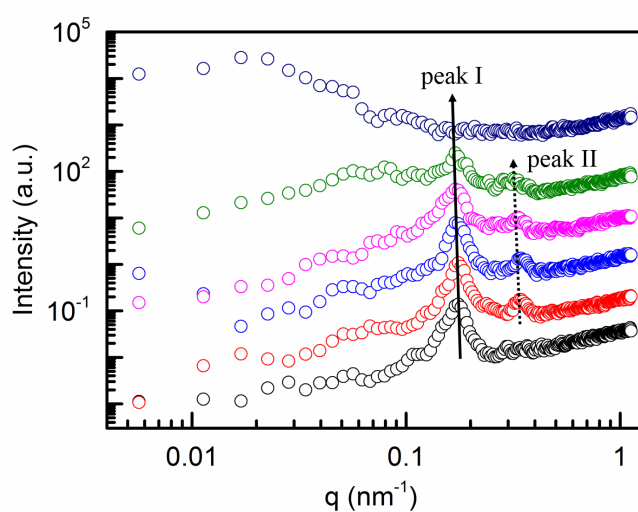


Figure 8.5: Power spectral density (PSD) profiles obtained from the FFT patterns of the SEM graphs at different NP concentrations: 0, 0.5, 1, 3, 7, and 15 wt% (from bottom to top). Peak I originates from the lateral structure of the DBC microphase separation structure and peak II is the related second order peak. All curves are shifted along y axis for better comparison. (Reprinted with permission from [151] Copyright 2019 American Chemical Society.)

To quantify the degree of order of the surface structure, power spectral density (PSD) functions are calculated via an azimuthal integration of the intensity distribution of the 2D-FFT patterns. The extracted PSD profiles are plotted in Figure 8.5 with characteristic features being highlighted. Peak I originates from the microphase separation structure of the DBC. With increasing NP concentration, peak I initially gets slightly narrower and then broadens afterwards, which means that the order is initially enhanced by the addition of NPs before it decays. From the position of peak I, a periodic interdomain distance of around 36 nm is obtained for the bare DBC film (0 wt%). The slight shift of peak I to smaller q values represents an increase of the interdomain distance due to

the addition of NP. The second-order peak (peak II) follows the behavior and its position (ratio 1:2) underlines the lamellar-type order of the PMMA cylinders in the PS matrix in the fingerprint morphology. Peak II vanishes at the highest NP concentration due to a significantly reduced order.

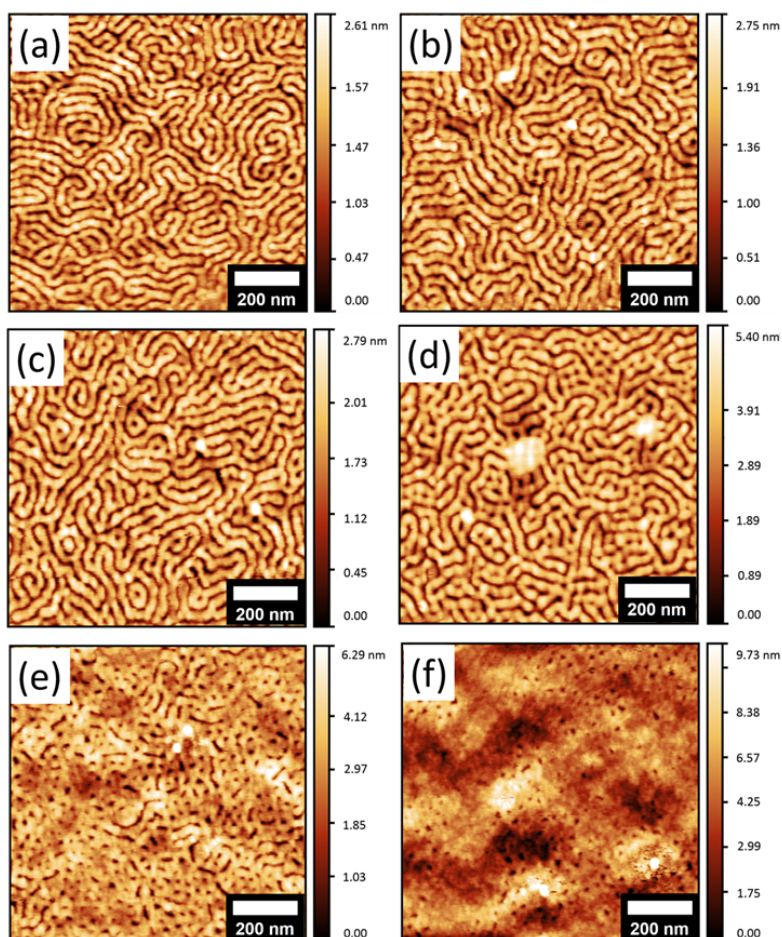


Figure 8.6: AFM height images of films containing different magnetic NP concentrations: (a) 0, (b) 0.5, (c) 1, (d) 3, (e) 7, and (f) 15 wt%. (Reprinted with permission from [151] Copyright 2019 American Chemical Society.)

To address the topographical information of the hybrid films, all the samples are probed with AFM via tapping mode. The AFM height graphs are displayed in Figure 8.6 with distinct characteristics at respective NP concentrations. Generally, all AFM images depict a similar surface morphology as observed from the SEM measurements. The image of the pure DBC film (Figure 8.6a) shows a parallel cylinder structure with a low local average height of 2.6 nm. Due to the different heights, the two polymer domains present as different colors (darker part shows PMMA block, and brighter part PS block) in the

image. Correlating the morphology to the SEM observation and regarding the PS volume fraction, the brighter part shows the PS block, and the darker part PMMA block.

After incorporating NPs into the films, the PS domains become even brighter, resulting from the height increase after swelling with NPs. With increasing NP concentration, the NP aggregates appear and increase in size, and the polymer nanostructure evolves following the same fashion as observed in the SEM images and described there. At the highest concentration, an ill-defined surface morphology forms, with the local average height increasing to 9.7 nm. Based on the NP diameter of 10 nm, one could speculate that part of the NPs aggregates are also buried inside the polymer matrix at the highest probed NP concentration. Similar observations were also found in our previous investigations [19, 87]. The root mean square roughness (R_{rms}) of all films is calculated from the AFM data. For the pure DBC film, a local R_{rms} of around 0.19 nm is found. As concentration increases, R_{rms} increases but still stays below 1.5 nm, which suggests that flat hybrid films can be prepared from the used printing technique. The roughness of all studied films are detailed in Figure 8.7.

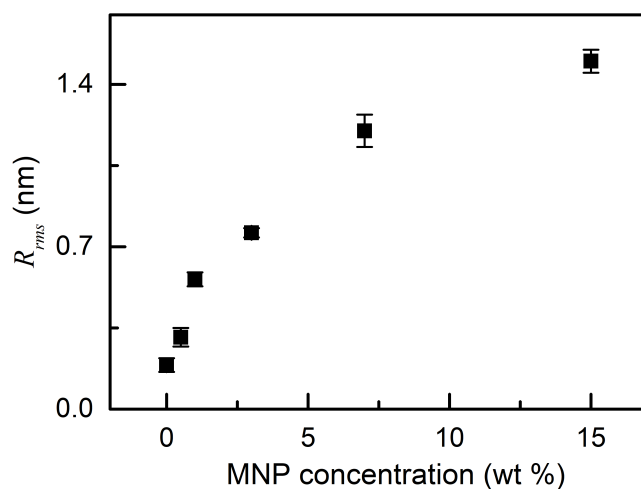


Figure 8.7: The root mean square roughness (R_{rms}) as a function of NP concentration. The R_{rms} is obtained using the software Gwyddion. Five random areas are chosen for roughness calculation in each image, and the average value is taken as the final roughness. (Reprinted with permission from [151] Copyright 2019 American Chemical Society.)

8.3 Inner structure

From AFM and SEM measurements, only the surface morphology can be probed, which is not sufficient to address the influence of NPs overall. In particular, the dispersion of NPs inside the hosting polymer matrix cannot be determined. To access the films' inner structure, grazing incidence small angle X-ray scattering (GISAXS) is performed. With GISAXS, the averaged structure information, such as structure sizes and size distributions, averaged over the illuminated thin film volume can be obtained.

8.3.1 Lateral nanostructure

The 2D GISAXS data are displayed in Figure 8.8. Distinct features can be clearly observed at different NP concentrations. To protect the detector from being saturated, a circular beamstop has been placed at the specular peak position in front of the detector. The incidence angle is chosen as 0.35° , so that the material characteristic Yoneda peaks can be well separated from specular peak.

From the q_y direction, information concerning lateral structure can be achieved. For the NP-free DBC film, a prominent rod-like pseudo-Bragg peak (at $q_y = 0.175 \text{ nm}^{-1}$, shown as the white arrow in Figure 8.8a) is seen together with a second-order peak (at $q_y = 0.317 \text{ nm}^{-1}$, shown as the yellow arrow in Figure 8.8a) having lower scattering intensity. The pseudo-Bragg peak results from the electron density contrast difference between the PMMA and PS blocks and the protrusions. The existence of the second-order peak shows that well-ordered structures seen at the film surface are also present inside the thin film. With low concentration NP incorporation (0.5 wt%), the intensity of both first- and second-order peaks is remarkably enhanced, which can be explained via the improved scattering contrast due to the localization of NPs inside the PS domains. Interestingly, a third-order peak (indicated by the orange arrow in Figure 8.8b), which is weak but still visible, appears at the position of a higher q_y value (at $q_y = 0.469 \text{ nm}^{-1}$). This suggests that an improved structural order is obtained inside the hybrid films after loading with NPs. Similar scattering features are also observed for films with a NP concentration of 1 wt% and 3 wt%. At 7 wt% NPs, the second- and third-order peaks vanish, and the intensity of the Bragg peak decreases. It almost disappears at 15 wt% NPs. This absence of side peaks at high NP concentrations reveals a loss in order inside the hybrid films.

To get more details from the scattering data, horizontal line cuts are made at the Yoneda peak position of the DBC in the 2D GISAXS data. All cuts are plotted in Figure 8.9a together with the corresponding fits, from which lateral structure information can be obtained. Figure 8.9a depicts the peaks marked with I, II and III as indicated by arrows.

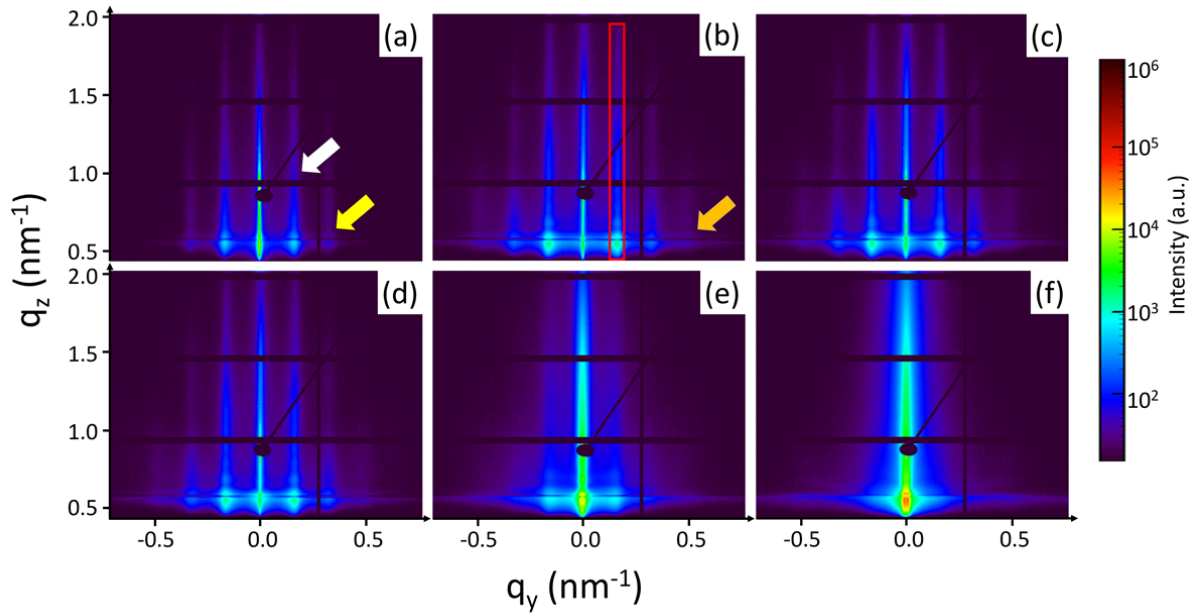


Figure 8.8: 2D GISAXS data of films with different NP concentrations: (a) 0, (b) 0.5, (c) 1, (d) 3, (e) 7 and (f) 15 wt%. All intensity patterns are displayed in logarithmic scale with the same intensity scale. The black horizontal and vertical lines are the gaps between modules of the detector. Arrows with different colors indicate the peaks caused by the structure: first-order (white), second-order (yellow) and third-order (orange). The red box in figure b shows the area where the off-detector cuts are extracted. (Reprinted with permission from [151] Copyright 2019 American Chemical Society.)

The line cuts are fitted using a model including form and structure factors, both of which are assumed to exhibit a Lorentzian size distribution. Peak II with the strongest intensity represents the first-order Bragg peak, and originates from the highly ordered microphase-separation structures of the DBC. For the data of the pure DBC film, a cylinder form factor is applied for the fitting. From the modeling, the position of the strong first-order peak (Peak II) and weaker second-order peak (indicated by the green dashed arrow) are obtained as $q_y = 0.175 \text{ nm}^{-1}$ and $q_y = 0.317 \text{ nm}^{-1}$. The ratio of the q_y values is 0.552 (close to $1/\sqrt{3}$), which matches with the cylinder geometry assumption. An interdomain distance of $34.9 \pm 0.3 \text{ nm}$ is obtained for the inner film structure, which deviates slightly from the value of the surface structure as probed with SEM ($\sim 36 \text{ nm}$). Thus, inner film structure and surface structure of the DBC film might not be fully identical, yet rather closely match.

Adding a small amount of NPs into the system contributes to a slightly sharper peak II and a remarkable intensity enhancement of the second-order peak (indicated by the dashed green arrow). Moreover, a distinguishable third-order peak (shown as dashed red

arrow) appears at $q_y = 0.469 \text{ nm}^{-1}$, which cannot be seen in the data of the NP-free DBC film. These features demonstrate that moderate NP loading helps to improve the order of the hybrid system and enhances contrast due to addition of NPs to the PS domains.

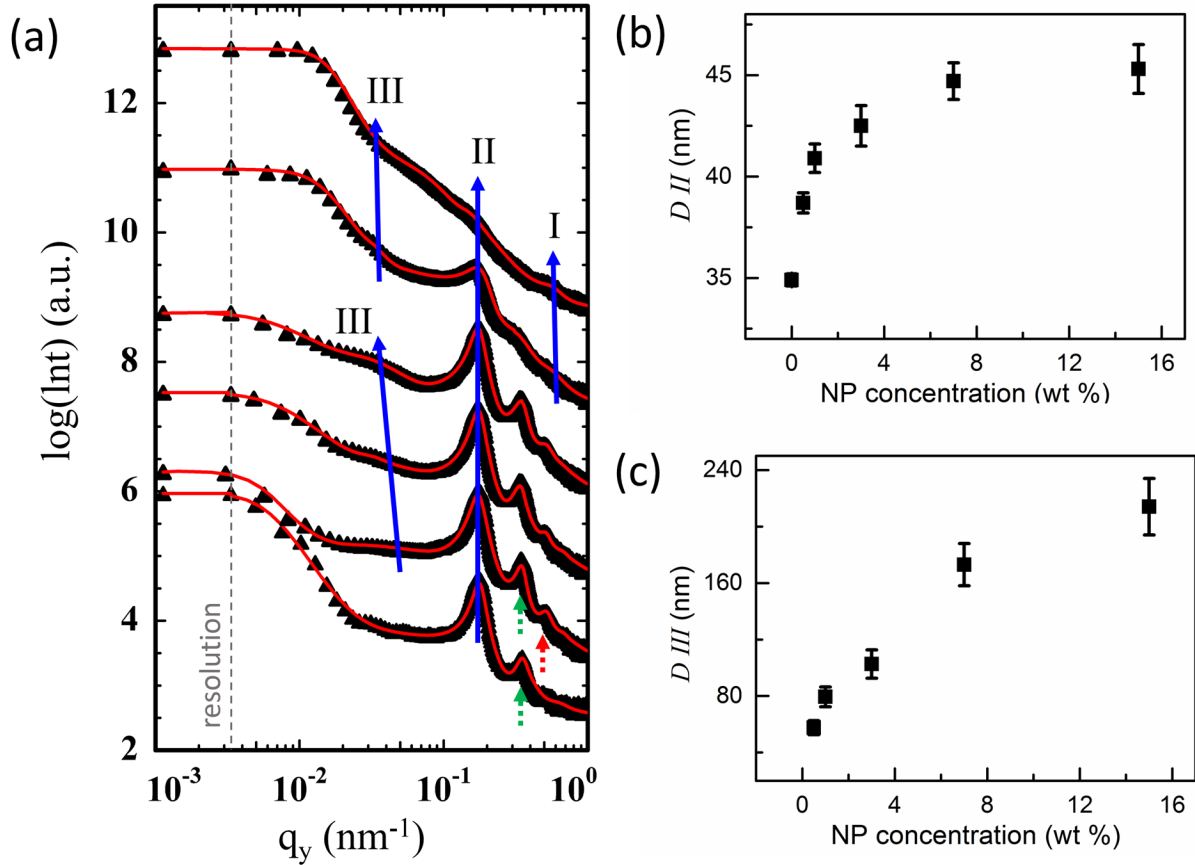


Figure 8.9: (a) Horizontal line cuts (black symbols) with the corresponding fits (red solid lines) of the films with different NP concentrations. From bottom to top: 0, 0.5, 1, 3, 7 and 15 wt%. All curves are shifted along the y axis for clarity. Featured peaks are indicated as: peak I (contribution of single NPs), peak II (DBC structure), and peak III (contribution of NP clusters). The green and red dashed arrows present at the bottom part show the second- and third-order peak, respectively. The interdomain distance (D_{II}) (b) and inter-NP-aggregate distance D_{III} (c) are extracted from the fitting and plotted versus NP concentration. (Reprinted with permission from [151] Copyright 2019 American Chemical Society.)

To quantify the contribution of loading NPs to the structural order improvement and contrast enhancement, the intensity increment of both peaks (first- and second-order peaks) compared with those from the NP-free film is studied. The results displayed in Figure 8.10 show that the intensity increase of the second-order peak is much higher than

that of the first-order peak irrespective of NP concentration. This suggests that loading NPs contributes more to the structural order than to the contrast enhancement. The position of peak II gradually shifts to lower q_y values with increasing NPs, due to an increase of the interdomain distance (D_{II}) in the lateral direction. Similar scattering features can also be found for the other samples with concentrations below 7 wt%. Additionally, another broad and weak peak (peak III) is observed in the lower q_y region for the NP-DBC hybrid films. This peak is attributed to the center-to-center spacing of NP aggregates (D_{III}). The concentration increase results in the formation of large NP aggregates with increasing spacing. Thus, a gradual shift of peak III to smaller q_y values is observed. At higher NP concentrations (7 wt% and 15 wt%), both peaks II and III become broader and weaker, and the second- and third-order peaks start to vanish. This is due to the fact that the order inside the films also decreases, which is observable by GISAXS. Since NPs are preferentially dispersed inside the PS blocks, extremely high loading of NPs leads to an excessive expansion of the PS domains, ending up with a perturbed and less-ordered inner structure. As seen already for the film surfaces with SEM and AFM also inside the films the well-ordered microphase separation structure is destroyed.

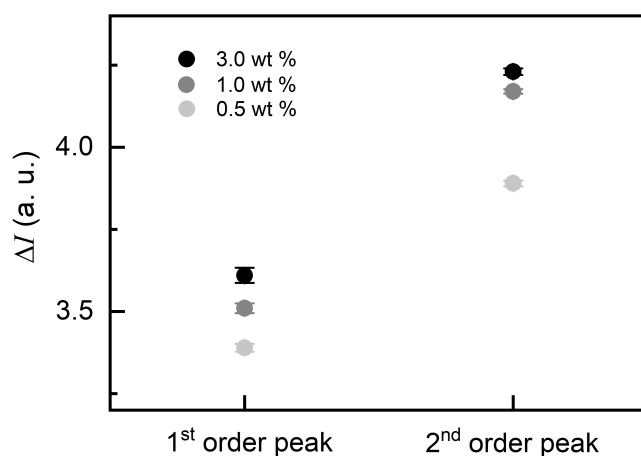


Figure 8.10: The intensity increment ΔI of the structure peaks (the first- and second-order peaks) at different NP concentrations. ΔI is calculated by $I_{\text{hybrid-}i} / I_{\text{pure-}i}$, where $I_{\text{hybrid-}i}$ and $I_{\text{pure-}i}$ are the intensity of the peak in the hybrid and pure film, respectively. $i = 1, 2$ shows the peak order. (Reprinted with permission from [151] Copyright 2019 American Chemical Society.)

Moreover, a further peak (peak I) arises with intensity getting stronger as the NP concentration increases. The position of peak I shows no dependence on the NP concentration, and a center-to-center distance of (10.0 ± 0.6) nm is extracted from the modeling,

which matches the diameter of the NPs. Combined with the observations in AFM and SEM data, in which large NP aggregates are present on the film surfaces at high NP concentrations, we can explain peak I as structure factor of the closely packed NPs. Similar phenomenon was also observed in previous investigations on NP containing hybrid films [19, 87].

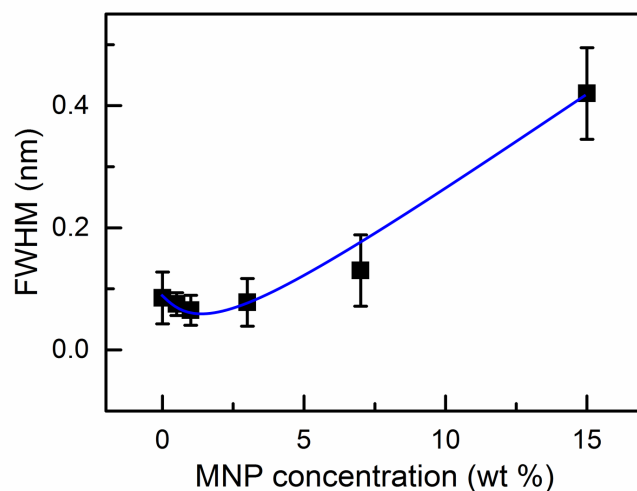


Figure 8.11: Full width at half maximum (FWHM) values extracted from the fitting are plotted as a function of the NP concentration. The solid line serves as a guide to eyes. (Reprinted with permission from [151] Copyright 2019 American Chemical Society.)

Values of D_{II} and D_{III} are extracted from the fitting and plotted as a function of NP concentration in Figure 8.8b and 8.8c. The inter-aggregate spacing D_{III} increases from (58 ± 5) nm to (214 ± 20) nm with a broad distribution, suggesting a random NP aggregate distribution having increasing distances by adding more NPs to the systems. Interestingly, the interdomain spacing D_{II} displays a similar trend as observed in the film thickness. It increases strongly with slight loading of NPs, but stays almost constant at high NP loading. Such behavior can be explained by a different localization of the NPs at different concentrations. At lower concentrations, the NPs selectively disperse well inside the PS domains, resulting in a domain expansion. At high concentrations, the PS domains are saturated, and most of the excess NPs assemble in aggregates on the film surface. A sort of overloading with NPs causes the formation of ill-defined structures inside the films. Since adding NPs can improve the order of the hybrid films to some extent, it is interesting to determine the concentration, at which the highest order is achieved. Accordingly, the values of full width at half maximum of peak II are plotted in Figure 8.11 as a function of NP concentration. A minimum value is reached between 1 and 3 wt%, showing the optimal concentration from the present experiment. Referring to the observations from

the SEM and AFM data, the PS domains are supposed to be saturated with NPs of 1 wt%. Further loading with NP causes formation of NP aggregates.

8.3.2 Vertical nanostructure

To investigate how the vertical (with respect to the substrate) nanostructure is influenced by the incorporation of NPs, off-detector cuts are made at the position of the microphase-separation structure ($q_y = 0.18 \text{ nm}^{-1}$, shown as the red box in Figure 8.8b). To visualize the structure information, the off-detector cuts are only shown in the most interesting q_z range ($0.4 \text{ nm}^{-1} - 0.9 \text{ nm}^{-1}$) in Figure 8.12a.

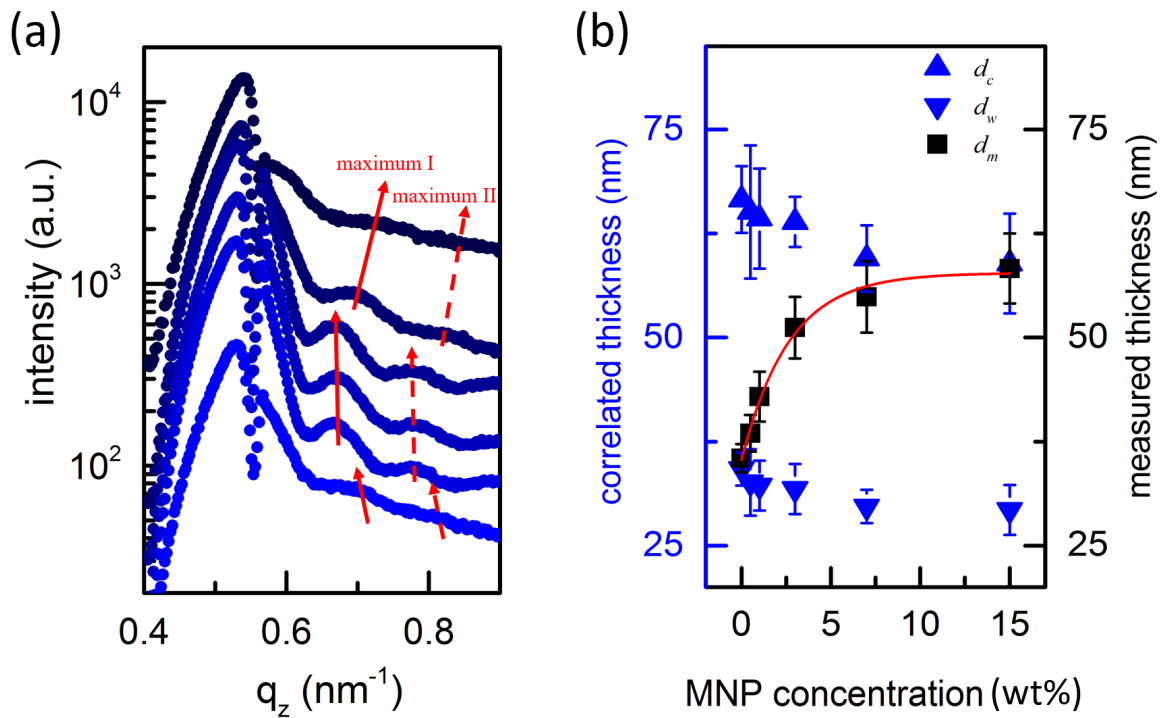


Figure 8.12: Off-detector cuts of 2D GISAXS data at $q_y = 0.18 \text{ nm}^{-1}$. The cuts are only shown in the most interesting q_z range, and shifted along the vertical direction for clarity with increasing NP concentration (from bottom to top: 0 wt%, 0.5 wt%, 1 wt%, 3 wt%, 7 wt% and 15 wt%). Intensity maxima are highlighted as maximum I and II and marked by the solid and dashed red arrows, respectively. (b) Correlated thickness extracted from the intensity modulation d_c based on the Bragg equation (blue up-triangles) and d_w (blue down-triangles) based on the modified Bragg equation for waveguides, respectively. The measured thickness d_m (black squares) is shown for comparison. The red line is plotted as guide to the eyes. (Reprinted with permission from [151] Copyright 2019 American Chemical Society.)

In the off-detector cuts intensity modulations are seen (marked as maximum I and II in Figure 8.12a), which result from resonant diffuse scattering due to a special case of interface correlation [164]. While in the NP-free DBC film the intensity modulation is weak, a slight addition of NP (< 7 wt%) makes the intensity modulation more pronounced, suggesting the presence of an enhanced long-range interface correlation in these NP-DBC hybrid films. Further incorporation of NPs smoothens the intensity oscillation gradually, which results from a rougher film surface with the presence of large-sized NP clusters being uncorrelated. Based on the distance of the adjacent peak positions (maximum I and II shown in Figure 8.12a), the correlated thickness, meaning the long-range correlation length in the vertical direction, can be calculated. Literature showed that both, simple roughness correlation and waveguide-like behavior can occur in nanocomposite thin films [164]. In case of simple roughness correlation, where the resonant diffuse scattering is caused by the coherence of the diffusely scattering intensity, the correlated thickness d_c can be determined from an one-dimensional Bragg equation [165]

$$d_c \approx \frac{2\pi}{\Delta q_z} \quad (8.2)$$

In case of waveguide-like behavior, where the interference fringes result from the refraction of the incident waves, the correlated thickness d_w can be calculated via the modified Bragg equation [164, 166]

$$d_w \approx \frac{\pi}{\Delta q_z} \quad (8.3)$$

Figure 8.12b shows the correlated thickness calculated with the two different equations as mentioned above. The d_c for the pure film is ~ 68 nm, while the d_w is ~ 34 nm. Since the thickness of the pure film is determined as (35.5 ± 1.7) nm by profilometry, a correlated interface distance of 68 nm is not possible. Consequently, the simple roughness correlation can be excluded, and the waveguide effect needs to be considered in the thin pure DBC film. This reveals that the thin pure DBC film seems to act as a waveguide in the X-ray scattering measurement. In other words, the incident X-ray wave can be guided to the detector through the film body constrained by the top surface and the substrate. At low NP concentrations (< 7 wt%), neither of the two correlated thickness values (d_c , d_w) matches the measured film thickness (d_m). Therefore, no simple explanation can be used for clarification. Interestingly, at high concentrations (7 wt% and 15 wt%), the correlated thickness (d_c) matches well with the measured film thickness (d_m), resulting from the swelling of films caused by NP incorporation. This suggests that a simple roughness correlation is present for the hybrid films with high NP loading.

8.4 Magnetic properties

The magnetic properties of the thin magnetic films are probed with a superconducting quantum interference device (SQUID). The magnetization as a function of the external magnetic field is collected at different temperatures ranging from 2 K to 200 K. To detail the magnetic properties, the influence of temperature and NP concentrations are addressed.

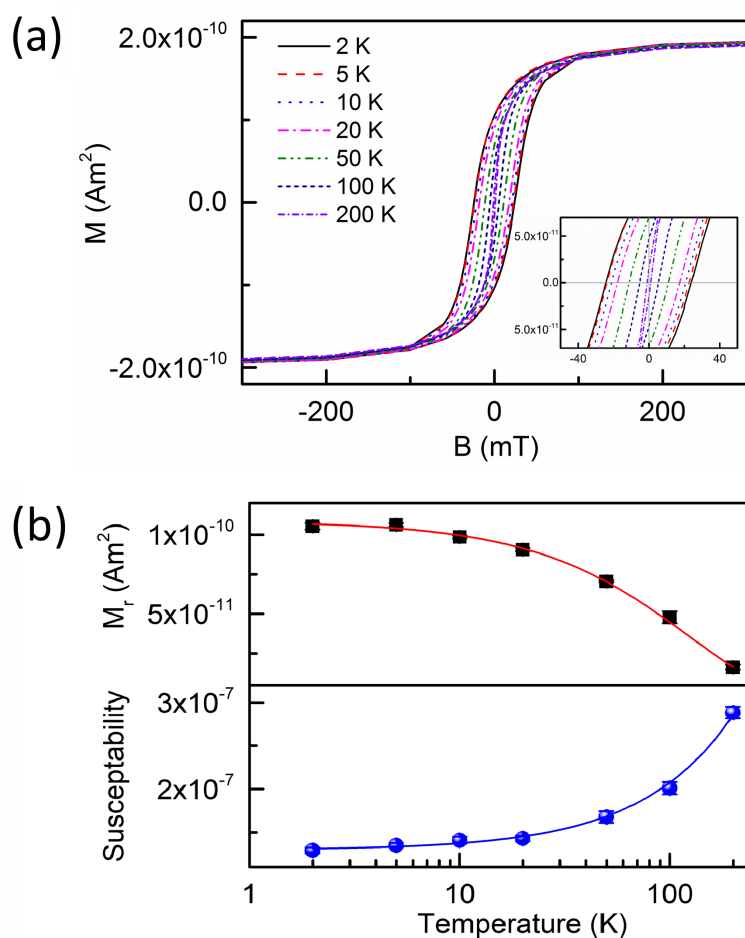


Figure 8.13: (a) Magnetization (M) curves obtained at various temperatures. (b) Remanence (M_r) and magnetic susceptibility (χ) obtained from corresponding magnetization data are plotted versus temperature. The magnetic susceptibility (χ) is calculated by applying a linear fit at the zero-remanence position. The data come from the film with 1 wt% NPs. All red solid lines are guides to the eyes. (Reprinted with permission from [151] Copyright 2019 American Chemical Society.)

8.4.1 Influence of temperature

Figure 8.13 displays the magnetization curves measured at different temperatures for the film with 1 wt% NPs. Figure 8.13 a shows a hysteresis loop at low temperature, which narrows down as temperature increases. Such observation evidences superparamagnetic behavior of the hybrid films [167].

To gain a quantitative analysis of the magnetic data, values of susceptibility (χ) and magnetic remanence (M_r) are obtained from the corresponding magnetization curves at different temperatures. Figure 8.13 shows that the magnetic susceptibility and remanence exhibit different temperature dependences. As temperature increases, remanence initially decays smoothly then rapidly afterwards. In contrary, the susceptibility displays an increasing tendency, which gets stronger at higher temperatures as compared to the behavior at lower temperatures. This suggests that the responsive behavior of the hybrid film differs at different temperatures. It tends to give a faster response to an external magnetic field when it is placed at higher temperature.

In order to study the blocking temperature, the coercivity values are extracted from corresponding magnetization curves at various temperatures, and fitted with the model shown in Chapter 5. Figure 8.14 shows the modeling results. A blocking temperature of 121.6 ± 29.5 K is obtained, which matches our previous study, where identical magnetic NPs were investigated [121].

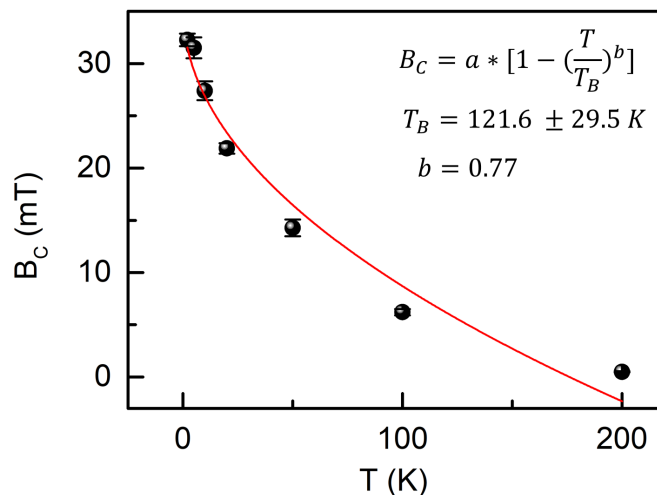


Figure 8.14: Coercive field (B_c) obtained from corresponding magnetization profiles is plotted versus temperature. The red line is the fitting result by using the model displayed at the top right. (Reprinted with permission from [151] Copyright 2019 American Chemical Society.)

8.4.2 Influence of NP concentration

To study the relationship between magnetic properties and NP concentration, magnetization data of films with different NP concentrations are compared in Figure 8.15a.

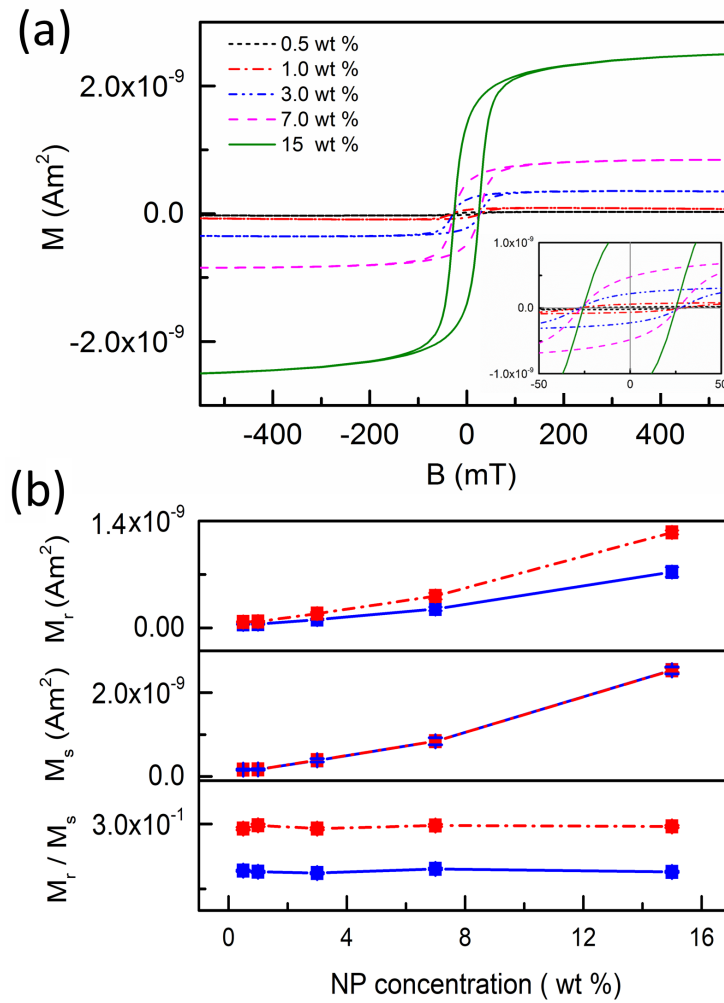


Figure 8.15: (a) Magnetization of hybrid films containing different amounts of NPs. Data are obtained at 2 K. (b) Remanence (M_r), saturation magnetization (M_s) and relative remanence (M_r / M_s) extracted from corresponding magnetization curves and plotted as a function of NP concentration. The red and blue symbols are data obtained at 2 K and 20 K, respectively. Lines serve as guides to eyes. (Reprinted with permission from [151] Copyright 2019 American Chemical Society.)

This set of magnetization curves is obtained at 2 K. For all curves, magnetic hysteresis loops can be clearly observed due to the low probing temperature ($T < T_B$). The blocked

magnetic moments can not flip spontaneously with the alteration of external magnetic field, ending up with magnetic hysteresis present in the profiles.

For a detailed analysis, values of remanence (M_r), saturation magnetization (M_s) and relative remanence (M_r / M_s) derived from corresponding magnetization curves are plotted as a function of NP concentration in Figure 8.15 b. Two set of data achieved at 2 K (red symbols) and 20 K (blue symbols) are compared to clarify the temperature influence. The result shows that both remanence and saturation magnetization exhibit similar concentration-dependent behavior. They increase as NP concentration increases, which is due to the increased contribution from more magnetic moments at high concentrations. Compared with the data measured at 2 K, smaller magnetic remanence is obtained at 20 K for identical hybrid films. Such phenomenon is caused by more thermal energy given to NP by higher temperature. Since the identical film (at each NP concentration) is measured at both temperatures, the same saturation magnetization is achieved. The relative remanence, which represents the data normalized to NP concentration, reveals the absence of NP interactions in the hybrid systems.

8.4.3 Influence of magnetic structure density

To address the benefit of the high magnetic structure density, a comparison of the magnetic susceptibility is made between the present thin film and the thicker films (~ 170 nm) studied in our previous work [121]. Identical magnetite NPs were used in the previous investigation, but the NPs were dispersed inside the minor domains (volume fraction: 0.34). It is worthy to note that the minor domains were saturated with NPs at 2 wt% and maintained a high structural order [121]. Therefore, it is meaningful to compare the two highly ordered NP-saturated films, namely the thin film containing 1 wt% of NPs in the present study and the thick film with 2 wt% of NPs in previous study. The susceptibility (normalized to the film thickness and the NP weight ratio) of the two films obtained at different temperatures are summarized in Figure 11. At low temperatures, similar values are found for both films, since most of the magnetic moments are frozen below the blocking temperature. As temperature increases, a faster response to the external magnetic field is observed in the thin film than the thicker one. At higher temperatures, the magnetic moments are unblocked and can flip freely. At the same time, the dense magnetic structure contributes more free moments. Therefore, the normalized number of free magnetic moments in the thin film is larger than that in the thick one at high temperatures, which explains the faster responsive behavior.

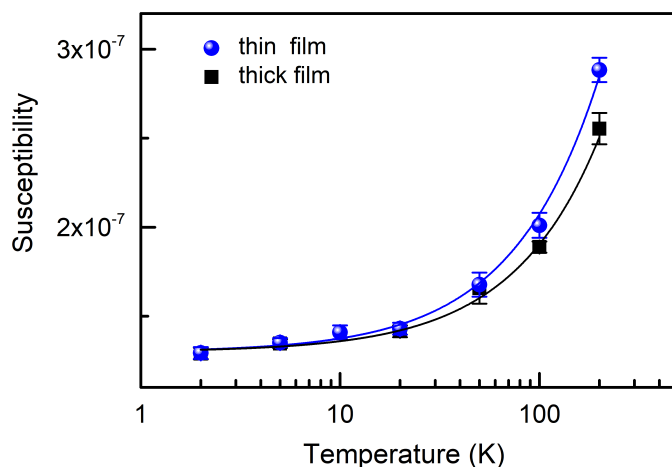


Figure 8.16: Comparison between the magnetic susceptibility of two different films. Blue circles: thin film with 1 wt% of NPs (present work) [151]. Black rectangles: thick film with 2 wt% of MNPs (previous work) [121]. The data are normalized to the NP weight ratio and the film thickness. Two solid lines are used to guide the eyes. (Reprinted with permission from [151] Copyright 2019 American Chemical Society.)

8.5 Summary

In this work, thin films with dense magnetic structures are successfully fabricated using a printing technique. By using the DBC PS-*b*-PMMA with a large PS volume fraction (0.685), a cylindrically structured template is achieved. Through solvent vapor annealing, a parallel alignment of the PMMA cylinders in the PS matrix is obtained (with respect to the substrate). Since the used magnetic NPs are selective to the PS domains, the fabricated PS-dominated template offers a high capacity to host NPs. The surface nanostructure is examined by the real-space techniques AFM and SEM as a function of the NP concentration. As a beneficial effect, upon slight NPs incorporation, the structural order is significantly enhanced. Further NP loading leads to the formation of large NP aggregates located on the film surface. The cylindrical structure is then perturbed and ends up in a disordered ill-defined morphology. The inner structure of thin films is probed with reciprocal-space technique GISAXS. Scattering data further proves the order improvement contributed by gentle NPs loading throughout the thin film. 1 wt% is found to be the critical concentration where the highest structural order is obtained in the hybrid film. From both real and reciprocal-space techniques, the PS domains are evidenced to be saturated with NPs at 1 wt% with only few aggregates present on the film surface. Therefore, a highly ordered thin film with dense magnetic structure capped by polymer materials is achieved. All hybrid films are studied with SQUID for magnetic

property investigation. Results show that all the NPs-DBC films exhibit a superparamagnetic behavior. Compared with our previous work, where identical NPs were used, the thin films show faster responsive behavior due to the high density of magnetic structure.

9 Conclusion and outlook

In the present thesis, the investigation is focused on three main topics: the up-scale fabrication technique to prepare magnetic anisotropic films, the kinetic process of NP-DBC film formation and the fabrication of hybrid films with dense magnetic nanostructures. Different NP-DBC systems are selected for different investigation topics. Printing, which can be potentially employed for large-scale production, proves to be an effective film fabrication technique. The film quality can be easily controlled via simply tuning the related printing parameters. By applying an external magnetic field during printing or solvent vapor annealing after printing to corresponding NP-DBC systems, hybrid films with magnetic anisotropy are successfully prepared. In addition, the film formation process is monitored *in situ* with advanced GISAXS technique. The scattering data shows that the presence of magnetic NPs accelerates the formation of an NP-DBC film compared to that of the NP-free film. Moreover, incorporation of magnetic NPs into the majority domain of a DBC system helps to the fabrication of dense magnetic nanostructures. Such magnetic films response to external magnetic field at an enhanced speed.

Lamellar-structured PS-*b*-PMMA as well as PS-coated maghemite NPs (γ -Fe₃O₄) are used for the printing experiment. The employed printer is made based on the working principle of a slot-die coating device. The film fabrication can be controlled by varying printing parameters like the printing speed, solution flow rate and concentration. Additionally, an external magnetic field is applied during the whole printing process to guide the alignment of the magnetic NPs. Through optical microscopy, wires are found in the printed hybrid films. The length and width of the wires changes with the NP concentration. AFM and SEM measurements show that these wires are composed of magnetic NPs. GISAXS data suggests that the external magnetic field also has an influence on the microphase-separated nanostructure of DBC. Above 1 wt% of NPs, the evolution of polymer domains differs in different orientations (parallel and perpendicular to the magnetic field direction). SQUID experiments prove that the printed films are magnetically anisotropic. When they are probed with NP wires parallel to the external magnetic field, a faster response behavior is observed compared to the other measuring orientation with NP wires perpendicular to the field.

Concerning the large scale production of magnetic anisotropic films, the application of an external magnetic field renders the fabrication process complicated. For the purpose of desirable simplification, a PS-*b*-PNIPAM with cylindrical morphology is employed to template the PS-selective magnetite NPs. To achieve cylinders with a suitable length, hybrid films are printed with a thickness (~ 200 nm) larger than the periodic domain distance (~ 32 nm). Then the printed films are shortly annealed in solvent vapor containing methanol and THF. Through solvent vapor annealing, on the one hand, perpendicular PS cylinders (with respect to the substrate) can be achieved due to the presence of PS-unfavored methanol in the solvent vapor. On the other hand, the polymer chains can reorganize themselves in the solvent vapor to form more ordered structures. Both real- and reciprocal space characterization show that the obtained films are highly ordered at low NP concentrations. It is found that, at 2 wt% of NP concentration, the PS cylinders are saturated with NPs, but are still aligned vertically with a high order on the substrate. SQUID results also show that the strongest magnetic anisotropy is observed at 2 wt%, which proves the successful fabrication of magnetically anisotropic films without applying any external magnetic fields.

To follow the hybrid film formation kinetics during fabrication, spray coating is chosen to deposit films composed of PS-*b*-PNIPAM and magnetite NPs. During the whole spray deposition, GISAXS is applied in an *in situ* mode to monitor the film evolution. To further clarify the influence of NPs on the film formation, a reference film without NPs is prepared following the identical spray protocol. The scattering data suggests small-sized polymer islands are formed at the initial spray stages, which merge to form larger ones and finally result in a complete film formation as the spray process proceeds. Compared to the reference of pure DBC film, the hybrid film exhibits a faster close film formation process. Due to the addition of magnetic NPs which improves the wetting behavior of the hybrid film, the merging process is sped up and a faster film formation is observed. Additionally, GISAXS illustrates that magnetic NPs aggregate into agglomerates with increasing size in the hybrid system as the spray process continues. In both reference and hybrid films, the respective nanostructures (nano-cylinders) formed through microphase separation stay stable and no changes in size are observed with spray time. Due to the expansion of PS domains caused by the preferential incorporation of magnetic NPs inside PS blocks, the obtained nano-cylinders in the hybrid film are slightly larger than those from the pure film.

In order to fabricate thin films with dense magnetic nanostructures, the DBC PS-*b*-PMMA with a large PS volume fraction (0.685) is employed. Through solvent vapor annealing, a cylindrically structured template, in which the PMMA cylinders orient parallel in the PS matrix with respect to the substrate, is achieved. Since the used magnetic

NPs are selective to the PS domains, the fabricated PS-dominated template offers a high capacity to host NPs. The real-space techniques (AFM and SEM) show that the structural order is significantly enhanced upon slight NPs incorporation. Further NP loading leads to the formation of large NP aggregates located on the film surface. The cylindrical structure is then perturbed and ends up in a disordered ill-defined morphology. The reciprocal-space technique GISAXS further proves the order improvement contributed by gentle NPs loading throughout the thin film. 1 wt% is found to be the critical concentration where the highest structural order is obtained in the hybrid film. From both real and reciprocal-space techniques, the PS domains are evidenced to be saturated with NPs at 1 wt% with only few aggregates present on the film surface. Therefore, a highly ordered thin film with dense magnetic structure capped by polymer materials is achieved. The SQUID results show that all the NPs-DBC films exhibit a superparamagnetic behavior. Compared with our previous work, where identical magnetic NPs were used, the thin films show faster responsive behavior due to the high density of magnetic structure.

Based on the results obtained in the present thesis, the investigation can be extended to several interesting aspects as follows. Firstly, as stated above, the external magnetic field applied during printing causes the anisotropy of both DBC nanostructure and magnetic structure, but the kinetics of anisotropic structure formation are still not clear. Hence, *in situ* GISAXS can be utilized to follow the structural evolution during printing. Secondly, it is already proven that the presence of magnetic NPs can accelerate the film formation. Therefore, it would be illuminating to systematically study the influence of the NP concentration on the film formation. Solutions with various NP concentrations could be used for spray coating, and the film deposition could then be monitored via *in situ* GISAXS technique. Thirdly, since post-treatment like thermal annealing or solvent vapor annealing can endow polymer chains with mobility, it would be attractive to apply an external magnetic field during the post-treatment to direct magnetic NPs into a better arrangement. Finally, concerning the thermol-responsive characteristics of PNIPAM polymer, it would also be interesting to probe the structural evolution of PS-*b*-PNIPAM with the change of humidity and temperature.

10 Appendix

Polarized neutron reflectivity investigation on PS-*b*-PNIPAM with embedded magnetic NPs

In chapter 7 and 8, we address the nanostructure and magnetic behavior of hybrid dry films consisting of magnetic NPs and the diblock copolymer (DBC) polystyrene-*block*-polyN-isopropylacrylamide (PS-*b*-PNIPAM). Results show selective incorporation of NPs into the PS domains and a morphological evolution from parallel cylinders to perpendicular ones at low NP concentrations. A superparamagnetic behavior is found irrespective of the NP concentration. Since PS-*b*-PNIPAM films are most interesting under wet conditions, we extend our investigation from dry films to wet ones in order to explore the swelling behavior of the hybrid films and its impact on the magnetic properties. For this purpose, neutron reflectivity (NR) is used to detect the morphology of hybrid films as a function of temperature in a humid atmosphere. In addition, polarized neutron reflectivity (PNR) is applied to probe the magnetic structure of the PS-*b*-PNIPAM films with maghemite NPs.

10.1 Materials and film fabrication

The employed DBC PS-*b*-PNIPAM is identical to the one used in chapter 7 and chapter 8. Maghemite NPs with the diameter of 10 nm are grafted with PS chains. More details regarding the magnetic NPs are described in Chapter 4 Section 4.1.2.

A 25 mg ml⁻¹ solution of PS-*b*-PNIPAM is prepared in 1,4-dioxane. To gain enough magnetic signal from NR, the concentration of magnetic NPs (weight ratio to DBC) is set to 20 wt%. Then spin-coating is used to establish the hybrid film on a silicon substrate with the size of 4 cm × 5 cm. The silicon substrate is pre-cleaned via a basic bath cleaning procedure (see details in Chapter 4, Section 4.2.2). Afterwards, the hybrid film is annealed in 1,4-dioxane vapor at room temperature for 7 min. A film thickness of 150 nm is obtained after the solvent annealing.

10.2 Chamber

In order to control the temperature and humidity of the experiment environment, a special chamber is fabricated with aluminum material. Figure 10.1 shows the interior and exterior view of the chamber. As seen from Figure 10.1a, the sample is standing vertically in the slit located on the chamber base, and fixed using two PTFE screws. On the chamber base (behind the sample), a reservoir is designed to store D_2O , so that a humidity can be established. In order to control the temperature of the chamber, a water cycling system (Julabo) is applied. To achieve a real-time monitoring on the temperature and relative humidity, a sensor (MHG 100, Proumid), which can be connected to computer via a cable, is used. During the whole measurement, the chip end of the cable is placed inside the chamber and the USB end is connected to a computer. The temperature and relative humidity are recorded via the software kit offered by the company.

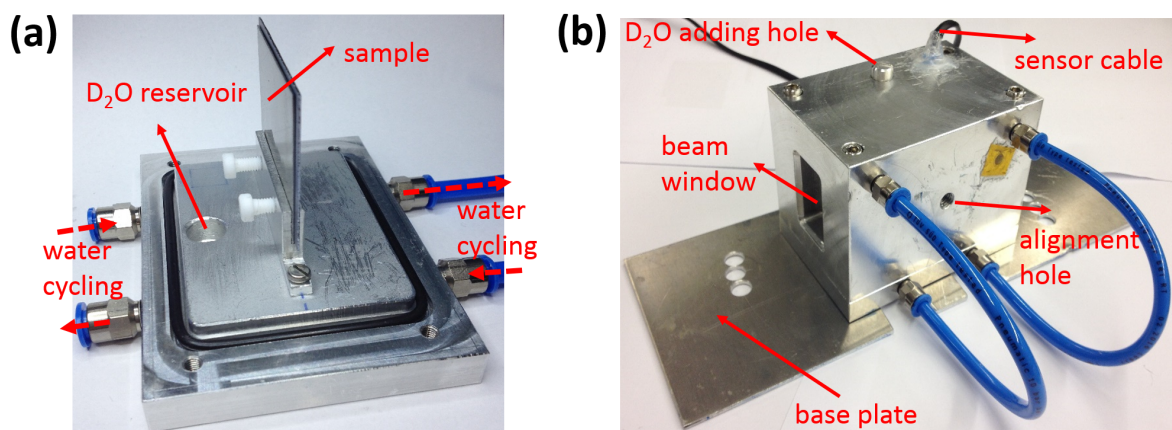


Figure 10.1: The temperature and humidity-control chamber used in the experiment. (a) interior view, (b) exterior view.

10.3 Polarized neutron reflectivity

The neutron reflectivity is performed at the instrument MARIA (Heinz Maier-Leibnitz Zentrum, Garching, Germany), which is schematically shown as Figure 10.2. During the measurement, the chamber is fixed on the hexapod sample table. For the polarized investigation, a magnetic field of 560 mT is applied using two controllable magnets shown in Figure 10.3a to magnetize the film.

To access the nanostructure of the film, a sample-to-detector distance is set as 2.4 m with the neutron beam size of 1.5 cm. The reflection of polarized neutron is used to detect the density, modulus and direction of the magnetization vector of the magnetic layer. To access a wide q_z range, two different wavelengths $\lambda = 10 \text{ \AA}$ and $\lambda = 5 \text{ \AA}$ are used to collect data from the low q range ($0.2 - 2 \text{ \AA}^{-1}$) and high q range ($0.8 - 3.5 \text{ \AA}^{-1}$), respectively.

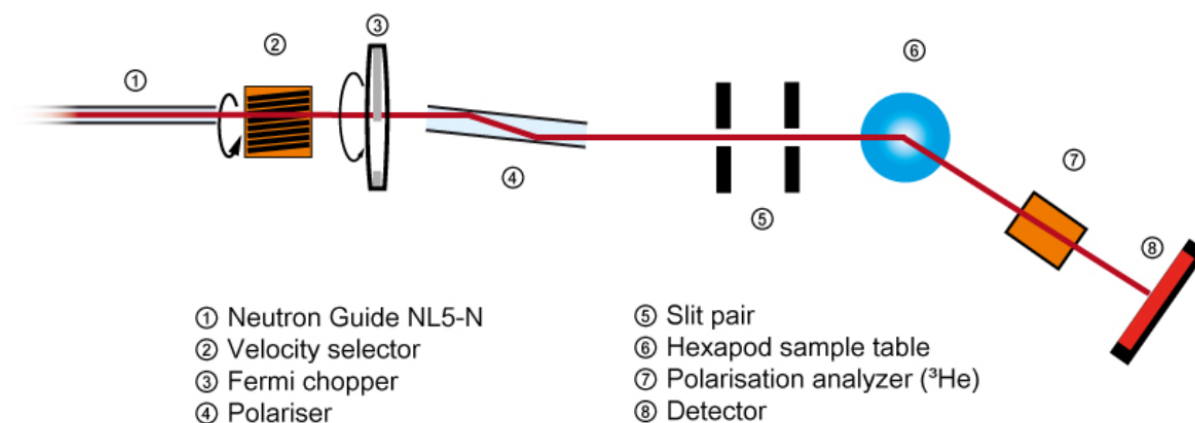


Figure 10.2: The schematic drawing of MARIA beamline. The figure is adapted from [168]

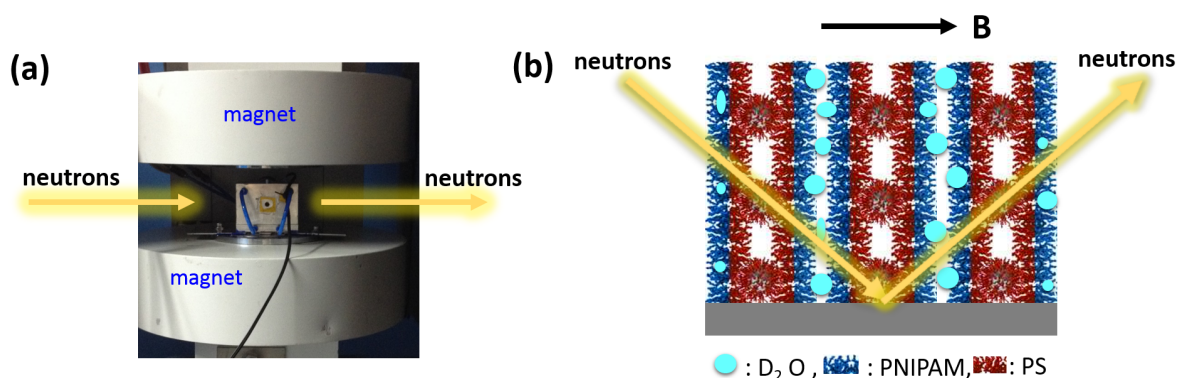


Figure 10.3: (a) The hexapod sample table for sample position between the magnets. (b) The sketch of the structured DBC-NPs film irradiated by neutron beam.

The investigation is performed via following a three-stage protocol shown in Figure 10.4. Stage 1: The dry film is measured at $20 \text{ }^\circ\text{C}$ (below the lower critical solution temperature (LCST)) in air, where a relative humidity of around 50 % is reached without adding D_2O . The dry film is firstly probed with unpolarized neutron beam for 3.6 h (1.8 h at each wavelength). Then an external magnetic field (560 mT) is applied to the film and PNR is used to investigate the magnetic structure of the hybrid film for 12 h (6 h at each wavelength). The magnetic field is oriented perpendicular to the film surface normal and

parallel to the Si substrate surface. Stage 2: The wet film is probed at 20 °C in humid atmosphere (relative humidity around 93 %) by adding 50 ml of D₂O into the cell. The swelling kinetics is followed with a time resolution of 10 min. After reaching the desired humidity (2 hours), the wet film is measured with PNR under an external magnetic field to see the influence of humidity on the film's magnetic behavior. The orientation and strength of the magnetic field are as before. Stage 3: The collapsed film is probed at 45 °C (above LCST) via the same method described in stage 2. Thus, the impact of temperature on the magnetic structure can be probed. During the whole measurement process, the temperature and relative humidity of the chamber are monitored by the applied sensor. The results are displayed in Figure 10.5.

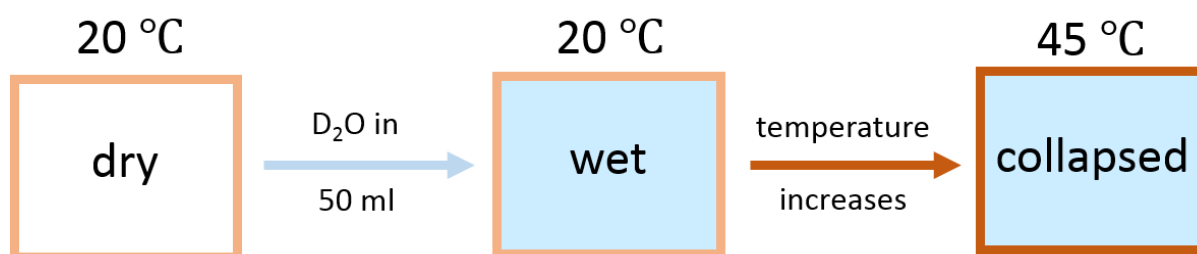


Figure 10.4: *The three-stage protocol for the PNR experiment.*

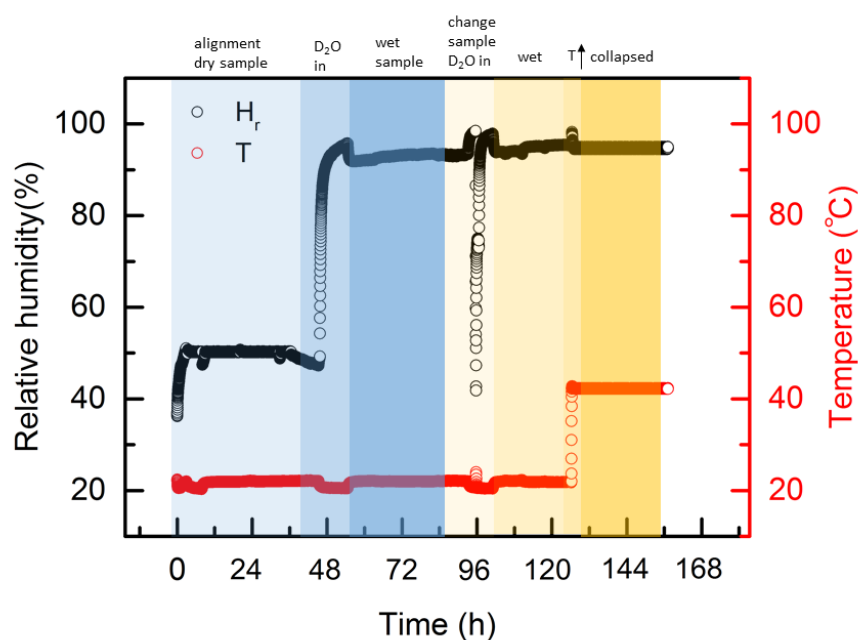


Figure 10.5: *Relative humidity and temperature of the chamber recorded during the entire PNR measurement.*

10.4 Surface structure

The surface structure of the magnetic film is probed by optical microscope (OM) and scanning electron microscope (SEM). Results are shown in Figure 10.6. The OM graphs (Figure 10.6 a and b) evidence a homogeneous hybrid film fabricated by spin-coating. Additionally, a layer of clusters with different sizes are present on the surface. The SEM data reveal that the clusters are composed of magnetic NPs. At a higher magnification (Figure 10.6d), the microphase-separated polymer nanostructure can be discovered. This suggests the presence of nanostructure even at high NP loading (20 wt%).

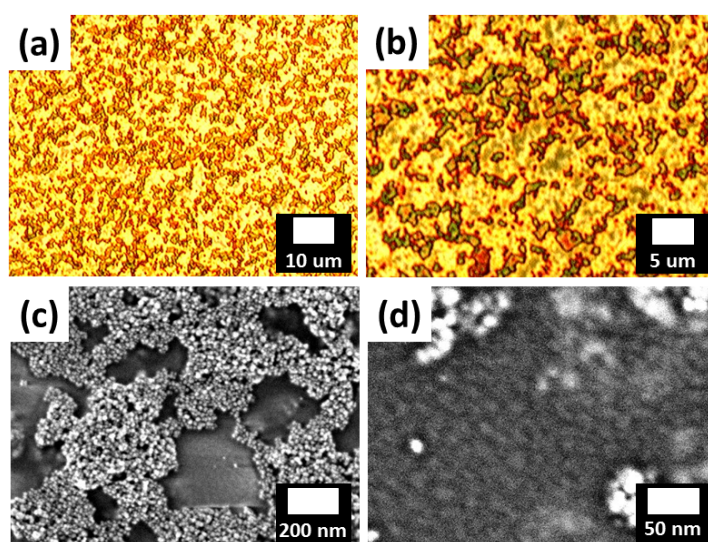


Figure 10.6: (a, b) OM and (c, d) SEM images displayed at different magnifications.

10.5 Magnetic structure

10.5.1 PNR data collected at three stages

The reflectivity data collected from the dry sample at 20 °C is shown in Figure 10.7a. Due to the surface roughness induced by the magnetic NPs on the film surface, no intensity fringes are observed in the NR data. Generally, The three sets of profiles obtained from nonpolarization and two polarization directions (spin up and spin down) overlap with each other. Only a slight intensity difference can be found in the low q_z region ($0.0104 - 0.0176 \text{ \AA}^{-1}$), seen in Figure 10.7b. A higher intensity can be clearly observed in the spin-up reflectivity profile as compared to the other two. This results from the same direction of neutron spin and magnetic moment of NPs. During the measurement, the

external magnetic field applied to the film guides the alignment of magnetic moments present inside the hybrid film. Provided the polarized neutron spin is oriented in the same direction as that of the magnetic moments, the intensity of collected reflectivity is enhanced (see the spin-up profile in Figure 10.7b). Otherwise a decreased intensity is obtained (see the spin-down profile in Figure 10.7b). The unpolarized profile lies in between the two polarized ones.

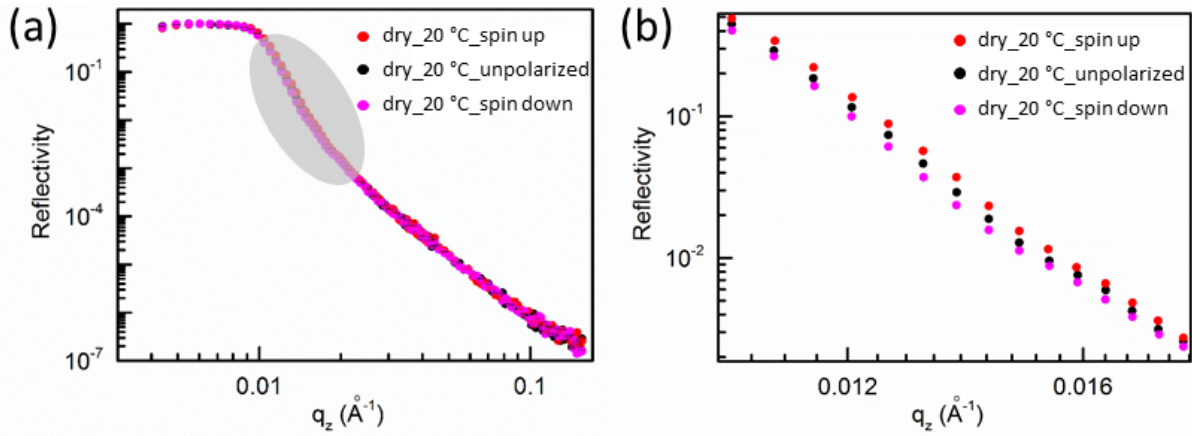


Figure 10.7: (a) Reflectivity data collected at 20 °C with the dry sample. The reflectivity profiles are for nonpolarization (unpolarized) and two polarization orientations (spin up and spin down) at the saturation magnetization of 560 mT. (b) An enlarged view of the reflectivity profile in the low q_z region from the area marked in gray in figure a.

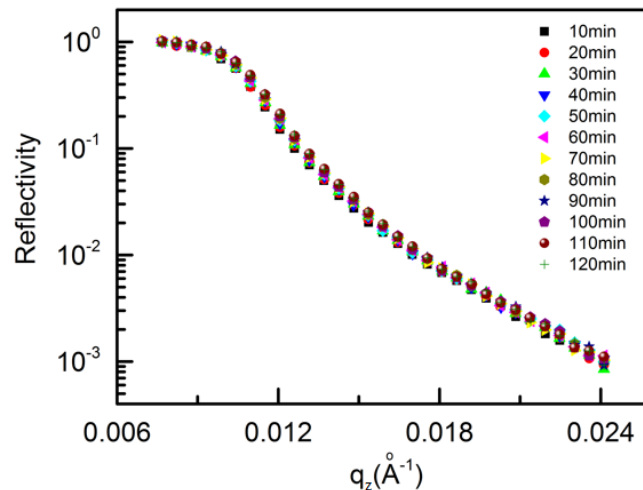


Figure 10.8: Kinetic neutron reflectivity measurement at 20 °C after D_2O being added into the chamber.

After adding 50 ml D_2O in to the chamber, the kinetic swelling behavior is followed

by measuring the neutron reflectivity without polarization. Figure 10.8 shows that the swelling equilibrium is reached within 2 h. The relative humidity is stable at around 93 % (seen in Figure 10.5). Afterwards, the wet magnetic film is measured with polarized neutron following the identical protocol as that for the dry film. Similar to the observation for the dry film, the intensity difference between the two polarization orientations appears only in the low q_z range (Figure 10.9).

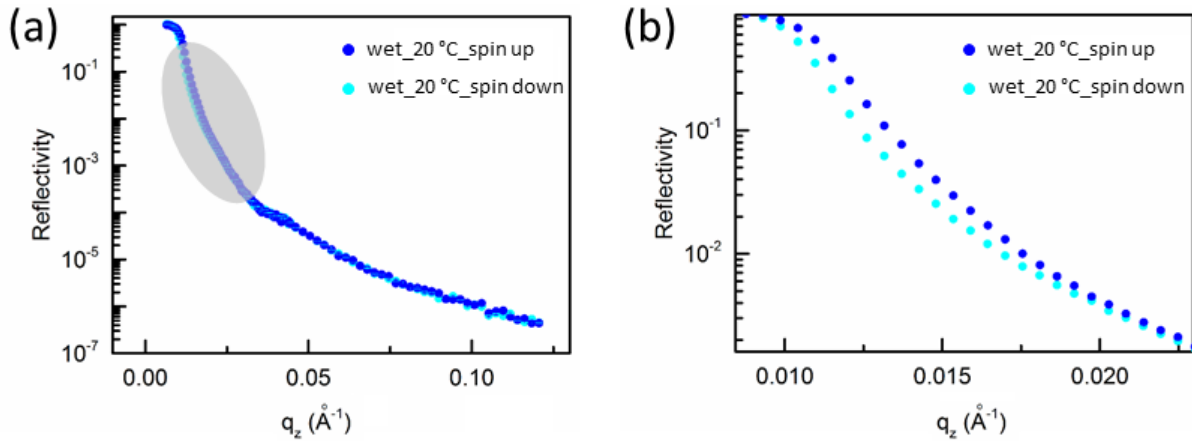


Figure 10.9: (a) PNR data collected at 20 °C with the wet sample at the saturation magnetization (560 mT). The reflectivity profiles are for two polarization orientations (spin up and spin down). (b) An enlarged view of the reflectivity in the low q_z region from the area marked in gray in figure a.

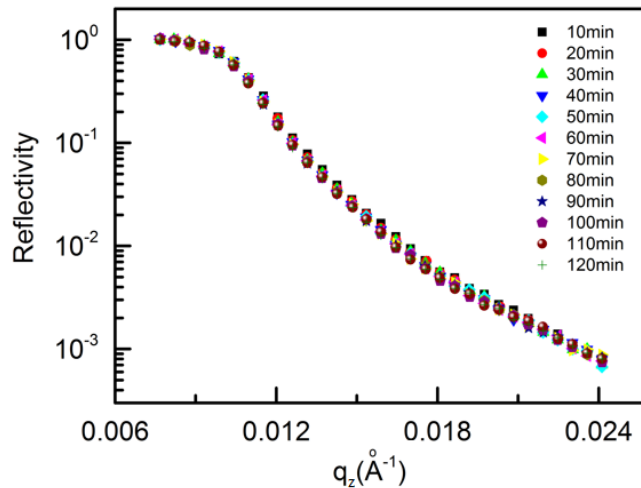


Figure 10.10: Kinetic neutron reflectivity measurement after the chamber temperature increases to 45 °C.

Finally, the temperature of the chamber increases to 45 °C and a stable relative humidity

of 93 % is achieved after the wet film reaches the equilibrium within 2 h (Figure 10.10). To gain an insight of the collapsing behavior of films at 45 °C, PNR is also performed. Similar to the phenomenon for the wet film, the sensitive wavelength to the film's magnetic behavior is also in the low q_z region (Figure 10.11).

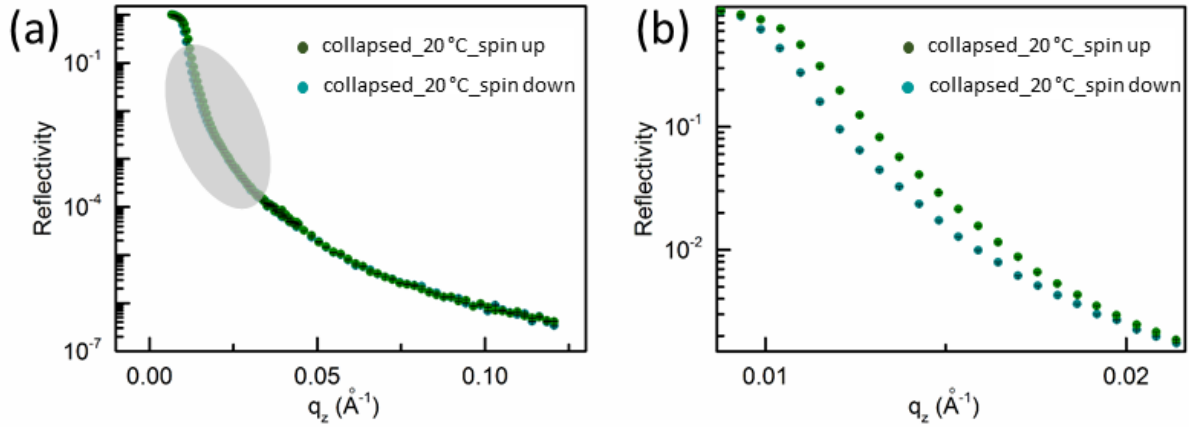


Figure 10.11: (a) PNR data collected at 45 °C with the collapsed sample at the saturation magnetization (560 mT). The reflectivity profiles are for two polarization orientations (spin up and spin down). (b) An enlarged view of the reflectivity in the low q_z region from the area marked in gray in figure a.

10.5.2 Influence of temperature/humidity on the magnetic behavior

To elucidate the influence of temperature and humidity on the film's magnetic behavior, a comparison is made based on the data collected at different experiment stages. Figure 10.11a displays an overview over the PNR measurements that are performed during the three stages (dry, wet and collapsed). Overall, different magnetic responsive behaviors of the hybrid film are observed. Figure 10.12a shows the PNR data collected in the low q_z range, where the influence of humidity and temperature on the reflectivity turns out to be strong by shifting the edge of the reflectivity curve. Compared with the dry film, the reflectivity intensity of the wet film collected at 20 °C is stronger, but decreases slightly after the temperature increases to 45 °C. Such behavior is observed in both spin directions. The intensity difference between spin up (I_{up}) and spin down (I_{down}) PNR data is shown in Figure 10.12b. The intensity difference of the dry film is much lower than that of the wet film showing that the magnetic response in the wet film is stronger. Additionally, at different q_z positions, a maximum in the intensity difference is found. Thus, the humidity has a clear impact on the magnetic properties of the hybrid film. The intensity difference is slightly higher and the maximum shifts smoothly to a lower q_z position, which suggests

a relatively weak influence of temperature on the film. Overall, the PNR measurements indicate a humidity/temperature dependent magnetic behavior of the hybrid film.

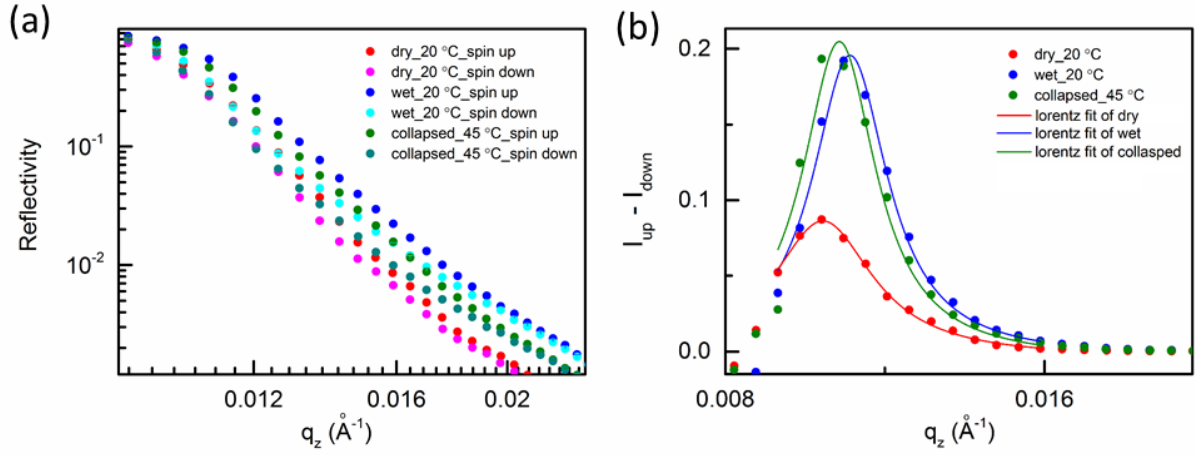


Figure 10.12: (a) Low q_z zoom-in of the PNR measurements of the hybrid film at different stages: dry (red: spin up, pink: spin down), wet (blue: spin up, aqua: spin down), collapsed (olive: spin up, light green: spin down). (b) Intensity difference between I_{up} (spin up) and I_{down} (spin down) extracted from PNR measurement of hybrid films at different states as indicated. The peaks are fitted with a Lorentz function.

Bibliography

- [1] R. Kodama, “Magnetic nanoparticles,” *Journal of Magnetism and Magnetic Materials*, vol. 200, pp. 359–372, oct 1999.
- [2] C. S. Lee, H. Lee, and R. M. Westervelt, “Microelectromagnets for the control of magnetic nanoparticles,” *Applied Physics Letters*, vol. 79, pp. 3308–3310, nov 2001.
- [3] G. Reiss and A. Hütten, “Applications beyond data storage,” *Nature Materials*, vol. 4, pp. 725–726, oct 2005.
- [4] A. Kaushik, P. R. Solanki, A. A. Ansari, G. Sumana, S. Ahmad, and B. D. Malhotra, “Iron oxide-chitosan nanobiocomposite for urea sensor,” *Sensors and Actuators B: Chemical*, vol. 138, pp. 572–580, may 2009.
- [5] D. Speliotis, “Magnetic recording beyond the first 100 years,” *Journal of Magnetism and Magnetic Materials*, vol. 193, pp. 29–35, mar 1999.
- [6] S. Kim, H. S. Wang, S. G. Jang, S.-H. Choi, B. J. Kim, and J. Bang, “Nanoparticles as structure-directing agents for controlling the orientation of block copolymer microdomain in thin films,” *Journal of Polymer Science Part B: Polymer Physics*, vol. 54, pp. 118–127, sep 2015.
- [7] S. Darling, “Directing the self-assembly of block copolymers,” *Progress in Polymer Science*, vol. 32, pp. 1152–1204, oct 2007.
- [8] C. Sinturel, M. Vayer, M. Morris, and M. A. Hillmyer, “Solvent vapor annealing of block polymer thin films,” *Macromolecules*, vol. 46, pp. 5399–5415, jun 2013.
- [9] S. Kim, M. Misner, T. Xu, M. Kimura, and T. Russell, “Highly oriented and ordered arrays from block copolymers via solvent evaporation,” *Advanced Materials*, vol. 16, pp. 226–231, feb 2004.
- [10] M. Sabzi, S. Mirabedini, J. Zohuriaan-Mehr, and M. Atai, “Surface modification of TiO₂ nano-particles with silane coupling agent and investigation of its effect on the properties of polyurethane composite coating,” *Progress in Organic Coatings*, vol. 65, pp. 222–228, jun 2009.

- [11] E. P. Plueddemann, "Adhesion through silane coupling agents," *The Journal of Adhesion*, vol. 2, pp. 184–201, jul 1970.
- [12] I. Barandiaran, E. Grana, D. Katsigiannopoulos, A. Avgeropoulos, and G. Kortaberria, "Nanocomposites based on nanostructured PI- b -PMMA copolymer and selectively placed PMMA-modified magnetic nanoparticles: Morphological and magnetic characterization," *European Polymer Journal*, vol. 75, pp. 514–524, feb 2016.
- [13] P. Posocco, Y. M. Hassan, I. Barandiaran, G. Kortaberria, S. Pricl, and M. Ferrmeglia, "Combined mesoscale/experimental study of selective placement of magnetic nanoparticles in diblock copolymer films via solvent vapor annealing," *The Journal of Physical Chemistry C*, vol. 120, pp. 7403–7411, mar 2016.
- [14] D. Celik, M. Krueger, C. Veit, H. F. Schleiermacher, B. Zimmermann, S. Allard, I. Dumsch, U. Scherf, F. Rauscher, and P. Niyamakom, "Performance enhancement of CdSe nanorod-polymer based hybrid solar cells utilizing a novel combination of post-synthetic nanoparticle surface treatments," *Solar Energy Materials and Solar Cells*, vol. 98, pp. 433–440, mar 2012.
- [15] W. Huynh, J. Dittmer, W. Libby, G. Whiting, and A. Alivisatos, "Controlling the morphology of nanocrystal-polymer composites for solar cells," *Advanced Functional Materials*, vol. 13, pp. 73–79, jan 2003.
- [16] M.-P. Pileni, "The role of soft colloidal templates in controlling the size and shape of inorganic nanocrystals," *Nature Materials*, vol. 2, pp. 145–150, mar 2003.
- [17] K. Sato, S. Kondo, M. Tsukada, T. Ishigaki, and H. Kamiya, "Influence of solid fraction on the optimum molecular weight of polymer dispersants in aqueous TiO₂nanoparticle suspensions," *Journal of the American Ceramic Society*, vol. 90, pp. 3401–3406, nov 2007.
- [18] Y. Yao, E. Metwalli, B. Su, V. Körstgens, D. M. González, A. Miasnikova, A. Laschewsky, M. Opel, G. Santoro, S. V. Roth, and P. Müller-Buschbaum, "Arrangement of maghemite nanoparticles via wet chemical self-assembly in PS- b-PNIPAM diblock copolymer films," *ACS Applied Materials & Interfaces*, vol. 7, pp. 13080–13091, jun 2015.
- [19] Y. Yao, E. Metwalli, M. Opel, M. Haese, J.-F. Moulin, K. Rodewald, B. Rieger, and P. Müller-Buschbaum, "Lamellar diblock copolymer films with embedded maghemite nanoparticles," *Advanced Materials Interfaces*, vol. 3, p. 1500712, feb 2016.

- [20] C. M. Palumbiny, F. Liu, T. P. Russell, A. Hexemer, C. Wang, and P. Müller-Buschbaum, “The crystallization of PEDOT:PSS polymeric electrodes probed in situ during printing,” *Advanced Materials*, vol. 27, pp. 3391–3397, apr 2015.
- [21] L. Song, W. Wang, V. Körstgens, D. M. González, F. C. Löhner, C. J. Schaffer, J. Schlipf, K. Peters, T. Bein, D. Fattakhova-Rohlfing, S. V. Roth, and P. Müller-Buschbaum, “In situ study of spray deposited titania photoanodes for scalable fabrication of solid-state dye-sensitized solar cells,” *Nano Energy*, vol. 40, pp. 317–326, oct 2017.
- [22] A. D. Jenkins, P. Kratochvíl, R. F. T. Stepto, and U. W. Suter, “Glossary of basic terms in polymer science (IUPAC recommendations 1996),” *Pure and Applied Chemistry*, vol. 68, pp. 2287–2311, jan 1996.
- [23] A. S. Burange, *Ziegler-Natta and Stereochemical control in polymerization*. Wilson College, Mumbai, 2017.
- [24] E. Open University, <http://www.open.edu/openlearn/ocw/mod/oucontent/view.php?id=3484&extra>
- [25] G. Strobl, “The physics of polymers.” Springer-Verlag Berlin Heidelberg, 3rd ed., 2007.
- [26] U. Eisele, “Introduction to polymer physics,” 1990.
- [27] T. G. Fox, *Influence of diluent and of copolymer composition on the glass temperature of a polymer system*, vol. 1 of pp. 22060-6218. Bull Am Phy Soc, 1956.
- [28] W. Hu, “Polymer phase separation,” 2013.
- [29] M. L. Huggins, “Thermodynamic properties of solutions of long-chain compounds,” *Annals of the New York Academy of Sciences*, vol. 4, pp. 107–107, 1942.
- [30] P. J. Flory, “Thermodynamics of high polymer solutions,” *The Journal of chemical physics*, vol. 10, no. 1, pp. 51–61, 1942.
- [31] F. S. Bates, “Block copolymer thermodynamics: Theory and experiment,” *Annu. Rev. Phys. Chem*, vol. 41, pp. 525–557, 1990.
- [32] E. Helfand and Z. R. Wasserman, “Statistical thermodynamics of microdomain structures in block copolymer systems,” *Polymer Engineering and Science*, vol. 17, pp. 582–586, 1977.
- [33] M. J. Fasolka and A. M. Mayes, “Block copolymer thin films: Physics and applications,” *Annual Review of Materials Research*, vol. 31, pp. 323–355, 2001.
- [34] M. J. Fasolka, P. Banerjee, A. M. Mayes, G. Pickett, and A. C. Balazs, “Morphology of ultrathin supported diblock copolymer films: theory and experiment,” *Macromolecules*, vol. 33, pp. 5702–5712, jul 2000.

- [35] D. G. Walton, G. J. Kellogg, A. M. Mayes, P. Lambooy, and T. P. Russell, "A free energy model for confined diblock copolymers," *Macromolecules*, vol. 27, pp. 6225–6228, 1994.
- [36] T. L. Morkved and H. M. Jaeger, "Thickness-induced morphology changes in lamellar diblock copolymer ultrathin films," *Europhysics Letters*, vol. 40, pp. 643–648, 1997.
- [37] S. Blundell, *Magnetism in Condensed Matter*. Oxford University Press, 2007.
- [38] J. Stohr and H. C. Siegmann, *Magnetism*. Springer-Verlag, Berlin, 2006.
- [39] M. Getzlaff, *Fundamentals of Magnetism*. Springer-Verlag, Berlin, 2008.
- [40] P. Weiss, "L'hypothèse du champ moléculaire et la propriété ferromagnétique," *Journal de Physique Théorique et Appliquée*, vol. 6, no. 1, pp. 661–690, 1907.
- [41] S. Saini, R. Frankel, D. Stark, and J. Ferrucci, "Magnetism: a primer and review," *American Journal of Roentgenology*, vol. 150, pp. 735–743, apr 1988.
- [42] S. Bedanta and W. Kleemann, "Supermagnetism," *Journal of Physics D: Applied Physics*, vol. 42, p. 013001, dec 2008.
- [43] C. P. Bean and I. S. Jacobs, "Magnetic granulometry and superparamagnetism," *Journal of Applied Physics*, vol. 27, pp. 1448–1452, dec 1956.
- [44] L. Néel, "Thermoremanent magnetization of fine powders," *Reviews of Modern Physics*, vol. 25, pp. 293–295, jan 1953.
- [45] T. Thomson, "Magnetic properties of metallic thin films," in *Metallic Films for Electronic, Optical and Magnetic Applications*, pp. 454–546, Elsevier, 2014.
- [46] T. K. Jain, J. Richey, M. Strand, D. L. Leslie-Pelecky, C. A. Flask, and V. Labhasetwar, "Magnetic nanoparticles with dual functional properties: Drug delivery and magnetic resonance imaging," *Biomaterials*, vol. 29, pp. 4012–4021, oct 2008.
- [47] M. Knobel, W. C. Nunes, L. M. Socolovsky, E. D. Biasi, J. M. Vargas, and J. C. Denardin, "Superparamagnetism and other magnetic features in granular materials: A review on ideal and real systems," *Journal of Nanoscience and Nanotechnology*, vol. 8, pp. 2836–2857, jun 2008.
- [48] W. M. C. M Gopal and L. d. Jonghe, "Room temperature synthesis of crystalline metal oxides," *Journal of Materials Science*, vol. 32, no. 22, pp. 6001–6008, 1997.
- [49] M. Tolan, "X-ray scattering from soft-matter thin films." Springer-Verlag, Berlin, Heidelberg, 1999.

- [50] A. Duparré, J. Ferre-Borrull, S. Gliech, G. Notni, J. Steinert, and J. M. Bennett, “Surface characterization techniques for determining the root-mean-square roughness and power spectral densities of optical components,” *Applied Optics*, vol. 41, p. 154, jan 2002.
- [51] L. Nevot and P. Croce, “Characterization of surfaces by grazing x-ray reflection—application to the study of polishing of some silicate glasses,” *Rev. Phys. Appl.*, vol. 15, no. 761, 1980.
- [52] H. Kiessig, “Interferenz von röntgenstrahlen an dünnen schichten,” *Annalen der Physik*, vol. 402, no. 7, pp. 769–788, 1931.
- [53] A. Naudon, D. Babonneau, D. Thiaudière, and S. Lequien, “Grazing-incidence small-angle x-ray scattering applied to the characterization of aggregates in surface regions,” *Physica B: Condensed Matter*, vol. 283, pp. 69–74, jun 2000.
- [54] P. Müller-Buschbaum, “A basic introduction to grazing incidence small-angle x-ray scattering,” in *Applications of Synchrotron Light to Scattering and Diffraction in Materials and Life Sciences*, pp. 61–89, Springer Berlin Heidelberg, 2009.
- [55] G. Renaud, R. Lazzari, and F. Leroy, “Probing surface and interface morphology with grazing incidence small angle x-ray scattering,” *Surface Science Reports*, vol. 64, pp. 255–380, aug 2009.
- [56] M. D. Abramoff, “Imagej as an image processing tool and library,” *Microscopy and Microanalysis*, vol. 13, 2007.
- [57] D. Necas and P. Klapetek, “Gwyddion: an open-source software for spm data analysis,” *Open Physics*, vol. 10, 2012.
- [58] B. Nandan, B. K. Kuila, and M. Stamm, “Supramolecular assemblies of block copolymers as templates for fabrication of nanomaterials,” *European Polymer Journal*, vol. 47, pp. 584–599, apr 2011.
- [59] L. G. Parratt, “Surface studies of solids by total reflection of x-rays,” *Physical Review*, vol. 95, pp. 359–369, jul 1954.
- [60] R. Hosemann, W. Vogel, D. Weick, and F. J. Baltá-Calleja, “Novel aspects of the real paracrystal,” *Acta Crystallographica Section A*, vol. 37, pp. 85–91, jan 1981.
- [61] B. D. Josephson, “Possible new effects in superconductive tunnelling,” *Physics letters*, vol. 1, pp. 251–253, 1962.
- [62] Q. Design, “Magnetic property measurement system mpms xl hardware reference manual.” San Diego, CA, 1996.

- [63] S. Makharza, J. Auisa, S. A. Sharkh, J. Ghabboun, M. Faroun, H. Dweik, W. Sultan, and M. Sowwan, "Structural and thermal analysis of copper-doped poly(*n*-isopropylacrylamide) films," *International Journal of Polymer Analysis and Characterization*, vol. 15, pp. 254–265, may 2010.
- [64] N. A. D. Burke, H. D. H. Stöver, and F. P. Dawson, "Magnetic nanocomposites preparation and characterization of polymer-coated iron nanoparticles," *Chemistry of Materials*, vol. 14, pp. 4752–4761, nov 2002.
- [65] S. E. Bowles, W. Wu, T. Kowalewski, M. C. Schalmat, R. J. Davis, J. E. Pemberton, I. Shim, B. D. Korth, and J. Pyun, "Magnetic assembly and pyrolysis of functional ferromagnetic colloids into one-dimensional carbon nanostructures," *Journal of the American Chemical Society*, vol. 129, pp. 8694–8695, jul 2007.
- [66] J. Pyun, "Nanocomposite materials from functional polymers and magnetic colloids," *Polymer Reviews*, vol. 47, pp. 231–263, apr 2007.
- [67] P. Y. Keng, I. Shim, B. D. Korth, J. F. Douglas, and J. Pyun, "Synthesis and self-assembly of polymer-coated ferromagnetic nanoparticles," *ACS Nano*, vol. 1, pp. 279–292, nov 2007.
- [68] B. D. Korth, P. Keng, I. Shim, S. E. Bowles, C. Tang, T. Kowalewski, K. W. Nebesny, and J. Pyun, "Polymer-coated ferromagnetic colloids from well-defined macromolecular surfactants and assembly into nanoparticle chains," *Journal of the American Chemical Society*, vol. 128, pp. 6562–6563, may 2006.
- [69] Y. Zhao, K. Thorkelsson, A. J. Mastroianni, T. Schilling, J. M. Luther, B. J. Rancatore, K. Matsunaga, H. Jinnai, Y. Wu, D. Poulsen, J. M. J. Fréchet, A. P. Alivisatos, and T. Xu, "Small-molecule-directed nanoparticle assembly towards stimuli-responsive nanocomposites," *Nature Materials*, vol. 8, pp. 979–985, oct 2009.
- [70] S. Darling, "Mechanism for hierarchical self-assembly of nanoparticles on scaffolds derived from block copolymers," *Surface Science*, vol. 601, pp. 2555–2561, jul 2007.
- [71] C. Lo, B. Lee, V. G. Pol, N. L. D. Rago, S. Seifert, R. E. Winans, and P. Thiagarajan, "Effect of molecular properties of block copolymers and nanoparticles on the morphology of selfassembled bulk nanocomposites," *Macromolecules*, vol. 40, pp. 8302–8310, nov 2007.
- [72] H. Yuan, I. J. Zvonkina, A. M. AlEnizi, A. A. Elzatahry, J. Pyun, and A. Karim, "Facile assembly of aligned magnetic nanoparticle chains in polymer nanocomposite films by magnetic flow coating," *ACS Applied Materials Interfaces*, vol. 9, pp. 11290–11298, mar 2017.

- [73] V. Cabuil, N. Hochart, R. Perzynski, and P. J. Lutz, "Synthesis of cyclohexane magnetic fluids through adsorption of end-functionalized polymers on magnetic particles," in *Trends in Colloid and Interface Science VIII*, pp. 71–74, Steinkopff, 1994.
- [74] J. Wu, H. Li, S. Wu, G. Huang, W. Xing, M. Tang, and Q. Fu, "Influence of magnetic nanoparticle size on the particle dispersion and phase separation in an aba triblock copolymer," *The Journal of Physical Chemistry B*, p. 140213144409001, feb 2014.
- [75] Y. Yao, E. Metwalli, M. A. Niedermeier, M. Opel, C. Lin, J. Ning, J. Perlich, S. V. Roth, and P. Müller-Buschbaum, "Nano- and microstructures of magnetic field-guided maghemite nanoparticles in diblock copolymer films," *ACS Applied Materials & Interfaces*, vol. 6, pp. 5244–5254, mar 2014.
- [76] P. Müller-Buschbaum, N. Hermsdorf, S. Roth, J. Wiedersich, S. Cunis, and R. Gehrke, "Comparative analysis of nanostructured diblock copolymer films," *Spectrochimica Acta Part B: Atomic Spectroscopy*, vol. 59, pp. 1789–1797, oct 2004.
- [77] P. Müller-Buschbaum, "Influence of surface cleaning on dewetting of thin polystyrene films," *The European Physical Journal E*, vol. 12, pp. 443–448, nov 2003.
- [78] W. Wang, G. Kaune, J. Perlich, C. M. Papadakis, A. M. B. Koumba, A. Laschewsky, K. Schlage, R. Roßhlsberger, S. V. Roth, R. Cubitt, and P. Müller-Buschbaum, "Swelling and switching kinetics of gold coated end-capped poly(*n*-isopropylacrylamide) thin films," *Macromolecules*, vol. 43, pp. 2444–2452, mar 2010.
- [79] G. Sebastian, *Properties of printed polymer blend films*. PhD thesis, Technische Universität München, München, Germany, 2013.
- [80] Y. Lin, A. Böker, J. He, K. Sill, H. Xiang, C. Abetz, X. Li, J. Wang, T. Emrick, S. Long, Q. Wang, A. Balazs, and T. P. Russell, "Self-directed self-assembly of nanoparticle/copolymer mixtures," *Nature*, vol. 434, pp. 55–59, mar 2005.
- [81] B. C. Berry, A. W. Bosse, J. F. Douglas, R. L. Jones, and A. Karim, "Orientational order in block copolymer films zone annealed below the order-disorder transition temperature," *Nano Letters*, vol. 7, pp. 2789–2794, sep 2007.
- [82] T. Thurn-Albrecht, R. Steiner, J. DeRouchey, C. M. Stafford, E. Huang, M. Bal, M. Tuominen, C. J. Hawker, and T. P. Russell, "Nanosopic templates from oriented block copolymer films," *Advanced Materials*, vol. 12, pp. 787–791, jun 2000.
- [83] X. Gu, I. Gunkel, A. Hexemer, W. Gu, and T. P. Russell, "An in situ grazing incidence x-ray scattering study of block copolymer thin films during solvent vapor annealing," *Advanced Materials*, vol. 26, pp. 273–281, nov 2013.

- [84] M. A. Chavis, D.-M. Smilgies, U. B. Wiesner, and C. K. Ober, “Widely tunable morphologies in block copolymer thin films through solvent vapor annealing using mixtures of selective solvents,” *Advanced Functional Materials*, vol. 25, pp. 3057–3065, apr 2015.
- [85] C.-C. Chang and C.-T. Lo, “Effect of particles on the structure of solvent-annealed block copolymer/nanoparticle composite thin film,” *The Journal of Physical Chemistry B*, vol. 115, pp. 2485–2493, mar 2011.
- [86] C. Lai, W. B. Russel, and R. A. Register, “Scaling of domain spacing in concentrated solutions of block copolymers in selective solvents,” *Macromolecules*, vol. 35, pp. 4044–4049, may 2002.
- [87] S. Xia, E. Metwalli, M. Opel, P. A. Staniec, E. M. Herzig, and P. Müller-Buschbaum, “Printed thin magnetic films based on diblock copolymer and magnetic nanoparticles,” *ACS Applied Materials & Interfaces*, vol. 10, pp. 2982–2991, jan 2018.
- [88] Y. Yao, E. Metwalli, J.-F. Moulin, B. Su, M. Opel, and P. Müller-Buschbaum, “Self-assembly of diblock copolymer–maghemite nanoparticle hybrid thin films,” *ACS Applied Materials & Interfaces*, vol. 6, pp. 18152–18162, oct 2014.
- [89] X. Xia, E. Metwalli, M. A. Ruderer, V. Körstgens, P. Busch, P. Böni, and P. Müller-Buschbaum, “Nanostructured diblock copolymer films with embedded magnetic nanoparticles,” *Journal of Physics: Condensed Matter*, vol. 23, p. 254203, jun 2011.
- [90] M. R. Hammond and E. J. Kramer, “Edge effects on thermal disorder in laterally confined diblock copolymer cylinder monolayers,” *Macromolecules*, vol. 39, pp. 1538–1544, feb 2006.
- [91] M. M. A. Kashem, J. Perlich, L. Schulz, S. V. Roth, W. Petry, and P. Müller-Buschbaum, “Maghemite nanoparticles on supported diblock copolymer nanostructures,” *Macromolecules*, vol. 40, pp. 5075–5083, jul 2007.
- [92] I. Barandiaran, J. Gutierrez, A. Tercjak, and G. Kortaberria, “Thin film nanocomposites based on SBM triblock copolymer and silver nanoparticles: Morphological and dielectric analysis,” *Macromolecular Materials and Engineering*, vol. 302, p. 1700169, jul 2017.
- [93] X. Zhao, C. Hinchliffe, C. Johnston, P. J. Dobson, and P. S. Grant, “Spray deposition of polymer nanocomposite films for dielectric applications,” *Materials Science and Engineering: B*, vol. 151, pp. 140–145, jun 2008.
- [94] J. Bravo, L. Zhai, Z. Wu, R. E. Cohen, and M. F. Rubner, “Transparent superhydrophobic films based on silica nanoparticles,” *Langmuir*, vol. 23, pp. 7293–7298, jun 2007.

- [95] A. Pierre, M. Sadeghi, M. M. Payne, A. Facchetti, J. E. Anthony, and A. C. Arias, "All-printed flexible organic transistors enabled by surface tension-guided blade coating," *Advanced Materials*, vol. 26, pp. 5722–5727, jun 2014.
- [96] B. Chen, T. Cui, Y. Liu, and K. Varahramyan, "All-polymer RC filter circuits fabricated with inkjet printing technology," *Solid-State Electronics*, vol. 47, pp. 841–847, may 2003.
- [97] H. Yan, Z. Chen, Y. Zheng, C. Newman, J. R. Quinn, F. Dötz, M. Kastler, and A. Facchetti, "A high-mobility electron-transporting polymer for printed transistors," *Nature*, vol. 457, pp. 679–686, jan 2009.
- [98] F. Garnier, R. Hajlaoui, A. Yassar, and P. Srivastava, "All-polymer field-effect transistor realized by printing techniques," *Science*, vol. 265, pp. 1684–1686, sep 1994.
- [99] S. Sivaramakrishnan, P.-J. Chia, Y.-C. Yeo, L.-L. Chua, and P. K.-H. Ho, "Controlled insulator-to-metal transformation in printable polymer composites with nanometal clusters," *Nature Materials*, vol. 6, pp. 149–155, dec 2006.
- [100] C. Hoth, S. Choulis, P. Schilinsky, and C. Brabec, "High photovoltaic performance of inkjet printed polymer:fullerene blends," *Advanced Materials*, vol. 19, pp. 3973–3978, nov 2007.
- [101] F. C. Krebs, "Fabrication and processing of polymer solar cells: A review of printing and coating techniques," *Solar Energy Materials and Solar Cells*, vol. 93, pp. 394–412, apr 2009.
- [102] S. Pröllner, F. Liu, C. Zhu, C. Wang, T. P. Russell, A. Hexemer, P. Müller-Buschbaum, and E. M. Herzig, "Following the morphology formation in situ in printed active layers for organic solar cells," *Advanced Energy Materials*, vol. 6, p. 1501580, oct 2015.
- [103] D. Kokkinis, M. Schaffner, and A. R. Studart, "Multimaterial magnetically assisted 3d printing of composite materials," *Nature Communications*, vol. 6, oct 2015.
- [104] Y. Hao, F. J. C. no, C. A. Ross, B. Vögeli, M. E. Walsh, and H. I. Smith, "Magnetization reversal in lithographically patterned sub-200-nm co particle arrays," *Journal of Applied Physics*, vol. 91, no. 10, p. 7989, 2002.
- [105] M. Tsige and G. S. Grest, "Solvent evaporation and interdiffusion in polymer films," *Journal of Physics: Condensed Matter*, vol. 17, pp. S4119–S4132, nov 2005.
- [106] S. A. Jenekhe, "Effects of solvent mass transfer on flow of polymer solutions on a flat rotating disk," *Industrial and engineering chemistry fundamentals*, vol. 23, pp. 425–432, 1984.

- [107] M. Tanase, L. A. Bauer, A. Hultgren, D. M. Silevitch, L. Sun, D. H. Reich, P. C. Searson, and G. J. Meyer, "Magnetic alignment of fluorescent nanowires," *Nano Letters*, vol. 1, pp. 155–158, mar 2001.
- [108] R. Grau-Crespo, A. Y. Al-Baitai, I. Saadoune, and N. H. D. Leeuw, "Vacancy ordering and electronic structure of γ -Fe₂O₃(maghemite): a theoretical investigation," *Journal of Physics: Condensed Matter*, vol. 22, p. 255401, jun 2010.
- [109] M.-P. Pileni and A.-T. Ngo, "Mesoscopic structures of maghemite nanocrystals: Fabrication, magnetic properties, and uses," *ChemPhysChem*, vol. 6, pp. 1027–1034, jun 2005.
- [110] A.-H. Lu, E. Salabas, and F. Schüth, "Magnetic nanoparticles: Synthesis, protection, functionalization, and application," *Angewandte Chemie International Edition*, vol. 46, pp. 1222–1244, feb 2007.
- [111] S. L. Biswal and A. P. Gast, "Micromixing with linked chains of paramagnetic particles," *Analytical Chemistry*, vol. 76, pp. 6448–6455, nov 2004.
- [112] L. Schulz, W. Schirmacher, A. Omran, V. R. Shah, P. Böni, W. Petry, and P. Müller-Buschbaum, "Elastic torsion effects in magnetic nanoparticle diblock-copolymer structures," *Journal of Physics: Condensed Matter*, vol. 22, p. 346008, aug 2010.
- [113] P. Müller-Buschbaum, "Grazing incidence small-angle x-ray scattering: an advanced scattering technique for the investigation of nanostructured polymer films," *Analytical and Bioanalytical Chemistry*, vol. 376, pp. 3–10, mar 2003.
- [114] L. de Oliveira, A. Pentón-Madrigal, A. Guimarães, and J. Sinnecker, "Thermally activated processes and superparamagnetism in bi 12 MnO 20 nanoparticles: A comparative study," *Journal of Magnetism and Magnetic Materials*, vol. 401, pp. 890–896, mar 2016.
- [115] H. Mamiya, M. Ohnuma, I. Nakatani, and T. Furubayashim, "Extraction of blocking temperature distribution from zero-field-cooled and field-cooled magnetization curves," *IEEE Transactions on Magnetics*, vol. 41, pp. 3394–3396, oct 2005.
- [116] A. T. Ngo and M. P. Pileni, "Cigar-shaped ferrite nanocrystals: Orientation of the easy magnetic axes," *Journal of Applied Physics*, vol. 92, pp. 4649–4652, oct 2002.
- [117] A. T. Ngo and M. P. Pileni, "Assemblies of ferrite nanocrystals: partial orientation of the easy magnetic axes," *The Journal of Physical Chemistry B*, vol. 105, pp. 53–58, jan 2001.
- [118] Y. Sahoo, M. Cheon, S. Wang, H. Luo, E. P. Furlani, and P. N. Prasad, "Field-directed self-assembly of magnetic nanoparticles," *The Journal of Physical Chemistry B*, vol. 108, pp. 3380–3383, mar 2004.

- [119] C. Xu, K. Ohno, V. Ladmiral, and R. J. Composto, "Dispersion of polymer-grafted magnetic nanoparticles in homopolymers and block copolymers," *Polymer*, vol. 49, pp. 3568–3577, jul 2008.
- [120] O. Jarjayes, P. Fries, and C. Bidan, "New nanocomposites of polypyrrole including γ -Fe₂O₃ particles: electrical and magnetic characterizations," *Synthetic Metals*, vol. 69, pp. 343–344, mar 1995.
- [121] S. Xia, L. Song, V. Körstgens, M. Opel, M. Schwartzkopf, S. V. Roth, and P. Müller-Buschbaum, "Magnetic nanoparticle-containing soft–hard diblock copolymer films with high order," *Nanoscale*, vol. 10, no. 25, pp. 11930–11941, 2018.
- [122] P. Antonel, R. Negri, A. Leyva, and G. Jorge, "Anisotropy and relaxation processes of uniaxially oriented CoFe₂O₄ nanoparticles dispersed in PDMS," *Physica B: Condensed Matter*, vol. 407, pp. 3165–3167, aug 2012.
- [123] P. Allia, G. Barrera, T. Nardi, Y. Leterrier, and P. Tiberto, "Anisotropic magnetic polymer nanocomposite with self-assembled chains of titania-coated magnetite nanoparticles," *Materials Today Communications*, vol. 7, pp. 32–41, jun 2016.
- [124] A. Suhendi, C. W. Kartikowati, R. Zulhijah, T. Ogi, T. Iwaki, and K. Okuyama, "Preparation and characterization of magnetic films of well-dispersed single domain of core–shell α -Fe₃O₄/Al₂O₃ nanoparticles," *Advanced Powder Technology*, vol. 26, pp. 1618–1623, nov 2015.
- [125] T. Kimura, H. Ago, M. Tobita, S. Ohshima, M. Kyotani, and M. Yumura, "Polymer composites of carbon nanotubes aligned by a magnetic field," *Advanced Materials*, vol. 14, pp. 1380–1383, oct 2002.
- [126] M. Cetintas and M. Kamperman, "Self-assembly of PS- b -PNIPAM- b -PS block copolymer thin films via selective solvent annealing," *Polymer*, vol. 107, pp. 387–397, dec 2016.
- [127] H. Ahmad, "Solubility parameter of acrylamide series polymers through its components and group contribution technique," *Journal of Macromolecular Science: Part A - Chemistry*, vol. 17, pp. 585–600, mar 1982.
- [128] S.-A. Chen, "Polymer miscibility in organic solvents and in plasticizers—a two-dimensional approach," *Journal of Applied Polymer Science*, vol. 15, pp. 1247–1266, may 1971.
- [129] V. Lauter-Pasyuk, H. Lauter, G. Gordeev, P. Müller-Buschbaum, B. Toperverg, W. Petry, M. Jernenkov, A. Petrenko, and V. Aksenov, "Parallel and perpendicular lamellar phases in copolymer–nanoparticle multilayer structures," *Physica B: Condensed Matter*, vol. 350, pp. E939–E942, jul 2004.

- [130] J. Huh, V. V. Ginzburg, and A. C. Balazs, “Thermodynamic behavior of particle/diblock copolymer mixtures: simulation and theory,” *Macromolecules*, vol. 33, pp. 8085–8096, oct 2000.
- [131] W. F. Brown, “Thermal fluctuations of a single-domain particle,” *Physical Review*, vol. 34, pp. 1319–1320, 1963.
- [132] S. Xia, L. Song, N. Hohn, K. Wang, S. Grott, M. Opel, M. Schwartzkopf, S. V. Roth, and P. Müller-Buschbaum, “Spray coating magnetic thin hybrid films of PS-b-PNIPAM and magnetite nanoparticles,” *Advanced Functional Materials*, vol. 29, p. 1808427, feb 2019.
- [133] W. Wu, Z. Wu, T. Yu, C. Jiang, and W.-S. Kim, “Recent progress on magnetic iron oxide nanoparticles: synthesis, surface functional strategies and biomedical applications,” *Science and Technology of Advanced Materials*, vol. 16, p. 023501, apr 2015.
- [134] P. W. Majewski and K. G. Yager, “Reordering transitions during annealing of block copolymer cylinder phases,” *Soft Matter*, vol. 12, no. 1, pp. 281–294, 2016.
- [135] J. L. Wilson, P. Poddar, N. A. Frey, H. Srikanth, K. Mohamed, J. P. Harmon, S. Kotha, and J. Wachsmuth, “Synthesis and magnetic properties of polymer nanocomposites with embedded iron nanoparticles,” *Journal of Applied Physics*, vol. 95, pp. 1439–1443, feb 2004.
- [136] J. Gass, P. Poddar, J. Almand, S. Srinath, and H. Srikanth, “Superparamagnetic polymer nanocomposites with uniform fe₃o₄ nanoparticle dispersions,” *Advanced Functional Materials*, vol. 16, pp. 71–75, jan 2006.
- [137] Y. Zheng, R. Wu, W. Shi, Z. Guan, and J. Yu, “Effect of in situ annealing on the performance of spray coated polymer solar cells,” *Solar Energy Materials and Solar Cells*, vol. 111, pp. 200–205, apr 2013.
- [138] G. Susanna, L. Salamandra, T. M. Brown, A. D. Carlo, F. Brunetti, and A. Reale, “Airbrush spray-coating of polymer bulk-heterojunction solar cells,” *Solar Energy Materials and Solar Cells*, vol. 95, pp. 1775–1778, jul 2011.
- [139] N. Hohn, S. J. Schlosser, L. Bießmann, S. Grott, S. Xia, K. Wang, M. Schwartzkopf, S. V. Roth, and P. Müller-Buschbaum, “Readily available titania nanostructuring routines based on mobility and polarity controlled phase separation of an amphiphilic diblock copolymer,” *Nanoscale*, vol. 10, no. 11, pp. 5325–5334, 2018.
- [140] D. Vak, S.-S. Kim, J. Jo, S.-H. Oh, S.-I. Na, J. Kim, and D.-Y. Kim, “Fabrication of organic bulk heterojunction solar cells by a spray deposition method for low-cost power generation,” *Applied Physics Letters*, vol. 91, p. 081102, aug 2007.

- [141] K. Sarkar, E. V. Braden, S. Pogorzalek, S. Yu, S. V. Roth, and P. Müller-Buschbaum, “Monitoring structural dynamics of in situ spray-deposited zinc oxide films for application in dye-sensitized solar cells,” *ChemSusChem*, vol. 7, pp. 2140–2145, jun 2014.
- [142] B. Su, H. A. Caller-Guzman, V. Körstgens, Y. Rui, Y. Yao, N. Saxena, G. Santoro, S. V. Roth, and P. Müller-Buschbaum, “Macroscale and nanoscale morphology evolution during in situ spray coating of titania films for perovskite solar cells,” *ACS Applied Materials & Interfaces*, vol. 9, pp. 43724–43732, dec 2017.
- [143] M. Al-Hussein, M. Schindler, M. A. Ruderer, J. Perlich, M. Schwartzkopf, G. Herzog, B. Heidmann, A. Buffet, S. V. Roth, and P. Müller-Buschbaum, “In situ x-ray study of the structural evolution of gold nano-domains by spray deposition on thin conductive p3ht films,” *Langmuir*, vol. 29, pp. 2490–2497, feb 2013.
- [144] Y. Yoneda, “Anomalous surface reflection of x rays,” *Physical Review*, vol. 131, pp. 2010–2013, sep 1963.
- [145] R. Lazzari, “IsGISAXS: a program for grazing-incidence small-angle x-ray scattering analysis of supported islands,” *Journal of Applied Crystallography*, vol. 35, pp. 406–421, jul 2002.
- [146] R. Hosemann and S. N. Bagchi, “The interference theory of ideal paracrystals,” *Acta Crystallographica*, vol. 5, pp. 612–614, sep 1952.
- [147] P. Jenny, D. Roekaerts, and N. Beishuizen, “Modeling of turbulent dilute spray combustion,” *Progress in Energy and Combustion Science*, vol. 38, pp. 846–887, dec 2012.
- [148] S. Sharma, M. H. Rafailovich, D. Peiffer, and J. Sokolov, “Control of dewetting dynamics by adding nanoparticle fillers,” *Nano Letters*, vol. 1, pp. 511–514, oct 2001.
- [149] K. A. Barnes, A. Karim, J. F. Douglas, A. I. Nakatani, H. Gruell, and E. J. Amis, “Suppression of dewetting in nanoparticle-filled polymer films,” *Macromolecules*, vol. 33, pp. 4177–4185, may 2000.
- [150] R. S. Krishnan, M. E. Mackay, P. M. Duxbury, C. J. Hawker, S. Asokan, M. S. Wong, R. Goyette, and P. Thiyagarajan, “Improved polymer thin-film wetting behavior through nanoparticle segregation to interfaces,” *Journal of Physics: Condensed Matter*, vol. 19, p. 356003, aug 2007.

- [151] S. Xia, L. Song, W. Chen, V. Körstgens, M. Opel, M. Schwartzkopf, S. V. Roth, and P. Müller-Buschbaum, "Printed thin diblock copolymer films with dense magnetic nanostructure," *ACS Applied Materials & Interfaces*, vol. 11, pp. 21935–21945, may 2019.
- [152] P. Müller-Buschbaum, "Dewetting and pattern formation in thin polymer films as investigated in real and reciprocal space," *Journal of Physics: Condensed Matter*, vol. 15, pp. R1549–R1582, aug 2003.
- [153] R. Seemann, S. Herminghaus, and K. Jacobs, "Dewetting patterns and molecular forces: A reconciliation," *Physical Review Letters*, vol. 86, pp. 5534–5537, jun 2001.
- [154] G. Reiter, "Dewetting of thin polymer films," *Physical Review Letters*, vol. 68, pp. 75–78, jan 1992.
- [155] B. Sarkar and P. Alexandridis, "Block copolymer–nanoparticle composites: Structure, functional properties, and processing," *Progress in Polymer Science*, vol. 40, pp. 33–62, jan 2015.
- [156] Y. S. Jung and C. A. Ross, "Solvent-vapor-induced tunability of self-assembled block copolymer patterns," *Advanced Materials*, vol. 21, pp. 2540–2545, jun 2009.
- [157] J. Peng, D. H. Kim, W. Knoll, Y. Xuan, B. Li, and Y. Han, "Morphologies in solvent-annealed thin films of symmetric diblock copolymer," *The Journal of Chemical Physics*, vol. 125, p. 064702, aug 2006.
- [158] T. P. Russell, R. P. Hjelm, and P. A. Seeger, "Temperature dependence of the interaction parameter of polystyrene and poly(methyl methacrylate)," *Macromolecules*, vol. 23, pp. 890–893, 1990.
- [159] T. Russell, P. Lambooy, G. Kellogg, and A. Mayes, "Diblock copolymers under confinement," *Physica B: Condensed Matter*, vol. 213-214, pp. 22–25, aug 1995.
- [160] G. J. Kellogg, D. G. Walton, A. M. Mayes, P. Lambooy, T. P. Russell, P. D. Gallagher, and S. K. Satija, "Observed surface energy effects in confined diblock copolymers," *Physical Review Letters*, vol. 76, pp. 2503–2506, apr 1996.
- [161] G. Coulon, T. P. Russell, V. R. Deline, and P. F. Green, "Surface-induced orientation of symmetric, diblock copolymers: a secondary ion mass-spectrometry study," *Macromolecules*, vol. 22, pp. 2581–2589, nov 1989.
- [162] J. Peng, Y. Xuan, H. Wang, B. Li, and Y. Han, "Solvent vapor induced dewetting in diblock copolymer thin films," *Polymer*, vol. 46, pp. 5767–5772, jul 2005.
- [163] U. Jeong, D. Ryu, D. Kho, J. Kim, J. Goldbach, D. Kim, and T. Russell, "Enhancement in the orientation of the microdomain in block copolymer thin films upon the addition of homopolymer," *Advanced Materials*, vol. 16, pp. 533–536, mar 2004.

-
- [164] M. M. A. Kashem, J. Perlich, L. Schulz, S. V. Roth, and P. Mller-Buschbaum, “Correlated roughness in polymer films containing maghemite nanoparticles,” *Macromolecules*, vol. 41, pp. 2186–2194, mar 2008.
- [165] D. W. Schubert and T. Dunkel, “Spin coating from a molecular point of view: its concentration regimes, influence of molar mass and distribution,” *Materials Research Innovations*, vol. 7, pp. 314–321, oct 2003.
- [166] D. Babonneau, S. Camelio, D. Lantiat, L. Simonot, and A. Michel, “Waveguiding and correlated roughness effects in layered nanocomposite thin films studied by grazing-incidence small-angle x-ray scattering,” *Physical Review B*, vol. 80, oct 2009.
- [167] C. P. Bean and J. D. Livingston, “Superparamagnetism,” *Journal of Applied Physics*, vol. 30, pp. S120–S129, apr 1959.
- [168] S. Mattauch, A. Koutsioubas, and S. Ptter, “MARIA: Magnetic reflectometer with high incident angle,” *Journal of large-scale research facilities JLSRF*, vol. 1, aug 2015.

List of publications

Publications related to the dissertation

- S. Xia, L. Song, K. Wang, S. Grott, M. Opel, M. Schwartzkopf, S. V. Roth, P. Müller-Buschbaum, “Spray-Coating Magnetic Thin Hybrid Films of PS-*b*-PNIPAM and Magnetite Nanoparticles”, *Adv. Funct. Mater.*, vol. 29, pp.1808427, 2019.
- S. Xia, L. Song, W. Chen, V. Körstgens, M. Opel, M. Schwartzkopf, S. V. Roth, P. Müller-Buschbaum, “Printed Thin Diblock Copolymer Films with Dense Magnetic Nanostructure”, *ACS Appl. Mater. Interfaces.*, vol. 11, pp. 21935–21945, 2019.
- S. Xia, L. Song, V. Körstgens, M. Opel, M. Schwartzkopf, S. V. Roth, P. Müller-Buschbaum, “Magnetic Nanoparticle-Containing Soft–Hard Diblock Copolymer Films with High Order”, *Nanoscale*, vol. 10, pp.11930–11941, 2018.
- S. Xia, E. Metwalli, M. Opel, P. A. Staniec, E. M. Herzig, P. Müller-Buschbaum, “Printed Thin Magnetic Films Based on Diblock Copolymer and Magnetic Nanoparticles”, *ACS Appl. Mater. Interfaces.*, vol. 10, pp. 2982–2991, 2018.

Further publications

- K.Wang, S.Xia, W.Cao, N.Hohn, S.Grott, L.P.Kreuzer, M.Schwartzkopf, S.V.Roth, P. Müller-Buschbaum, “Comparison of UV Irradiation and Sintering on Mesoporous Sponge-like ZnO Films Prepared from PS-*b*-P4VP Templated Sol-gel Synthesis ”, *ACS Appl. Nano Mater.*, vol. 1, pp.7139–7148, 2018.
- R.Wang, Y.Tong, K.Wang, S.Xia, E.Kentzinger, O.Soltwedel, P. Müller-Buschbaum, H.Frielinghaus “Monitoring the Morphological Evolution in Mixed-Dimensional Lead Bromide Perovskite Films with Lamellar-stacked Perovskite Nanoplatelets”, *Nanoscale Horiz.*, DOI:10.1039/C9NH00156E, 2019.

- N.Li, L.Song, L.Biessmann, S.Xia, W.Ohm, C.J.Brett, E. Hadjixenophontos, G.Schmitz, S.V.Roth, P. Müller-Buschbaum, “Morphology Phase Diagram of Slot-Die Printed TiO₂ Films Based on Sol–Gel Synthesis”, *Adv. Matter. Interfaces.*, pp.190058, 2019.
- L. Zheng, X. Wang, Y. Xia, S. Xia, E. Metwalli, B. Qiu, Q. Ji, S. Yin, S. Xie, K. Fang, S. Liang, M. Wang, X. Zuo, Z. Liu, J. Zhu, P. Müller-Buschbaum, Y. J. cheng, “Scalable in Situ Synthesis of Li₄Ti₅O₁₂/Carbon Nanohybrid with Supersmall Li₄Ti₅O₁₂ Nanoparticles Homogeneously Embedded in Carbon Matrix”, *ACS Appl. Mater. Interfaces*, vol. 10, pp.2591–2602, 2018.
- S. Yin, D. Zhao, Q. Ji, Y. Xia, S. Xia, X. Wang, M. Wang, J. Ban, Y. Zhang, E. Metwalli, X. Wang, Y. Xiao, X. Zuo, S. Xie, K. Fang, S. Liang, L. Zheng, B. Qiu, Z. Yang, Y. Lin, L. chen, C. Wang, Z. Liu, J. Zhu, P. Müller-Buschbaum, Y. J. cheng, “Si/Ag/C Nanohybrids with in Situ Incorporation of Super-Small Silver Nanoparticles: Tiny Amount, Huge Impact”, *ACS.Nano*, vol. 12, pp.861–875, 2018.
- N. Hohn, S. J. Schlosser, L. Biessmann, L. Song, S. Grott, S. Xia, K. Wang, M. Schwartzkopf, S. V. Roth, H. Iglev, R. Kienberger, P. Müller-Buschbaum, “Impact of Catalytic Additive on Spray Deposited and Nanoporous Titania Thin Films Observed via in Situ X-ray Scattering: Implications for Enhanced Photovoltaics”, *ACS Appl. Nano. Mater.*, vol. 1, pp. 4227–4235, 2018.
- N. Hohn, S. J. Schlosser, L. Biessmann, S. Grott, S. Xia, K. Wang, M. Schwartzkopf, S. V. Roth, P. Müller-Buschbaum, “Readily Available Titania Nanostructuring Routines Based on Mobility and Polarity Controlled Phase Separation of an Amphiphilic Diblock Copolymer”, *Nanoscale*, vol. 10, pp. 5325–45334, 2018.
- M. Wang, Y. Xia, X. Wang, Y. Xiao, R. Liu, Q. Wu, B. Qiu, E. Metwalli, S. Xia, Y. Yao, G. Chen, Y. liu, Z. Liu, J. Meng, Z. Yang, L. Sun, C. Yan. P.Müller-Buschbaum, J. Pan, Y. J. cheng, “Silicon Oxycarbide/Carbon Nanohybrids with Tiny Silicon Oxycarbide Particles Embedded in Free Carbon Matrix Based on Photoactive Dental Methacrylates”, *ACS Appl. Mater. Interfaces*, vol. 8, pp. 13982–13992, 2016.
- T.Cheng, G.Zhang, Y.Xia, Z.Sun, Z.Yang, R.Liu, S.Xia, E.Metwalli, Y.Xiao, X.Wang, M.Wang, J.Ban, L.Yang, Q.Ji, B.Qiu, G.Chen, H.Chen, Y.Lin, X.Pei, Q.Wu, J.Q.Meng, Z.Liu, L.Chen, T.Xiao, L.-D.Sun, C.-H.Yan, H.J.Butt, P.Müller-Buschbaum, Y.J.Cheng, “Porous Titania/Carbon Hybrid Microspheres Templated by in situ Formed Polystyrene Colloids”, *J. Colloid Interface Sci.*, vol. 469, pp. 242–256, 2016.

Scientific reports

- S. Xia, K. Biswas, M. Opel, S. Lafuerza, P. Glatzel, P. Müller-Buschbaum, “Crystalline polymer films embedded with magnetite nanoparticles”, *Lehrstuhl für Funktionelle Materialien, Annual Report*, 2018.
- S. Xia, L. Song, V. Körstgens, M. Opel, M. Schwartzkopf, S. V. Roth, P. Müller-Buschbaum, “In situ investigation on sprayed polymer films embedded with magnetic nanoparticles”, *Lehrstuhl für Funktionelle Materialien, Annual Report*, 2018.
- S. Xia, E. Metwalli, A. Koutsoumpas, P. Müller-Buschbaum, “Neutron reflectivity investigation on thermo-responsive copolymers with embedded magnetic nanoparticles”, *Heinz Maier-Leibnitz Zentrum*, 2017.
- S. Xia, L. Song, V. Körstgens, M. Opel, M. Schwartzkopf, S. V. Roth, P. Müller-Buschbaum, “Magnetic nanoparticles-containing diblock copolymer films with high order”, *Lehrstuhl für Funktionelle Materialien, Annual Report*, 2017.
- S. Xia, E. Metwalli, M. Opel, P. A. Staniec, E. M. Herzig, P. Müller-Buschbaum, “Printed diblock copolymer films embedded with magnetic nanoparticles”, *Lehrstuhl für Funktionelle Materialien, Annual Report*, 2016.
- S. Xia, E. Metwalli, M. Opel, P. A. Staniec, E. M. Herzig, P. Müller-Buschbaum, “Diblock copolymer films embedded with magnetic nanoparticles”, *Lehrstuhl für Funktionelle Materialien, Annual Report*, 2015.
- S. Xia, E. Metwalli, Y. Yao, P. Müller-Buschbaum,, “Magnetic field guided hybrid films of diblock copolymer and iron oxide nanoparticles”, *Lehrstuhl für Funktionelle Materialien, Annual Report*, 2014.

Conference talks

- S. Xia, J. Kang, C. Ko, “Dynamic investigation on polymer solution”, *E13 Polymer Physics Summer School*, Obertauern (Austria), June 2018.
- S. Xia, V. Körstgens, M. Opel, M. Schwartzkopf, S. V. Roth, P. Müller-Buschbaum, “Investigation on printed diblock copolymer film embedded with magnetic nanoparticles”, *8th international workshop on polymer metal nanocomposites*, Prague (Czech Republic), September 2017.
- S. Xia, E. Metwalli, M. Opel, P. A. Staniec, E. M. Herzig, P. Müller-Buschbaum, “Magnetic thin films printed with diblock copolymer and magnetic nanoparticles”, *E13 Polymer Physics Summer School*, Grainau (Germany), June 2017.

- S. Xia, E. Metwalli, M. Opel, P. A. Staniec, E. M. Herzig, P. Müller-Buschbaum, “Printed block copolymer films with embedded magnetic nanoparticles”, *DPG-Frühjahrstagung*, Dresden (Germany), March 2017.
- S. Xia, D. Yang, “Block copolymers”, *E13 Polymer Physics Summer School*, Ober-
tauern (Austria), June 2016.
- S. Xia, E. Metwalli, M. Opel, P. A. Staniec, E. M. Herzig, P. Müller-Buschbaum, “Magnetic nanoparticles embedded in diblock copolymer films”, *The polymer-metal interface*, Garching (Germany), March 2016.

Conference poster presentations

- S. Xia, E. Metwalli, A. Koutsioumpas, P. Müller-Buschbaum, “Neutron reflectivity investigation on thermo-responsive copolymers with embedded magnetic nanoparticles”, *German conference for research with synchrotron radiation, neutrons and ion beams at large facilities*, Garching (Germany), September 2018.
- S. Xia, E. Metwalli, A. Koutsioumpas, P. Müller-Buschbaum, “Neutron reflectivity study on thermo-responsive copolymers embedded with magnetic nanoparticles”, *JCNS-Workshop "Neutron Scattering on Nano-Structured Soft Matter"*, Tutzing (Germany), October 2017.
- S. Xia, E. Metwalli, P. Müller-Buschbaum, “Neutron Reflectivity Investigation on Thermo-responsive Copolymers Embedded with Magnetic Nanoparticles”, *German conference on neutron scattering*, Kiel (Germany), September 2016.
- S. Xia, E. Metwalli, Y. Yao, P. Müller-Buschbaum, “Printed nanostructured block-copolymer/metal-oxide hybrid films”, *DPG-Frühjahrstagung*, Regensburg (Germany), April 2016.
- S. Xia, E. Metwalli, Y. Yao, M. Schwartzkopf, D. Chekrygina, B. Beyersdorff, S.V. Roth, P. Müller-Buschbaum, “In-situ GISAXS investigation of aluminum deposition on PS-b-P3HT diblock copolymer thin films ” *DPG-Frühjahrstagung*, Berlin (Germany), March 2015.

Acknowledgments

To begin with, I am grateful to my supervisor Prof. Dr. Peter Müller-Buschbaum for offering me the opportunity to work in the field of magnetic polymer films. He provides a good experimental and working environment as well as helpful suggestions and guidance throughout my whole Ph.D. period. His solid knowledge and expertise are a strong support for me to overcome all challenges in my scientific research. Besides scientific support, his trust, encouragement and patience always raise my spirits to keep on my Ph.D. studies. Thanks very much for him to help me to bolster my confidence in scientific research. Furthermore, the experience of beamtimes and conferences will be a precious treasure in my future life, thanks go to him again.

The China Scholarship Council (CSC) is gratefully acknowledged for funding. Its financial support liberate me from economic worry about my living expense during the Ph.D. period.

Many thanks to Dr. Ezzeldin Metwalli Ali for his infinite patience to help me get started in my Ph.D. studies. Also, a great thank to Dr. Weijia Wang and Dr. Ling Song, who patiently guided me to all data process techniques involved in my work. I enjoy the time working with them and hope they will have a bright future.

I will not accomplish my research without the aid of my dear colleagues. In no specific order, I want to thank Dr. Volker Körstgens, Dr. Eva M. Herzig, Dr. Martine Philipp, Dr. Qi Zhong, Dr. Shuai Guo, Dr. Claudia M. Palumbiny, Dr. Christoph Schaffer, Dr. Daniel Moseguí González, Dr. Bo Su, Dr. Yuan Yao, Dr. Johannes Schlipf, Dr. Stephan Pröller, Dr. Nitin Saxena, Dr. Nuri Hohn, Dr. Lorenz Bießmann, Franziska Löhner, Lucas Kreuzer, Tobias Widmann, Dan Yang, Kun Wang, Sebastian Grott, Julian Heger, Nuri Hohn, Anna-Lena Oechsle, Roy Schaffrinna, Simon Jakob Schaper, Sebastian Grott, Dominik Schwaiger, Wei Chen, Wei Cao, Nian Li, Xinyu jiang, Shanshan Yin. Within their helps over numerous experiments, data analysis and extensive discussions, I am able to push my research forward. Particularly, many thanks go to the colleagues involved in the beamtimes with me. Without their efforts, I would not obtain reasonable experimental results. Besides the scientific research, I really enjoy the friendly working atmosphere built up by all people from Lehrstuhl für Funktionelle Materialien. Non-scientific activities in

our chair such as summer and winter hikes, summer BBQs, Christmas parties, beer-festive trips bring me countless moments of joy throughout my whole Ph.D. period. Thanks to the people who I have not yet mentioned: Prof. Dr. Christine M. Papadakis, Dr. Anatoly Berezkin, Dr. Xiaohan Zhang, Dr. Jenny Lebert, Bart-Jan Niebuur, Jia-Jhen Kang, Florian Jung, Mihael Čorić, Oliver Filonik, Lennart Reb, Shambhavi Pratap, Marion Waletzki, Carola Kappauf, Susanna Fink.

The support from experienced beamline scientists and technicians is a guarantee for the success of all beamtimes. Many thanks for their guidance, help and patience. I would like to thank Prof. Dr. Stephan V. Roth, Dr. Matthias Schwartzkopf (P03/DESY), Dr. Alexandros Koutsoumpas (MLZ). Besides beamline scientists, many thanks to Prof. Dr. Alexander W. Holleitner and Peter Weiser from WSI, who provide me the access to AFM and SEM measurements. Also many thanks to Dr. Matthias Opel (WMI) who performed the SQUID measurements for me.

I am sincerely grateful to Dr. Volker Körstgens, Dr. Lin Song, Dr. Nitin Saxena, Dr. Lorenz Bießmann, Franziska Löhner, Tobias Widmann and Lucas Kreuzer, Roy Schaf-frinna, Simon Jakob Schaper, Dominik Schwaiger, Sebastian Grott, Julian Heger and Christina Geiger for proof reading of the present thesis. All corrections are valuable for the improvement of my thesis.

I would like to thank our secretaries Marion Waletzki, Carola Kappauf and Susanna Fink. They offer me great helps on my administration, visa extension, trips, purchases and reimbursements. In addition, many thanks to Dr. Volker Körstgens and Dr. Nitin Saxena, who can always be found when I have problems regarding German translation. With respect to the life outside of work, I would like to thank Dr. Weijia Song, Dr. Lin Song, Dr. Shuai Guo, Wei Liu, Franziska Löhner and Mihael Čorić to invite me to their private activities.

Finally, a big thank-you goes to my family. My wife, parents, parents-in-law and sister always give me unconditional support whenever I need. My family is the warmest harbor, where I always feel happy, reliable and at ease. Particularly, I want to thank my fabulous wife Leyan Zheng for her accompaniment throughout my whole Ph.D. study as well as for her enormous endorsement in my work and personal life.